Thermally generated convection and precipitation over volcanoes: Numerical modelling of flow over Montserrat

A thesis submitted to the School of Environmental Sciences of the University of East Anglia in partial fulfilment of the requirements for the degree of Doctor of Philosophy

By Alexandros-Panagiotis Poulidis

April 2015

Abstract

Atmospheric flow over orography is a classic research area, while the atmospheric response to surface heating has become a focus more recently in the context of solar heating and forest fires. Here, for the first time, these forcing mechanisms are superposed to examine atmospheric flow over a mountain with a heated summit, i.e. an active volcano.

Intense rainfall over active volcanoes is known to trigger dangerous volcanic hazards, from remobilising loose surface material into lahars or mudflows, to initiating explosive activity such as pyroclastic flows. The effect of a heated volcanic surface on the atmospheric circulation is investigated here – including examining the triggering of precipitation over the volcano. Recent activity at the Soufrière Hills Volcano (SHV), Montserrat, Eastern Caribbean, is a well-documented example of such rainfall–volcano interactions. Hence, Montserrat is used as a template for the experiments, although the experimental setup is general so the results will have applicability for other tropical island volcanoes.

The Weather Research and Forecasting (WRF) atmospheric model has been used for the study, run in an idealised configuration with horizontal grid sizes down to 100 m. Initially, the effect of the heated surface is studied through idealised simulations over a Gaussian mountain with an imposed surface temperature anomaly on the volcano summit. Subsequently, a digital elevation model (DEM) of Montserrat is used to study the effects over this specific island. The atmospheric structure in most simulations is that of a typical tropical setting – easterly Trade Winds, capped by a temperature inversion. In these cases, localised convection triggered by the heat source can overcome convective inhibition and force deep convection, if there is sufficient convective available potential energy. A significant increase in precipitation over the volcano covering a 4 km^2 area is consistently simulated for surface temperature anomalies above 40°C, an area-average value that is exceeded at the SHV. For a range of realistic atmospheric conditions, covering up to 18% of days in a relevant climatological study in the Caribbean, the precipitation increase is well above the observed threshold (5–10 mm hr^{-1}) required to trigger explosive volcanic activity. Hence, the thermal forcing of the atmosphere due an active, but non-erupting, volcano appears to be an important factor in rainfall–volcano interactions and should be taken into account in hazard assessment.

Acknowledgements

"The Patrician was a pragmatist. He never tried to fix things that worked. Things that didn't work, however, got broken."

–Terry Pratchett, Soul Music

First of all I would like to thank Ian Renfrew and Adrian Matthews for (among other things) giving me the opportunity to do this research, for their help, endless patience, support, understanding, and kindness... The list goes on and trying to enumerate all the reasons why I am grateful for their supervision would become a thesis on its own. Most of all, I would like to thank them for making me believe in myself at times that I though it was impossible.

I would also like to thank my family for their support throughout this endeavour - my father for teaching me to ask questions and search for answers, my sister for being a role model for me, and my brother for always making sure that I have somewhere I can call home, even if I am thousands of kilometers away. I'd also like to thank my mother for helping me become the person I am. I can always only hope that I would make her proud. I'd like to thank all of my friends for the help and support - Gerasimos for the hours spent talking on the phone discussing about our respective anxieties, Honza for all the beers and the late nights in the office, Eleni for her beautiful voice, everyone in the UEA Japan Society and Karate Club, Luke, Tom, Kostas, Nikos, Ed, Ilia, and everyone else that helped me through the years.

I would like to thank Daniel Kirshbaum for the interesting discussions, his involuntary impact on my project, and for inspiring me through his research, Chris Steele for his help in getting started with WRF, Mel Froude and Mel Plail for sharing their expertise (and data) of Montserrat, as well as the rest of office 3.16 for all the fun we had together. Also, I would like to thank the WRF-Help mailing service, as well as the HPC and linux support in UEA.

Finally, most of all, I would like to thank Mariko for her love, support and unwavering faith and confidence in me... I'm sorry I made you wait so much.

Contents

Chapter 1

Introduction

1.1 Introduction

Volcanoes have always been a source of awe and fear, often being deified and revered by local people. Their beauty is matched by their potential for destruction, with a number of devastating hazards such as pyroclastic flows, lahars and tsunamis being associated with volcanic eruptions. The study of volcanic hazards, like many geological hazards, is made difficult by the complexity of the underlying physics of the initiation mechanisms. In the case of volcanoes, rainfall is featured prominently, acting as a trigger for explosive eruptions, pyroclastic flows, and lahars. Due to this link, the impact of rainfall on volcanoes is a topic that has been investigated over the years. However, the opposite, the impact of a volcano on rainfall and atmospheric flow in general remains an unexplored field.

The aim of this study is to analyse the effect of surface heating due to volcanic activity on the atmospheric circulation and rainfall. Thus, the main hypothesis tested by the study is that: *the thermal forcing by a volcano can generate atmospheric circulation changes that can cause localised rainfall and impact the behaviour of the volcano*. The conceptual model being tested (Figure 1.1) uses a framework of an easterly background flow with a tradewind inversion. The flow over the top of the volcano is subject to thermal forcing via the surface fluxes from the strongly heated volcanic surface. This is hypothesised to be sufficient for convective plumes to break through the inversion, releasing the high values of convective available potential energy (CAPE) present in the background state, and leading to intense localised rainfall over the volcano.

This chapter is organised as follows. Initially the basic theory of atmospheric flow in

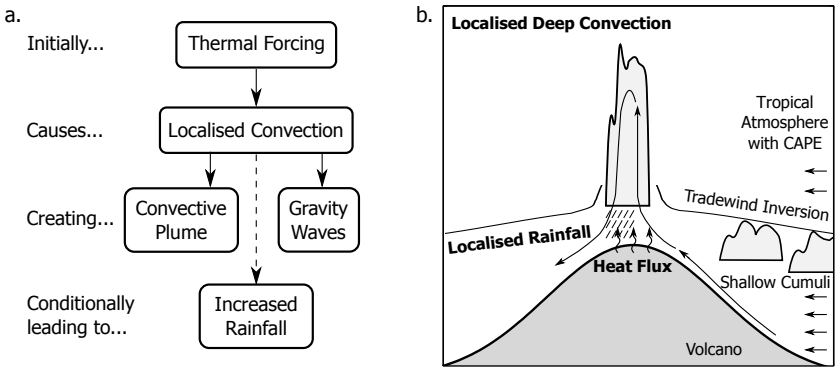

Figure 1.1: (a) Conceptual model under study. (b) Schematic describing the proposed mechanism. A background of easterlies with a shallow cumulus field under the tradewind inversion meets the volcano. The flow over the summit of the volcano is heated and locally breaks through the inversion, resulting in deep convection and high local rainfall rates.

the vicinity of mountains and related phenomena will be presented (Section 1.2), followed by a brief discussion on orographic rainfall (Section 1.3), and flow over heated terrain (Section 1.4). After this some basic characteristics of volcanic lava domes and volcanic hazards will be presented (Section 1.5), followed by an introduction to Montserrat, the island that has provided a motivation and a "template" for this study (Section 1.6). Finally there is a short discussion (Section 1.7) and a presentation of the thesis structure.

1.2 Orographic flow and gravity waves

Orographic flow is the resulting flow as the air in the atmosphere is forced to interact with isolated mountains or mountain ranges. This interaction creates a variety of phenomena depending on a number of parameters, such as mountain height and aspect ratio, atmospheric stability and wind speed among others. The area has been heavily researched in the last century, starting with studies such as the ones by Queney (1948), Eliassen and Palm (1961) and Drazin (1961). The starting point for obtaining a linear solution here is the following set of equations for a stratified Boussinesq fluid (a fluid studied under the Boussinesq approximation, where density differences are considered sufficiently small to be neglected if they are not multiplied by g):

$$\rho_0 \frac{D\mathbf{u}}{Dt} = -\nabla p - \rho g \mathbf{k} + \mu \nabla^2 \mathbf{u} \tag{1.1}$$

$$\nabla \mathbf{u} = 0 \tag{1.2}$$

$$\frac{D\rho}{Dt} = \kappa\nabla^2\rho \tag{1.3}$$

where ρ_0 is a constant reference density, $\mathbf{u}$ is the velocity vector, p is pressure, ρ is density, g is the acceleration due to gravity, μ is viscosity and κ is the von Kármán constant. Equation 1.1 is the Navier-Stokes equation (a form of the Cauchy momentum equation), Equation 1.2 is the continuity equation, and Equation 1.3 is used to allow for mass diffusion. Three assumptions are made to simplify the equations, that the flow is: *(i) inviscid*, and *(ii) non-diffusive*, or $\partial/\partial t = \mu = \kappa = 0$, and that the horizontal scale is significantly larger that the vertical ($L_H L_V^{-1} \gg 1$). Finally, these are used with two conservation laws, *Bernoulli's Law* and the *conservation of potential vorticity*, to produce:

$$p * (x, y, z) = g \int_z^\infty \rho' dz \tag{1.4}$$

where $p*$ is the difference between the pressure at a point (x,y,z) and at a point at the same elevation far away ($\inf$,$\inf$,z), ρ' is the density anomaly. Despite the complexity, progress in the mathematical approach towards a solution has been made by the use of linear theory: for example to study the resulting gravity waves (also known as mountain waves) as the flow is forced to go over the obstacle (Smith, 1980, 1989).

There are two kinds of gravity waves, internal and external. Although there is familiarity with external gravity waves (the waves seen at the surface of water) internal gravity waves are more difficult to picture. These are created in the same way by the restoring forces of buoyancy: as an air parcel is vertically displaced (for example due to forced ascent or descent), in a stably stratified atmosphere, a restoring force will act to accelerate the parcel back towards the original level of equilibrium. In the absence of pressure gradient forces the parcel will oscillate vertically at a frequency called the Brunt-Väisälä frequency (N):

$$N^2 = \frac{g}{\theta_0}\frac{d\overline{\theta}}{dz} \tag{1.5}$$

where θ_0 is the potential temperature at the surface, and $d\overline{\theta}/dz$ is the mean vertical gradient of the ambient potential temperature. Note, N is only defined for a statically stable

atmosphere. Oscillations at any frequency less that N can be accommodated by a certain angle in the sloping trajectory. It is, though, impossible to have oscillations at higher frequencies. The linearised solution of airflow over an idealised mountain, along with a schematic of the distributions of various physical quantities is presented in Figure 1.2. For a comprehensive presentation of the original equations and solutions, the reader is referred to Queney (1948) and Smith (1989).

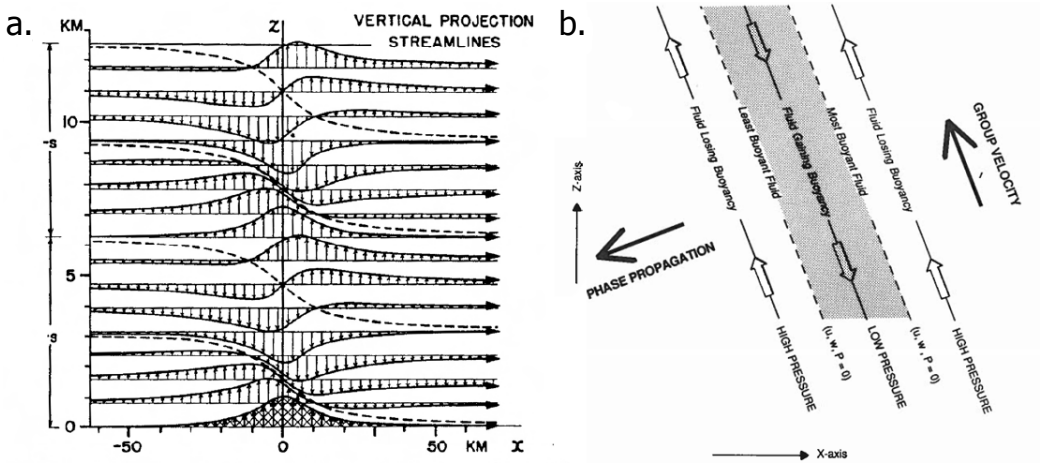

Figure 1.2: (a) Linearised solutions by Queney (1948) for hydrostatic airflow over a Witch-of-Agnesi shaped ridge. The steady pattern is composed of vertically propagating gravity waves which do not disperse (Smith, 1989). Panel (a) shows vertical velocity as a function of height through the troposphere (b) The instantaneous distribution of velocity, pressure and buoyancy perturbations in an internal gravity wave on the x-z plane. The phase of the wave is constant along the slanting, dashed and solid lines. Velocity and pressure perturbations have extrema along the solid lines; buoyancy perturbations are zero along the solid lines. Buoyancy perturbations have extrema, and velocity and pressure perturbations are zero along the dashed lines. Small arrows indicate the perturbation velocities, which are always parallel to the lines of constant phase. Large arrows indicate the direction of the phase propagation and the group velocity (Durran, 1990)

Aside from the gravity wave response in the flow, several other effects can be observed. Based on results from linear theory, Smith (1989) was able to produce a regime diagram of the non-dimensional mountain height ($\hat{h} = H\ N\ U^{-1}$, where H is the height of the obstacle, N is the Brunt-Väisälä frequency and U is the incoming wind speed) against the aspect ratio of the mountain ($R = L_y\ L_x^{-1}$, where $R = L_i$ is the length of the mountain in the i direction), detailing the limits within which the different effects would be observed (Figure 1.3a). Aside from mountain waves, the two responses noted in the figure are "flow splitting" and "wave breaking". Flow splitting necessitates the existence of a point at a certain height where, due to the lack of kinetic energy, the air parcel cannot ascend and splits into two parts flowing around the mountain (Figure 1.3d). The existence or not of flow splitting, along with the Froude number (the inverse of non-dimension

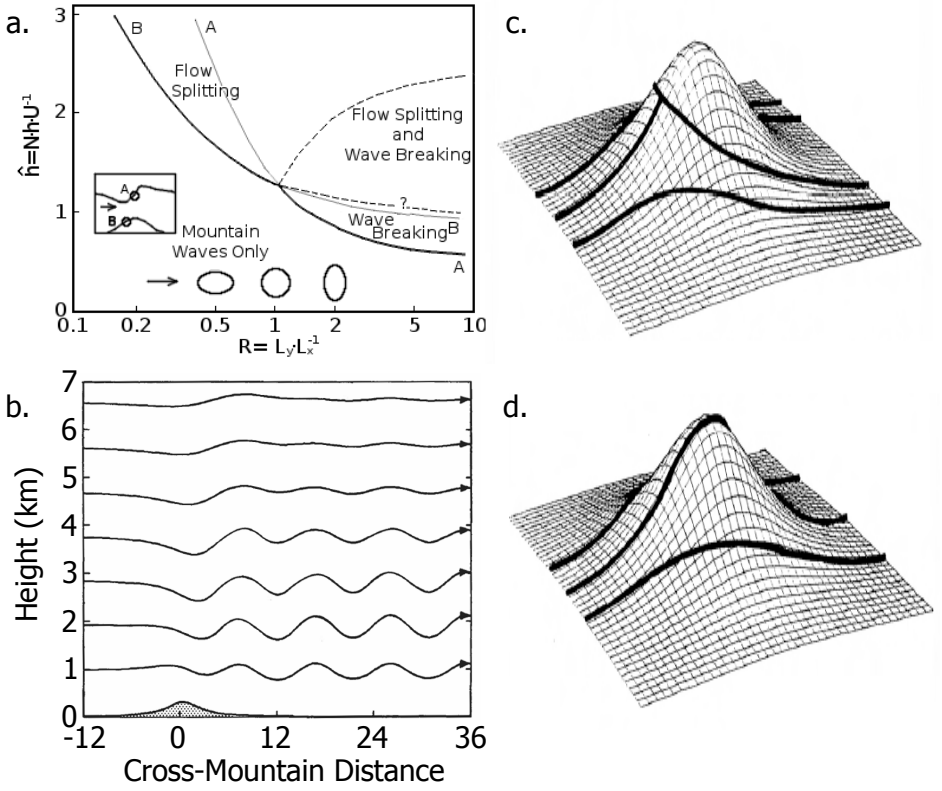

Figure 1.3: (a) Regime diagram based on Smith (1989). The diagram defines flow regimes as a function of the non-dimensional mountain height $\hat{h}$ and the aspect ratio of the hill (R). Curve A/B shows the limit of stagnation aloft (wave breaking)/in the windward slope (flow splitting). The dotted lines signify the area beyond which linear theory is technically invalid, while dashed lines are the suggested critical values for flow splitting and wave breaking within the non-linear regime (Ólafsson and Bougeault, 1996). (b) Streamlines in steady airflow over an isloated ridge when the Scorer parameter permits trapped lee waves (Durran, 1990). Right side: Possible geometry of (c) nonsplit (flow over) and (d) split (flow around) flow past a hill. Split flow is characterised by the existence of a stagnation point at which streamlines can divide. Streamlines shown on the lower boundary.

mountain height, $Fr = \hat{h}^{-1}$) can help broadly characterise the flow regime as a "flow around" (low kinetic energy, flow splitting or "blocked") or "flow over" (high kinetic energy, no flow splitting) regime (Figure 1.3c). Wave breaking is the phenomenon where, due to the unsustainable amplitude of the oscillation, energy from the wave is transformed to turbulent kinetic energy. Both effects signify a non-linear response and cannot be fully explained by linear theory. The validity of this regime diagram (Figure 1.3a) has been broadly confirmed by Ólafsson and Bougeault (1996), while phenomena in the non-linear areas were first investigated by Smolarkiewicz and Rotunno (1989, 1990). Despite the fact that the accuracy and exact limits of the chart have been questioned (specifically the critical value for wave breaking; Ólafsson and Bougeault, 1996), it is still used in order to obtain general insight on the expected phenomena, especially for cases that fall within

the linear theory area. Vertical variations in the incoming flow speed and Brunt-Väisälä frequency can also lead to a qualitatively different kind of wave - a trapped lee wave (Figure 1.3b). In this case the activity is largely confined in the troposphere. The existence of such waves is based on the Scorer parameter ($l = N\,U^{-1}$): in a two layer setting trapped lee waves are expected when $l_L^2 - l_U^2 > 0.25\,\pi^2\,H^{-2}$, where l_L and l_U are the Scorer parameters for the lower and upper atmosphere respectively.

As computational power and numerical models have become more advanced, computational modelling has allowed studies in the non-linear regime. Smolarkiewicz and Rotunno (1989, 1990) studied the mountain wave response as well as the flow characteristics in the very non-linear areas ($Fr \ll 1$). Some basic results from these studies are presented in Figure 1.4. For $Fr = 0.2$ (Figure 1.4a) there is an absence of a strong gravity wave response, instead there is the generation of rotors and the creation of two twin counter-rotating vortices in the lee of the mountain. As the Froude number increases ($Fr = 0.2$; Figure 1.4b) the response becomes more linear with the propagation of gravity waves. Additionally, in both cases areas of hydraulic jumps (almost vertical jumps in the streamlines) can also be seen in the lee, starting at low heights in Figure 1.4b and higher in Figure 1.4c. Long (1954) suggested that a hydraulic jump occurs due to the transition from subcritical ($Fr < 1$) to supercritical ($Fr > 1$) flow at the top of the mountain. As a parcel is forced to descend, under these circumstances, the parcel continues to accelerate during descent, producing very high wind speeds (known as downslope wind), and the parcel can rapidly return to its original level as the potential energy of the parcel can be transformed to kinetic energy in a hydraulic jump. For a more comprehensive analysis the reader is directed to Smith (1989) and Durran (1990).

1.3 Orographic rainfall

Orographic rainfall occurs as a result of air mechanically lifted over an obstacle (a mountain or ridge). The phenomenon is based on the Clausius-Clapeyron relation - as air is forced to ascend over a mountain it will adiabatically cool until it saturates and the water vapour will start condensing into liquid water, eventually leading to rainfall on the windward side (Figure 1.5). Understanding in the area has been expanded by the use of

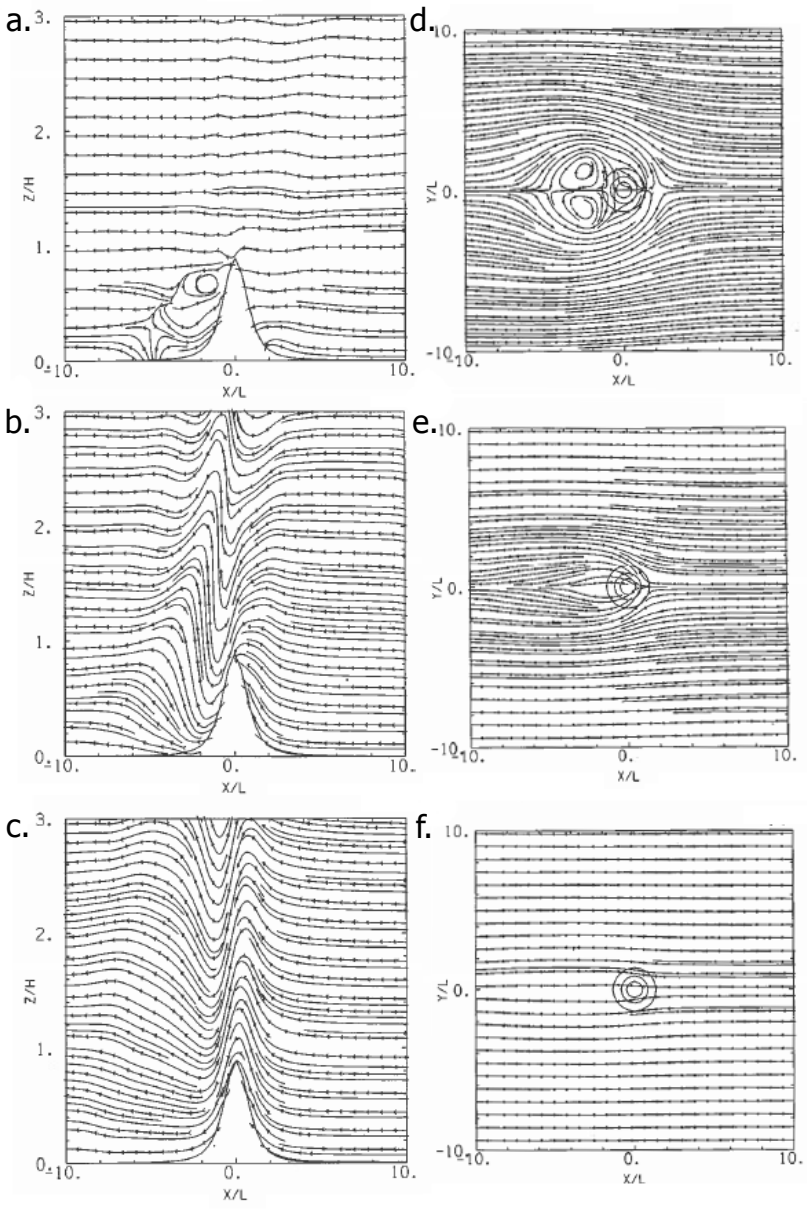

Figure 1.4: Streamlines in the x-z (left column) and x-y (right column) plane through the centre of a circular bell-shaped mountain (left column) and on the surface of the topography (right column), for (a), (d) $Fr = 0.2$, (b), (e) $Fr = 0.7$, (c), (f) $Fr = 2.2$. Airflow is from right to the left. From Smolarkiewicz *et al.* (1988).

observational data along with mathematical and computational modelling, helping establish a deeper understanding of the underlying physics (Roe, 2005). As with orographic flow studies, mathematical modelling tends to focus on applying linear theory to parts that can be approximated by linear processes (e.g. Smith and Barstad, 2004), while computational modelling is used for a mix of studies with ranging degrees of idealisation, to help understand specific phenomena, the relation between the numerous control parameters (mountain, location or atmosphere-related) and the resulting rainfall, and case

studies, used to test our understanding and offer insights on specific, and sometimes extreme, events (Miglietta and Buzzi, 2001; Kirshbaum and Durran, 2004; Chen and Lin, 2005).

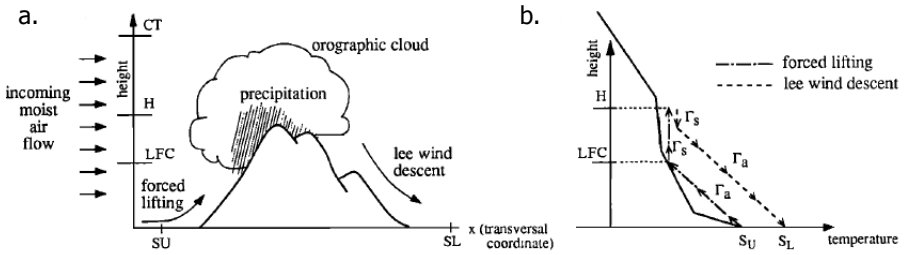

Figure 1.5: Development of orographic cloud systems: (a) illustration of the orographic lifting effect and (b) pseudoadiabatic chart representations. Shown on the figure are the level of free convection (LFC), and the unsaturated and saturated adiabats (Γ_a and Γ_s respectively). Modified from (Barros and Lettenmaier, 1994)

The stability of the atmosphere can greatly affect the resulting flow, with a stable atmosphere leading to reduced orographic rainfall, and an unstable environment leading to enhanced orographic rainfall, connected to the convective instability (CIN) of the atmosphere that is triggered by the flow (Figure 1.6). Although when dealing with dry atmosphere cases it is fairly easy to categorise the expected flow into the "flow around" and "flow over" regimes as seen in Section 1.2, it becomes impossible to categorise moist cases based solely on the moist Froude number, as other parameters such as convective available potential energy (CAPE) and an inversion in the temperature profile can heavily affect the flow (Chen and Lin, 2005).

Due to the potential impact this process can have in the local climate it has been featured prominently in research at the midlatitudes (see review papers by Roe, 2005; Houze, 2012). There has been a notable gap of focus in the Tropics or sub-Tropics as outlined by (Minder *et al.*, 2013). There, the local climate is dominated by humid, easterly winds known as the trade winds. Although islands tend to be less significant in size than mountain ranges the interactions between the very moist air flowing over the sea and the mountains can have a significant impact heavily depending on the location and the topographic characteristics. Recent studies have shown that aside from the diurnally-forced deep convection and tropical cyclones (Houze, 2012), shallow convection, controlled not by thermal forcing but forced ascent, can have a significant effect on the local precipitation, for example in Dominica (Kirshbaum and Smith, 2009; Minder *et al.*, 2013) and

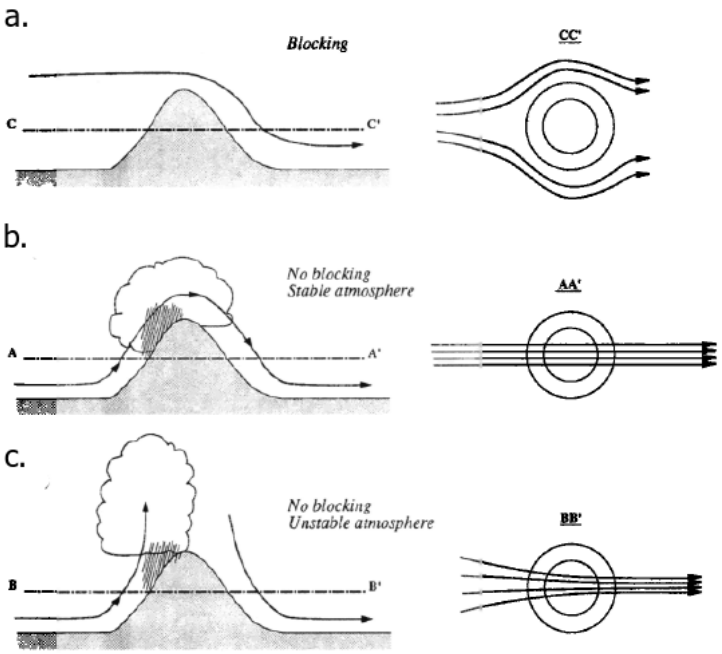

Figure 1.6: Orographic influences on atmospheric circulation: (a) blocking, (b) no blocking in a stable atmosphere, and (c) no blocking in a conditionally unstable atmosphere. (Barros and Lettenmaier, 1994)

Guadeloupe (Cécé *et al.*, 2014). Although the resulting flows vary depending on the location and the size of the island and the mountain, the general response can be summarised as greater cloud cover over the windward side, with enhanced convection and precipitation as the cumulus field created over the ocean interacts first with the coastline and then with the mountain. Depending on the mountain characteristics, the resulting orographic rainfall can be substantially higher (a factor of 10) than both the rainfall over the sea, and the rainfall caused by the convection as the flow meets the land (Kirshbaum and Smith, 2009; Smith *et al.*, 2009). For a more comprehensive discussion on orographic rainfall the reader is directed to Barros and Lettenmaier (1994), Roe (2005) and Houze (2012).

1.4 Flow over heated terrain

Another area that has benefited greatly by the advance of computational models is the study of (dry or moist) flows over heated terrain. For this kind of perturbation to have an effect on the flow, the heating needs to be applied in a way that creates baroclinicity - either uniform heating over a mountain or differential heating over a flat surface (Crook and Tucker, 2005).

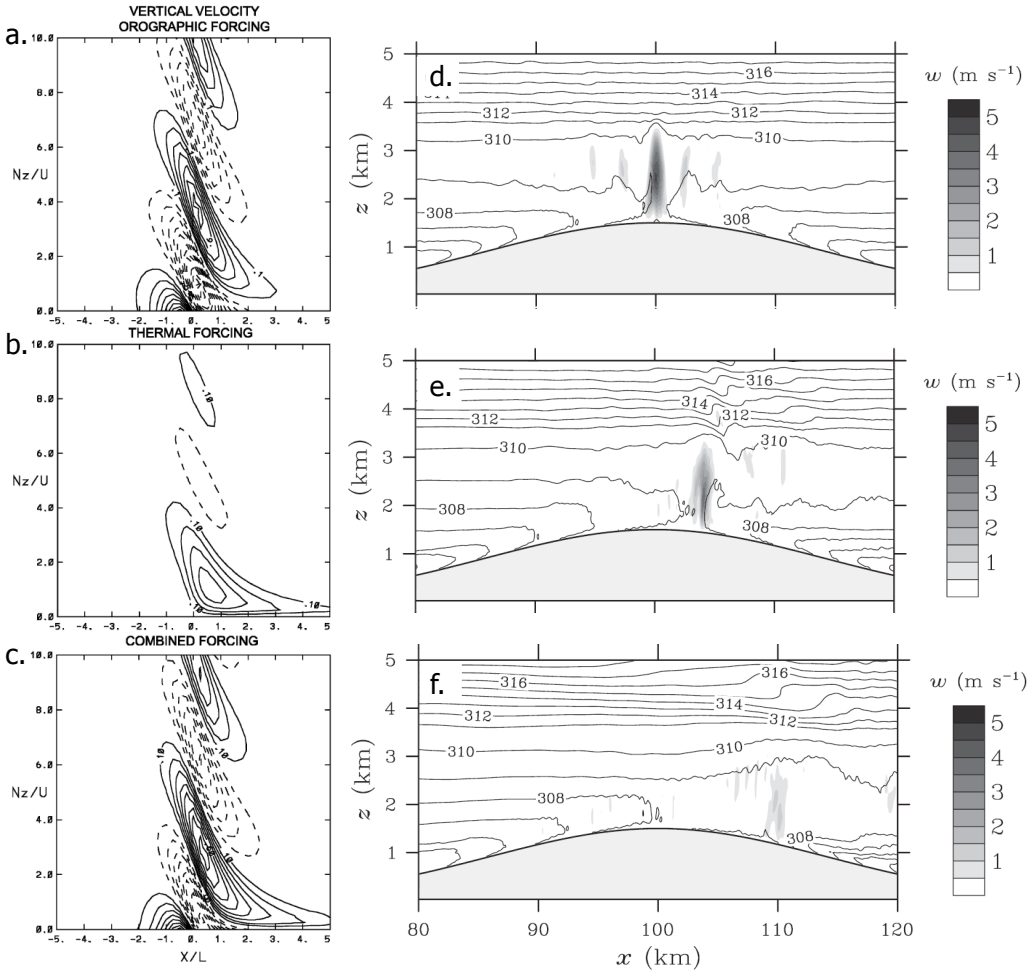

Figure 1.7: Results from studies on flow over heated terrain. Left column: Normalised vertical velocity for flow past heated terrain based on a linear solution: (a) the orographic response, (b) thermal response, (c) combined response. Contour interval is 0.1 (non-dimensionalised vertical velocity). From Crook and Tucker (2005). Right column: The strength of thermally induced mountain updrafts, as shown by vertical velocity (shading) over a 60–min window on hours 5–6 of a dry simulation for: (d) $U = 0$ m s^{-1}, (e) $U = 1.5$ m s^{-1}, (f) $U = 3$ m s^{-1}. Flow from left to right. The overlaid black contours are potential temperature isolines. From Kirshbaum (2011).

Crook and Tucker (2005) created a mathematical model based on linear theory that was able to capture the essential features of numerical model runs and real case studies (Figures 1.7a–1.7c; Tucker and Crook, 2005). They showed that, for a linear case, the flow responds in a very similar way to the mountain, i.e. by a series of gravity waves of characteristics depending on the heating source. As this is a linear approximation, the combined forcing resulted in the combined effect of the two forcings. Kirshbaum (2011) also studied the effect of solar heating on a mountain, by use of computational modelling (results from the dry simulations can be seen in Figures 1.7d–1.7f). Without background wind (Figure 1.7d) the heating leads to a symmetric, localised convective

cell but as the wind grows stronger the cell is moved towards the lee of the mountain and almost dissipates (Figures 1.7e–1.7f). Much like the thermal forcing in Figure 1.7b, gravity waves propagating on top of the convective cell can also be seen in Figures 1.7e–1.7f.

Kirshbaum (2013) expanded this research in an effort to study the limits of linear theory, as well as to further study and categorise possible regimes in the flow. For this study he used dry simulations and tested two theories: linear theory (modified from Crook and Tucker, 2005) and the heat-engine theory, based on thermodynamics that was initially proposed by Rennó and Ingersoll (1996) and later extended in numerous studies (Souza *et al.*, 2000; Tian and Parker, 2003; Kirshbaum, 2013). Kirshbaum (2013) demonstrated that the application of linear theory for two layer flows (for example an atmospheric structure with characteristics varying between the boundary layer and the troposphere) is severely limited due to the non-linear effects that are introduced by the difference between the layers. The flow responses were separated into three groups, "Growth-Decay" (GD), "Ventilation" (VE), and "Stratification" (ST), depending on the relative magnitude of the forcings. The GD response happens when the heating term is balanced by the time-dependancy of the heating source and/or dissipation terms. For the VE regime the heating is balanced by the linear advection term and for the ST regime, the heating is balanced by the stability term.

As in Section 1.3, this kind of mechanism can be associated with the strengthening or generation of severe storms in a similar way as mountains can enhance rainfall: they can act as a trigger for convection that, in a combination with an unstable or conditionally unstable atmosphere can produce severe weather (Crook and Tucker, 2005; Kirshbaum, 2011). The initiation of such a storm can be seen in Figure 1.8. Kirshbaum (2011) argued that instead of deep ascent of a single updraft, it is more likely that the convection is caused by a rapid succession of thermals vented through the convergence zone into a deepening cloud mass. This can be seen in Figure 1.8f, where the updrafts noted as C1 and C2 merge and develop to form deep convection.

Recently attention has also focused on the impact of wild fires in the generation of pyrocumulus clouds (Gatebe *et al.*, 2012) and the initialisation of storms (Cunningham and Reeder, 2009). Wild fires lead to a localised maximum in surface temperature, along

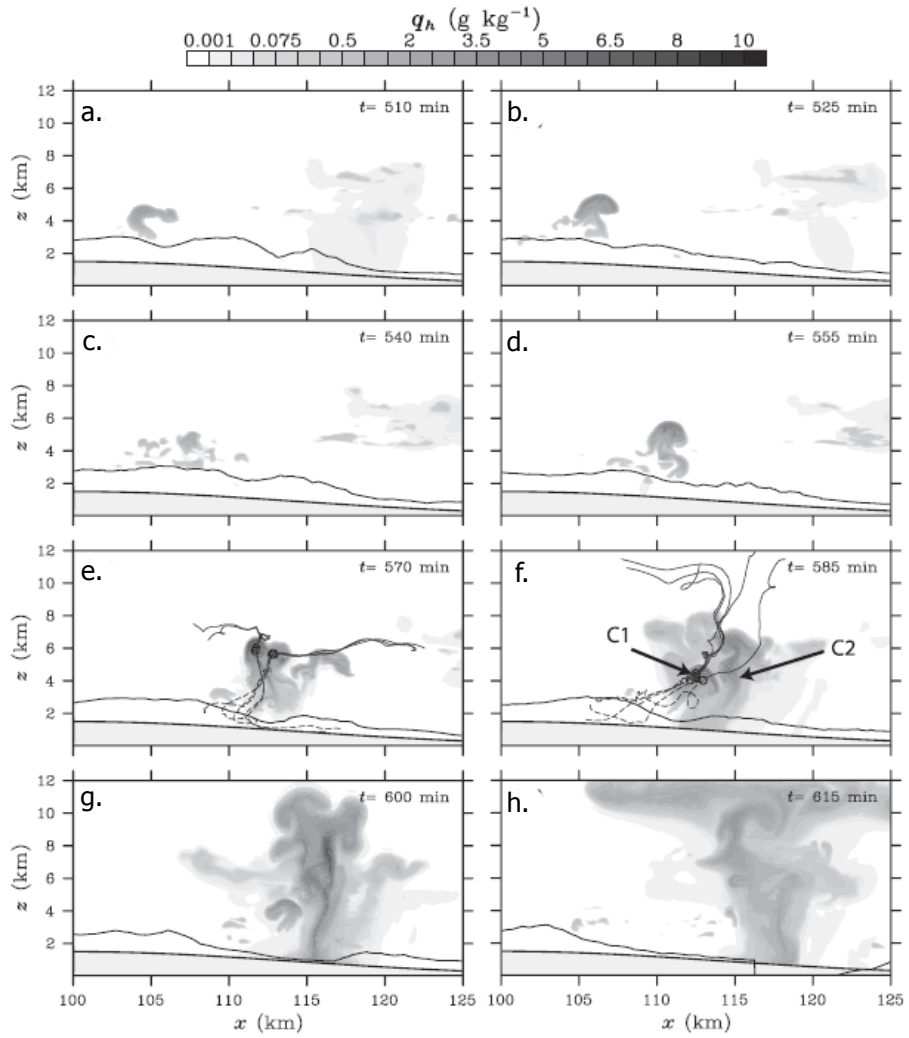

Figure 1.8: Plots of the mixing ratio of hygrometeors in simulations on initiation of deep convection by Kirshbaum (2011). Plots shown for t =510–615 min. The boundary layer top, is shown by the thick black line. A period of shallow convection during t =510–570 min is followed by the initiation of deep convection during t =585–615 min. Forward (black solid lines) and backward (black dashed lines) 30–min parcel trajectories are overlaid on (e) and (f) to show the origin and evolution of air parcels within the updrafts. The C1 and C2 labels on (f) correspond to two active updrafts that later merge to initiate deep convection. (Kirshbaum and Smith, 2009)

with the release of water vapour and chemical by-products from burning. Depending on the atmospheric structure they can generate deep convection, pyrocumulus clouds and severe storms. As in the solar heating cases, the result is a localised convection cell that is able to break through the convective inhibition of the lower atmosphere and force deep convection extending up to the tropopause. Unlike the solar heating cases, these storms often occur under strong winds, but the extension and propagation of the storm still depends heavily on the atmospheric structure (Cunningham and Reeder, 2009).

Finally, another similar area is rainfall enhancement by the urban heat island (UHI),

specifically by the anomalous increase in sensible heat flux over a large city. The link between this sensible heat flux and rainfall over and downwind major cities has been studied based on both statistical analysis of observational data (over Atlanta; Dixon and Mote, 2003) as well as based on numerical modelling (over northern Taiwan; Lin *et al.*, 2011). Results in both cases have shown significant enhancement in the generation of rainfall, consistent with the results from other studies on flow over heated terrain.

1.5 Lava domes and volcanic hazards

The aim of the study is to extend the research on heated terrain to flows over "dome-building" volcanoes. These are volcanoes with high-viscosity magma that solidifies quickly as it reaches the surface, forming a high temperature plug (a "lava dome") blocking the conduit (Figure 1.9). After it forms, the lava dome continues to grow, either endogenically or exogenically. In the first case the dome expands internally to accommodate the increase in lava and in the second case the dome grows externally as fresh lava is piled above the surface of the dome (Parfitt and Wilson, 2008). Due to non-linear dynamics caused by crystallization and degassing of the highly viscous lava, domes evolve unpredictably and the growth style can change with time during an eruptive period (Melnik and Sparks, 1999; Hale and Wadge, 2008). Lava domes can grow to reach several hundreds of metres both horizontally and vertically and can grow steadily on various timescales, from days to years (Francis, 2008). Due to the intermittent buildup of gas pressure, erupting domes can often experience episodes of explosive eruption and erosion which in time leads to instability, explosive eruption and the wholesale destruction of the dome before the cycle starts anew (Francis, 2008). This destruction is called a "dome collapse".

A key point for the atmospheric response is the surface temperature of the dome. Along with the area and the height of the dome, the surface temperature also changes over time depending on a variety of factors, mainly to do with the magma composition, growth style and atmospheric conditions. Hicks *et al.* (2009) created a mathematical model for a dome in an effort to predict the equilibrium surface temperature by studying the surface energy balance (Figure 1.10a). They conclude that the surface temperature of a dome is a function of the carapace thickness (depth of solidified lava), wind speed, and gas flux from the interior (Figure 1.10b). Furthermore they identify two characteristic timescales for the

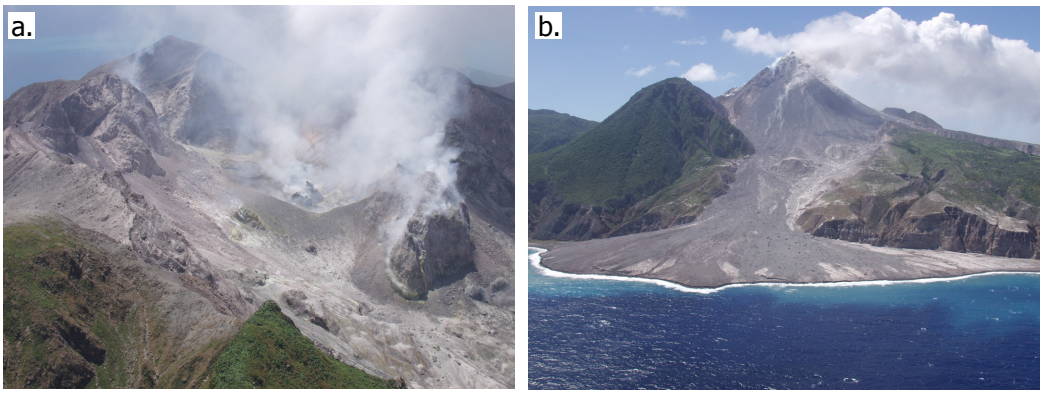

Figure 1.9: (a) Initiation of a new lava dome in the Soufrière Hills volcano. The Tar River Delta and Valley looking to the west on 21 February 2003. The Tar River slopes to the East from the SHV dome. (b) The large dome (summit c. 1050 m asl) has an apparent conical profile. Since the previous large collapse on 29 July 2001, 19 months of deposition from pyroclastic flows has filled much of the Tar River Valley and expanded the delta. Image copyright NERC/Government of Montserrat. (Wadge *et al.*, 2014)

thermal evolution of a dome: one has an order of magnitude of minutes, over which the dome carapace reaches a quasi-steady state and one with an order of magnitude of days as the thermal profile approaches the new equilibrium state.

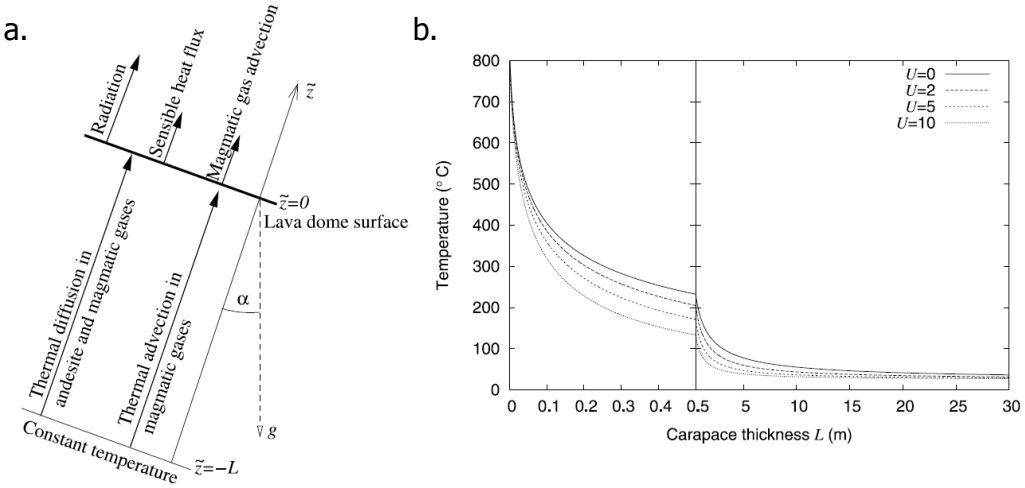

Figure 1.10: (a) Schematic diagram showing diffusive heat fluxes in the dome and magmatic gas and advective heat fluxes in the magmatic gas in a dome interior. Surface heat fluxes are due to radiation, atmospheric convection, and magmatic gas advection. All heat fluxes are assumed to be perpendicular to the lava dome surface and at an angle α to the vertical. (b) Steady-state temperatures in an impermeable dome, as a function of carapace thickness L, for radiative heat fluxes only ($U = 0$ m s^{-1}) and radiative and convective heat fluxes with $U = 2$, 5, and 10 m s^{-1}. From Hicks *et al.* (2009).

As a dome-building volcano, SHV features various volcanic hazards. An *explosive eruption* is an energetic eruption, producing ash and other volcanic material as well as ballistic debris. Note the difference to an *effusive eruption*, when the products are mainly

lava flows and volcanic domes. These two kinds of eruptions are characterised by different time scales: an explosive eruption takes place over hours or days, while an effusive eruption can take place over months or years. An explosive eruption can occur during an effusive eruption. This is the case in Montserrat where the main effusive eruption started in 1995 continuing until the present and is at times marked by explosive eruptions (see Section 1.6). For a dome-building volcano, an explosive eruption is usually accompanied by a partial or wholesale dome collapse. An explosive eruption can also be accompanied by a *pyroclastic flow*. Pyroclastic flows (or *pyroclastic density currents*) are mixtures of hot, dry rock fragments and gases that due to their high density flow over the ground at high speeds. Pyroclastic flows can also occur without an eruption if unstable parts of a dome fail. They are generally comprised of two parts, a flow of course fragments moving along the ground, accompanied by a turbulent cloud of ash that rises above the flow. Rainfall during or after the eruption can initiate *lahars*. A lahar is a cement-like debris flow caused by the remobilisation of hot or cold volcanic material (either during or after an eruption) rapidly flowing down the slopes and/or river valleys of a volcano. Pyroclastic flows are considered to be the deadliest volcanic hazard due to their speeds, temperatures and generally unpredictable nature, followed by lahars: in the 20th century pyroclastic flows had caused more than 36000 deaths, while lahars 28400 (Tilling, 1989). For more detailed information on volcanic hazards the reader is directed to the US Geological Society volcano hazards program site[1], as well as Francis (2008) and Parfitt and Wilson (2008).

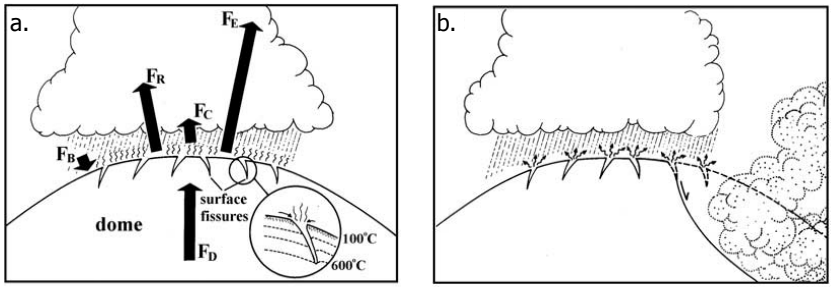

Figure 1.11: Schematic diagram of a thermodynamical model for rainfall-triggered dome collapse. (a) Fluxes of energy within and at the surface of the hot dome; diffusive heat flux (FD), surface radiative cooling (FR), convective heat flux (FC), background surface radiative warming (FB), surface latent heat flux (FE). The inset shows the surface temperature structure at a fissure, and the accumulation of liquid water at the surface and percolation into surface fissures, once the surface has cooled to 100 C. (b) Vapourisation of water within the fissures into high pressure steam, leading to dome collapse and pyroclastic flows. From Matthews and Barclay (2004).

[1] volcanoes.usgs.gov/vsc/glossary/

Both of these volcanic hazards are associated with heavy rainfall over the volcano. In the case of lahars this connection is obvious and straightforward - rainwater acts as a trigger, mobilising sediment down the flanks of the volcano. Heavy rainfall has also been implicated in triggering explosive eruptions, dome collapses, and pyroclastic flows at a number of volcanoes, such as Mount St. Helens, U.S.A. (Mastin, 1994), Unzen, Japan (Yamasato *et al.*, 1998), Merapi, Indonesia (Voight *et al.*, 2000), Piton de la Fournaise, Réunion Island (Violette *et al.*, 2001), Soufrière Hills Volcano (SHV), Montserrat (Matthews *et al.*, 2002; Carn *et al.*, 2004; Barclay *et al.*, 2006; Matthews *et al.*, 2009) and Stromboli, Italy (Hort *et al.*, 2003). Several mechanisms have been hypothesised for this rainfall triggering, including mechanical erosion of the surrounding talus fan and gravitational destabilisation of the dome, and the formation of a rainfall-saturated cap that blocks the upward flow of magmatic gas leading to a pressurised failure (Figure 1.11; Matthews and Barclay, 2004; Hicks *et al.*, 2010, 2014).

1.6 Montserrat and the Soufrière Hills Volcano

The island of Montserrat is a British Overseas Territory, part of the Lesser Antilles in the West Indies, located in the Caribbean. It is approximately 16 km long and 11 km wide and has several peaks, the highest being SHV, whose height varies depending on the state of the dome, 1050 m asl at the time of writing (Wadge *et al.*, 2014). Montserrat is a subtropical island and as such easterly trade winds play a major role in determining the climate. Aside from the trade winds the island is also affected by hurricanes and the rainy season lasts typically from June until November (Barclay *et al.*, 2006).

The SHV is a Peléan lava dome complex consisting mainly of hornblende andesite (Rea, 1974). Compared to other volcanoes found in the central islands of the Lesser Antilles arc it is a small volcano. It is monitored by the Montserrat Volcano Observatory, stationed on the island (the location is marked as MVO Figure 1.12).

SHV is one of the most intensively studied volcanoes in the world and has had a varied recent eruption history. From the initial eruption in 1995 the volcano has produced over a cubic kilometre of andesitic magma and has had undergone numerous cycles of lava dome creation (both endogenically and exogenically) and collapses, producing an almost uncountable amount of pyroclastic flows and lahars. The recent activity of the volcano

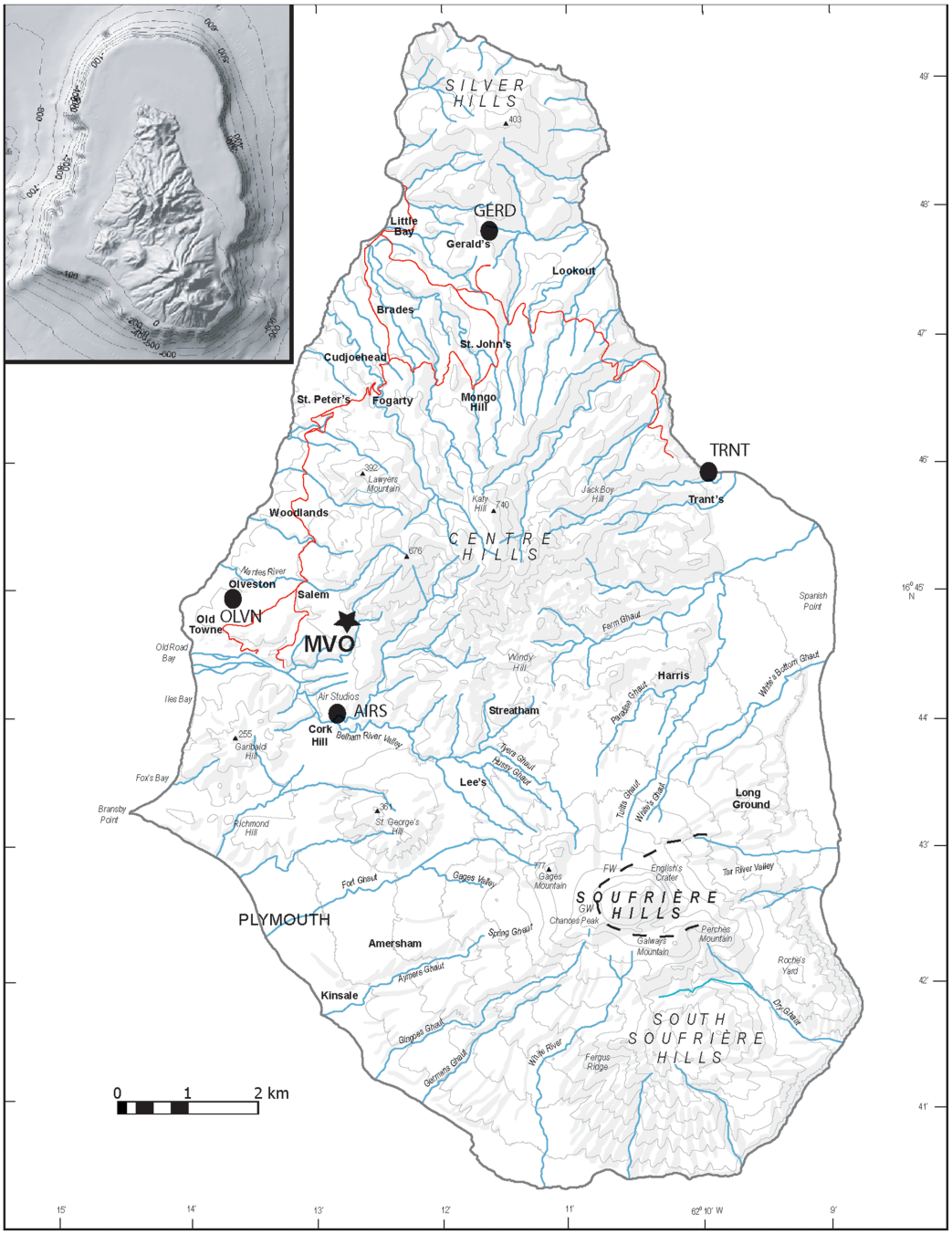

Figure 1.12: Map of Montserrat with the topography as it was in late 2009. Contours are at 100 m intervals, the main roads in red. The outline of the largely buried English's Crater is shown by the dashed black line with GW marking Gages Wall and FW marking Farrells Wall. The location of the MVO is marked with a star. A shaded relief digital elevation model (DEM) image of Montserrat and its submarine shelf is inset. (Wadge *et al.*, 2014)

is split in five phases tied with specific domes. Phase 1 (November 1995–March 1998) was marked with a 4-month precursory episode and accelerating dome growth, commonly accompanied by collapses and explosions. Before the eruption in 1995 the island's population is estimated at 13000, but during this initial phase two-thirds of the population

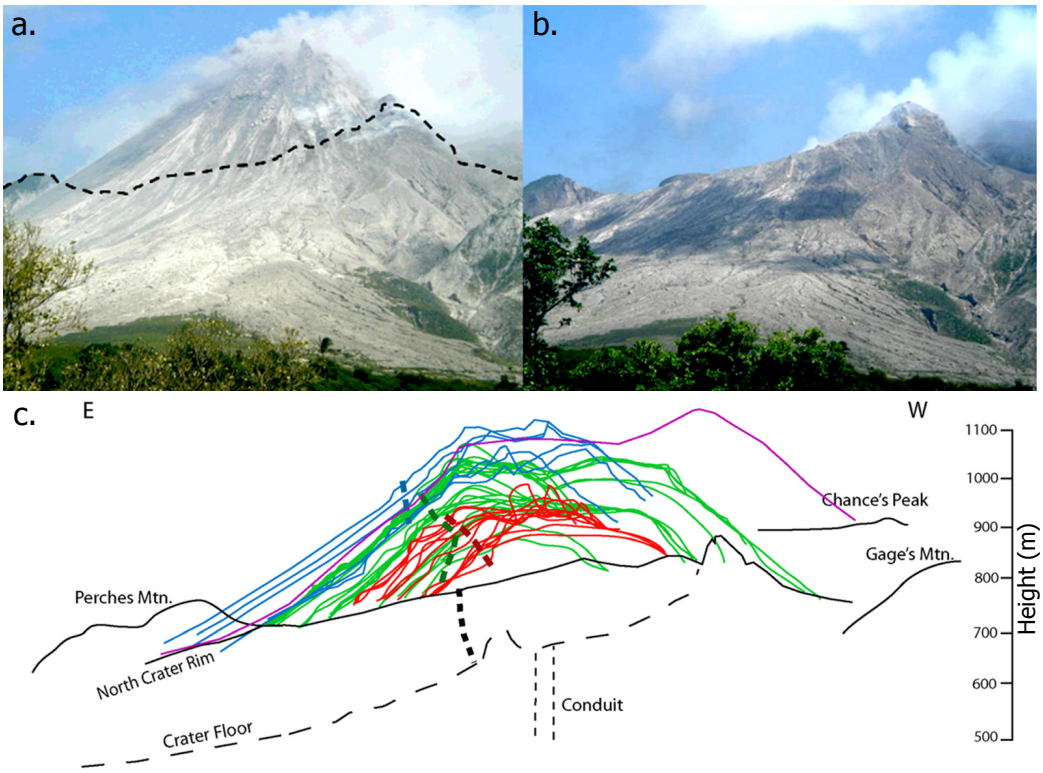

Figure 1.13: (a), (b), Images taken from Windy Hill (4 km NNW of the dome) looking south to the volcano (a) before (b) and after the dome collapse of 12–13 July 2003. The dashed black line shows the skyline after the collapse. The summit of the dome was about 1100 m asl before and about 850 m asl after the collapse. The post-collapse summit known as the NW Buttress on the right was itself destroyed during the explosion of 4 March 2004. Image copyright NERC/Government of Montserrat. (c), Superimposed profiles of the dome at different times, from the same location. Blue profiles are from Phase 2 (1999–2003), red profiles are from Phase 3 (2005–May 2006) and green profiles are from Phase 4 (May 2006–April 2007). The purple profile is based on an AVTIS-3 radar image in May 2011. Thick dashed lines represent the approximate positions of the boundary between core lava and the talus on different domes. (Wadge *et al.*, 2014)

were forced to flee as the southern part of the island was abandoned and put into an exclusion zone. Nineteen deaths were caused by pyroclastic flows (Voight *et al.*, 1999). Infrastructure, including the previous capital, Plymouth, and the W. H. Bramble airport were buried due to a succession of pyroclastic flows and lahars. In phase 2 (November 1999–July 2003, Figure 1.13) after two major collapses followed the creation of the largest dome built to date. The period ended with an increase in pyroclastic flows leading to the collapse of the dome. Phase 3 (August 2005–April 2007) featured precursory phreatomagmatic activity and one dome collapse but ended with a large dome in place. Phase 4 (July 2008–January 2009) featured two short episodes, explosions and extrusion on the western side of the dome. Finally, Phase 5 (October 2009–February 2010) featured extrusion to the west, south and north, explosions and ended in a large north-directed collapse. Figure 1.13c, shows profiles of the lava dome at various times during the different

phases. Note the change in the horizontal and vertical extent. For a more detailed record of the SHV eruption the reader is referred to two comprehensive reviews of the eruption history, focusing on the 1995–1999 period (Sparks and Young, 2002) and the overall eruption (Wadge *et al.*, 2014).

1.6.1 Meteorological monitoring in Montserrat

Barclay *et al.* (2006) carried out a long field campaign in Montserrat during Phases 1 and 2 (from 1998 to 2003). The aim of this campaign was two-fold, to examine the impact of rainfall on volcanic activity and secondary hazards (including pyroclastic flows, dome collapses, explosions, and lahars), as well as to study the weather systems responsible for rainfall in Montserrat.

Results reveal a statistically significant link between rainfall and activity: more than 20 mm of rain on a random day cause an 2.9% increase in the probability of a dome collapse to a total of 9.2%, and an increase by a factor of 2.6 for pyroclastic flows and 5.4 for explosions. It has been noted, though, that results are sensitive to the state of the volcano. Identifying lahars is a difficult task as their seismic signal is often masked by stronger seismic activity, leading to underestimates, however, the study noted that there was a 56% probability for lahar activity for days with $>$ 20 mm of rain, 26% for 10–20 mm, and 18% for days with $<$ 10 mm.

Rainfall in Montserrat was seen to have a strong annual cycle with the majority of heavy rainfall occuring during the wet season, from May to December. Heavy rainfall in Montserrat has been caused by forecastable, large-scale systems over 50% of the time, however, the remaining days were associated with small-scale, effectively unforecastable systems. The study, thus, concludes with a recommondation that monitoring and warning programmes in Montserrat should use a network, and not a single rain gauge.

1.7 Summary

In the current chapter a brief review of several different topics relevant to the thesis has been presented. The various research areas covered in this chapter are expected to provide context for this study. Several phenomena associated with orographic flows, such as gravity waves, wave splitting and hydraulic jumps, can be anticipated in the numerical

modelling experiments. The most directly related research area is that of the effect of heated terrain. Research in the field is still at an early stage, but relevant characteristics that have been identified include a strong localised convection in the area of the heating and rainfall intensification.

Changes in rainfall patterns in the vicinity of volcanoes, especially dome-building ones, such as the Soufrière Hills Volcano located in the island of Montserrat, are of extreme importance when it comes to hazard assessment as two of the deadliest volcanic hazards, pyroclastic flows and lahars, are directly or indirectly associated with heavy rainfall. It is thus envisaged that results pointing towards rainfall intensification over a volcano can be of great use in future hazard assessment and mitigation.

1.7.1 Thesis Structure

The rest of the thesis is structured as follows:

Chapter 2 - Methodology and experimental setup

A thorough description of the numerical model and its configurations, plus other elements of methodology and experimental settings used in the following chapters.

Chapter 3 - Flow over an idealised volcano: Dry runs

Presentation of a set of heavily idealised simulations carried out for an initial test of the study's hypothesis where moisture and microphysics are switched "off" in the model configurations.

Chapter 4 - Flow over an idealised volcano: Moist runs

Presentation of semi-realistic runs over idealised topography. This setting was chosen to allow for a meaningful analysis of the associated phenomena that can be applied in any volcano situated in the tropics.

Chapter 5 - Deep convective rainfall over Montserrat and implications for volcanic hazards

Focus on more realistic runs and the implications the study has for the volcanic hazard assessment in Montserrat.

Chapter 6 - Conclusions and future work

General discussion on the results of the study as a whole and summary of the conclusions.

Chapter 2

Methodology and experimental setup

2.1 Introduction

In this chapter, a thorough description of the model setup for the experiments examined in this study is presented. All simulations are carried out using the Weather Research and Forecast (WRF) model, specifically version 3.3.1 in idealised setting. The model was developed by a variety of collaborative partners and is now primarily maintained and supported by the National Center for Atmospheric Research (NCAR) in Colorado, USA. WRF features a fully compressible, three-dimensional nonhydrostatic model, with the governing equations solved in flux-form. The model adopts an Arakawa-C grid, a time-splitting explicit advection scheme and a terrain-following height coordinate (Skamarock *et al.*, 2008). More information about the model can be found at the model's website at: http://www.wrf-model.org. WRF was chosen as it supports a large range of physical and dynamical parameterisation schemes and is open-source software, allowing for easy customisation of the source code.

The basic model domain for each chapter, along with the parameterisation choices are outlined in Sections 2.2 and 2.3. Sections 2.4 and 2.5 feature an analysis of the surface temperature distribution of a lava dome and its representation in the WRF simulations. Finally, a small study of sounding data for the Caribbean is presented and compared to the atmospheric profiles that are used to initialise the simulations (Sections 2.6 and 2.7).

2.2 WRF domain

This section details the different ways the domain was set up in the simulations of Chapters 3–5, including information on grid and domain size, mountain characteristics, land-use and boundary conditions among others.

The basic domain consists of an isolated volcano, located near the centre of the domain and surrounded by flat land (Chapter 3) or ocean (Chapters 4 and 5). Note that the terms "volcano" and "mountain" are used interchangeably throughout the thesis. In Chapters 3 and 4, the volcano's characteristics remain the same in all simulations; it is represented by a Gaussian equation with a half-width of approximately 10 km and a height of 1 km (Figure 2.1a), using the following equation:

$$h(x,y) = h_{top}\ \exp\left[-\left(\frac{x-x_s}{L_x}\right)^2 - \left(\frac{y-y_s}{L_y}\right)^2\right] \tag{2.1}$$

where x_s and x_y are the coordinates of the volcano's centre, h_{top} (1000 m) is the maximum height and L_x and L_y are parameters relating to the half-width (in our case both were set at 5700 m). Although the simulations are idealised, the specific values are chosen so that the mountain has similar characteristics to the topography of Montserrat. A detailed list of the characteristics can also be seen in Table 2.1, showing each chapter as a column of the table.

Characteristic	Chapter 3	Chapter 4	Chapter 5
Run Time (h)	12	12	9
Time Step (sec)	2	2	1.5/0.5
Grid Size (m)	300	300	300/100
Model Top (km)	11	16	16
Grid Points E-W	400	680	500/200
Grid Points S-N	400	250	200/200
Grid Points Vert	75	147	147
Mountain Height (km)	1	1	DEM
Mountain Width (km)	20	20	DEM
Sea	No	Yes	Yes
Boundary Conditions	Periodic	Periodic	Periodic/Nested

Table 2.1: Domain choices for the WRF model.

For Chapter 3 (Figure 2.1b) the mountain is positioned in the centre of the domain while the domain dimensions are 120×120 km. The grid spacing (Δx) is 300 m, leading to 400 grid points in both directions. The top of the domain is at 11 km, with the vertical

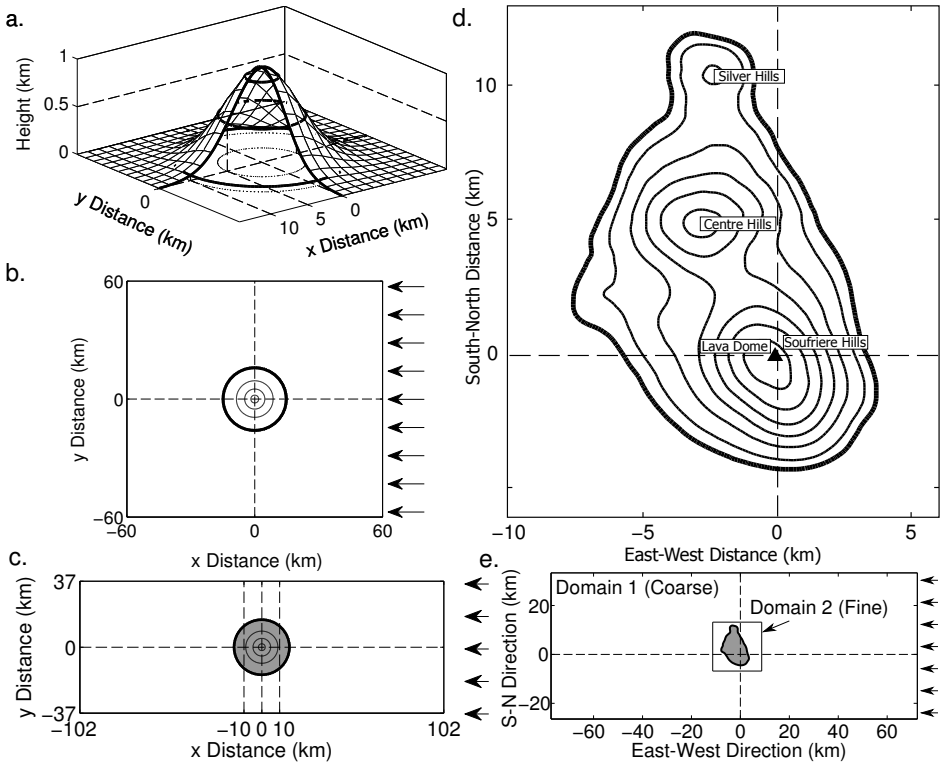

Figure 2.1: (a) Gaussian mountain used in the simulations for Chapters 3 and 4. (b), (c) Domains for Chapters 3 and 4 respectively. (d) Smoothed DEM for Montserrat used in Chapter 5. (e) Domain used in the simulations for Chapter 5. Height contours in (b) and (c) are at 5, 100, 500 and 900 m, while in (d) every 100 m starting at 5 m. Grid points outside of the grey area in (c) and (e) are set as water. The wind in all cases is easterly, as indicated by the arrows.

grid (75 levels) spacing varying with height as detailed later in the section. The domain is comprised of land for all grid points and all of the boundaries are set to periodic.

In Chapter 4 (Figure 2.1c) the domain length is 204 km in the x and 70 km in the y direction, with a grid spacing of $\Delta x = 300$ m, leading to a 680×250 grid. Grid points where the height would be less that 1 m are explicitly set to 0 m and are marked as "water", thus introducing the difference between land and sea (Figure 2.1c). The mountain is placed in the centre of the domain, at a distance of 102 km upstream (distance from the eastern boundary) to allow for the air to cover a sufficient distance over sea, allowing for a field of cumuli to be developed (similarly to Kirshbaum, 2011). The top of the domain is at 16 km over 147 grid points, again varying with height.

In Chapter 5 the model domain consists of an isolated island (Montserrat) featuring the volcano, surrounded by water (Figures 2.1d,2.1e). Nesting was used in Chapter 5 in order to cover complex processes in detail. The grid spacing is 300 m (100 m in the inner domain) and the domain represents a 150×60 km (20×20 km) area it is now represented

by a 500×200 grid (200×200). The DEM used in the simulations was derived from data from the Advanced Spaceborn Thermal Emission and Reflection Radiometer (ASTER) mission. The 30 m resolution original data were converted to 300 m resolution, smoothed and imported to the initialisation code for the simulations. Note that some experiments in Chapter 5 required a change in the wind direction. Instead of changing the wind direction in the prescribed input sounding, the DEM data were rotated and input at the appropriate angle. This was done to make sure that the domain was set up properly with respect to the boundaries, and at the same time keep the computational time relatively short to allow for numerous experiments.

Vertical spacing increases with height, varying between 50 and 500 m for Chapter 3 and 1000 m for Chapters 4 and 5, as seen on Figure 2.2. Figure 2.2a shows the grid point height in meters, while Figure 2.2b shows the eta levels, which is what is input into the model code. "Eta level" is a normalised pressure unit starting at 1 for the surface, going down to 0 at the model top (Skamarock *et al.*, 2008). The distribution used for the simulations allows higher resolution in the lower part of the atmosphere where cloud formation and generally more detailed physics are needed, while the vertical resolution remains moderate (ranging from 200–500 m) up until the tropopause.

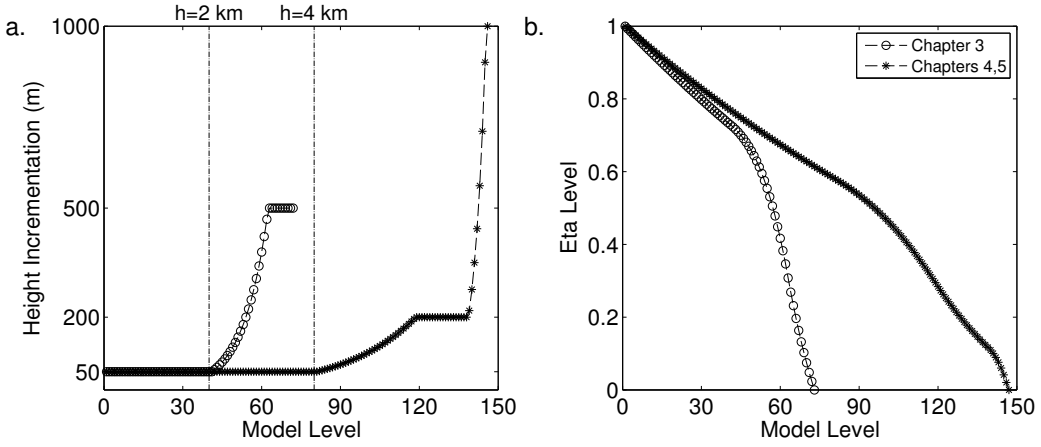

Figure 2.2: (a) Height increment and (b) eta level, by model level, for Chapters 3–5.

The simulation time for all experiments is set between 9–12 hours. The first 3 hours are spent on model "spin up" (hours 1–2) and approaching a quasi-steady state (hours 2–3). The simulations continue for an additional 6–9 hours to provide the output required for the study. For all runs, the final 3–6 hours are mainly used to make sure that the model did not diverge radically from the quasi-steady state within this period but are not used

in the analysis. It was decided not to allow the model to run more than 12 hours in total when running idealised experiments, as the boundary conditions are open and so there is no direct control on the vertical structure of the atmosphere. After a certain amount of time the model strays too far away from the initial conditions and outside the chosen parameter space.

The simulations are carried out on the University of East Anglia's (UEA) high performance cluster, Grace[1]. Grace has a total of 4148 cores, running Red Hat compatible Centos 5.8 and the Platform LSF workload manager. The theoretical peak performance is 65 TFlops.

2.3 WRF parameterisation

2.3.1 Physics

The choice of the physics' modules used in the simulations can be seen in Table 2.2, with each chapter represented by a column.

Characteristic	Chapter 3	Chapter 4	Chapter 5
Microphysics	n/a	Lin et al (6-class)	Lin et al (6-class)
Surface Layer	Monin-Obukhov	Monin-Obukhov	Monin-Obukhov
Soil Model	Thermal Diffusion	Thermal Diffusion	Thermal Diffusion
Boundary Layer	n/a	n/a	n/a
Radiation	n/a	n/a	n/a

Table 2.2: Physics parameterisation module choices for all chapters.

Microphysics

No microphysics' module is used in Chapter 3 as the focus of the study is on the flow dynamics for a dry atmosphere. The Purdue Lin scheme (based on the studies by Lin *et al.*, 1983 and Rutledge and Hobbs, 1983), a relatively complex 6-phase scheme, is used for Chapters 4 and 5. This scheme was chosen because deep convection past the freezing point, extending up until the tropopause is expected and the Purdue Lin scheme has been used extensively in storm-related research (Hong and Lin, 2006). Furthermore the focus of the study is on rainfall so an accurate representation of the complex microphysical processes is essential for the validity of the results.

Surface layer

[1] http://rscs.uea.ac.uk/high-performance-computing

A simple Monin-Obukhov similarity theory based scheme is used for all of the simulations discussed in the thesis (Skamarock *et al.*, 2008).

Soil model

A 5-layer thermal diffusion model (Noah Scheme) is used throughout all of the simulations (Skamarock *et al.*, 2008). Using a soil physics prameterisation for the duration of the simulations was vital for the study as this allows for specification of the surface temperature. The scheme provides heat and moisture fluxes to the boundary layer scheme. For Chapters 3 and 4 the "Barren and Sparsely Vegetated" class (z_0 = 0.01 m) of the scheme is used as the land type.

Other (Radiation, boundary layer, cumulus)

The radiation scheme is switched off for all simulations. While it is acknowledged that diurnal effects play a major role in mesoscale circulations in the tropics, we want to isolated the impact of volcanic heating on the atmosphere without the complication of a diurnal cycle. Furthermore, it has been established that for moderate to strong trade winds impacting a mesoscale island, forced convection due to ascent governs the dynamics, rather than solar forcing (Smith *et al.*, 2009; Minder *et al.*, 2013). The lack of a radiation scheme does not affect the order of magnitude of the surface heat fluxes (that are mainly calculated by the soil model) and, as no simulations lasts more that 12 hours and as the focus of the study was not in the daily change in rainfall, it is decided that the an extra level of complexity added to the results by the introduction of a change in the fluxes throughout the day is better to be avoided. At the current resolution the boundary layer scheme is not needed as primary eddies are explicitly resolved (Kirshbaum and Fairman, 2014). A turbulence closure scheme is used instead. As for the cumulus scheme, the grid resolution is sufficiently high so that rain is produced by the model without needing the added effect of a parametrisation scheme.

2.3.2 Dynamics

Details of the dynamics' choices used in the simulations can be seen in Table 2.3, with each chapter represented by a column.

Diffusion and TKE closure

The option for evaluation of mixing terms in physical space, along with the 1.5 turbulence

Characteristic	Chapter 3	Chapter 4	Chapter 5
Diffusion	Mixing Terms	Mixing Terms	Mixing Terms
Numerical Diffusion	6th Order	6th Order	6th Order
TKE Closure	1.5 Order Closure	1.5 Order Closure	1.5 Order Closure
Damping Layer	Inverse Rayleigh	Inverse Rayleigh	Inverse Rayleigh
Layer Depth (km)	5	5	5

Table 2.3: Dynamics parameterisation module choices for all chapters.

order closure is chosen for all of the simulations (Skamarock *et al.*, 2008). On top of that, sixth-order monotonic horizontal diffusion is applied to all variables for stability and to minimise spurious behaviour at poorly resolved scales (Knievel *et al.*, 2007).

Damping layer

A w-Rayleigh damping layer is utilised in order to prevent reflection of gravity waves propagating upwards from the top of the domain (Klemp *et al.*, 2008). The strength of the damping layer increases exponentially by height. As the top of the domain differs between the simulations of Chapter 3 and Chapters 4 and 5, the depth of this sponge layer changes from 15 km in the first case to 8 km in the final simulations.

2.4 Lava dome temperature analysis

Fine details of the distribution of surface temperature (T_{sfc}) of lava domes are difficult to acquire (Macfarlane *et al.*, 2012). This is mainly due to the lack of appropriate equipment to observe the usually cloud-covered, lava domes effectively and independently of the weather. Despite this, a rudimentary analysis of the surface temperature distribution has been undertaken here in order to obtain values that are appropriate to use in the atmospheric model.

A picture of the Soufrière Hills lava dome, presented by Macfarlane *et al.* (2012), is shown in Figure 2.3a, along with a near simultaneous surface temperature, recorded using an infra-red camera (Figure 2.3b). The lava dome in the picture is approximately 300×200 m and shot at an angle. Although not visible in the current crop, further away from the dome the surface temperature quickly drops to a background temperature of 300 K.

Even though in the simulations for all chapters the horizontal resolution is sufficient for orographic flows, it leads to the volcanic dome being resolved in the model as a small

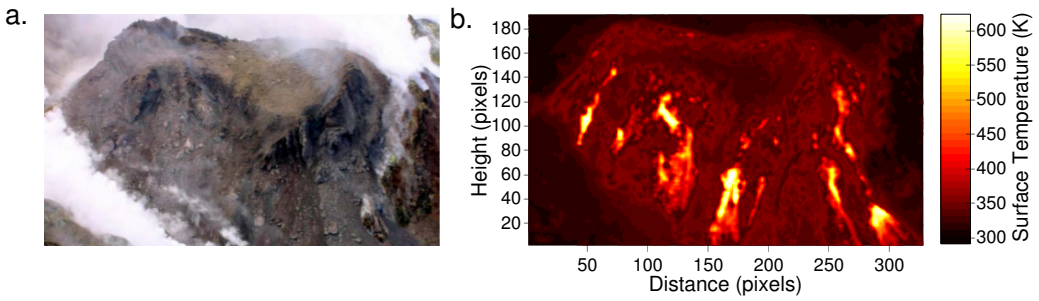

Figure 2.3: Image of a volcanic dome and the surface temperatures recorded by an infra-red camera and analysed in Matlab. Images taken over a period of 45 min on the 4th Nov, 2005 (Macfarlane *et al.*, 2012). Note that one pixel is approximately one meter in both horizontal and vertical directions.

number of grid points, especially in Chapters 3 and 4. As the fine surface temperature details of the dome cannot be represented in the WRF surface boundary conditions, it is only the average values that are of interest.

The surface temperature distribution can be split in two parts, an average increase in temperature over the area of the dome (at a temperature of approximately 350–360 K) and perturbations added on top of this increase (hot spots with temperatures up to approximately 600 K, corresponding to the yellows in Figure 2.3b). Despite the random element added by these hotspots it can be seen that the mean result is a rather uniform distribution. To further study the relation between these two factors surface temperature histograms were produced (Figure 2.5). Each histogram features specific surface temperature windows, shown along with the percentage of the area covered.

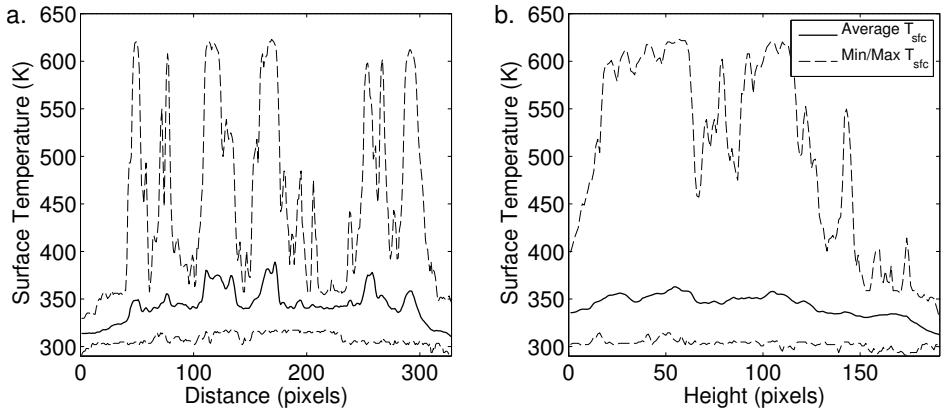

Figure 2.4: Average surface temperature (solid line) across Figure 2.3, (a) horizontally and (b) vertically, surrounded by minimum and maximum temperatures across each direction (dashed lines).

Figure 2.5a shows that the temperature distribution is very skewed towards the lower temperatures, showing that approximately 80% of the area is covered by temperatures

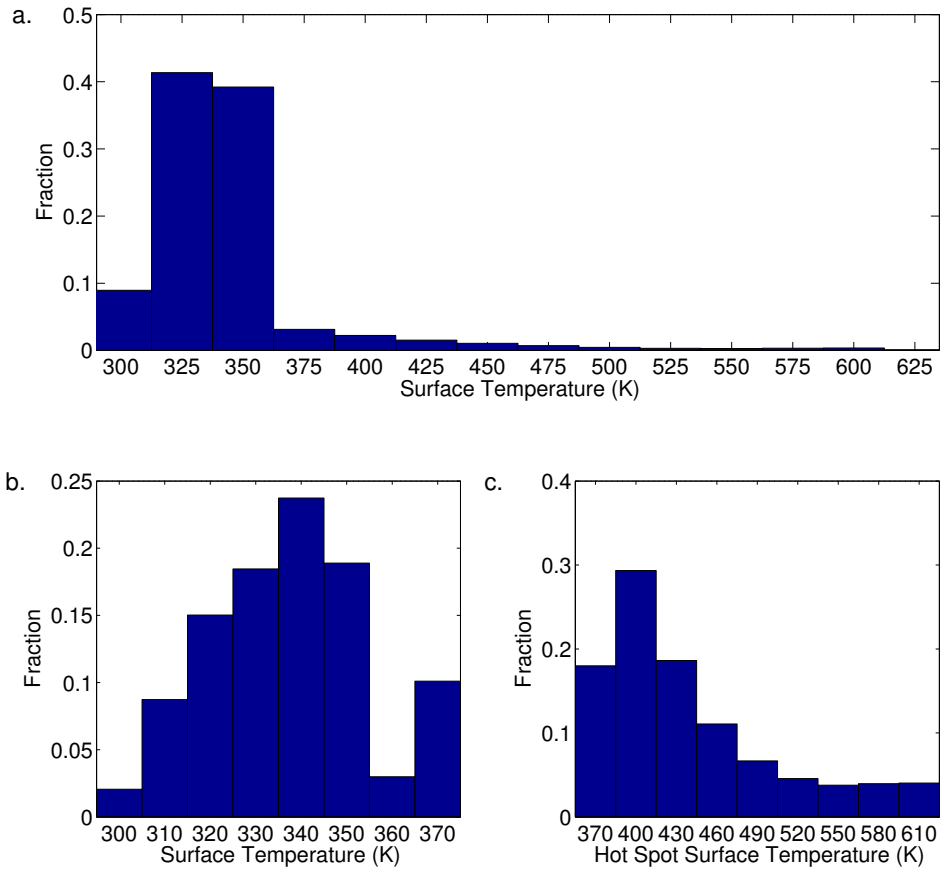

Figure 2.5: Histograms of surface temperature using: (a), (b) the whole data, (c) only the data for hot spots. In panel b all the the hot spots ($T_{sfc} > 370$ K) are shown as a single bin.

ranging between 320–350 K. The rest of the area is split evenly between low, almost unperturbed temperatures (300–310 K) and hot spots (370–610 K). As far as the hot spots are concerned (Figure 2.5c) the distribution is once again skewed towards lower hot spot temperatures with an average of 400 K. Judging from the histogram it can be seen that the average increase in temperature can be mainly attributed to the average part and not to the hotspots. Despite the very high surface temperatures of the hotspots, when averaged over the dome, they are typically only approximately 7 K perturbations over the relatively uniform dome anomaly ($T_{sfc} = 350$ K). The amount of hotspots in the picture was calculated to be 10%, as seen in Figure 2.5b. Other infra-red pictures of the lava dome sent from the volcanic observatory generally present a similar surface temperature distribution.

Dome size and temperature both vary from the time that the dome is created until it collapses. The declining effect the dome would have is studied in Chapter 3 and thus the temperature anomaly values were generally restricted between 20 and 60 K. Although average dome values above 60 K can be expected, especially in the early stages of the

dome creation, it was decided to focus on the most typical situations, especially as during the initial stages the lava dome is relatively small in extent.

2.5 Surface temperature specification

The different settings for the surface temperature anomaly (T_a) can be seen in Table 2.4. The *dome diameter* (D_d) is calculated as the number of grid points with a specified increased temperature in Chapter 3, or twice the half-width of the distributions used in Chapters 4 and 5, multiplied by the respective grid spacing.

Characteristic	Chapter 3	Chapter 4	Chapter 5
T_a (K)	0:20:60	0:20:60	0,60
D_d (m)	2500	2500	2500

Table 2.4: Temperature anomaly choices for all chapters.

The surface temperature in the model is specified through the initialisation code. Specifying a surface heat flux value was also considered. However it was decided that specifying the surface temperature would be simpler as it was more directly connected with the characteristics of the dome that were used as motivation. The surface temperature anomaly is time independent in each experiment, leading to a nearly-constant surface heat flux once the simulation has reached a quasi-steady state. In all chapters the surface temperature anomaly was added as a perturbation over the ambient surface temperature using the (Figure 2.6). A typical dome at SHV ranges between 500 and 1000 m in diameter (Wadge *et al.*, 2014), shaded in all panels of Figure 2.6.

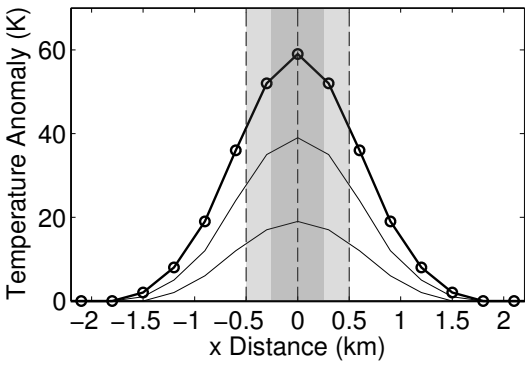

Figure 2.6: Surface temperature anomaly distributions used in all simulations.

The progressive reduction in the surface temperature anomaly distributions leads to a wider surface temperature anomaly than the typical dimensions for the dome in Soufrière

Hills, Montserrat. This smooth profile was utilised in order to avoid computational errors and model instability that occurred due to the overly steep changes in the values. For a cross-section across the centre of the volcano the temperature anomaly is imposed over roughly 9 grid points following Equation 4.2:

$$T'(x,y) = T_a \ \exp\left[-\left(\frac{x-x_0}{W_x}\right)^2 - \left(\frac{y-y_0}{W_y}\right)^2\right] \tag{2.2}$$

where T' is the temperature perturbation, x_0 and y_0 are the coordinates of the lava dome, T_a is the maximum temperature anomaly and W_x and W_y are parameters relating to the half-width (both set at 900 m). The surface temperature anomaly is time independent in each experiment, leading to a nearly-constant surface heat flux once the simulation has reached a quasi-steady state.

2.6 Brief atmospheric sounding study

2.6.1 General description

In order to construct the input soundings used in Chapters 4 and 5, a small sounding study was carried out, based on data from the radiosonde station on the island of Guadeloupe in the Caribbean. Guadeloupe was chosen due to the proximity to Montserrat and the amount of sounding and rainfall data available. Specifically the analysis was done using soundings from Le Raizet airport over the month of August 2011 (Figure 2.7). This month was selected as atmospheric conditions seemed representative of a typical rainy season for the Caribbean, with most of the days featuring an unstable atmosphere and the passing of Tropical Storm Emily (1–2 August) and Hurricane Irene (21–24 August) over the island. Although the period of study is relatively short results are in agreement with results from extended climatological studies (Jordan, 1958; Dunion, 2011) and field projects (Siebasma *et al.*, 2003).

The soundings were obtained from the University of Wyoming atmospheric soundings' web page[2] and information about the cyclones was obtained from the University of Wisconsin-Madison web page[3]. Finally rainfall data were gathered from the Tropical

[2] weather.uwyo.edu/upperair/sounding.html
[3] tropic.ssec.wisc.edu/storm_archive/atlantic.php

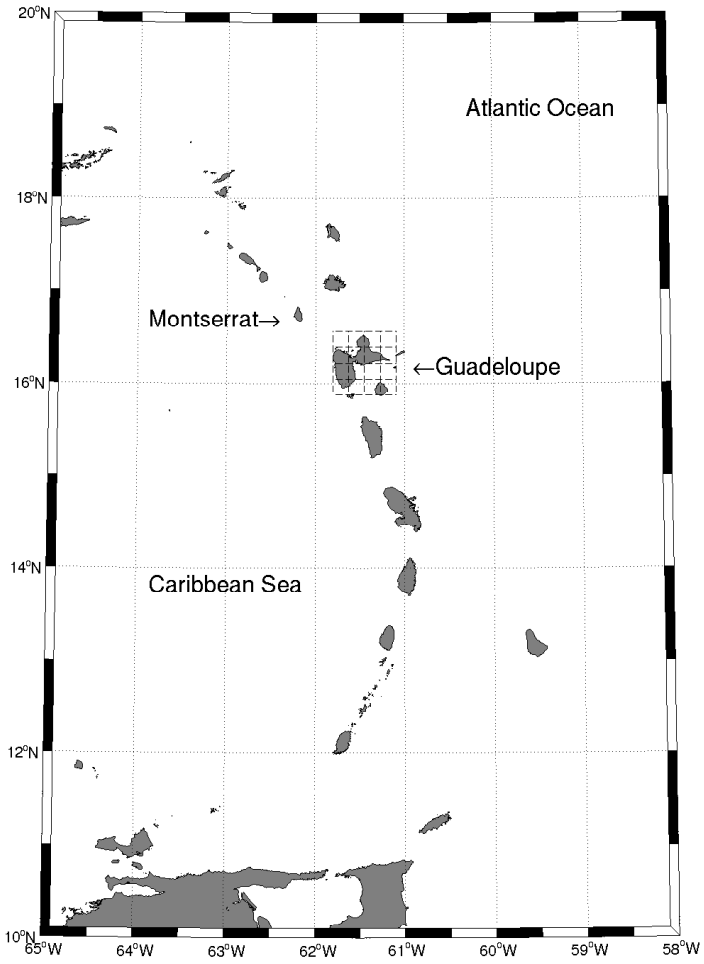

Figure 2.7: Map of area of study. Guadalupe data were used due to the proximity to Montserrat. The box around Guadeloupe shows the grid points of the TRMM data used for the rainfall analysis.

Rainfall Measuring Mission (TRMM) database[4].

In general, the atmospheric conditions for most of the days of August 2011 can be split into three categories that share common characteristics (Table 5.1). Characteristics related to the atmospheric stability and rainfall were studied. The lifted index is used to determine the stability of the lower half of the troposphere, with negative values indicating higher possibility of thunderstorms. The convective available potential energy (CAPE) is a measure of the amount of energy available for convection, with higher values indicating greater potential for severe weather. The convective inhibition (CIN) is a measure of the amount of energy needed to initiate convection and is always negative, with more negative values indicating greater stability. Finally precipitable water is a measure of the depth of liquid water at the surface if all of the water vapour in a vertical column (extending from

[4]trmm.gsfc.nasa.gov/

the 300 mb surface) would precipitate.

CAPE/CIN	Lifted Index	CAPE (J kg^{-1})	CIN (J kg^{-1})	Prec Water (mm)	#Days
All days	-2 ± 2	1128 ± 764	-77 ± 82	47 ± 9	31
High/Low	-4 ± 2	1740 ± 587	-15 ± 11	51 ± 10	14
High/High	-3 ± 1	1099 ± 557	-50 ± 22	47 ± 9	2
Low/High	-1 ± 1	342 ± 275	-185 ± 64	41 ± 5	13

Table 2.5: Some general characteristics for the August 2011 soundings. The soundings are split into three categories depending on the value and the relative relation of CAPE and CIN (leftmost column). All values shown are averages among the days in the group under study along with the standard deviation.

In most of the days the atmosphere is either unstable or has a very shallow neutral or stable layer topped with an unstable upper part of the atmosphere. Many days feature an inversion capping an unstable lower troposphere. The vast majority of days exhibits an, at least marginally, unstable boundary layer (as evident from the lifted index values). Precipitable water is the least changeable parameter, with an average at 47 mm and small standard deviation. Over the whole month (for days with CAPE and CIN values), CAPE ranges between 3 and 2528 J kg^{-1}, with an average of 1128 J kg^{-1}, while CIN ranges from -0.31 to -289 J kg^{-1} with an average of -77 J kg^{-1}. The time series for both CAPE and CIN can be seen at Figure 2.8, along with scatter plots for the duration of August. Although not necessarily so, the majority of days features either a combination of high CAPE and low CIN or the opposite (as seen in Table 5.1).

2.6.2 Rainfall

The TRMM data set was used to obtain values for rainfall (Figure 2.8b). As Guadeloupe is roughly sixteen grid points in the data two values are presented, the overall maximum (plotted in blue) and the average (plotted in red). It can be seen that the month is approximately evenly split between days with little to no rainfall and days an average rainfall of approximately 20 $\mathrm{mm\ day}^{-1}$ and maximum values of 60 $\mathrm{mm\ day}^{-1}$. Only on one day both average and maximum are over 100 $\mathrm{mm\ day}^{-1}$.

A distinction between days with shallow and deep convective rainfall can be seen in Figure 2.9. Despite the fact that rainfall values consistent with shallow convective rainfall (between 0 to 30 mm day^{-1}) can be seen even for days with very little CAPE and high CIN, higher amounts of rainfall are limited to days with CIN ranging from 0 to -50 J kg^{-1}. On top of that days with very high amounts of rainfall are limited in the upper right part

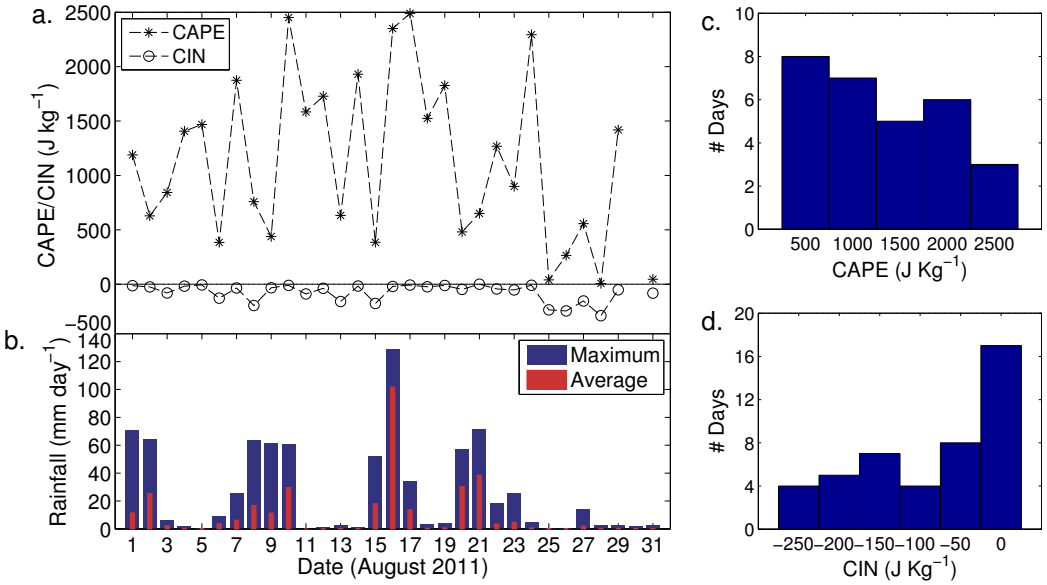

Figure 2.8: Time series of: (a) CAPE and CIN, (b) rainfall, and histograms of (c) CAPE and (d) CIN over August 2011. The rainfall data are for all of the days of August 2011, obtained by the TRMM dataset. As sixteen grid points were used for the calculations two values are presented, maximum over the 6 points (blue bar) and average (red bar).

of the graph, having CIN less that -25 J kg^{-1} and CAPE more that 1500 J kg^{-1}.

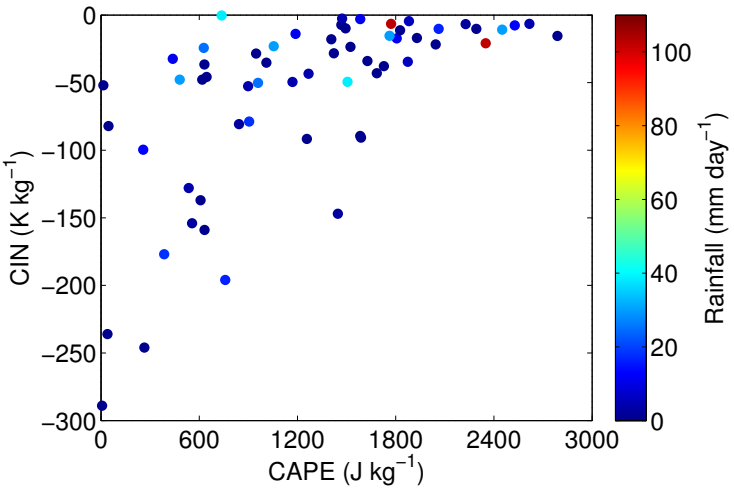

Figure 2.9: Scatter plot of CAPE and CIN. Contouring indicates the amount of rainfall.

There were 17 occurrences of an inversion throughout the studied dataset. Figure 2.10 shows a scatter plot of inversion height and inversion size with the average rainfall as contours. The size of the inversion is calculated as the difference of the pressure levels from the point the atmosphere becomes stable up to the point it becomes conditionally unstable. The highest amount of rainfall occurs on days when the inversion size is small (starting at 150 hPa) and the inversion is located fairly low in the atmosphere (at around 750 hPa). Overall, on days with an inversion the rainfall is limited to less that 40 mm

day^{-1}, showing that an inversion can act to limit the amount of rainfall to values close to those of shallow convection.

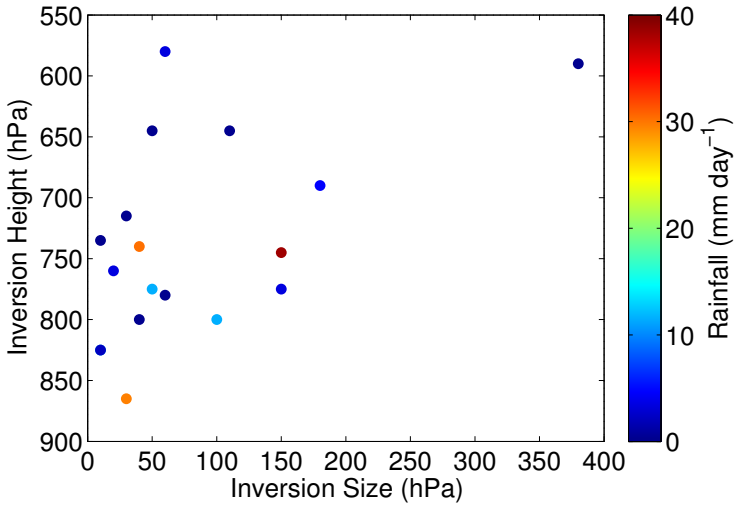

Figure 2.10: Inversion height, inversion size and rainfall for the August 2011 soundings.

2.6.3 Vertical structure

Averages of vertical profiles (potential temperature, wind speed, relative humidity, and mixing ratio) are now studied for days featuring an inversion in the temperature profile. The inversion is located between the heights of 2 and 3 km. Above the inversion the atmosphere is, on average, convective with the stratosphere capping located approximately at 14 km. Wind speed remains constant above the boundary layer for the lower part of the troposphere and is then reduced towards the upper troposphere, before reaching a peak of approximately 2–3 times the lower tropospheric value in the stratosphere. Below the inversion, the atmosphere has a layer with high relative humidity, with an average of approximately 70%, but it decreases significantly above the inversion, leading to a much drier upper troposphere. Relative humidity is one of the most changeable characteristics with the area one standard deviation away from the mean value covering values from 10–70% for the biggest part of the atmosphere.

2.6.4 Wind speed

Wind speed was studied for a layer between 1000 and 1700 m in order to be representative for the lower parts of the atmosphere but high enough as to not be influenced by the boundary layer. The distribution is relatively symmetric, but has a slight skew towards

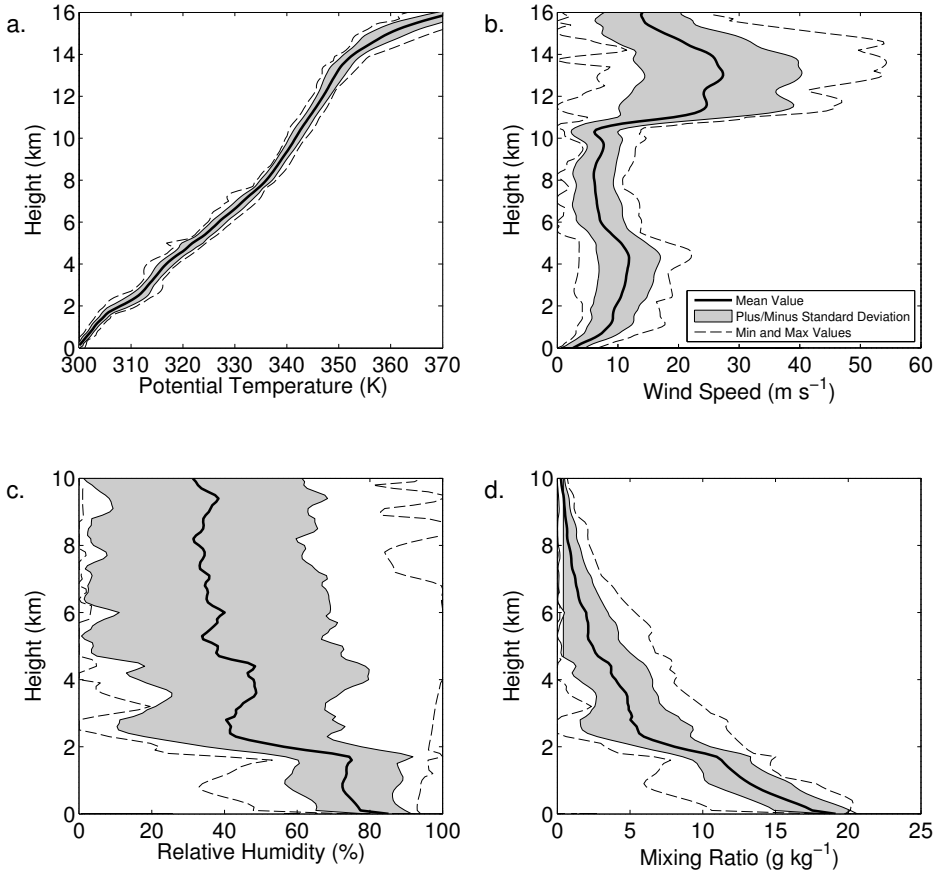

Figure 2.11: (a) Potential temperature, (b) Wind speed, (c) Relative humidity, and (d) Mixing ratio for the days with an inversion in Guadalupe, August 2011. The thick black line is the mean value, shaded areas are one standard deviation away and dashed lines are minimum and maximum values.

lower wind values. The average value is 5 m s^{-1} while the standard deviation is 3 m s^{-1}. For the wind direction, the data were averaged until the height of 1700 m. The prevalent wind direction was easterly, with an average at $80°$ and a standard deviation of $20°$.

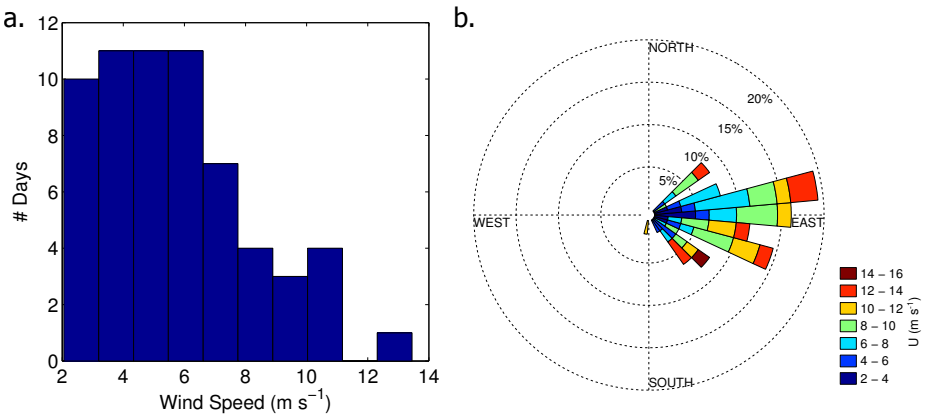

Figure 2.12: (a) Histogram of low tropospheric wind values. (b) Wind rose for data averaged across the low troposphere. Based on the August 2011 soundings.

2.7 Input sounding specification

Different soundings are used between the different chapters. For Chapter 3 the focus of the study is on the dry dynamics and thus a very idealised atmospheric structure is used, with the Brunt-Väisälä frequency (N) being constant with height and no humidity (blue line in Figure 2.13). Chapter 4 explores a more complicated parameter space and a total of 4 input soundings are used, all based on a similar atmospheric structure; a relatively neutral boundary layer capped by an inversion at about 2 km, followed by an unstable upper atmosphere. An example initial sounding can be seen in Figure 2.13, marked by the red line. Wind speed for all simulations is set to easterly and, above the boundary layer, is constant with height typically at -1, -4, -7, and -10 m s^{-1}.

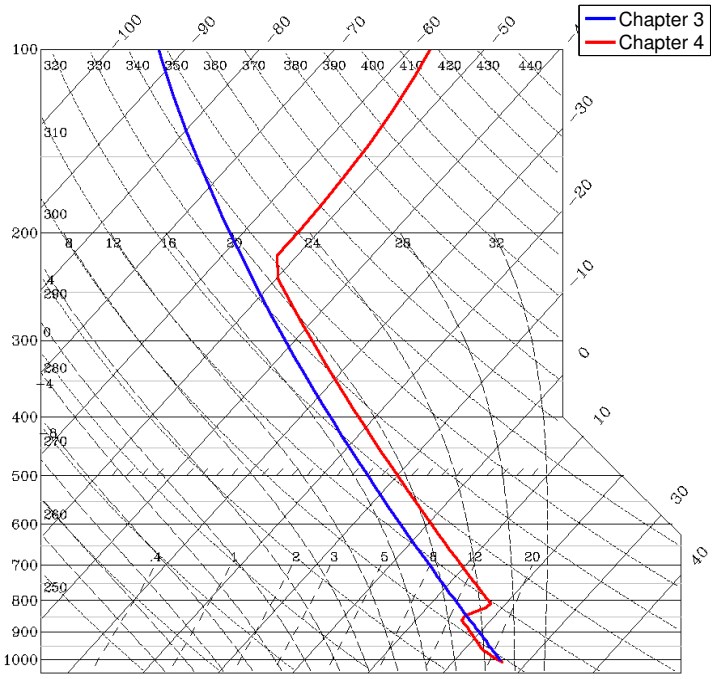

Figure 2.13: A skew-T diagram with the sounding used in the simulations for Chapters 3 (blue line) and 4 (red line), representing an idealised atmosphere where N is constant with height and a quasi-realistic atmospheric structure with an inversion. The red line is for the strong inversion case.

Figure 2.14 shows the different sounding types used in Chapter 4, namely strong and weak inversion (Figure 2.14a) and dry and wet atmosphere above the inversion (Figure 2.14b), for a range of different wind speeds (Figure 2.14c, showing the 6 and 15 m s^{-1} cases). The maximum difference in potential temperature between the strong and weak inversion profiles is 1 K at the peak of the inversion (at a height of 2 km). The "Dry" and

"Wet" tropospheric humidity profiles are similar near the surface with an almost saturated layer between 0 and 2 km with the "wet" relative humidity 5% higher. In the "dry" profile the relative humidity drops steeply, while the "wet" profile features a moister troposphere (10% difference on average).

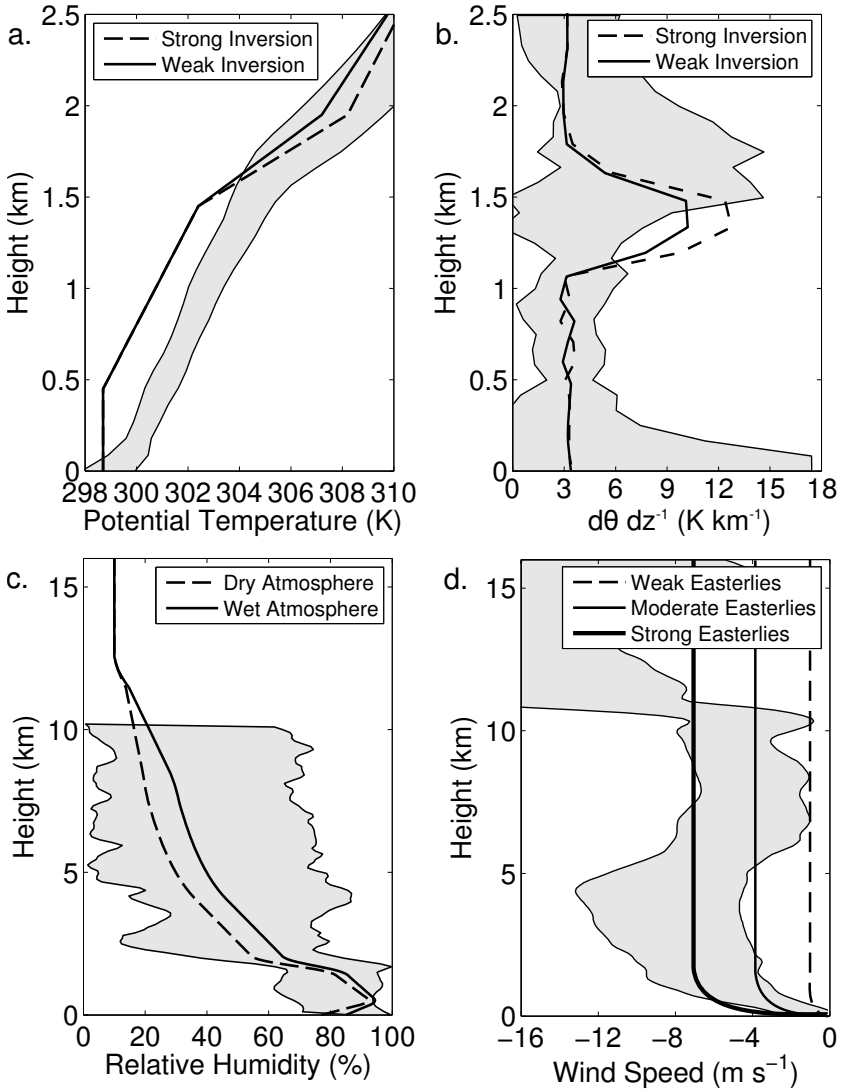

Figure 2.14: Details from the 4 different profiles used in Chapter 4. (a) Potential temperature profile for the first 2.5 km (b) Differential of potential temperature with respect to height (c) Relative humidity profiles featuring a wet and dry troposphere above the inversion (d) Wind speed profiles. The shaded areas in all plots show the area around the mean values plus and minus one standard deviation, as obtained from the sounding analysis and shown previously in Figure 2.11.

Comparing the profiles used to the profiles obtained from the sounding analysis, it can be seen that as far as potential temperature is concerned (Figure 2.14a,b) the profiles used differ slightly compared to the values obtained from the soundings. Namely the inversion on average tends to be located slightly higher, approximately at a height of 2.5 km, and the upper atmosphere tends to be less convective but is still unstable. Nevertheless they have

the same qualitative behaviour and ultimately the reason why this specific structure was used in for the potential temperature profile was to facilitate comparison with literature as it is based in the study done by (Siebasma *et al.*, 2003) and later used by Kirshbaum and Smith (2009) for a study in the Caribbean. As far as humidity is concerned (Figure 2.14c), it can be seen that the profiles used are in good agreement with the values obtained from the soundings, as the "dry" profile is close to the average value minus one standard deviation, while the "wet" profile is closer to the average. Finally, although the profile used for the wind speed is not detailed it is close to the profiles obtained from the sounding analysis, at least for the lowest 1–2 km in the atmosphere (Figure 2.14d). It must be noted here that the majority of the effects studied here are expected to develop with the first 2 km of the atmosphere so a larger focus was given at this area.

2.8 Summary

The input data and settings for the simulations were chosen to be representative of the conditions for a lava dome in the Tropics, specifically for an island in the Caribbean. The specific values of the surface temperature anomaly were chosen as they were a good approximation of the conditions in the Soufrière Hills volcano, as demonstrated by the analysis of infra-red imagery. Furthermore, for Chapters 4 and 5, an effort was made to choose representative and realistic initial conditions in a complex parameter space. For this reason a small climatological study was done for August 2011 with data from Guadeloupe. It was shown that average atmospheric conditions during the rainy season are unstable, demonstrated by a combination of high CAPE and low CIN values. This instability leads to a high amount of rainfall, typically 20–30 mm day^{-1} with higher amounts of rainfall possible. Furthermore an inversion in the atmosphere is a frequent feature and can generally act to limit the amount of convection and consequently rainfall. A number of input soundings were created broadly conforming to these results, featuring a low-level inversion of varying strength, with appropriate profiles for relative humidity, wind speed and atmospheric instability.

Chapter 3

Flow over an idealised volcano: Dry experiments

3.1 Introduction

As a first step in studying the interaction of a volcano and the atmosphere, a simplified problem is considered. The model atmosphere at this stage is highly-idealised: stably stratified and unchanging with height. It is also "dry", meaning that there is no water in any state. This approach is taken in order to study the atmospheric response at a fundamental level, without the complexity of moist processes. The volcano is also idealised, represented by a mountain with a heated summit. The general understanding gained from this chapter will then be used in later chapters to help interpret the results of more realistic and complex simulations.

Orographic flow in the vicinity of mountains and ridges is a classic problem in meteorology, with initial studies such as the ones by Queney (1948), Eliassen and Palm (1961) and Drazin (1961). In order to study a Boussinesq flow, the basic equations that describe the flow are the momentum and continuity equations, along with the equation for mass diffusion. Progress in the mathematical approach towards a solution for this orographic flow was made by the use of linear theory to study the resulting gravity waves (also known as mountain waves) as the flow is forced to go over the obstacle (Smith, 1980, 1989). Linear theory can be used to create an analytical solution for a complex mathematical

equation. Using linear theory, an equation is analysed to series of progressively less significant (higher order) terms, and only first order terms are kept. As such, a linear solution exhibits features simpler that the general, non-linear case and can only be used for certain limits, in which the assumption that higher-order terms are less significant holds; for example, in the case of orographic flow, that the wind speed is sufficiently high. Due to the limitations of linear theory and with the rapid advance of computational power and mesoscale models, computational modelling quickly become a staple, helping research focus on non-linear phenomena (Smolarkiewicz and Rotunno, 1989, 1990) as well as the effects of more advanced physics that initially had to be neglected; for example the effect of the Coriolis force (Ólafsson and Bougeault, 1996; Hunt *et al.*, 2001) or the existence of a boundary layer (Weng *et al.*, 1997; Belcher and Hunt, 1998; Petersen *et al.*, 2003; Smith, 2007).

The main result of these idealised studies has been the investigation of the flow- and gravity wave-related phenomena (such as flow splitting, wave breaking, mountain wakes and lee waves). Using linear theory, Smith (1989) created a flow regime chart to broadly categorise flows and link them with expected phenomena (Figure 3.1). To do this he investigated two key parameters: non-dimensional mountain height ($\hat{h}$) which is defined as $\hat{h} = H\ N\ U^{-1}$, where H is the height of the obstacle, N is the Brunt-Väisälä frequency and U is the wind speed, and the aspect ratio of the hill (R), defined as $R = L_y\ L_x^{-1}$ (Figure 3.1). Note that the non-dimensional mountain height is equivalent to an inverse Froude number, i.e. $Fr = UN^{-1}H^{-1}$ in this study. The validity of the chart has been broadly confirmed by Ólafsson and Bougeault (1996), while phenomena in the non-linear areas were first investigated by Smolarkiewicz and Rotunno (1989, 1990). Despite the fact that the accuracy and exact limits of wave breaking in the chart have been questioned (Ólafsson and Bougeault, 1996), it is still used in order to obtain general insight on the expected phenomena, especially for cases that fall within the linear theory area. Simulations carried out for this chapter start at a regime of non-linearity (higher Fr^{-1} - low wind speeds) where the formation of lee vortices in the lee is expected (Smolarkiewicz and Rotunno, 1989), and progress towards a regime of linearity without complex phenomena (low Fr^{-1} - high wind values). Unlike the vertically propagating mountain waves, trapped lee waves are caused by vertical variations in the incoming flow speed and the

Brunt-Väisälä frequency. For an atmosphere to allow lee waves the Scorer parameter ($l = N\,U^{-1}$) between two layers (for example the boundary layer and the free atmosphere) must fulfil the following criteria: $l_L^2 - l_U^2 > 0.25\,\pi^2\,H^{-2}$, where l_L and l_U are the Scorer parameters for the lower and upper atmosphere respectively. The existence of a boundary layer also causes a shift of gravity wave patterns further upstream, weakening of the wave intensity and a consequent reduction in drag and momentum flux (Jiang *et al.*, 2008).

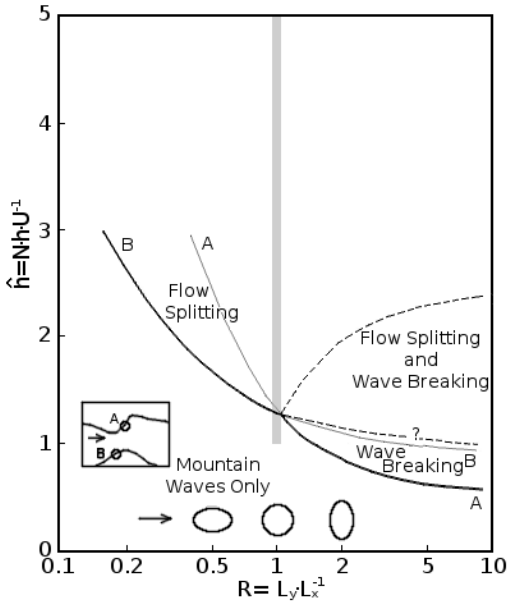

Figure 3.1: Regime diagram based on Smith (1989). The diagram defines flow regimes as a function of the non-dimensional mountain height $\hat{h}$ and the aspect ratio of the hill (R). Curve A/B shows the limit of stagnation aloft (wave breaking)/in the windward slope (flow splitting). The dotted lines signify the area beyond which linear theory is technically invalid, while dashed lines are the suggested critical values for flow splitting and wave breaking within the non-linear regime. The shaded area is an indication of the regime areas under study in this chapter (extending up to $\hat{h} = 100$).

Recently the effect of surface temperature forcing on orographic flow has been receiving an increasing amount of attention. Crook and Tucker (2005), considering the case of solar heating, investigated the effect of heated terrain on flow over a mountain setting, using computational modelling to test the results produced by the theory. Kirshbaum (2013) and Kirshbaum and Wang (2014) extended this work and tested two theories: a linear theory (modified from Crook and Tucker, 2005) and a heat-engine theory, based on the thermodynamics of the flow that was initially proposed by Rennó and Ingersoll (1996) and later extended in numerous studies (Souza *et al.*, 2000; Tian and Parker, 2003; Kirshbaum, 2013). Kirshbaum (2013) demonstrated that the application of linear theory

for two layer flows (for example an atmospheric structure with characteristics varying between the boundary layer and the troposphere) is severely limited due to the non-linear effects that are introduced by the difference between the layers. In a different context, Cunningham *et al.* (2005) and Cunningham and Reeder (2009) studied the effect of wild fires and the generation of convection and pyrocumulus clouds. Although this regime is closer to the research topic of this study, the focus has been on investigating moist processes. Additionally, no general theory has yet been proposed, as research is mainly focused on computational modelling and case studies.

Across all studies the main result of the heating perturbation is the generation of a convective plume (Crook and Tucker, 2005; Cunningham *et al.*, 2005; Kirshbaum, 2013). Additionally, another series of gravity waves can be generated superimposed over the normal mountain waves (Crook and Tucker, 2005). Despite the fact that there is no expectation of quantitative similarities between the results, as the regimes under study are different both in respect to the intensity of the heating as well as the spatial extent, some qualitative similarities between the studies could be expected.

The aim here is to extend the theory of orographic flow over a heated surface for the case of an active dome-building volcano, not undergoing an explosive eruption. In these volcanoes as lava is extruded, it quickly solidifies due to its high viscosity and forms a brittle, high-temperature plug over the conduit (Parfitt and Wilson, 2008). The abrupt increase in surface temperature over the area of the dome will be referred to as the "surface temperature anomaly" (T_a). For more details see Chapter 2, Section 2.4. This study is carried out through a series of idealised simulations for varying wind speeds and surface temperature anomaly values.

The chapter is organised as follows. Section 3.2 details the setup for the numerical simulations, along with a justification of the choices made. Section 3.3 presents the control runs, i.e. simulations with no surface heating. Sections 3.4 and 3.5 present a series of perturbation simulations, studying changes brought by an increase in T_a and Fr respectively. Finally, an overall discussion covering the whole parameter space is presented in Section 3.6, after which the chapter concludes with a summary of the main findings.

3.2 Experimental configuration

The simulations presented in the chapter were carried out using the Weather and Research Forecast (WRF) model, version 3.1, running in idealised mode. The domain is set up with a 400×400 grid with equal horizontal spacing $\Delta x = \Delta y = 300$ m, representing 120 km in both the x and y directions (Figure 3.2a,b). The mountain is represented by the following Gaussian equation:

$$h(x, y) = h_{top} \exp\left[-\left(\frac{x - x_s}{L_x}\right)^2 - \left(\frac{y - y_s}{L_y}\right)^2\right] \tag{3.1}$$

where x_s and x_y are the coordinates of the volcano's centre, h_{top} (1000 m) is the maximum height and L_x and L_y are parameters relating to the half-width (both set at 5700 m). Although the simulations are idealised, these dimensions were chosen so that the mountain has similar topography to that of Monsterrat.

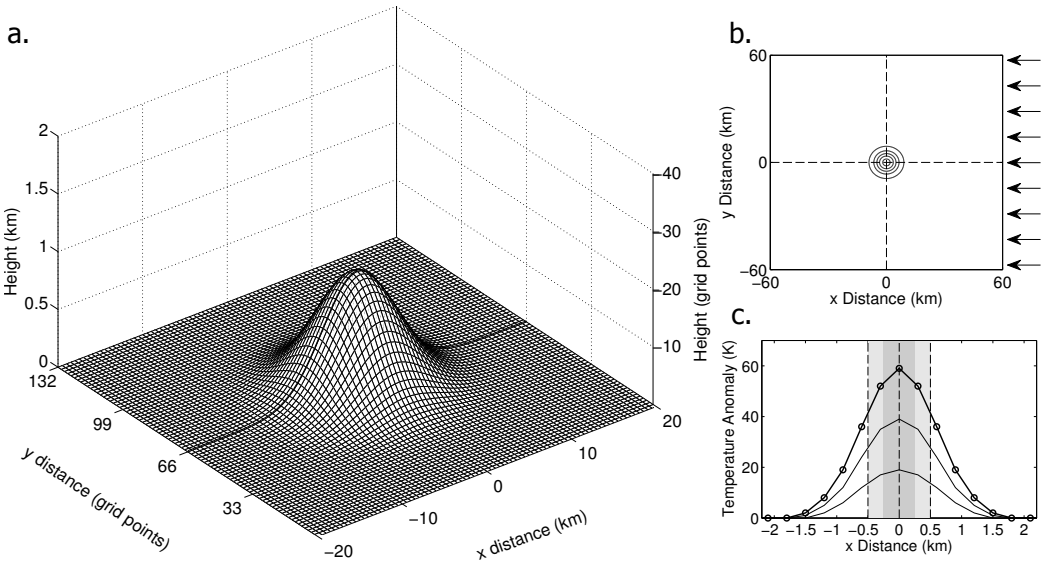

Figure 3.2: (a) Domain used in the experiments. Dimensions are written both in kilometres and number of grid points to allow for appreciation of both the grid size and the corresponding dimensions of the simulation. The z-axis in the simulations goes up to 11 km. The black line represents the cross-section shown in vertical plots. (b) The whole domain of the simulations. (c) Surface temperature anomaly profiles. The shaded area shows the typical Soufrière Hills lava dome diameter (0.5–1 km).

There are 75 levels in the vertical. The vertical grid spacing is 50 m from the surface up to 2 km, then increases linearly to 500 m over 4 km and remains 500 m up to the model top, at 11 km. The time step is 2 seconds and each simulation lasts for 6 hours. Sensitivity tests with a 1 second time step revealed no changes in the results. The first

3 hours are spent on model "spin up" (hours 1-2) and approaching a quasi-steady state (hours 2–3). All results presented are 3h averages from hours 3 to 6 during quasi-steady state conditions. Sensitivity tests up to 12h showed only minor changes in the output.

The surface-layer related physics schemes are used to implement the surface heating on the top of the volcano, specifically a thermal diffusion model for the soil scheme and a Monin-Obukhov scheme for the atmospheric surface layer (Skamarock *et al.*, 2008). No boundary layer, microphysics or radiation schemes were utilised during the simulations (See Chapter 2 for more information).

The atmospheric sounding used for the initial conditions represents a completely idealised atmosphere with $N = 0.01\ \mathrm{s}^{-1}$ being constant with height. Simulations are carried out for four incoming flow speeds (constant with height), ranging from $0.1\ \mathrm{m\ s}^{-1}$ up to $10\ \mathrm{m\ s}^{-1}$, corresponding to Froude number values from 0.01 up to 1.

With respect to the surface temperature anomaly, simulations were run for four values in total, for $T_a = 0$ K (no temperature anomaly, control runs), and $T_a = 20$ up to 60 K, by increments of 20 K (Table 3.1). The surface temperature anomaly (approximately 9 grid points wide) is imposed on top of the normal mountain lapse rate and is represented by the following Gaussian equation:

$$T'(x, y) = T_a\ \exp\left[-\left(\frac{x - x_0}{W_x}\right)^2 - \left(\frac{y - y_0}{W_y}\right)^2\right] \tag{3.2}$$

where T' is the temperature perturbation, x_0 and y_0 are the coordinates of the lava dome, T_a is the maximum temperature anomaly and W_x and W_y are parameters relating to the half-width (both set at 900 m), see Figure 3.2c. Despite the fact that this progressive reduction leads to a wider surface temperature anomaly than the typical dimensions for the dome in Soufrière Hills, Montserrat (in this setup the "dome" covers an overall area of 2500×2500 m, compared to an average size of 400×1000 m; Wadge *et al.*, 2014), this smooth profile was utilised in order to avoid computational errors and model instability that occurred due to the overly steep change in the values. The full range of simulations can be seen in Table 3.1.

The key parameters (e.g. Fr, T_a, U, N, H etc) were defined to cover a reasonable amount of parameter space for flow over an isolated mountain (see Figure 3.1), yet also

Parameter	Values
T_a (K)	0:20:60
W_x, W_y (m)	900
Fr	0.01, 0.1, 0.4, 0.7, 1
$\|U\|$ (m s^{-1})	0.1, 1, 4, 7, 10
N (s^{-1})	0.01
h_{top} (m)	1000
L_x, L_y (m)	5700

Table 3.1: The full range of parameters chosen for the simulations discussed in this chapter. Note that the Froude number is calculated using values of $|U|$ between 0.5 and 2 km.

keep the simulations physically realistic and their number manageable. Since this investigation ultimately aims to be used for case studies in Montserrat, it was decided that characteristics of the obstacle that are similar in terms of the control parameters, such as mountain height and half-width, would remain unchanged.

3.3 Control runs

Initially, results from the control simulations ($T_a = 0$ K) are analysed and compared to the theoretically expected flows. Figures with multiple plots in this section start from the $Fr = 0.1$ case ($|U| = 1$ m s^{-1}; Panel a) and end with the $Fr = 1$ case ($|U| = 10$ m s^{-1}; Panel d). Horizontal plots are shown at the third model level (a height of 150 m) to be representative of the low-level flow but not affected adversely by the surface layer. Note, the colour axis is always saturated at both ends (dark blue and red values).

3.3.1 General features

All four panels show easterly flow impinging on the mountain, leading to ascent on the windward slopes and descent on the lee side. Starting from a low Froude number ($Fr = 0.1$, a non-linear regime; Figure 3.3a) as the wind increases there is a progression from a "flow around" towards a "flow over" regime (for example $Fr = 1$; Figure 3.3d).

For low Froude numbers, non-linear phenomena such counter-rotating vortices in the lee of the mountain can also be seen (Figures 3.3b,c). Unlike many studies a non-slip condition is not used here, leading to friction in the lower levels and the development of a boundary layer. This leads to the presence of other complex phenomena, such as flow separation, seen in the lee of the mountain, mainly in Figures 3.3c,d.

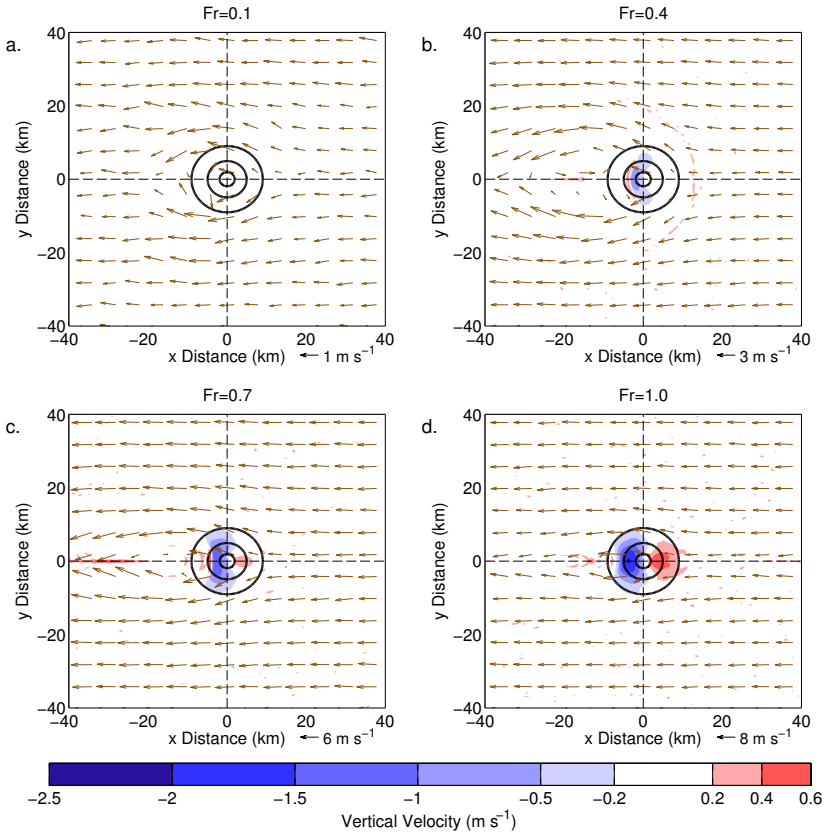

Figure 3.3: Vertical velocity (shaded contours) with the horizontal wind vectors for: (a) $Fr = 0.1$, (b) $Fr = 0.4$, (c) $Fr = 0.7$ and (d) $Fr = 1.0$, on the third model level (150 m). Note the scaling of the horizontal wind vector changes over the four panels. Height contours at 100, 500, and 900 m. $T_a = 0$ K across all panels.

3.3.2 Gravity waves

As the easterly flow approaches the mountain, the flow is forced over and around, and gravity waves are generated in the lee (Figure 3.4), leading to areas of vertical acceleration and deceleration (Figure 3.5). The strength of the gravity waves increases with Fr as more flow is forced over the mountain.

At low Froude numbers (Figures 3.4a and 3.5a) the flow is too weak to go over the mountain so it is forced to diverge (indicated by the horizontal isentropes), creating an area of flow blocking in the windward side and a small area of flow reversal in the lee, similar to Smolarkiewicz and Rotunno (1989) (Figures 3.4a and 3.5a). The situation changes gradually as the Froude number increases with the gravity waves becoming stronger and the vertical velocity range changing by one order of magnitude. Aside from vertically propagating mountain waves for $Fr \geq 0.7$, there is a pronounced lee wave response (Figures 3.4c,d). This is caused by the existence of turbulence and the boundary layer

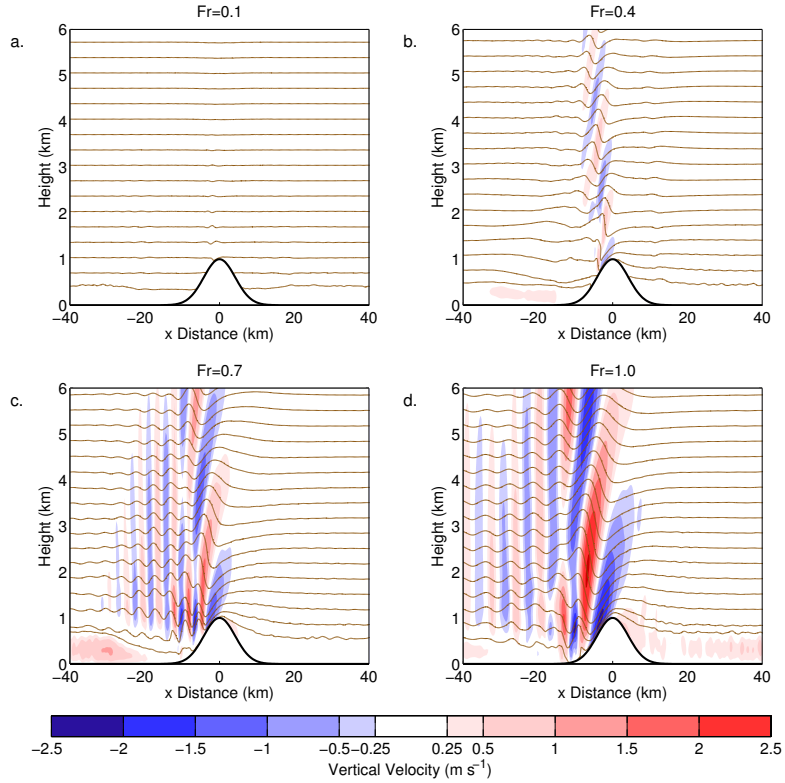

Figure 3.4: Vertical velocity (shaded contours) with isentropes (brown lines) overlaid, across a cross-section in the middle of the domain, for: (a) $Fr = 0.1$, (b) $Fr = 0.4$, (c) $Fr = 0.7$, (d) $Fr = 1$. Isentropes plotted between 299 and 316 K, every 1 K. $T_a = 0$ K across all panels. Control runs.

as for both cases the Scorer parameter criteria is fulfilled (a maximum boundary layer velocity of approximately 5.7 m s^{-1} for $Fr > 0.7$). An extensive area of flow reversal can be seen in the lee for $Fr > 0.4$ (Figure 3.5), maximised at $Fr = 0.4$ and being reduced to two separate rotors for $Fr = 1$. Small hydraulic jumps can also be seen in all cases except for the $Fr = 0.1$, similarly to Ólafsson and Bougeault (1996).

To further investigate the vertical velocity characteristics, three vertical profiles, at locations -3, +3 and +15 km (see Figure 3.6) are shown in Figure 3.7. Although the upper limits are influenced by the damping layer the figures act to illustrate the gross changes in wave activity as the Froude number increases.

Starting from Figure 3.7b, wave activity is evident. In Figures 3.7c,d, gradually stronger amplitudes of gravity waves are seen. The windward point always starts at positive values, capturing the ascent of the flow, while the leeward point always starts with negative values, capturing the descent. Descent in the lee is always stronger than ascent on the windward side, due to augmentation by downslope winds. As the Froude number

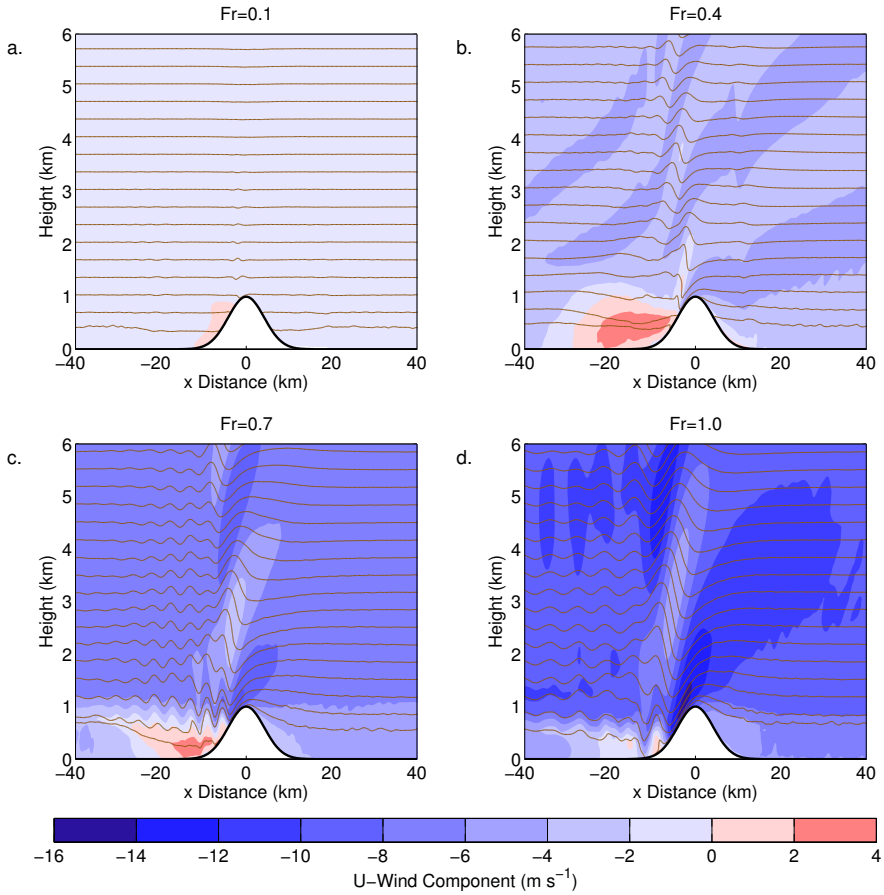

Figure 3.5: As Figure 3.4 but contour plots of U wind component. Isentropes plotted between 299 and 316 K, every 1 K. Control runs.

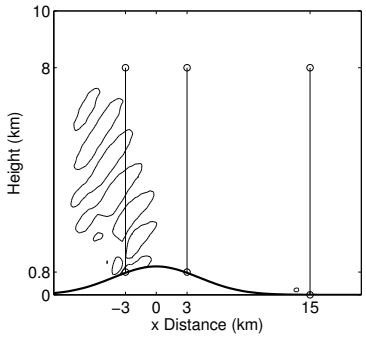

Figure 3.6: Location of points used for the vertical velocity profiles presented in Figure 3.7. The thin black lines represent the $\mathrm{w} = 0\ \mathrm{cm\ s^{-1}}$ vertical velocity contours for the $\mathrm{Fr} = 0.4$ case.

increases there is an increase in the height of both the maximum and minimum values for both windward and lee points, as well as an increase in the wave length. This is consistent with the change in the tilt of the mountain waves as previously discussed and with previous work (Smith, 1989; Smolarkiewicz and Rotunno, 1989).

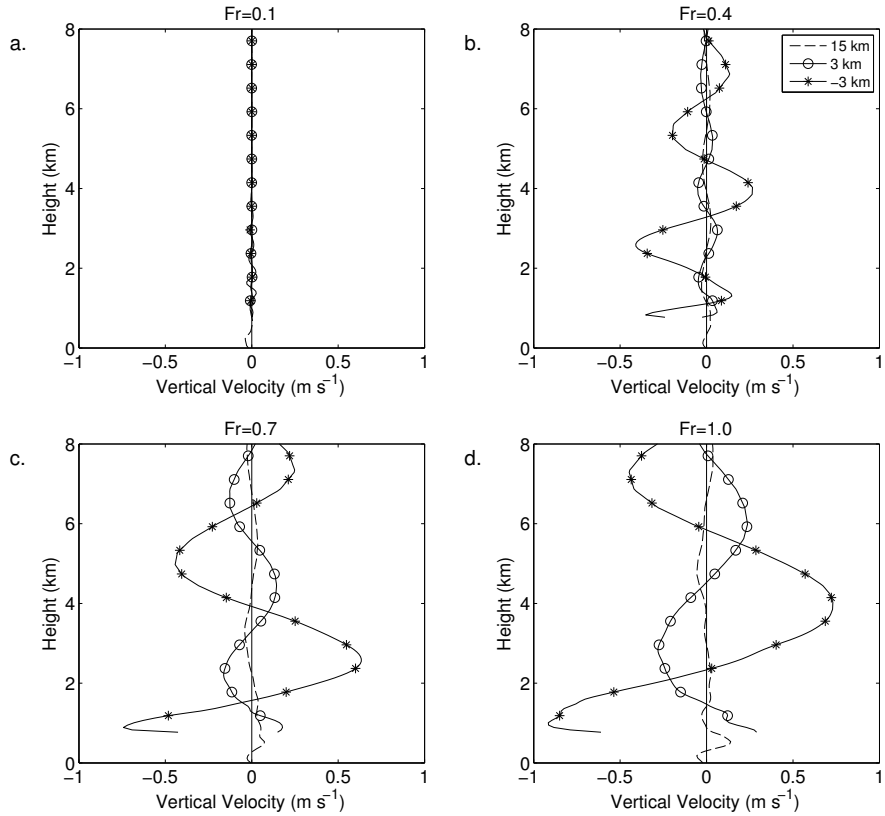

Figure 3.7: Vertical structure of vertical velocity at the three points seen in Figure 3.6, for the cases under study: (a) $\mathrm{Fr} = 0.1$, (b) $\mathrm{Fr} = 0.4$, (c) $\mathrm{Fr} = 0.7$ and (d) $\mathrm{Fr} = 1$.

3.3.3 Turbulence characteristics

Subgrid turbulent kinetic energy (TKE) as output by the model, can be seen in Figures 3.8 and 3.9. As the wind speed increases throughout the four simulations, there is a visible increase in turbulence in the lee.

The maximum values of turbulent kinetic energy (ranging between 0.2 and 1 $\mathrm{m}^2\ \mathrm{s}^{-2}$) can be found in the lee for higher Froude number values, forced closer to the surface due to the increasingly strong downslope winds for higher Froude numbers (Figure 3.8). Due to the stratification in the atmosphere the increase in TKE is largely constrained within about 1 km of the surface.

At $Fr = 0.7$ there is a substantial increase in TKE in the lee of the mountain, with a peak close to the mountain and a secondary peak further downwind. A further increase in the Froude number results in larger TKE values but the horizontal distribution become narrower and is drawn closer to the mountain (Figure 3.9c,d). A similar increase in TKE (both in magnitude and distribution) has been noticed in studies of atmospheric flow past three-dimensional obstacles, for example by Eckermann *et al.* (2010), while experiments

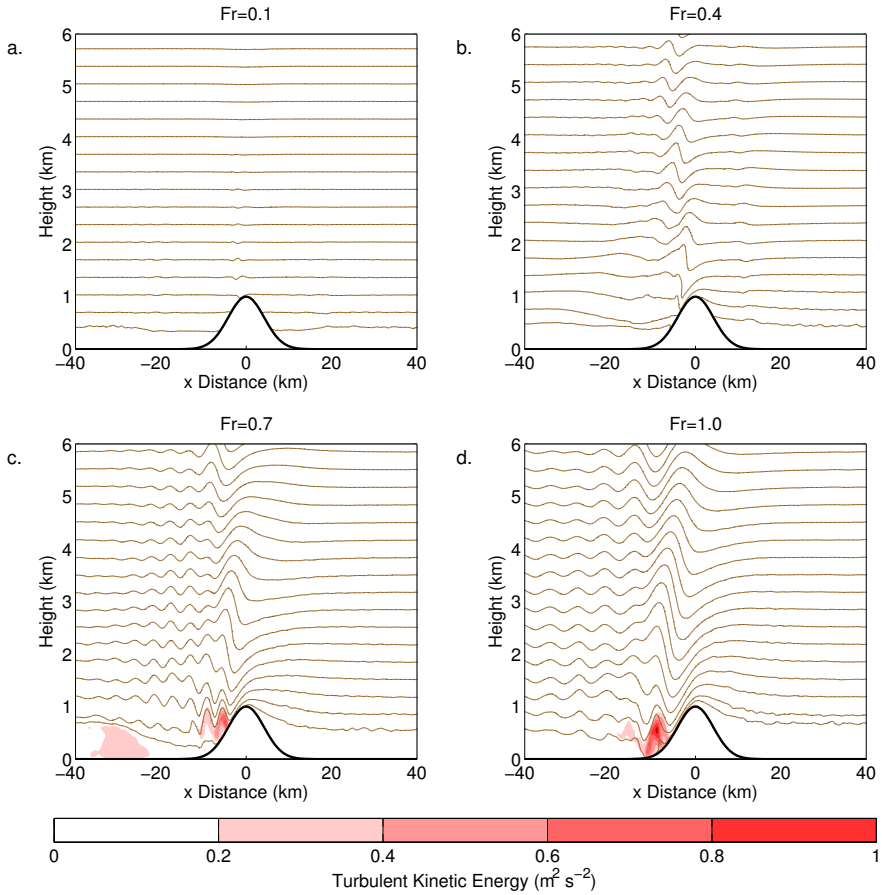

Figure 3.8: As Figure 3.4 but for TKE. Isentropes plotted between 299 and 316 K, every 1 K. Control runs.

by Minder *et al.* (2013) showed a qualitatively similar increase in TKE in the lee of the mountain of Dominica, but with higher values (up to 17 m^2 s^{-2}) due to the fact that resolved turbulence is also included and a combination of moist convection, higher incoming flow speed, and use of more realistic, steeper and aerodynamically rougher terrain.

3.3.4 Overview of control runs

Figure 3.10 shows several diagnostics across all the control simulations as a function of Froude number. Figure 3.10 illustrates that the increase of vertical velocity is roughly symmetrical with the peak values reached at the gravity wave response area (see also Figures 3.4 and 3.7). Maximum positive (reverse) horizontal winds are found in the lee of the mountain and reach a peak at $Fr = 0.4$ (Figure 3.10b). Finally, as seen in Section 3.3.3, an increase in the incoming flow speed leads to a large increase in TKE of the system, especially between $Fr = 0.2$ and 0.4, located mainly in the lee of the mountain (Figure 3.10c). This is due to the onset of wave activity and turbulence in the lee, as seen

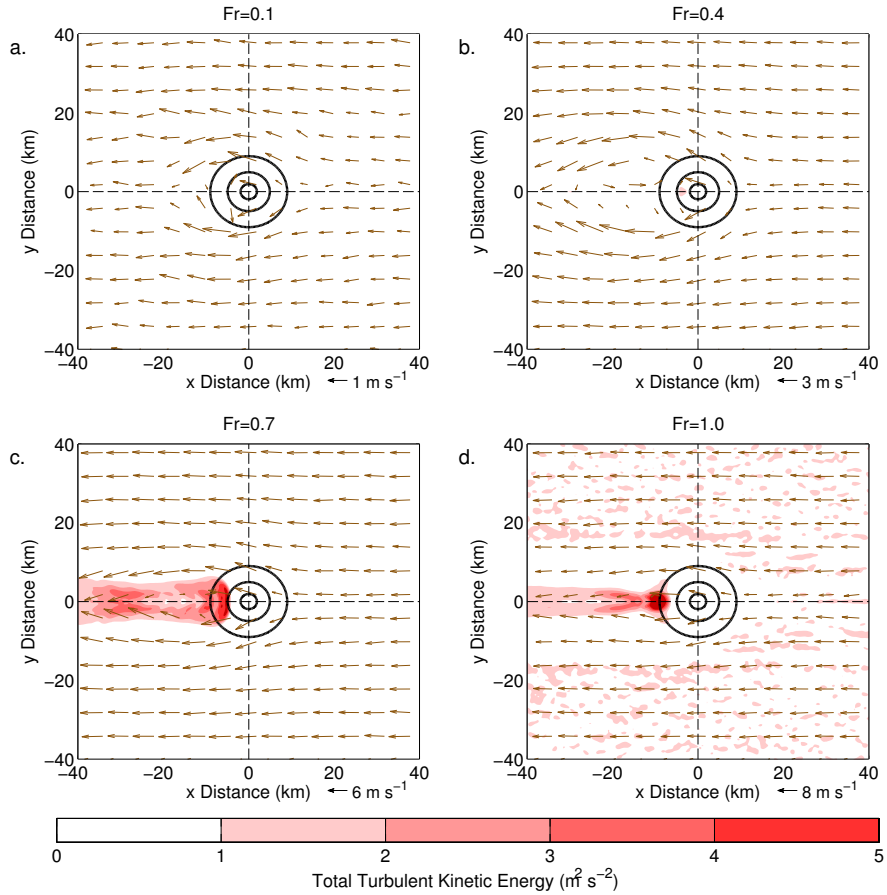

Figure 3.9: Total TKE across the height of the atmosphere for the control runs.

in Figure 3.9. Note that the TKE value here is the maximum and not the total across the atmosphere. The maximum height of the trail is always close to 1 km after strong mixing is triggered (Figure 3.10d). Note that the "TKE trail" introduced here is an important characteristic of the flow as it will be used as a proxy for the convective plume triggered by the surface temperature anomaly, with the "TKE trail height" showing the height up to which volcanically-induced turbulent mixing occurs. Values shown here will be used as a baseline for the comparison.

As discussed throughout this section, the model was found to replicate the theoretically expected results, e.g. (Smith, 1989; Smolarkiewicz and Rotunno, 1989; Eckermann *et al.*, 2010). Characterisation of the flows by the use of the Froude number is justified as the flow changes from a "flow around" regime in low Froude number simulations, towards a "flow over" regime as the Froude number is increased. For cases with relatively high Froude number ($Fr > 0.4$) a series of gravity waves were triggered, with characteristics as expected by linear theory (Smith, 1989) and tested in numerous studies (Smolarkiewicz

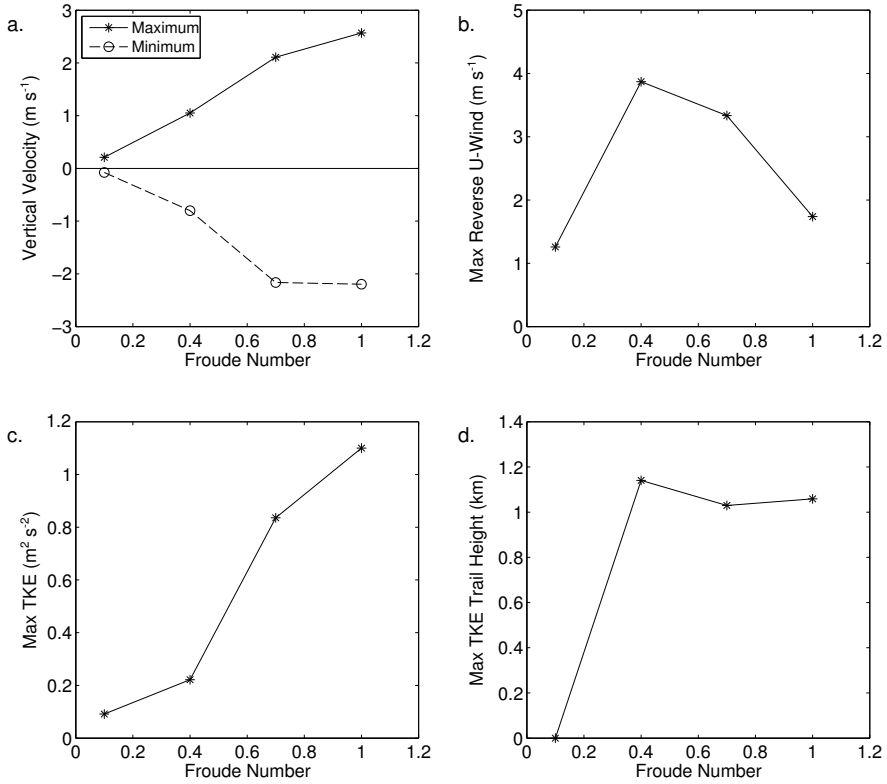

Figure 3.10: (a) Maximum and minimum vertical velocity against Froude number. (b) Maximum (positive) U wind component. (c) Maximum TKE, and (d) maximum height where TKE$>$ 0.2 m^2 s^{-2}. All simulations carried out at $T_a = 0$ K (control simulations).

and Rotunno, 1989; Ólafsson and Bougeault, 1996). In the non-linear regime lee vortices, lee waves and flow reversal in the lee were apparent in the simulations as expected by the studies of Smolarkiewicz and Rotunno (1989). The turbulent kinetic energy of the system also increases in response to the increase Froude number in a way similar to previous studies (Eckermann *et al.*, 2010; Minder *et al.*, 2013).

3.4 Surface temperature anomaly runs for constant Fr

The effect of different temperature anomalies imposed over a moderate wind field, characterised by a Froude number of 0.4, is now considered. For ease of comparison figures with multiple plots will start with the control case ($T_a = 0$ K, Panel a in all figures, as presented in the previous section), and then progress through increasingly higher temperature anomalies (Panels b to d in all figures, with $T_a = 20$, 40 and 60 K respectively). Note that many of the figures in the section are more focused over the mountain top.

3.4.1 General features

Figure 3.11 shows the atmospheric flow response to the range of surface temperature anomalies. An area of ascent in the lee the mountain summit is created, interacting destructively with the area of downslope wind in the lee, disrupting the control pattern. The more intense the thermal forcing, the closer the area of ascent is to the summit. The ascent indicates a convective plume which introduces an area of flow reversal with weak leeside-vortices drawing air back towards the plume centre. This acts in tandem with the flow reversal already found in the lee (as shown previously in Figure 3.3). This area of flow reversal is less noticeable for low T_a values ($T_a = 20$ K), but reaches a peak with reverse winds of approximately 1.5 m s^{-1} (half of the incoming flow speed) in the $T_a = 60$ K case (Figure 3.11d). Horizontally, the area affected is relatively small and even in the stronger cases does not extend outside of the 5×5 km area, constrained on the lee of the temperature anomaly.

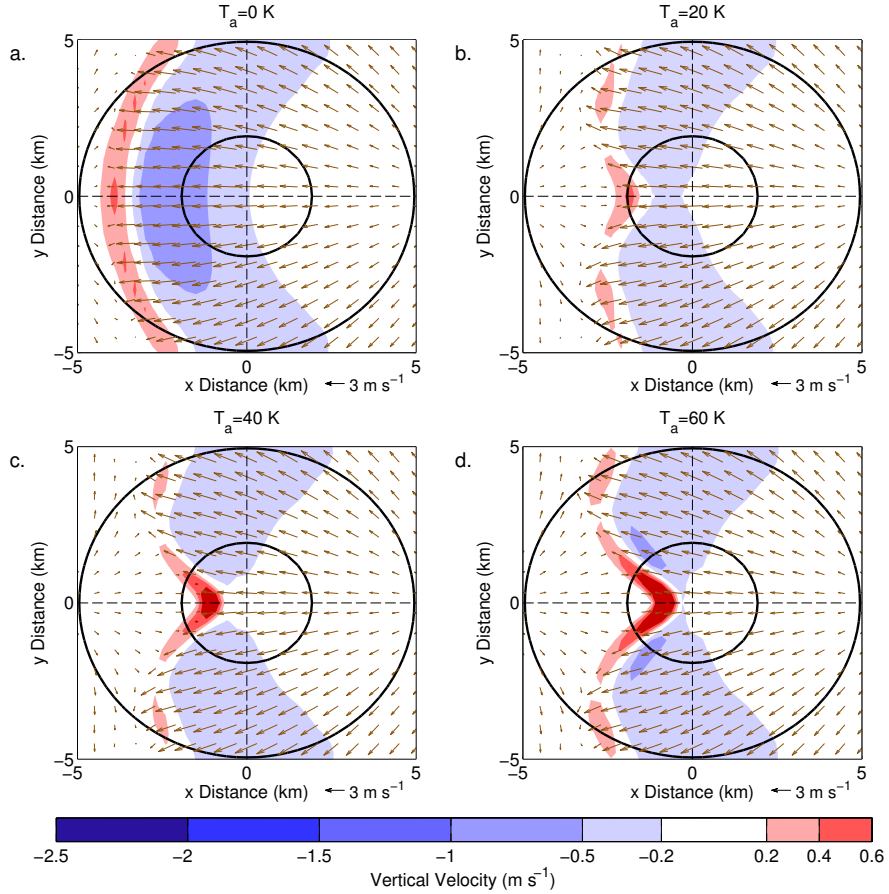

Figure 3.11: Surface contour plots of vertical velocity with the horizontal wind vectors on the third model level (150 m): (a) $T_a = 0$ K, (b) $T_a = 20$ K, (c) $T_a = 40$ K, and (d) $T_a = 60$ K. Height contours at 500 and 900 m. $Fr = 0.4$ across all panels.

The term "convective plume" will be used to describe an area of increased convection and mixing over or on the lee of the surface temperature anomaly. This will either be identified using vertical velocity ($w_{max} > 2$ m s^{-1}) or sub-grid TKE (TKE$_{max}$ >0.2 m^2 s^{-2}). Note that, while in low Froude number cases this is easily identifiable due to the otherwise low values in w and TKE, it becomes more difficult to isolate it in higher Froude number cases. As such, for $Fr > 0.4$ comments about the plume will be made based on comparisons with respective control cases. When studying particular characteristics, data for TKE will be used (see Section 3.6 for details).

3.4.2 Convective plume and gravity waves

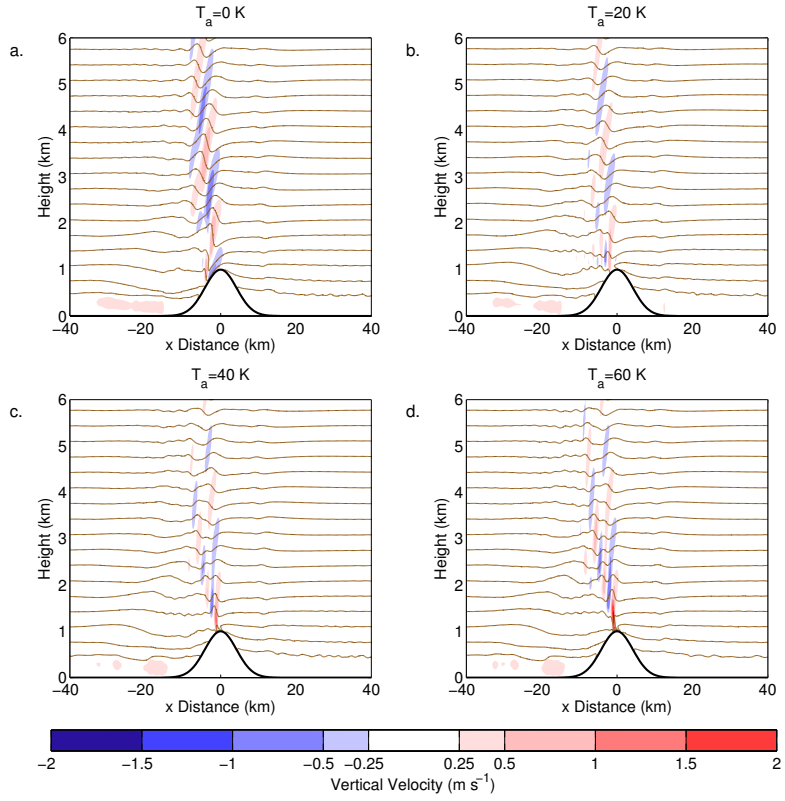

Figure 3.12: Vertical velocity (shaded contours) with isentropes (brown lines) overlaid, across a cross-section in the middle of the domain, for: (a) $T_a = 0$ K, (b) $T_a = 20$ K, (c) $T_a = 40$ K, (d) $T_a = 60$ K. Isentropes plotted between 299 and 316 K, every 1 K. $Fr = 0.4$ across all panels.

The control case reflects a standard isentrope cross-section where a series of stationary gravity waves propagate upwards (Figure 3.12a). As seen in the horizontal plots the temperature anomaly acts to introduce a convective plume just downwind of the summit, manifested by an increase in vertical velocity and a series of small-scale gravity waves, similar to results for dry simulations presented by Kirshbaum (2011).

Even for relatively weak thermal forcing ($T_a = 20$ K – Figure 3.12b), the circulation enforced by the plume is superposed on the gravity wave activity and acts to alter the mountain wave response. As the convective plume intensifies, this superposition of the plume activity and the normal mountain wave response leads to different activity patterns. This behaviour is consistent with previous research (Crook and Tucker, 2005). In the vicinity of the temperature anomaly the strong descent that dominates the leeside of the control simulation effectively disappears for $T_a > 20$ K. The dependency of the plume-generated response to the plume characteristics can be clearly identified. In this respect the plume can be said to act as "virtual terrain", effectively acting as a steep, tall hill, overlaid on top of the normal mountain, forcing the flow that is not directly in the vicinity to go over and around it. Although the immediate effects of the plume are very localised, noticeable alterations in the flow extend as far as 20 km downstream.

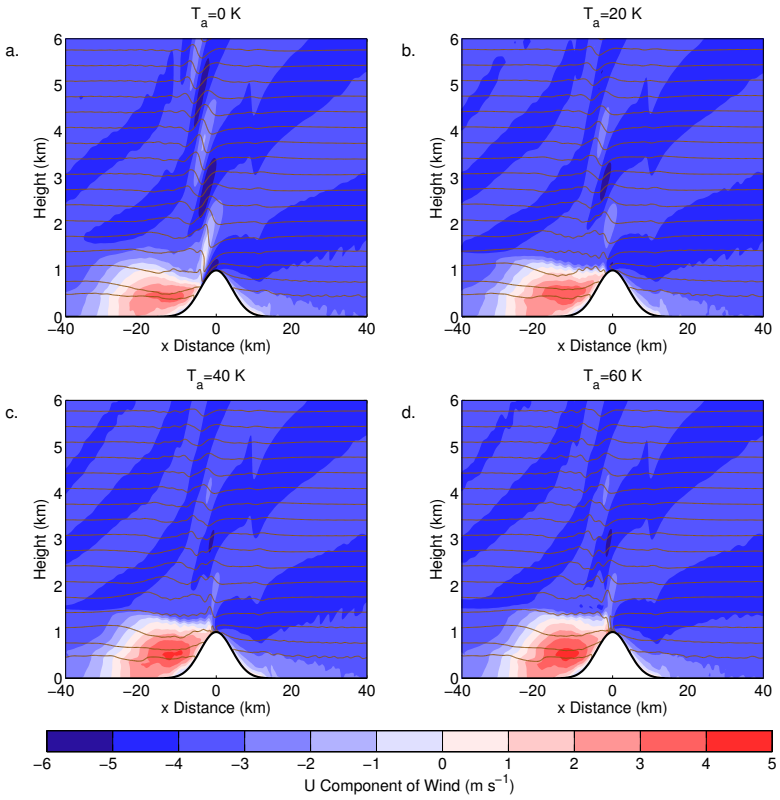

Figure 3.13: As Figure 3.12 but contour plots of U-wind component. Isentropes plotted between 299 and 316 K, every 1 K.

In the U-wind component plots, a more extended area of flow separation and reversal can be seen in the lee (Figure 3.13), with increasingly stronger positive values as the strength of the thermal forces increases - with reverse flow up to 5 m s^{-1} (Figure 3.13d).

As noted earlier, the area of downslope wind disappears and is replaced by the area of flow reversal that starts closer to the summit as the surface temperature anomaly strength increases. This can have implications for mixing of ash and other volcanic emissions in the lee of a volcano.

Looking at the vertical profiles of w it can be seen that the +3 km profile (on the windward side) remains unaffected by the temperature anomaly, remaining almost identical throughout the set of simulations. On the other hand the lee-side profiles change drastically. What can be seen here is the effect of the superposition of the two different sets of gravity waves along with the area of flow separation. Starting at Figure 3.14b, the lower area in the atmosphere that featured the maximum downwards values of vertical velocity is now taken up by a heavily damped oscillation that is of a similar amplitude and slightly lower frequency, as would be expected from a steep but short obstacle, superimposed over the normal mountain waves. For stronger thermal forcing the vertical velocity profile for the lower atmosphere switches from negative to positive values - the disappearance of the downslope wind detailed previously.

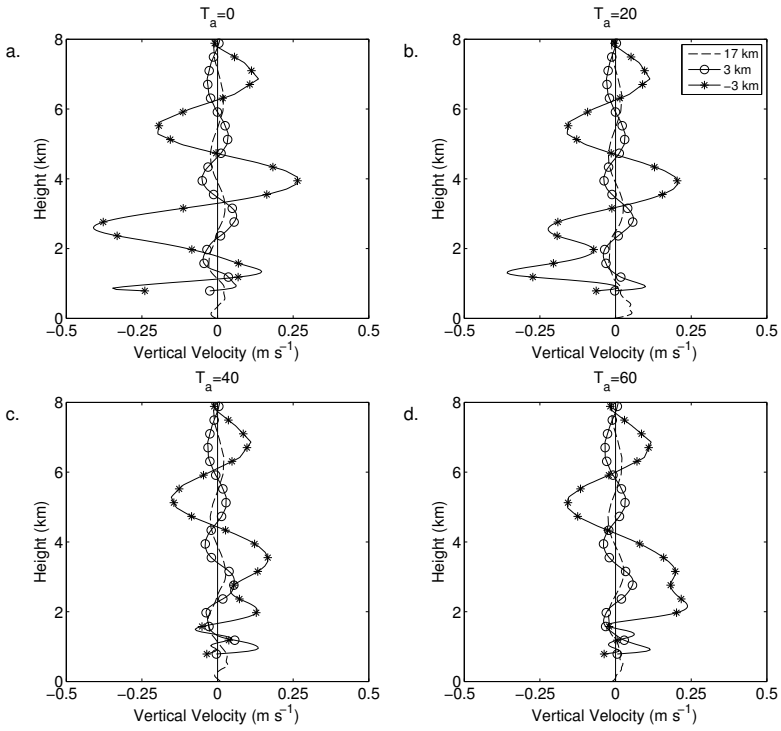

Figure 3.14: Vertical structure of vertical velocity at three points, 17 km away from the peak towards the windward side and 3 km before and after the peak, all across the middle of the domain, for the cases under study.

3.4.3 Turbulence characteristics

The convective plume is marked by a considerable increase in TKE – over one order of magnitude in the simulations with surface heating – signifying the amount of mixing carried out. The control case is marked by relatively low sub-grid TKE values (for this $Fr = 0.4$ setting), so here, TKE can be used as a proxy for the plume (Figure 3.15). As expected, the turbulent kinetic energy reaches a peak in the area of the plume with values up to roughly 1 m^2 s^{-2} close to the surface. Although most of the area of high turbulence seems to be confined to the plume, as the imposed temperature anomaly is increased there is an area on the lee side (at 8 km) with small but noticeable TKE values – this is the area where the flow reversal is aided as seen previously in Figures 3.12 and 3.13. Note that, due to the strong stratification of the cases presented here, advection of TKE follows the atmospheric layers closely, as seen previously in Figure 3.8.

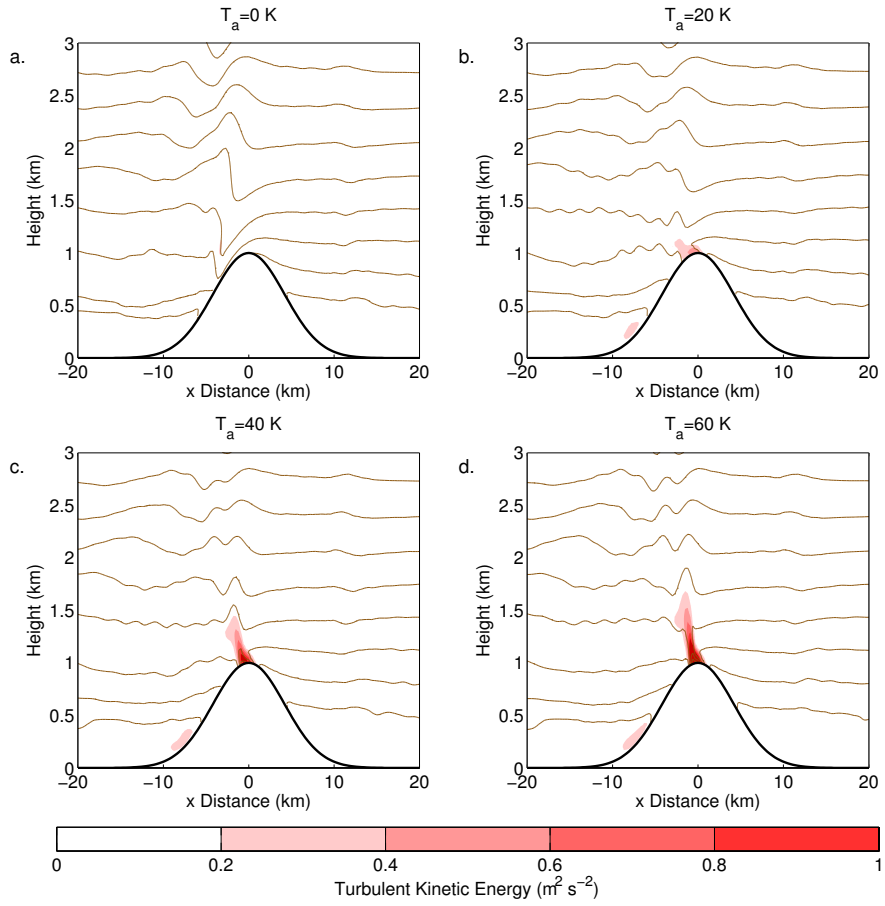

Figure 3.15: As Figure 3.12 but contour plots of TKE. Isentropes plotted between 299 and 316 K, every 1 K.

3.4.4 Summary of changes by T_a

Overall, the plume, even for low surface temperature anomaly values, has a significant effect on the atmospheric flow. At $Fr = 0.4$ (not a very energetic flow) the introduction of the plume can be seen by several diagnostics marked by nearly a tripling of vertical velocity at $T_a = 60$ K (Figure 3.16a), an increase in the strength of the flow reversal area in the lee (Figure 3.16b), an increase of the maximum TKE by one order of magnitude (Figure 3.16c), and a progressively higher plume height – shown by the increase in the maximum TKE height (Figure 3.16d).

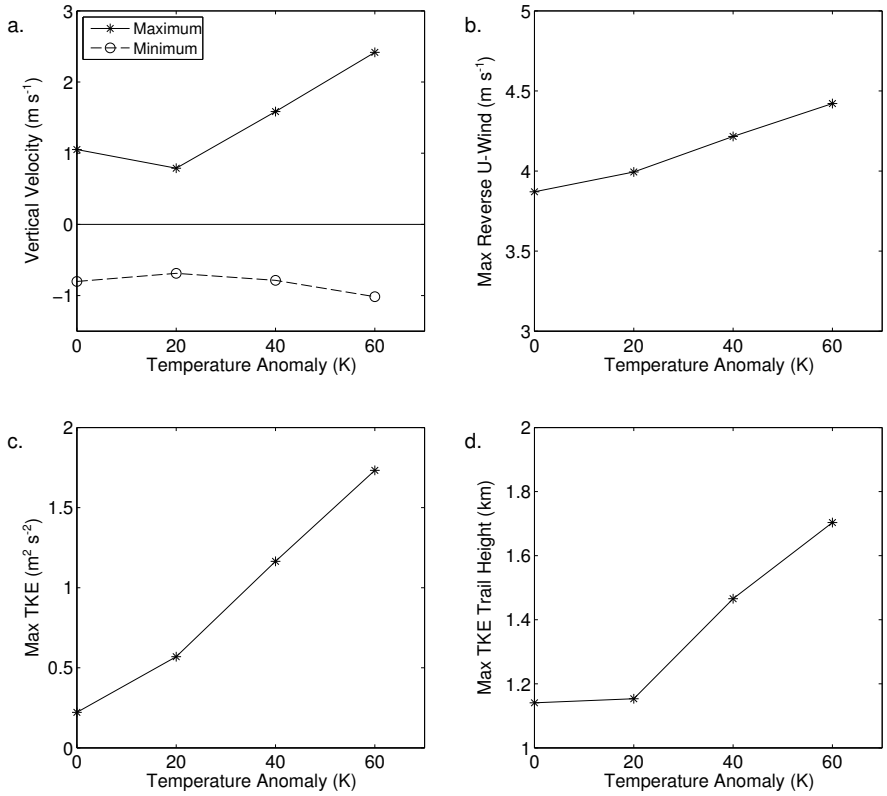

Figure 3.16: (a) Maximum and minimum vertical velocity against surface temperature anomaly. (b) Maximum (positive) U wind component. (c) Maximum TKE, and (d) maximum height where TKE> 0.2 m^2 s^{-2}. All simulations carried out at $Fr = 0.4$.

The main effect of the surface temperature anomaly was seen to be the introduction of a convective plume. The plume has been seen to act superposed over the normal mountain wave activity of the mountain, modifying areas of original strong ascent or descent, including the area of strong downslope wind close to the surface. The plume acts as "virtual terrain" forcing the incoming flow to go over and around it. The introduction of this extra obstacle acts to trigger a set of plume-generated gravity waves that are superimposed over

the control (i.e. normal) mountain waves. Finally, the plume was seen to increase the area and strength of flow reversal in the lee.

As far as mixing is concerned, it was shown that having the addition of the anomaly intensifies mixing over the peak of the hill leading to values at least an order of magnitude higher than in the control cases. Due to this dramatic increased in the TKE of the flow, identification of areas of high TKE is proposed as a diagnostic to help identify the extent and impact of the plume.

3.5 Surface temperature anomaly runs for constant T_a

The effect of different incoming flow speeds on a plume for a specified surface temperature anomaly ($T_a = 60$ K) is now analysed. By keeping the stability of the atmosphere constant throughout the experiments, changes in the incoming flow speed ($|U| = 1$–10 m s^{-1}) cause a change in Fr (0.1–1). Figures with multiple plots in this section will start from the $Fr = 0.1$ case (Panel a) and end with the $Fr = 1$ case (Panel d), i.e. the layout mirrors that of Section 3.3 and so figures can be directly compared.

3.5.1 General features

Several features are highlighted in this section. First of all, it can be seen that the shape of the plume is very sensitive to the wind speed – this is a change from a fairly symmetric circular shape towards a "$>$" shape (Figure 3.17). The position and strength of the plume are also strongly affected due to advection by the wind: in the weak wind cases the plume develops almost on top of the temperature anomaly, while as the wind intensifies the plume is advected further downwind, as far as 4 km downwind for the $Fr = 1$ case. The relative strength of the plume compared to the rest of the flow decreases as the flow becomes stronger. While the plume has a strong localised effect in the flow for the $Fr = 0.4$ case (as discussed in depth in Section 3.4), the effect on the large-scale flow is lessened for the $Fr = 0.7$ and 1 cases.

3.5.2 Convective plume and gravity waves

As seen previously, as the Froude number is increased, advection acts to push the plume (as seen by the strong convection) further downwind, creating different interactions with

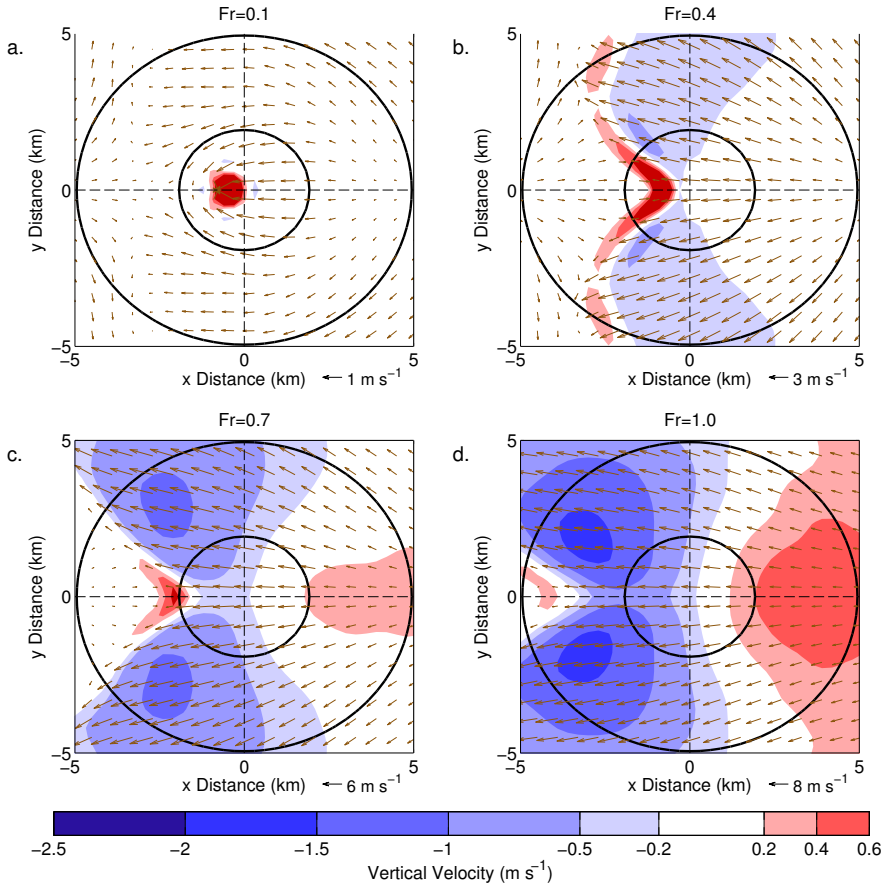

Figure 3.17: Surface contour plots of vertical velocity with the horizontal wind vectors on the third model level (150 m) for: (a) Fr $= 0.1$, (b) Fr $= 0.4$, (c) Fr $= 0.7$ and (d) Fr $= 1.0$. Maximum vector lengths are shown beneath each plot. $T_a = 60$ K across all panels.

the large-scale flow and related wave activity (Figure 3.18). For low Froude number values (Figure 3.18a,b) the plume effects dominate the flow, while for higher Froude numbers the plume plays a secondary role, depending on the relative positioning of the plume and the gravity waves triggered by the mountain. In this respect, the plume can be said to act as "virtual terrain", forcing the flow over and around it and producing a set of secondary gravity waves in a similar way a mountain would, clearly seen in Figure 3.18b. The difference here is that the plume is a highly variable "mountain" and is greatly affected by the incoming flow speeds, starting with a height of 1 km, but changing shape and height under a stronger wind. The secondary gravity wave response also varies as the "virtual terrain" characteristics change, however they can always be seen interacting with the normal mountain waves.

For a very low incoming flow speed ($Fr = 0.1$) a plume-induced circulation can be seen very close to the surface heating anomaly: with strong ascent enveloped by two areas

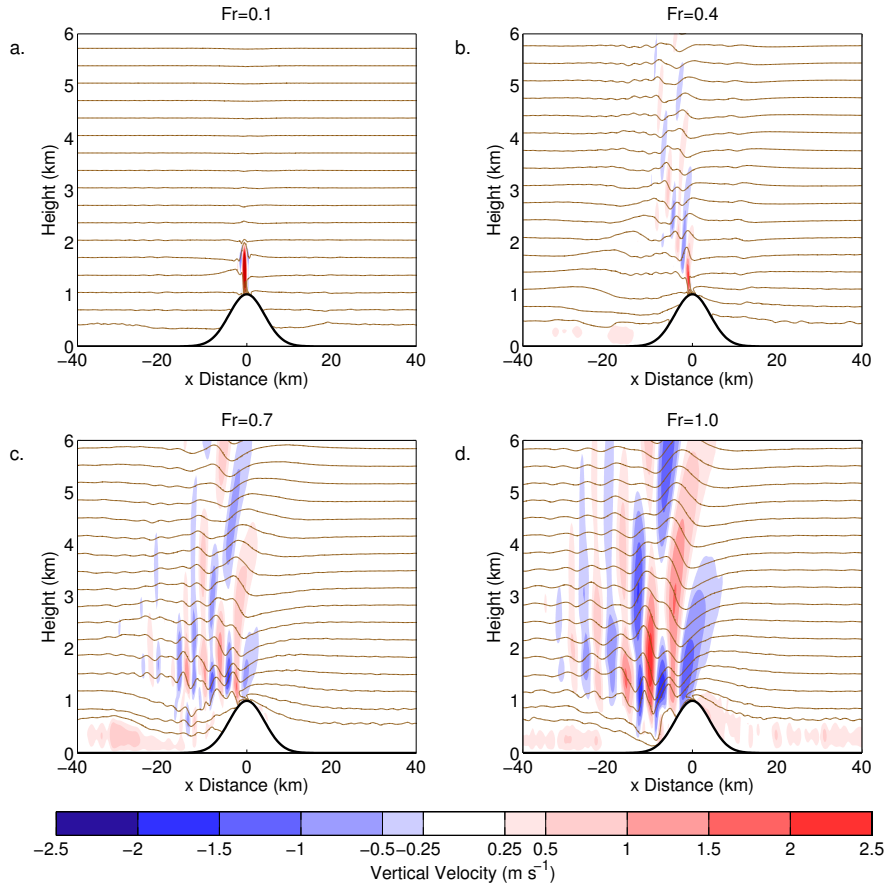

Figure 3.18: Vertical velocity (shaded contours) with isentropes (brown lines) overlaid, across a cross-section in the middle of the domain, for: (a) $Fr = 0.1$, (b) $Fr = 0.4$, (c) $Fr = 0.7$, (d) $Fr = 1$. Isentropes plotted between 299 and 316 K, every 1 K. $T_a = 60$ K across all panels.

of negative vertical velocity. There is convergence into the plume with higher U values on the windward side and flow reversal in the lee so air is drawn in into the plume (Figure 3.19a). At the top of the plume there is the inverse, with air diverging (see Figures 3.18 and 3.19). For $Fr > 0.1$ the plume interacts with lee wave activity creating different areas of destructive and constructive interference. As seen previously this is the reason why there is no downslope wind across the centre of the mountain (Figures 3.19b, c). For strong surface forcing, the plume is advected downwind, as seen by division of the downslope wind area (approximately at -10 km; Figure 3.18d), enhanced by constructive interference. This disrupts the resonance that naturally occurs at $Fr = 1$: in the control case lee waves continue for for than 40 km (Figure 3.4d), while in the for $T_a = 60$ K they stop at approximately 30 km downwind Figure (3.18d).

Looking at the U-wind component, it can be seen that for very weak incoming flow the temperature anomaly is able to overcome the easterly flow and create its own weak plume

circulation (Figure 3.19a) of approximately 1 m s^{-1} at the top of the plume. This weak circulation becomes overwhelmed by the oncoming flow for $Fr > 0.1$ and the effect of the plume changes from very localised to a larger-scale change in the flow reversal zone, affecting both maximum flow reversal wind values and area. This is illustrated by comparing Figure 3.19 to Figure 3.5), when there is surface heating the leeside reverse flow is significantly stronger for all Froude numbers.

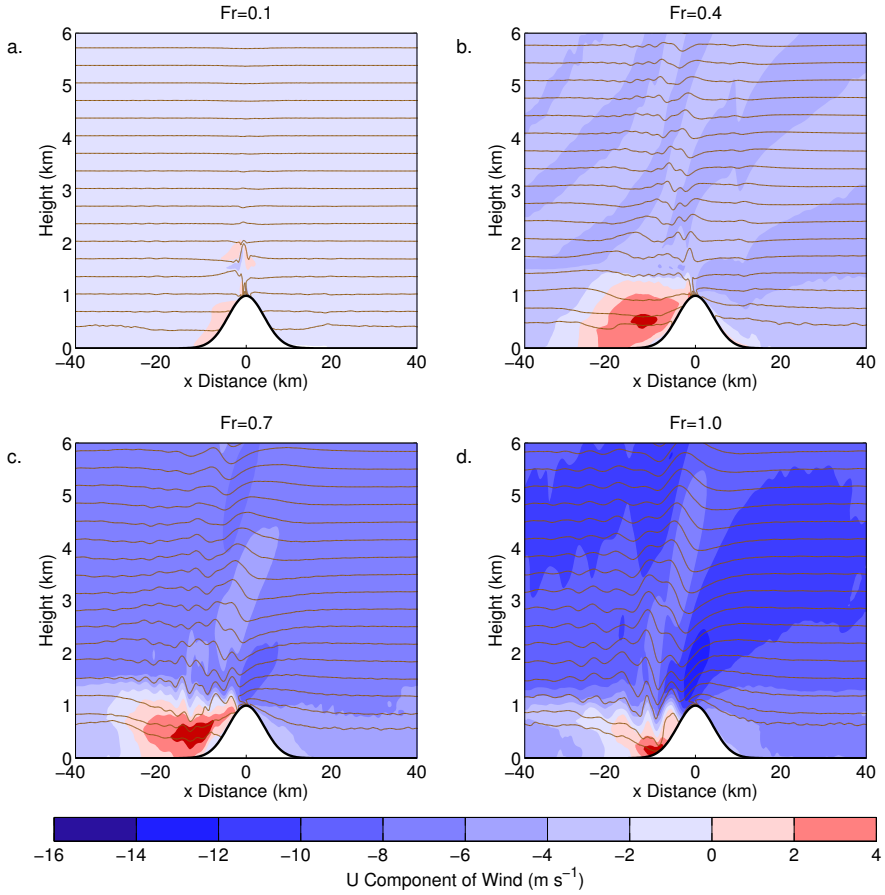

Figure 3.19: As Figure 3.18 but contour plots of the U-wind component. Isentropes plotted between 299 and 316 K, every 1 K.

3.5.3 Summary of changes by Fr

Several diagnostics are now used to summarise the changes discussed in this section. For low Froude numbers the plume can be clearly seen as the increase in the maximum vertical velocity (Figure 3.20a). For higher Froude number values (Figure 3.20b–d) the impact is lessened due to a combinations of strong advection and the fact that the flow is able to go over the mountain and, thus, maximum vertical velocities are now comparable to the plume. The increase seen for $Fr = 1$ is possibly the combination of a very energetic flow

and the constructive interference of the plume and lee waves as discussed previously. The maximum U-wind component (Figure 3.20b) increases with the Froude number, however, unlike the control simulations (Figure 3.10), the peak value is now at $Fr = 1$, as the plume was seen to enhance rotor activity in the lee, while control simulations' peak was at $Fr = 0.4$. In contrast to the control simulations, here the maximum in TKE values is driven by the mixing occurring in the plume and not the orography forcing. The maximum TKE remains largely unchanged across all experiments, showing that there is a limit to the energy input from the plume (Figure 3.20c). The maximum TKE height (in this case strongly related to the convective plume height) decreases drastically with increasing Froude number as the plume is strongly advected by the wind (Figure 3.20d).

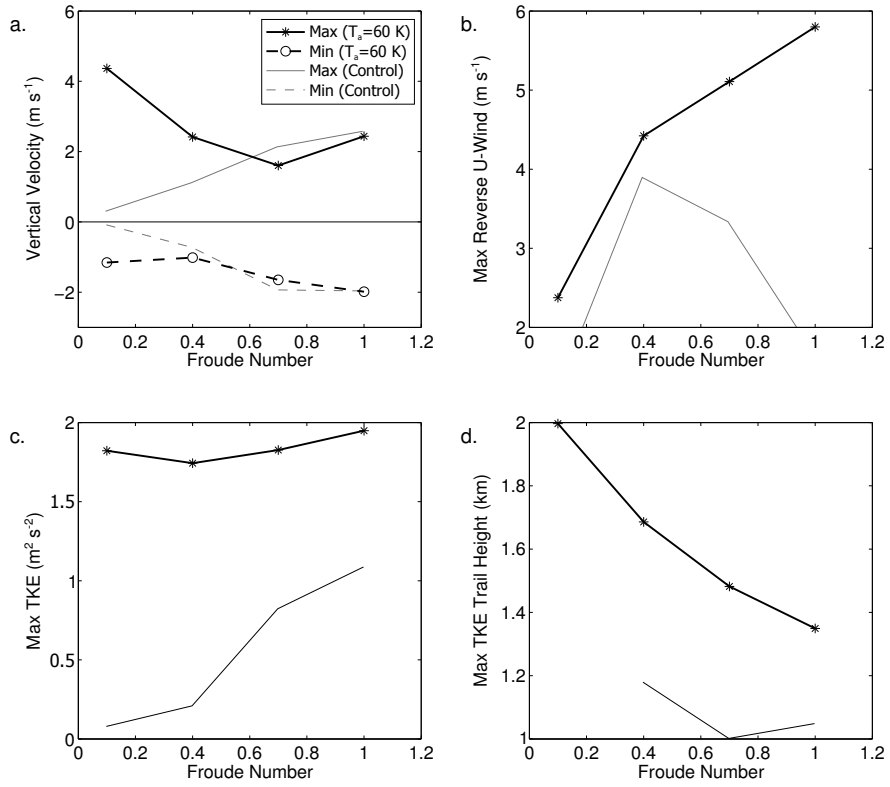

Figure 3.20: (a) Maximum and minimum vertical velocity against Froude number. (b) Maximum (positive) U wind component. (c) Maximum TKE, and (d) maximum height where TKE> 0.2 m^2 s^{-2}. Results from simulations with $T_a = 60$ K are plotted in black, while control simulations are shown with gray lines.

It has been shown that the response to the temperature anomaly is highly sensitive to the Froude number of the incoming flow, with two different flow regimes in evidence. For small Froude numbers (between 0.1 and 0.4), the flow is dominated by a primarily vertical plume-induced circulation. For Froude numbers larger than 0.4 the oncoming flow is able

to alter the plume and the result is different patterns of wave activity depending on the constructive and destructive interference of the plume and the mountain waves.

3.6 Surface temperature anomaly runs - Overall changes

3.6.1 Convective plume definition and features

So far the TKE trail has been used as a useful proxy for the convective plume. Here, a justification for this reasoning will be provided, using computational and theoretical arguments. From the computational side, even though the current resolution is high enough to efficiently resolve the plume (with a width of approximately 900 m, or $3\Delta x$, for the $T_a = 60$ K, $Fr = 0.1$ case shown at Figure 3.11a) the internal structure of the plume cannot be resolved at this scale. Hence, mixing occurring at smaller scale would be parameterised and output by the model as sub-grid turbulence. It was seen that, especially for low Froude number cases, the plume introduces the largest amount of TKE in the system and thus a clear signal can be retrieved. For higher Froude number cases where the system already has turbulent mixing in the lee of the mountain or a more energetic boundary layer the response becomes mixed but is still a good indication for the plume.

According to air parcel theory, an air parcel heated over the lava dome would rise adiabatically following the dry adiabat, until it reaches a height where it is no longer buoyant – the height where the environmental potential temperature and the potential temperature of the heated air parcel are equal. To test whether the height calculated by the TKE trail conforms to this theory, the temperature the air over the lava dome is heated to is calculated and plotted against the respective height of the unperturbed potential temperature isoline upstream (Figure 3.21).

The temperature of the air over the lava dome increases linearly with T_a for each Froude number setting. As the Froude number increases, air is advected away more rapidly and mixed, resulting in increased ventilation of the plume and a decrease in the maximum temperature. For $Fr > 0.4$ this also appears to be an almost linear reduction closely following the low air temperature for the control case. It can be expected that for $Fr \gg 1$ this behaviour will change and all lines will converge towards the control case due to plume being completely ventilated, however this is not seen here. In the $Fr = 0.01$

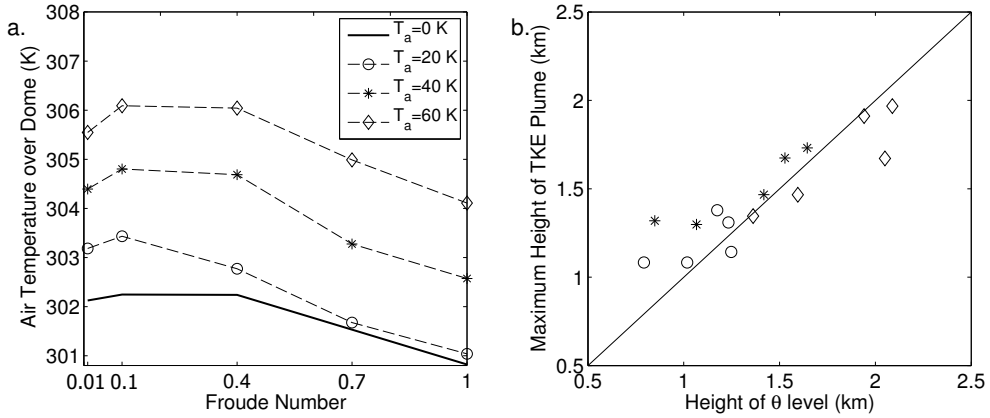

Figure 3.21: (a) Air temperature directly over the lava dome against Froude numbers for the different surface temperature anomaly values. (b) Scatter plot of maximum TKE plume height against the height of the unperturbed potential temperature isoline corresponding to the temperature the air parcels over the temperature anomaly were heated up to, shown in Panel a.

($|U| = 0.1$ m s^{-1}) cases, the maximum air temperature is less than the $Fr = 0.1$ cases. This is most likely due to weak downwelling in the simulations – due to the low amount of energy in the system a weak katabatic flow is created bringing colder air from higher altitudes over the lava dome. This is reflected in a small decrease of air temperatures in the control simulations.

As expected from air parcel theory, there is a good correlation between the projected height of the heated air parcel and the TKE trail. This is especially true for low Froude number cases that feature less complicated physics due to the absence of advection, distinguishable as the points featuring the highest plumes per data set in Figure 3.21b. Thus, at the current grid spacing and for a temperature anomaly of this magnitude, the TKE output directly by the model can be used as an indication of the plume trail. This analysis also shows that it is possible to express plume height as a function of potential temperature, a more objective choice than height above ground, as this would appear to change depending on the atmospheric profile. In brief, the plume acts in accordance with an air parcel model.

Several diagnostics concerning the convective plume as well as the resulting flow in general are now studied (Figure 3.22). All calculations were carried out for a cross-section across the middle of the domain. As previously, the "TKE Trail Height" was calculated as the maximum height where TKE> 0.2 m^2 s^{-2}. Cases where the maximum TKE was lower than the threshold were omitted. Both "TKE Trail Length" and "Flow Reversal Length" were calculated as the length of an area starting over or in the lee of the lava

dome, from the point where TKE> 0.2 m^2 s^{-2} and $U > 1$ m s^{-1} until the first point where the values dropped below the respective thresholds.

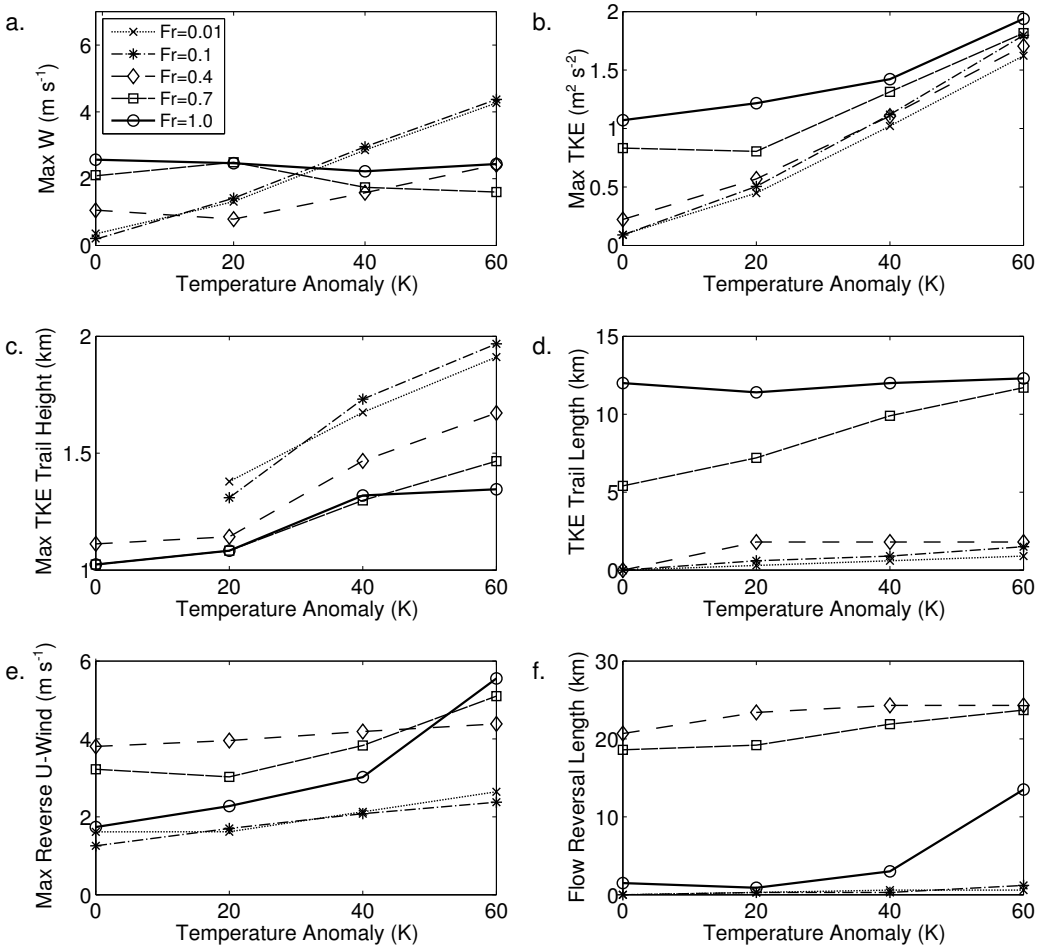

Figure 3.22: Various diagnostics against surface temperature anomaly (x-axis) for different Froude numbers (lines): (a) Maximum vertical velocity, (b) Maximum turbulent kinetic energy, (c) Maximum height of the TKE trail, (d) TKE trail length, (e) Maximum positive (reverse) value for the U-wind component, (f) Flow reversal area length. All diagnostics are calculated for a cross-section across the middle of the domain.

As noted previously, the most notable increase in the maximum vertical velocity occurs for $Fr \leq 0.4$. For $Fr < 0.4$ the increase in the maximum value is linear as T_a increases, while for $Fr \sim 0.4$ a linear increase is apparent for $T_a > 20$ K. After this threshold the flow becomes too energetic for the convective plume to cause a discernible increase (Figure 3.22a). An increase in T_a is mirrored in the maximum TKE values across all cases, but for $Fr \leq 0.4$ this is a clear and linear increase, while for more energetic flows and smaller surface temperature anomalies the increase is less substantial (Figure 3.22b).

The height of the TKE trail is proportional to the thermal forcing and inversely proportional to the Froude number (Figure 3.22c). For low Froude numbers the increase is almost linear, while for higher Froude numbers, the TKE trail seemingly reaches a plateau for the $Fr = 1$ cases. The TKE trail length provides a distinct categorisation for the different flow regimes and a diagnostic for the degree of skewing in the plume (Figure 3.22d). For $Fr \leq 0.4$ the length is between 1–1.5 km (similar to the diameter of the lava dome), suggesting a mostly vertical plume. For $Fr > 0.4$ the values increase to values of 5–12 km, showing that the plume is advected, heavily ventilated and no longer vertical.

For most cases the maximum reverse U-wind component increases with T_a, but the most significant increase is seen for the $Fr = 0.7$ and 1 cases, where between T_a =40 and 60 K, U_{max} is increased by a factor of 1.5 and 1.8 respectively (Figure 3.22e). The flow reversal area length can also be used as a diagnostic for the categorisation of the flow regime (Figure 3.22f). For a Froude number between 0.4 and 0.7 the flow reversal area length is approximately 20 km, while for lower or higher numbers it is between 0 and 3 km. For most cases it is insensitive to changes in T_a, with the exception of $Fr = 1$, where the length increases from 3 to 13 km between T_a =40 and 60 K – signifying a change in the flow regime.

3.6.2 Discussion of plume characteristics

Figure 3.23 shows a regime diagram for the parameter space under study. There are three categories and each of the simulations is represented as a symbol depending on the characteristics of the flow.

The first category, “No Plume”, marked as an asterisk in the diagram, covers the cases where there is either no temperature anomaly ($T_a = 0$ K), a strong vertical plume is not apparent, and rotor activity is not enhanced – practically cases that do not belong in the two remaining categories due to a potential combination of weak thermal forcing and strong advection. The second category, “Vertical Plume” features cases where the ratio of the length of the TKE trail (from the top of the mountain) to its height is less than 3, so $(H_{TKE} - 1) * L_{TKE} < 3$, where H_{TKE} and L_{TKE} are the height and length of the TKE trail respectively. The final category, “Enhanced Rotors” are cases where there is a significant increase in either the flow reversal U-wind component compared

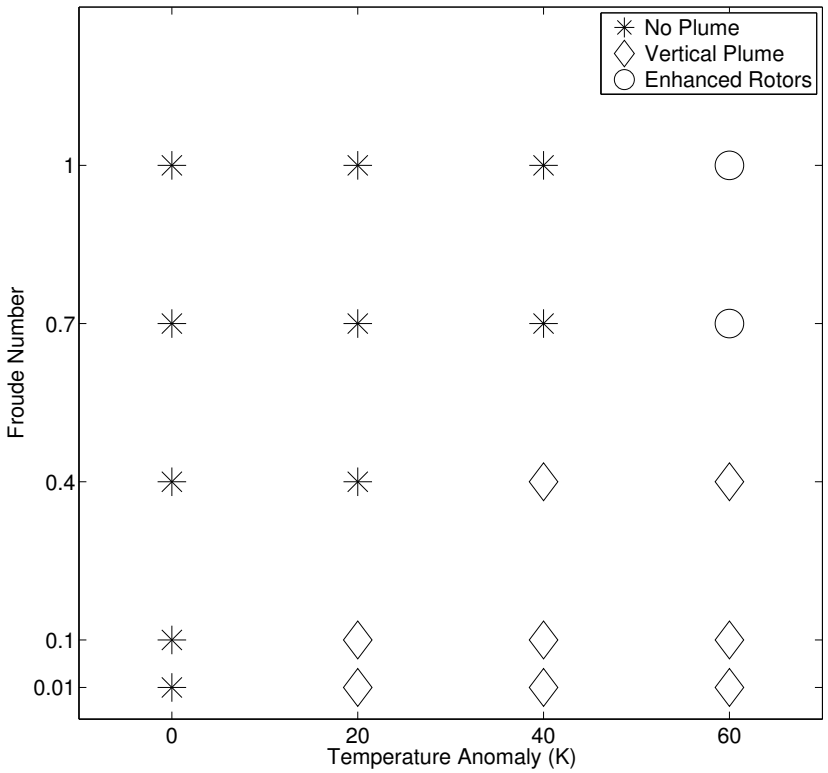

Figure 3.23: Regime diagram for the simulations presented in the chapter.

to the control case ($U_{max}|_{T_a>0} > 1.5\, U_{max}|_{T_a=0}$) and the length of the flow reversal zone is over 10 km. Note that, as seen in Sections 3.4 and 3.5, the plume always causes enhanced rotor activity, but here a relatively high limit was set in order to isolate cases where the convective plume had a considerable impact on rotor activity. A simulation could potentially be characterised by a combination of the last two categories, however this did not occur within the parameter space studied here. Note, although an effort to produce quantitative criteria was made here, some degree of qualitativeness remains.

From this regime diagram it can be seen that, for the plume to have a noticeable effect on the flow, a temperature anomaly threshold between 20 and 40 K is necessary, closer to 40 K for higher Froude numbers. Potentially, this, coupled with the fact that the temperature anomaly that was used in the simulations was wider than the observed lava dome, might lead to a further increase in the threshold value. For typical conditions in Montserrat both categories are potentially important – the "Vertical Plume" category can create a very strong localised perturbation, while the "Enhanced Rotors" category could enhance recirculation and affect the distribution of volcanic emissions in the lee of the lava dome. As seen in Chapter 2 (Section 2.6, Figure 2.12) the average wind speed

was approximately 5 m s^{-1} and the values were distributed evenly between 1–8 m s^{-1}, meaning that depending on the lava dome temperature both flow regimes can be expected. Although the heating regime was markedly different, similar vertical plumes, enhanced flow reversal and generally interaction with the mountain wave pattern has been noted by (Kirshbaum and Wang, 2014), studying flow past a heated mountain.

3.7 Summary

The aim of this chapter was to study the orographic flow over a heated surface in a new heating regime, that of a strong but relatively small heat source, referred to as "surface temperature anomaly", on the top of a mountain. This configuration simulates a hot lava dome, on top of an active, non-erupting volcano. A parameter space consisting of a range of realistic wind and temperature anomaly values was chosen, representing a sufficient amount of typical atmospheric and volcanic conditions.

The main change brought on by the temperature anomaly is the addition of a convective plume in the vicinity of the anomaly. A temperature anomaly of at least 20 K is required for a plume. The main force that drives the flow is the amount that an air parcel is heated while it passes over the temperature anomaly, as the plume is created to lift the air parcel to the level in the atmosphere where the surrounding potential temperature is equal to the new temperature of the air parcel. The stronger the increase in the air parcel temperature, the more abrupt this ascent is. It was seen through the experiments that the maximum plume height is reached for a 0.1–1 m s^{-1} wind ($Fr = 0.01$–0.1), where the lack of strong advection allowed for a warming of the air over the lava dome by 3–6 K. At the current grid resolution the subgrid TKE was found to be a useful diagnostic to identify the convective plume.

Low incoming flow speeds allow the plume to develop predominantly into the vertical and the result in the flow remains localised. Higher incoming flow speeds have two effects: the air is heated by a smaller amount and the plume is advected towards the lee side of the dome. This acts to enhance rotor activity in the lee and creates complex interactions between the plume and gravity wave activity – both vertically propagating mountain waves and horizontally propagating lee waves. The resulting flow is broadly seen as a superposition of the convective circulation and the "normal" orographic flow response,

pointing towards a linear behaviour in the response for both of the forcings. In extreme cases, where a weak temperature anomaly is faced with a strong wind it was shown that the wind has the capability to effectively dissipate the plume, eliminating the effect of the lava dome.

Chapter 4

Flow over an idealised volcano: Moist experiments

4.1 Introduction

In an effort to thoroughly analyse the effects of an active, non-erupting volcano on atmospheric flow, the idealised component of this study has been split into two parts. The first part (presented in Chapter 3) featured a series of highly idealised "dry" simulations (dry in the sense that moisture in the atmosphere was explicitly set to zero and no microphysics modules were employed in the model). The second part (this chapter) simulates the effect of the heated volcanic surface on a "moist" atmospheric circulation, with water simulated in all phases. Here, the simulations focus on the role of the volcano in changing the flow and associated rainfall.

Rainfall is a well-established trigger for volcanic hazards. This link is self-evident for "secondary" volcanic activity such as lahars – volcanic mudflows composed of remobilised volcanic sediment and rainwater (Major and Newhall, 1989; Smith and Fritz, 1989). Perhaps unexpectedly, rainfall can also trigger "primary" volcanic activity such as pyroclastic flows and volcanic dome collapses, as documented at Mount St. Helens, U.S.A. (Mastin, 1994), Unzen, Japan (Yamasato *et al.*, 1998), Merapi, Indonesia (Voight

Parts of the chapter have been reviewed for publication:
Poulidis, A.-P., Renfrew, I. A. and Matthews, A. J. (2015) Thermally induced convection and precipitation over a volcano. Journal of the Atmospheric Sciences (under revision).
The experimental setup was agreed on by all authors. I have carried out the simulations, the data analysis and wrote the first draft of the paper. This was then revised based on comments from the co-authors.

et al., 2000), Piton de la Fournaise, Réunion Island (Violette *et al.*, 2001), Soufrière Hills Volcano (SHV), Montserrat (Matthews *et al.*, 2002; Carn *et al.*, 2004; Barclay *et al.*, 2006; Matthews *et al.*, 2009) and Stromboli, Italy (Hort *et al.*, 2003).

Interestingly, there is, however, a further unexplored possibility: that the heated summit of a volcano interacts with the orographic flow to force atmospheric convection and enhanced precipitation, thus potentially creating a positive volcano-rainfall feedback. Here this possibility will be examined through numerical modelling. The numerical experiments presented here are generalised, but are carried out for the tropical atmospheric conditions representative of those at SHV, Montserrat, where such rainfall-volcanic interactions are well established. It is worth noting that, nearly half of the approximately 1500 active or potentially active volcanoes in the world lie in the tropics (Simkin and Siebert, 1994).

Even though orographic rainfall, the result of air mechanically forced to ascend over a hill or mountain, can greatly affect precipitation in the Tropics, it is a field that has received relatively little attention. Recent studies as part of the Dominica Experiment (DOMEX; Smith *et al.*, 2012) have shown that, aside from diurnally-forced deep convection and tropical cyclones (Houze, 2012), shallow convection from forced ascent can have a significant effect on the local precipitation (Kirshbaum and Smith, 2009; Smith *et al.*, 2009; Minder *et al.*, 2013). This has also been established for other islands in the Caribbean (Cécé *et al.*, 2014). Although the resulting flows vary depending on the location and the size of the island and the mountain, the general response can be summarised as greater cloud cover over the windward side, with enhanced convection and precipitation as the cumulus field created over the ocean interacts first with the coastline and then with the mountain. Depending on the mountain characteristics, the resulting orographic rainfall can be substantially higher (a factor of 10) than both the rainfall over the sea, and the rainfall caused by the convection as the flow meets the land (Kirshbaum and Smith, 2009; Smith *et al.*, 2009).

Orographic flow in the vicinity of hills and ridges is a classic problem in meteorology (see for example Queney, 1948; Eliassen and Palm, 1961; Drazin, 1961; Smith, 1980, 1989; Smolarkiewicz and Rotunno, 1989 and Ólafsson and Bougeault, 1996). However

orographic flow over heated topography has not been as widely studied. The main rationale behind previous research has been to investigate the impact of solar heating in triggering localised convective updrafts and their effect on weather systems (Crook and Tucker, 2005; Lewis *et al.*, 2008; Kirshbaum, 2011). The general result is a strengthening or generation of severe storms akin to the way mountains can enhance rainfall (Crook and Tucker, 2005; Kirshbaum, 2011). Although linear theory has been used to study the effect of sufficiently weak thermal forcing (Crook and Tucker, 2005; Tucker and Crook, 2005), Kirshbaum (2013) demonstrated that the application of linear theory for two layer flows is severely limited due to the non-linear effects that are introduced by the difference between the layers.

Recently, attention has focused on the impact of wild fires in the generation of pyrocumulus clouds (Gatebe *et al.*, 2012) and the initialisation of storms (Cunningham and Reeder, 2009). Wild fires lead to a localised maximum in surface temperature, along with the release of water vapour and chemical by-products from burning. Depending on the atmospheric structure they can generate deep convection, pyrocumulus clouds and severe storms. As in the solar heating cases, the result is a localised convection cell that can break through the convective inhibition of the lower atmosphere and force deep convection. Unlike the solar heating cases, these storms often occur under strong winds, but the extension and propagation of the storm still depends heavily on the atmospheric structure (Cunningham and Reeder, 2009).

The rationale for studying the effects of heated terrain on the atmosphere here is different: it is to examine how a volcano can influence the atmospheric flow. The focus of this study is on flows over active dome-building volcanoes, not undergoing an explosive eruption. Dome-building volcanoes are a category of volcanoes that extrude high-viscosity magma through a central conduit. The magma cools and solidifies, blocking further flow up the conduit and forming a pressurised lava dome. This lava dome can become unstable due its weight and internal pressure and fail, leading to explosive dome collapse and pyroclastic flows. Heavy rainfall has been implicated in triggering some such dome collapses and pyroclastic flows at a number of volcanoes, including SHV, Montserrat (Matthews *et al.*, 2002). Hence, any enhancement of rainfall by the heated surface of the volcanic

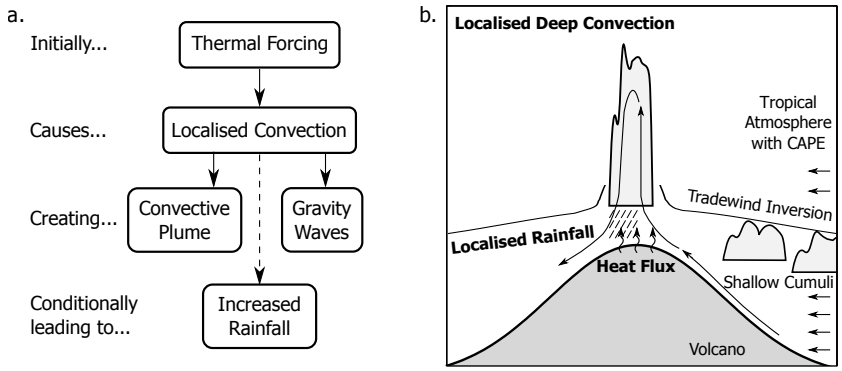

Figure 4.1: (a) Conceptual model under study. (b) Schematic describing the proposed mechanism.

dome may lead to a positive feedback, increasing the probability of these dangerous volcanic hazards.

As already discussed, the Soufrière Hills Volcano, Montserrat has been chosen as the "template" for the idealised simulations presented here. Montserrat is located in the Tropics (16.75° N, 62.20° W) and is part of the lesser Antilles, Eastern Caribbean. It has been volcanically active since 1995, with a series of devastating eruptions and active dome-building cycles over the last 20 years. For an overview of volcanic activity see Sparks and Young (2002) and Wadge *et al.* (2014).

The conceptual model being tested assumes a tradewind cumulus regime in an easterly background flow with a tradewind inversion (Figure 4.1). The flow over the top of the volcano is subject to thermal forcing via the surface fluxes from the strongly heated volcanic surface. This is hypothesised to be sufficient for convective plumes to break through the inversion, releasing the high values of convective available potential energy (CAPE) present in the background state, and initiating intense localised rainfall over the volcano. Although beyond the scope of this study, this enhanced rainfall may then trigger an already unstable volcanic dome to collapse (by the mechanisms described above) or secondary volcanic hazards such as lahars.

In the study, the volcano is simulated simply as a realistic increase in the surface temperature of an otherwise passive mountain. In reality volcanoes are a source of ash and various gaseous emissions. Although the volcanic gas composition varies significantly between different volcanoes, in general the gases released are formed of water vapour, carbon dioxide, sulphur dioxide and traces of other chemicals (Parfitt and Wilson, 2008).

These emissions, along with the volcanic ash, are known to have an impact on cloud microphysics in the vicinity of the volcanic conduit, for example affecting cloud seeding due to the abundance of cloud condensation nuclei (CCN) and other processes (Durant *et al.*, 2008) and causing acid rain (Lane and Gilbert, 1992). However, these secondary effects are not studied here. Rather, what is examined is the primary response of the atmospheric flow to the increase in temperature, i.e. a thermally-induced convective plume. The effect of the ash and gas emissions and any interactions with the thermal circulation will need to be considered in future work. Interactions between aerosols (for example the volcanic plume) and precipitation is still an open topic in research, with aerosols being implicated in both aiding and inhibiting rainfall (Rosenfeld *et al.*, 2008; Stevens and Feingold, 2009). On one hand, clouds with a low CCN concentrations rain out too quickly, but on the other hand, clouds with a heavy concentration evaporate much of their water (Rosenfeld *et al.*, 2008). Furthermore, the efficiency of coalescence (the main driver of rainfall in liquid cloud) increases with cloud water content and decreases with drop concentration – added CCN slow the conversion of cloud drops into raindrops by nucleating larger concentration of smaller drops. Hence, added aerosols (which increase drop concentration) are expected to reduce precipitation and have been known to shut off precipitation from shallow, short-lived clouds (Rosenfeld *et al.*, 2008; Stevens and Feingold, 2009). However, clouds with very high liquid-water content are too efficient at generating precipitation and are less susceptible to this mechanism (Stevens and Feingold, 2009). Finally, accelerating the conversion of cloud water to precipitation could enhance rainfall amounts (Rosenfeld *et al.*, 2008). As this is a very complex problem a large number of high resolution experiments would need to be carried out to test this in the context of volcanically-generated rainfall.

The chapter is organised as follows. Initially a short description of the experimental setup is presented (Section 4.2). Results are presented in two main sections: control experiments ($T_a = 0$ K; Section 4.3) and surface temperature anomaly experiments ($T_a > 0$ K; Section 4.4). The latter is further divided into three sub-sections discussing the sensitivity of the results to T_a (Section 4.4.1) and the atmospheric conditions (Section 4.4.2), followed by a section of further detailed analysis of results (Section 4.4.3). After that, the temporal evolution of the plume is analysed (Section 4.5). The chapter then concludes

with a brief discussion (Section 4.6) and a summary of the main results (Section 4.7).

4.2 Experimental configuration

4.2.1 Model setup

The numerical simulations were carried out using the Weather and Research Forecast (WRF) model, version 3.3.1, running in an idealised configuration. The model domain consists of an isolated volcano, located near the centre of the domain and surrounded by ocean (Figure 4.2). Note that the terms "volcano" and "mountain" are used interchangeably throughout the rest of the thesis. The domain has 680 by 250 grid points with a grid spacing of $\Delta x = \Delta y = 300$ m in both directions, so representing 204 km in the x and 75 km in the y direction. There are 147 levels in the vertical. The vertical grid spacing is 50 m up to a height of 4 km, increases linearly to 200 m up to 12 km and the increases linearly up to 1000 m until the model top, at 16 km. The time step is 2 seconds with each simulation run for 9 hours. The first 3 hours are spent on model "spin up" (hours 1-2) and approaching a quasi-steady state (hours 2–3). All results presented are 3h averages from hours 3 to 6. Sensitivity tests up to 9h showed only minor changes in the output. The height (h) of the volcano has a Gaussian profile with a half-width of approximately 10 km and a height of 1 km:

$$h(x,y) = h_{top}\ \exp\left[-\left(\frac{x-x_s}{L_x}\right)^2 - \left(\frac{y-y_s}{L_y}\right)^2\right] \tag{4.1}$$

where x_s and y_s are the coordinates of the volcano's centre, $h_{top} = 1000$ m is the maximum height and L_x and L_y are parameters relating to the half-width (both were set at 5700 m - see Figure 4.2a). Although the simulations are idealised, these dimensions were chosen so that the mountain has similar topography to that of SHV.

A suite of physical parametrisations are implemented in WRF. The surface-layer related physics schemes are used to implement the surface heating on the top of the volcano, specifically a thermal diffusion model for the soil scheme and the Monin-Obukhov scheme for the atmospheric surface layer (Skamarock *et al.*, 2008). The relatively complex 6-phase 'Purdue Lin' microphysics scheme is used based on the studies by Lin *et al.*

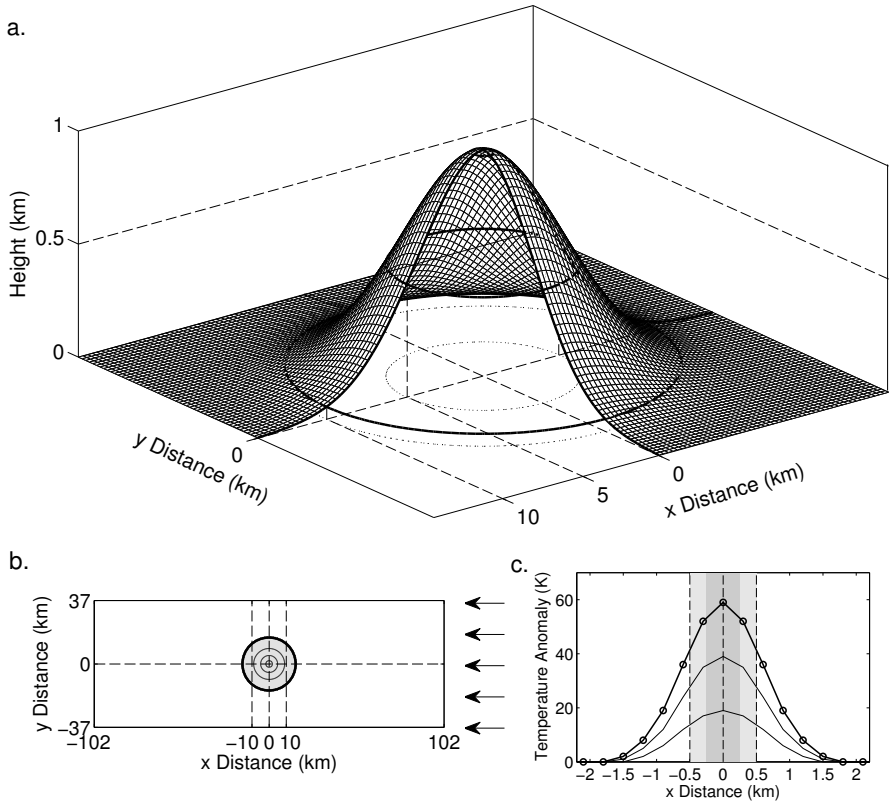

Figure 4.2: (a) Cut-away of the topography of the idealised Gaussian mountain. (b) Model domain. The mountain is centred at $x = 0$, $y = 0$. Selected height contours are shown at 1 m (bold) and then at 100, 500, and 900 m, corresponding to the bold contours in (a). The model surface type is land where the height is over 1 m (shaded area), and water everywhere else. The background wind is easterly, as indicated by the arrows on the eastern (upwind) boundary. (c) Cross-section through the centre of the volcano showing surface temperature anomaly (surface temperature minus ambient surface temperature). The shaded areas show typical lava dome dimensions.

(1983) and Rutledge and Hobbs (1983). This scheme was chosen because deep convection past the freezing point, up to the tropopause was expected (Hong and Lin, 2006). The radiation and boundary-layer schemes are switched off for all simulations. The lack of a radiation scheme does not grossly affect the magnitude of the surface heat fluxes (controlled by the soil model) and, as no simulations last more that 9 hours and as the focus of the study is on a quasi-steady response, then not implementing a radiation scheme is an appropriate simplification. Finally, at the current resolution a boundary layer scheme is not needed as primary eddies are explicitly resolved (Bryan *et al.*, 2003; Kirshbaum and Fairman, 2014). For a more detailed discussion see Chapter 2.

Aside from these schemes, an option for diffusion that evaluates mixing terms in physical space and 1.5-order TKE closure is used in all simulations. A Runge-Kutta third-order time scheme is used for the computations. A fifth-order and a third-order scheme are used for momentum and scalar advection, respectively, in the horizontal and

vertical dimensions (Skamarock *et al.*, 2008). A w-Rayleigh damping layer is used above 8 km to reduce the errors from spurious gravity waves being reflected on the top of the domain (Klemp *et al.*, 2008), and sixth-order monotonic horizontal diffusion is applied to all variables for stability and to minimise spurious behaviour at poorly resolved scales (Knievel *et al.*, 2007).

4.2.2 Initialisation sounding

All simulations have been initialised horizontally homogeneously from a prescribed atmospheric profile. The profiles used (Figure 4.3) are based on those of Siebasma *et al.* (2003), which are marine soundings from the Caribbean during the BOMEX experiment, that have been simplified and used in several previous modelling studies (e.g. Siebasma *et al.*, 2003; Kirshbaum and Smith, 2009). Several idealised profiles have been prescribed with changes in: inversion strength, tropospheric humidity, and ambient wind speed. The soundings include a temperature inversion at the top of the "tradewind cumulus" regime. The difference in the maximum potential temperature (θ_I) between the "Strong Inversion" and "Weak Inversion" profiles is 1 K at the peak of the inversion (close to 2 km, Figure 4.3a). Above the inversion the potential temperature continues to increase upwards with a constant dry Brunt-Väisälä frequency ($N_d = 0.01\ \mathrm{s}^{-1}$ – not shown). The "Dry" and "Wet" tropospheric humidity profiles are similar near the surface with an almost saturated layer between 0 and 2 km – 5% more saturated for the "wet" case (Figure 4.3b). In the "dry" profile the relative humidity drops steeply, while the "wet" profile features a moister troposphere. The combination of "Strong Inversion" and "Dry Atmosphere" profiles represents the sounding used by Kirshbaum and Smith (2009), while the "Weak Inversion" and "Wet Atmosphere" were chosen based on a trade-off between: (i) being able to force a regime changes, but at the same time (ii) represent realistic changes over that profile, based on the radiosonde study presented in Chapter 2. The wind speed profiles increase through the surface layer to constant values of 1, 4 and 7 m s^{-1} from the East, in keeping with a sub-tropical tradewind inversion climate. The characteristics of the profiles used here also broadly conform to the climatological profiles created by Dunion (2011), based on over 6000 July-October radiosondes from the Caribbean region.

The parameter choice in the prescribed atmospheric profiles leads to moist Froude

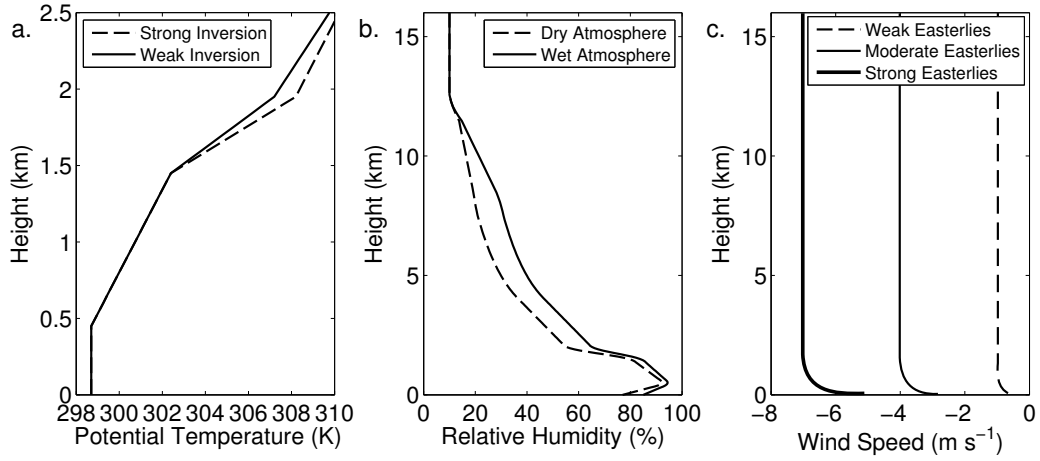

Figure 4.3: Thermodynamic profiles used in the simulations. (a) Potential temperature profiles for "weak inversion" (solid line) and "strong inversion" (dashed line). (b) Relative humidity profiles for "dry" atmosphere (solid line) and "wet" atmosphere (dashed line). (c) Wind speed profiles for "weak easterlies" (dashed line), "moderate easterlies" (solid line), and "strong easterlies" (thick line). Note the change in vertical structure.

number (F_w) values between approximately 0.1 and 0.7. Here the moist Froude number is defined as $F_w = U\ N_w^{-1}\ h^{-1}$, where U is the incoming flow speed, N_w is the moist Brunt-Väisälä (or buoyancy) frequency and h is the maximum height of the mountain. N_w is calculated using the virtual potential temperature profile. Note that, as both N_w and U change throughout the atmosphere, the calculation here was carried out for the lowest 2 km in the atmosphere. Although using the whole atmosphere would provide information for the temperature inversion it would decrease the value of the parameter in assessing the flow regime. Within this parameter space it is expected that the flow will be mainly confined to a "flow around" regime, with the higher wind cases on the border of being able to cross to the "flow over" regime (Smith, 1989). However, it should be noted that in a moist atmosphere it becomes inappropriate to categorise the flow based solely on the moist Froude number, as other parameters such as CAPE and temperature inversions can heavily affect the flow (Chen and Lin, 2005).

4.2.3 Imposed temperature anomaly on the volcano summit

The surface temperature in the model is specified at initialisation, by gradually increasing the surface temperature towards the summit. A grid spacing of 300 m was chosen for WRF, which although sufficient for resolving orographic flows and deep convection (Bryan *et al.*, 2003) does mean the volcanic dome is only crudely resolved by a relatively

small number of grid points, i.e. the fine surface temperature details of the dome (e.g. the hotspots; Chapter 2, Figure 2.3) are not represented in the WRF surface boundary conditions. Instead surface temperature anomalies of between 0 and 60 K are specified. For a cross-section across the centre of the volcano (Figure 4.2c) the temperature anomaly is imposed over roughly 9 grid points following Equation 4.2:

$$T'(x,y) = T_a \ \exp\left[-\left(\frac{x-x_0}{W_x}\right)^2 - \left(\frac{y-y_0}{W_y}\right)^2\right] \tag{4.2}$$

where T' is the temperature perturbation, x_0 and y_0 are the coordinates of the lava dome, T_a is the maximum temperature anomaly and W_x and W_y are parameters relating to the half-width (both set at 900 m). A typical dome at SHV ranges between 500 and 1000 m in diameter (Wadge *et al.*, 2014), shaded in Figure 4.2c. The surface temperature anomaly is time independent in each experiment, leading to a nearly-constant surface heat flux once the simulation has reached a quasi-steady state. This is the same surface temperature distribution as the one used in Chapter 3 to allow for direct comparison of results.

As the response of the flow to heated terrain has been found to be non-linear (Kirshbaum, 2013), the main simulations were carried out for a range from $T_a = 0$ (control runs) to $T_a = 60$ K by increments of 20 K (temperature forcing runs). The parameter combinations – average relative humidity ($\overline{RH}$), inversion strength (θ_I), wind speed ($|U|$), and surface temperature forcing (T_a) – used in the suite of model integrations are summarised in Table 4.1.

Experiment Name	$\overline{RH}$ (%)	θ_I (K)	$\lvert U\rvert$ (m s^{-1})	T_a (K)
Dry-Strong Inversion	50	308.2	1, 4, 7	0:20:60
Dry-Weak Inversion	50	307.2	1, 4, 7	0, 60
Wet-Strong Inversion	60	308.2	1, 4, 7	0, 60
Wet-Weak Inversion	60	307.2	1, 4, 7	0:20:60

Table 4.1: Summary of simulations. $\overline{RH}$ is the average relative humidity above the inversion, θ_I is the potential temperature at the peak of the inversion, $|U|$ is the value of the easterly winds above the inversion and T_a is the value of the temperature anomaly. Experiment names refer to the combination of the relative humidity and temperature inversion values.

4.3 Control experiments: Flow over an isolated island

Here, control simulations are presented in order to outline the basic flow response to the orography in the absence of any surface temperature forcing. Results are presented for

three wind values ($|U|$=1, 4, and 7 m s^{-1}, equivalent to $F_w = 0.1$, 0.4 and 0.7), for the two "extreme" atmospheres: a dry profile with a strong inversion and a wet profile with a weak inversion – i.e., those least and most conducive to moist convection. All figures presented have the same layout, columns have the same atmospheric structure characteristics (θ_I=308.2 K, $\overline{RH}$ =50 % for the left-hand column and $\theta_I = 307.2$ K, $\overline{RH} = 60$ % for the right-hand column), while rows have the same incoming flow speed ($|U|$=1 m s^{-1} for the top row, $|U|$=4 m s^{-1} for the middle row, and $|U|$=7 m s^{-1} for the bottom row). The first combination of characteristics will be referred to as "Dry-Strong Inversion", while the second "Wet-Weak Inversion". Note, all plots show restricted parts of the full domain and all data shown are 3h averages.

4.3.1 Flow response and rainfall

Figure 4.4 shows vertical velocity at the third model level on terrain following coordinates, overlaid with vectors for the horizontal wind. This level was chosen as it is representative of low-level flow (150 m above the surface), but outside of direct surface layer influence. All panels show easterly flow (coming from the right) with more ascent on the windward side and more descent in the lee side. Some degree of convection can be seen all over the domain. A number of streamlines are plotted to facilitate comparison between the different cases.

As $|U|$ increases the simulations change from a regime of "flow around" the mountain, where vertical motion is constrained to isolated cells (w approximately between ± 0.3 m s^{-1} – Figures 4.4a,b) to a regime of "flow over" the mountain with ascent on the windward slopes, and descent on the leeward slopes (w approximately between -2–1 m s^{-1} – Figures 4.4e,f). Isolated small-scale convective cells can be seen in all cases. For very low wind speeds the flow is heavily affected by localised circulation with numerous small-scale vortices resolved (highlighted in Figure 4.4b by the collapsed streamline). At $|U| = 4$ m s^{-1} two counter rotating vortices can be seen in the lee, as expected for a Froude number of 0.4 (Smolarkiewicz and Rotunno, 1989). For higher wind speeds a strong mountain wave response is triggered as the flow progresses towards the linear theory area (Smith, 1989). The results are in perfect agreement with results presented in Chapter 3 (for example Figure 3.3). No major changes can be seen in the general flow

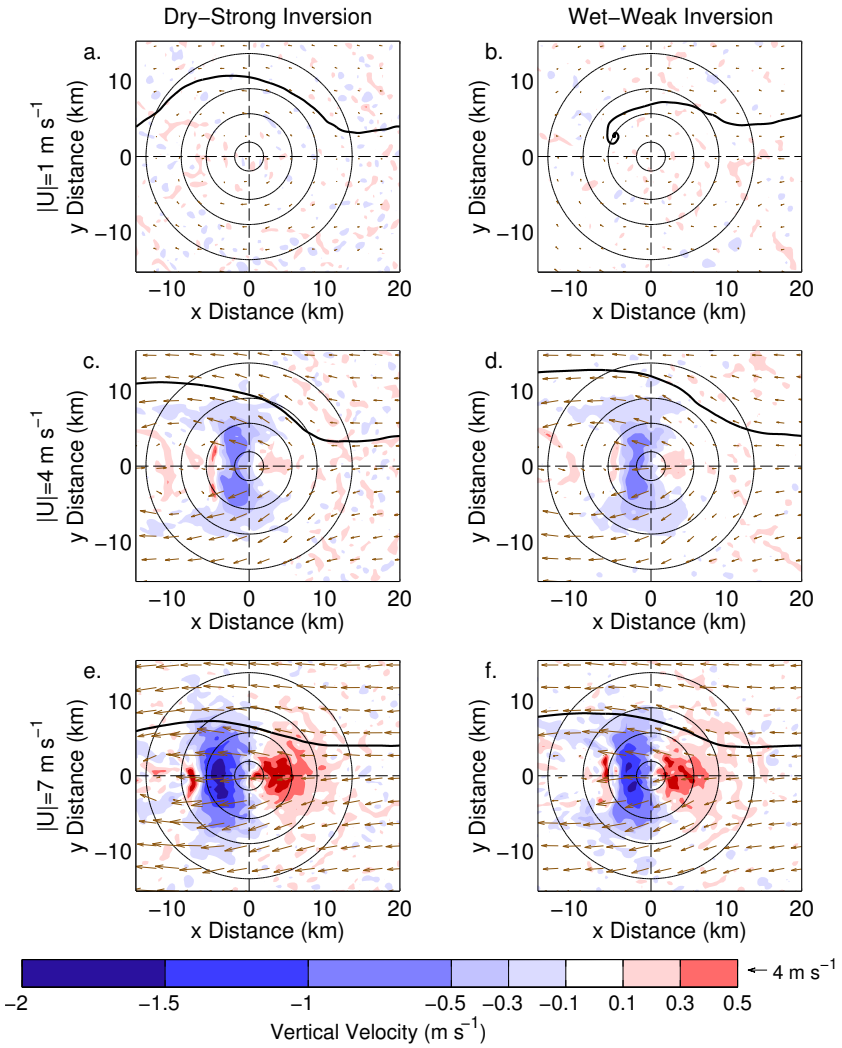

Figure 4.4: Vertical velocity (shading) with the horizontal wind vectors (every 10th is plotted) on the third model level for: (a) $|U| = 1$ m s^{-1}, "Dry-Strong Inversion", (b) $|U| = 1$ m s^{-1}, "Wet-Weak Inversion", (c) $|U| = 4$ m s^{-1}, "Dry-Strong Inversion", (d) $|U| = 4$ m s^{-1}, "Wet-Weak Inversion", (e) $|U| = 7$ m s^{-1}, "Dry-Strong Inversion", and (f) $|U| = 7$ m s^{-1}, "Wet-Weak Inversion". Note that the colour bar (as in most of the figures that follow) is non-linear near zero to make a clear distinction between positive and negative values. Streamlines shown starting at $y = 4$ km for all cases. Height contours are at 5, 100, 500 and 900 m. The fields shown are 3h averages here and in the rest of the section. Control runs ($T_a = 0$ K).

between the two different atmospheric structures (Dry-Strong and Wet-Weak Inversion).

Figure 4.5 shows horizontal contour plots of surface rainfall rates (R). All rainfall rates are averages over the study period (hours 3–6), converted to hourly rates. The rainfall response is very different depending on the atmospheric conditions. For low incoming flow speeds the rainfall is mainly convection based. In the Dry-Strong Inversion case there is rainfall in the lee of the mountain as a result of lee-side convergence (Roe, 2005), as well as scattered rainfall due to individual convective cells (Figure 4.5a). In the Wet-Weak

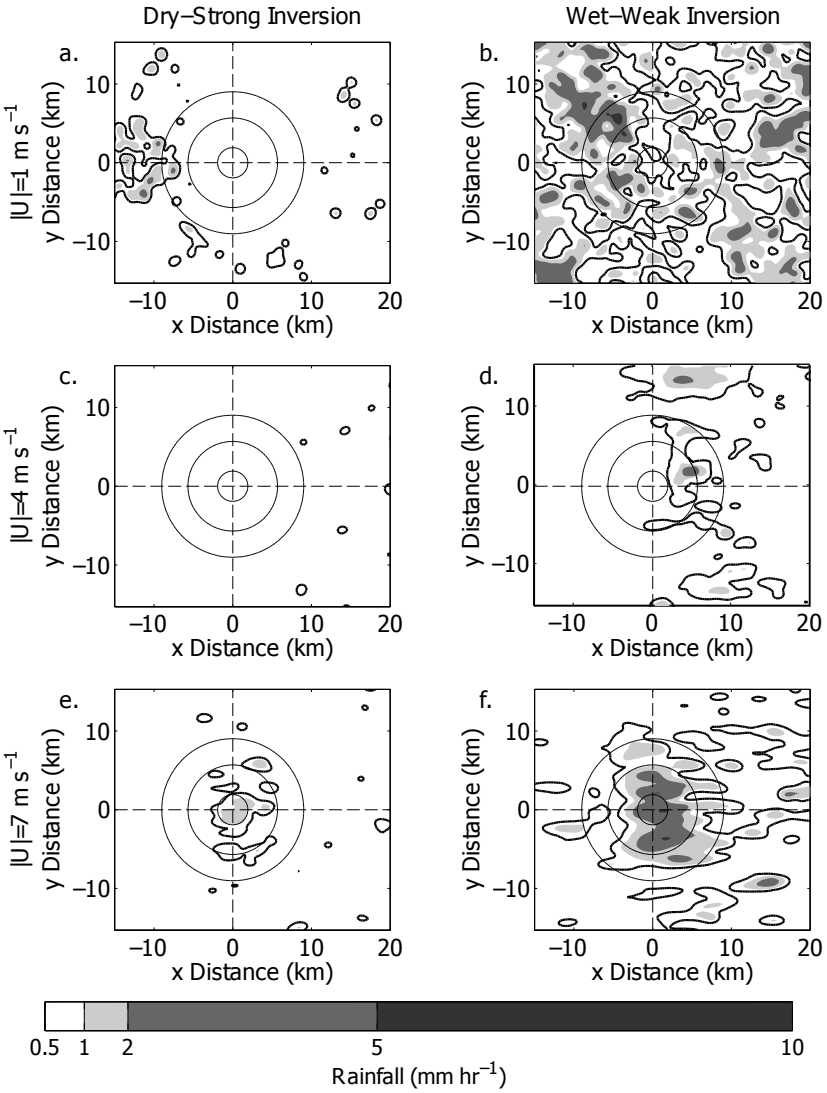

Figure 4.5: As Figure 4.4 but for rainfall rate (R). The thick black contour line signifies $R > 0.5$ mm hr^{-1}, while shaded areas show R over 1, 2, and 5 mm hr^{-1}. Control runs.

Inversion case, rainfall due to larger convective cells is visible, scattered around the domain, possibly due to the influence of strong individual cells in the flow (Figure 4.5b). Both cases feature rainfall rates of $R > 2$ mm hr^{-1}, consistent with moderate to deep convection. On average cloud tops below 5 km are associated with a rainfall rate of approximately 2.6 mm hr^{-1}, while cloud tops below 2 km are associated with 1.6 mm hr^{-1}. The term "deep convection" will be used here to describe rainfall rates of 2 mm hr^{-1}, on average associated with cloud tops over 3 km. This is used slightly inappropriately as it encompasses both deep convection and "moderate" convection, but it is used to make the distinction between convection below the inversion and above. For $|U| = 4$ m s^{-1} there is a switch towards a more orographically-forced rainfall regime, as the wind is

now strong enough to disrupt the evolution of strong convective cells. However, as seen in Figure 4.4c,d the flow is not energetic enough to go entirely over the mountain and as such the orographic response is minimal and can only be seen only in the Wet-Weak Inversion case (Figures 4.5c,d). At $|U| = 7$ m s^{-1} orographic rainfall dominates. Although convective rainfall can still be seen, elongated in the direction of the wind, the domain is now dominated by rainfall over the mountain – concentrated at the crest in the Dry-Strong Inversion case and more wide-spread in the Wet-Weak Inversion case (Figures 4.5e,f). In the Dry-Strong Inversion case the orographic rainfall is consistent with shallow convection ($R < 2$ mm hr^{-1}), while in the Wet-Weak Inversion case deep convection ($R > 2$ mm hr^{-1}) is triggered as the incoming flow is already close to saturation.

Figure 4.6 shows a vertical cross-section across the middle of the terrain, in the x direction. Results are averaged over 5 grid points (1.5 km) in the y direction. Vertical velocity is shaded, while black lines represent (liquid) cloud mixing ratio, and brown contours potential temperature. Below the main part of the plot, the first subplot shows mean (black lines) and maximum (brown dashed lines) rainfall intensity. Maximum values are values sustained for at least 30 mins to filter out very high but not long-lasting rainfall rates. Finally, the subplot below that shows the frequency for rainfall over a certain limit: 1 mm hr^{-1} (green), 5 mm hr^{-1} (blue), and 10 mm hr^{-1} (red). A frequency of 1 denotes continuous rainfall over the 3 hours of integration. Note that some extreme values in both vertical velocity and rainfall can be expected if the cross-section intersects a deep convective cell.

Results here show the progression from the "flow around" regime (flat isentropes, convective rainfall cells, no gravity waves or orographic rainfall), towards the "flow over" regime. For $|U| = 1$ m s^{-1} the cloud water mixing ratio is distributed fairly equally over the domain. In the Dry-Strong Inversion case, convection is contained beneath the tradewind inversion and significant amounts of rainfall are only found in the lee of the mountain (Figure 4.6a). In the Wet-Weak Inversion case, high maximum rainfall rates ($R > 5$ mm hr^{-1}) can be seen across the whole domain, however these are short-lived as they are not picked up by the rainfall frequency distribution, pointing towards randomly distributed quick deep convective bursts that quickly get mixed with the dry air above the inversion (Figure 4.6b). For $|U| = 4$ m s^{-1}, the flow is more strongly controlled and the

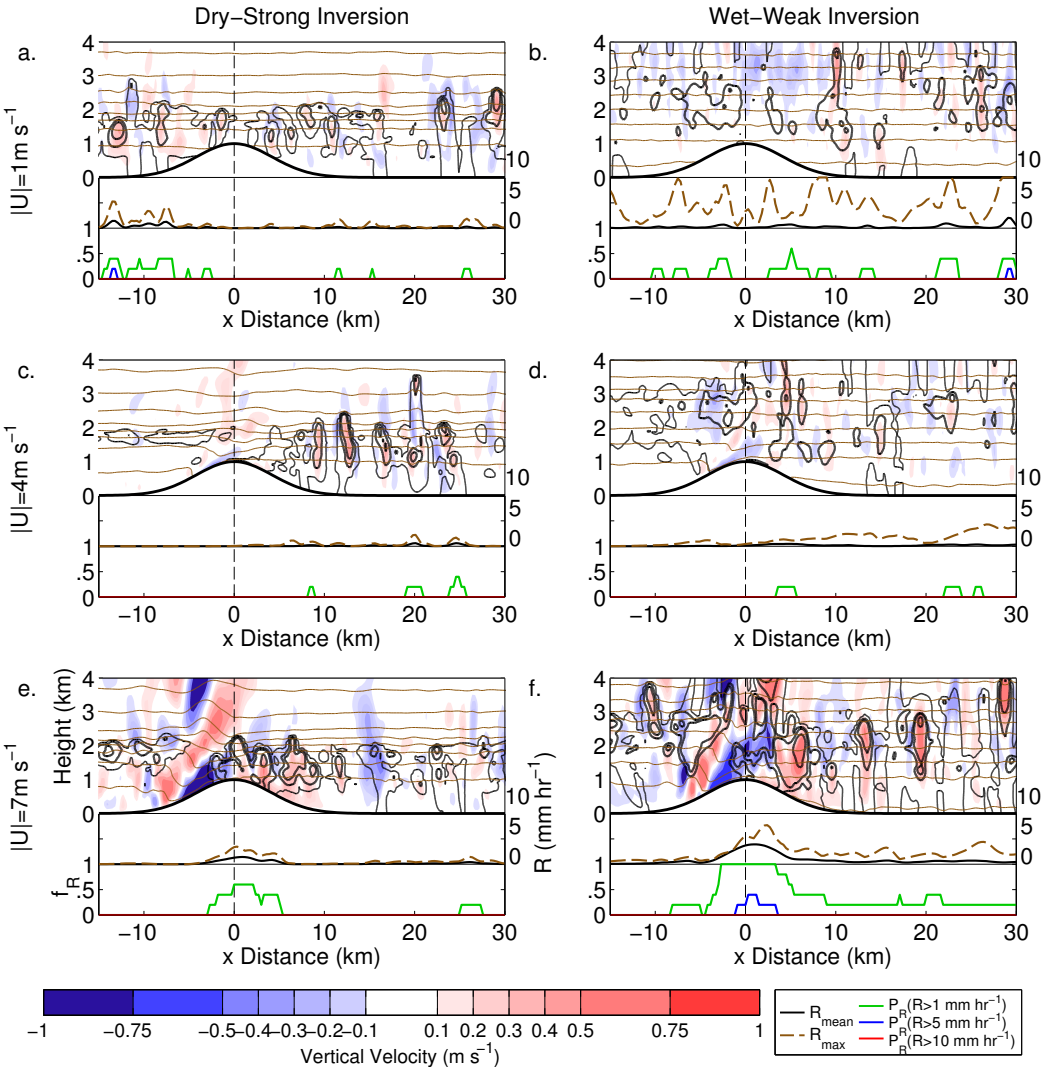

Figure 4.6: Vertical velocity (shading) with isentropes (brown lines) and cloud water mixing ratio (black lines) overlaid, along a cross-section in the middle of the domain. Rainfall water mixing ratio of 0.01 g kg^{-1} is denoted by the thin black line and the cloud water mixing ratio is shown at 0.1, 0.2, 0.5, 1 and 2 g kg^{-1}. Isentropes plotted between 299 and 308 K, every 2 K. Beneath each main plot, subplots show mean and maximum rainfall intensity in mm hr^{-1} (black and brown lines; right-hand axis), and the frequency of rainfall intensity over specific limits (green for 1 mm hr^{-1}, blue for 5 mm hr^{-1}, and red for 10 mm hr^{-1}; left-hand axis). Control runs.

influence of the mountain is more prominent as there is a relative decrease in cloud covering in the lee. Very little rainfall is seen in either cases as the flow prohibits convective motion more strongly (Figure 4.6c,d). Finally, for $|U| = 7$ m s^{-1}, cloud cover greatly intensifies as the flow is forced over the mountain and is accompanied by persistent rainfall. Mountain waves on the lee side, stronger in the Dry-Strong Inversion case as the atmosphere is more strongly stratified (Figure 4.6e). In the Wet-Weak Inversion case persistent deep convective rainfall can be seen (frequently over 5 mm hr^{-1} over the mountain top), triggered as the more moist flow impinges on the mountain (Figure 4.6f).

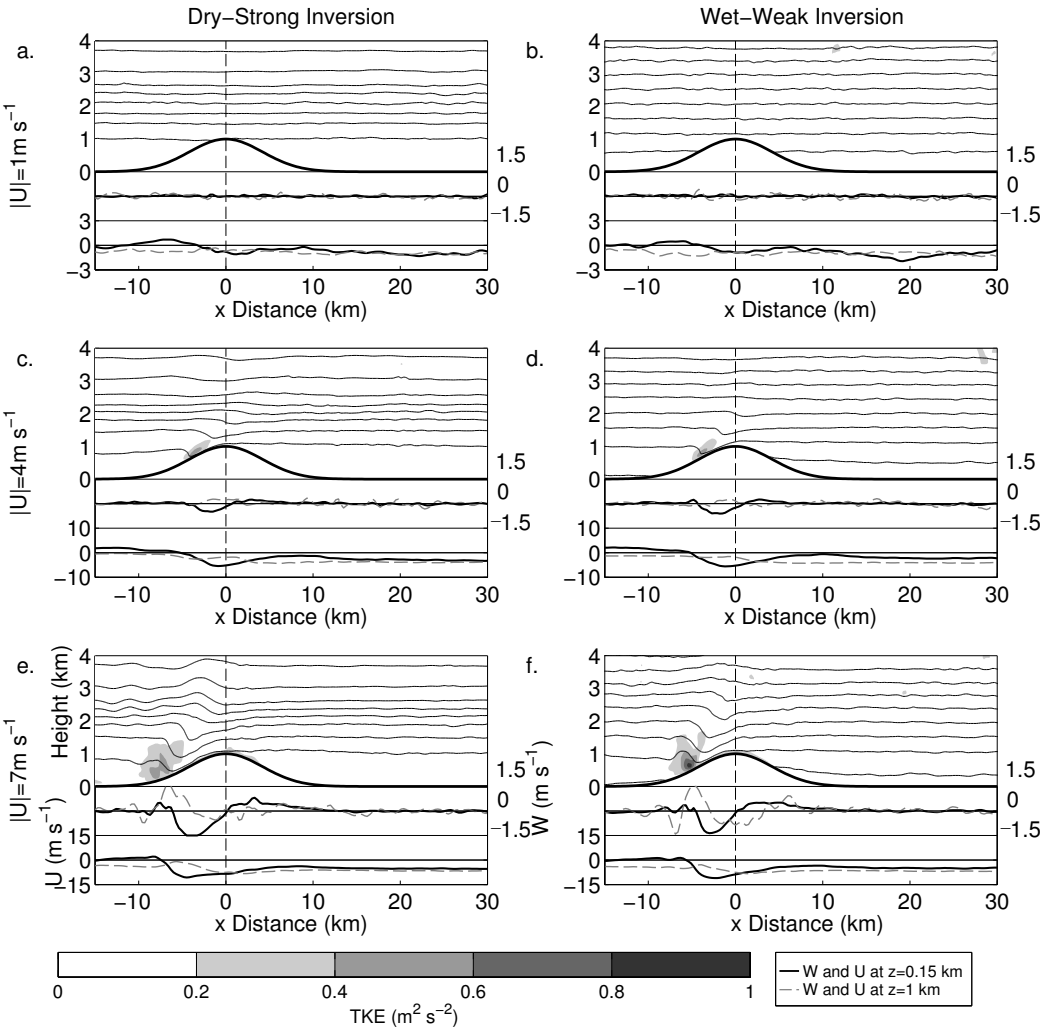

Figure 4.7: Turbulent kinetic energy (TKE; shaded) with isentropes. Beneath the main plot, subplots show vertical velocity and the U-wind component at a height of 150 m (black lines; right-hand axis) and 1 km (dashed gray lines; left-hand axis). Note the change in U scales. Control runs.

There is a build-up in turbulent kinetic energy (TKE) in the lee of the mountain as the flow becomes more energetic (Figure 4.7). For low incoming flow speed, w is close to zero everywhere in the domain, both at the surface and a height of 1 km. For higher $|U|$ there is ascent on the windward side and strong descent in the lee (as seen in Figure 4.6), enhanced by the katabatic (downslope) wind effect. Although this is a well-known and studied effect, its generation is still debated, with the most prevalent theory being that it is an analogous phenomenon to hydraulic jumps in shallow-water flows (Durran, 1990). The mountain wave response can also be seen in the $|U| = 7$ m s^{-1} case (Figure 4.7e,f). The U-wind component shows a fairly consistent behaviour for all simulations, decreasing in the windward side, increasing in the lee and then decreasing after that, with

a flow reversal area visible after that. The flow reversal zone never exceeds a height of 1 km. These results are in agreement with those presented in Chapter 3 for the dry runs (for example Figures 3.5 and 3.8) and are in agreement with other studies (Eckermann *et al.*, 2010).

Figure 4.8 shows vertical profiles of cloud water mixing ratio (q_C) and other hydrometeors (rain, snow, ice and graupel; q_H) for three areas, over the sea, over the windward side, and over the leeside of the mountain (marked as "Sea", "Windward" and "Lee" on the insert in Figure 4.8b). Once again, although a wider area was chosen, results can be influenced if a convective cell was within the area of study.

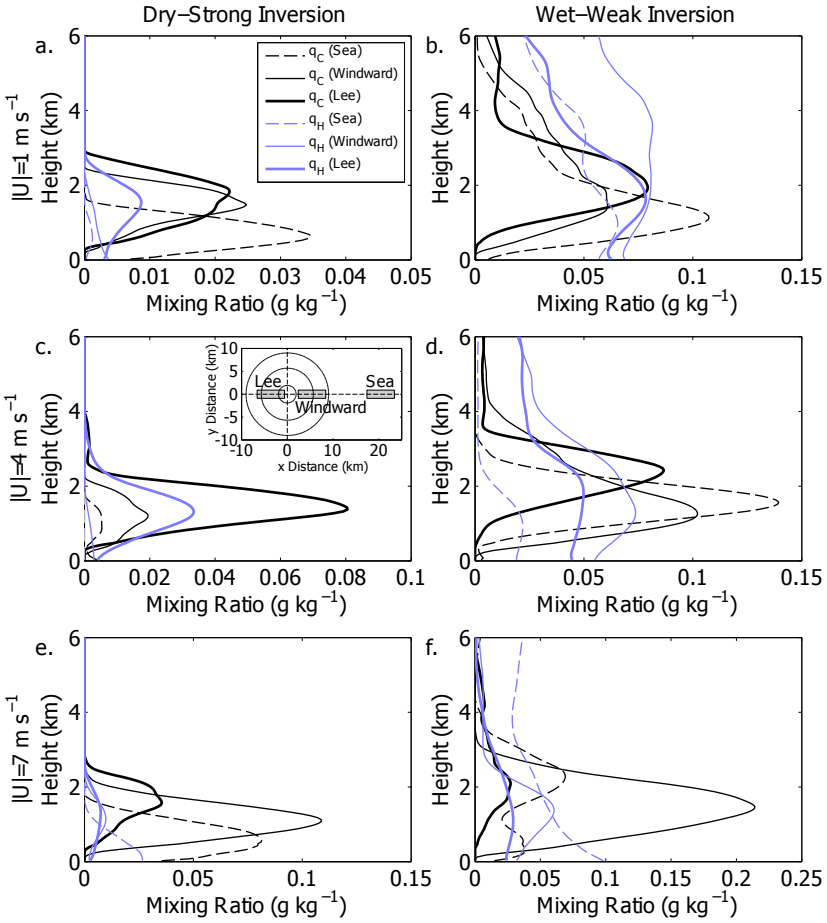

Figure 4.8: Vertical profiles of cloud water mixing ratio (q_C; black lines) and other hydrometeors (rain, snow, ice and graupel; q_H; blue lines) for locations "Sea", "Windward", and "Lee" as illustrated in the insert of Panel c. Note the change in the x axis. Control runs.

For $|U| = 1$ m s^{-1} cloud water mixing ratio and hydrometeor profiles appear relatively similar irrespective of the location (Figure 4.8a,b). This agrees with the results presented previously – for low incoming flow speeds the mountain plays a lesser role. All

characteristics peak beneath the inversion. In the Wet-Weak Inversion case, wider distribution can be seen for most characteristics as convection is more prevalent and the atmosphere is mixed more thoroughly, moving the inversion peak higher. For $|U| = 4$ m s^{-1}, in the Dry-Strong Inversion case (Figure 4.8c) a significant increase in cloud water mixing ratio can be seen in the lee as there is consistent high level cloud (also seen in Figure 4.6c). The Wet-Weak Inversion case appears fairly similar to the respective $|U| = 1$ m s^{-1} simulation, however values above the inversion are significantly decreased (Figure 4.8d). Finally, for $|U| = 7$ m s^{-1} the peak values can be seen for the windward side, higher than both the sea and leeside locations (Figures 4.8e,f). As previously, for the Dry-Strong Inversion case the distribution is more confined below the inversion.

4.3.2 Control experiments overview

The control results can generally be explained in terms of the atmospheric conditions and correspond well to previous studies of similar situations (e.g. Kirshbaum and Smith, 2009; Minder *et al.*, 2013). For low incoming flow speeds the flow is mainly controlled by random convection across the domain. As the flow passes over the sea a layer of low level (shallow) cumulus clouds is formed beneath the inversion due a combination of instability beneath the inversion, convection in the boundary layer, high humidity in the atmosphere, and moisture fluxes. In the Dry-Strong Inversion case, the convection is largely confined beneath the inversion, aside from the leeside, where there is rainfall due to convergence (Roe, 2005). In the Wet-Weak Inversion case deep convective bursts appear at random over the domain, owing to the more favourable conditions for moist convection. This leads to rainfall over the sea from sporadic deep convection, as the inversion is weakened and the atmosphere above the inversion becomes more humid. For low wind speeds Minder *et al.* (2013) found that although convective cells were triggered randomly in the domain, they were not strong enough to generate rainfall, something that agrees with the Dry-Strong Inversion experiment results. In the Wet-Weak Inversion case, strong convection and deep convective rainfall is generated due to the decreased strength of the inversion, as well as a more humid lower atmosphere. Note, low-level humidity has been known to play a major role in initiating moist convection (Kirshbaum, 2013).

As the incoming flow speed increases, convection is inhibited and the flow enters

a more mechanically-driven regime. As the flow crosses over land the cumulus field intensifies and high amounts of rainfall are consistently generated over the mountain, with an average rainfall intensity of at least 1 mm hr^{-1} – at least 5–10 times more that the average rainfall over the sea. In the Wet-Weak Inversion case this increases to up to 50 times higher rainfall rates over the windward side compared to the sea, as the more moist flow meets the mountain and deep convection is consistently generated. These results are in good agreement with studies focusing on trade winds impacting on a subtropical mountain (Cuijipers and Duynkerke, 1993; Kirshbaum and Smith, 2009; Minder *et al.*, 2013; Cécé *et al.*, 2014).

4.4 Temperature anomaly experiments: Flow over an isolated volcano

The response of the atmospheric circulation to the surface temperature anomaly on the volcano summit is now examined. Initially the focus is on the changes brought by differences in the surface thermal forcing, for the Dry-Strong Inversion and Wet-Weak Inversion simulations for $|U|$=1 m s^{-1}, and a range of temperature anomaly values between 0 and 60 K. Note that the same analysis carried out for the $|U| = 4$ m s^{-1} simulations yielded similar results. After that the focus will be on the changes brought by differences in the atmospheric conditions.

4.4.1 Sensitivity to thermal forcing

4.4.1.1 Flow response and rainfall

Figure 4.9 show horizontal plots of vertical velocity (shaded) and horizontal wind (vectors), following the format of Figure 4.4, for various values of T_a. Note that the figures are focused on a 5×5 km area at the top of the mountain, so that the resulting structure can be seen in some detail. The increase in the temperature anomaly forces a concentrated area of ascent mainly focused over the top of the mountain (Figure 4.9). This thermally-forced ascent is circular and always appears over and in the lee of the dome with $w > 1$ m s^{-1}. It is surrounded by weaker, scattered convection at random ($w < 0.3$ m s^{-1}) in the domain.

As T_a increases the magnitude of the flow response strengthens, the area of the plume

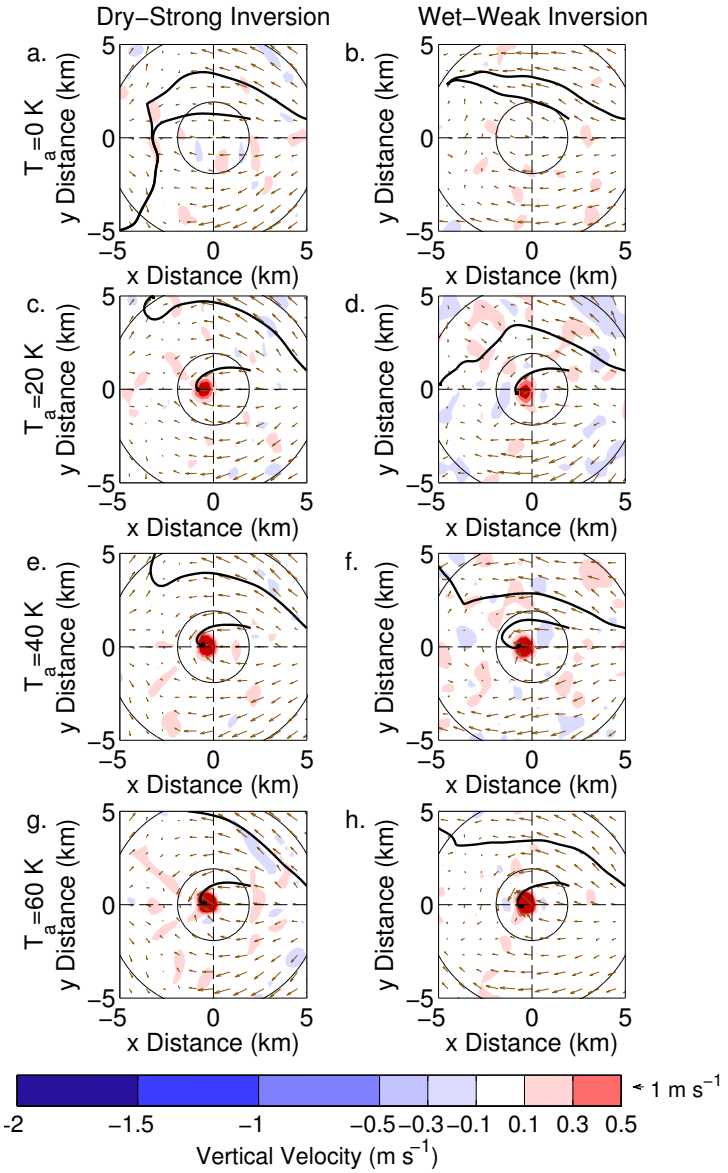

Figure 4.9: Left column: Dry-Strong Inversion, Right column: Wet-Weak Inversion volcanic heating simulations. Vertical velocity (shading) with horizontal wind vectors on the third model level for: T_a = (a) 0 K, (b) 20 K, (c) 40 K and (d) 60 K with $|U| = 1$ m s^{-1}. Height contours at 500 and 900 m.

becomes larger (the area of $w > 1$ m s^{-1}) and two counter-rotating vortices can be seen in the lee of the mountain top, drawing air back towards the convective plume – extra streamlines were initialised at $x = 2$ and $y = 1$ km emphasise this pattern. Such vortices are common features of wild fires (Cunningham *et al.*, 2005), but in this case they do not develop the same vertical structure and are only found near the surface, possibly due to the strength of the forcing. Although these vortices are a ubiquitous feature in plumes there is still debate on their generation and evolution (Cunningham *et al.*, 2005). The plume's major impact is limited to a 2×2 km area surrounding the temperature anomaly, focused

towards the lee of the dome. As with the control runs (Figure 4.4) the basic flow response is similar for the Dry-Strong Inversion and Wet-Weak Inversion cases.

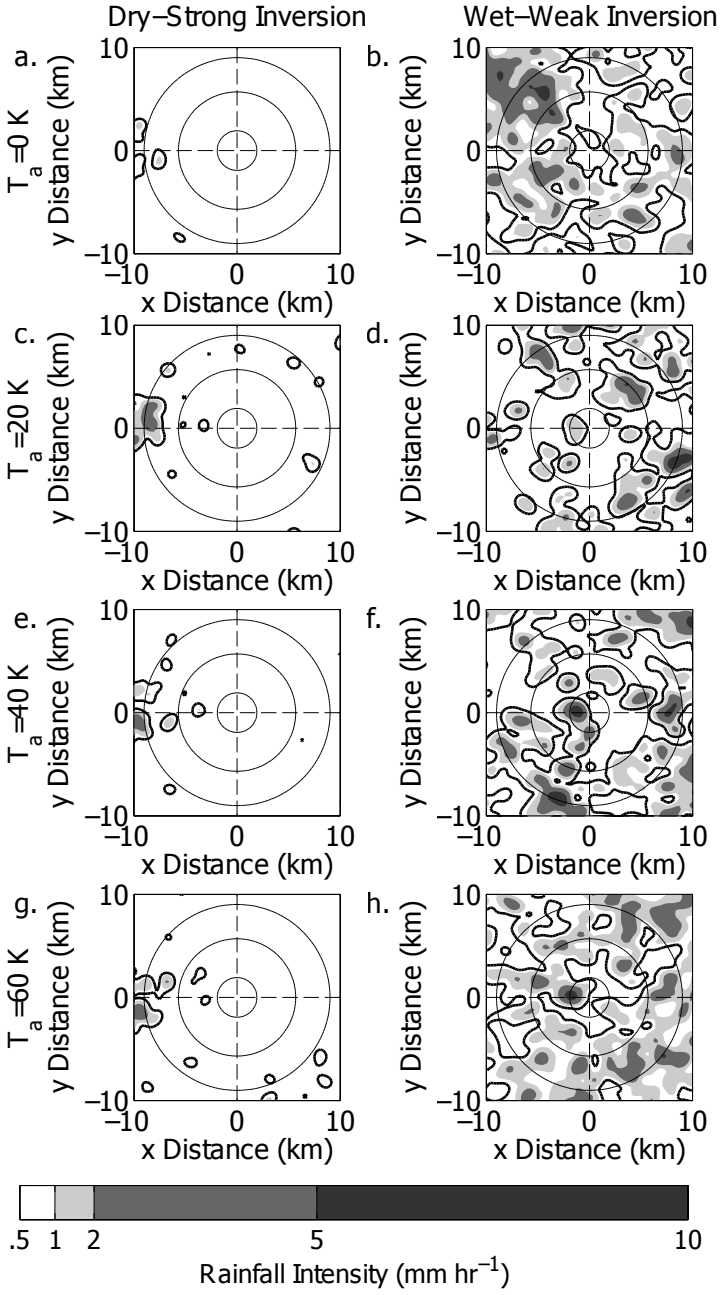

Figure 4.10: As Figure 4.9 but for rainfall. The thick black contour line signifies $R > 0.5$ mm hr^{-1}, while shaded areas show R over 1, 2, and 5 mm hr^{-1}. Dry-Strong Inversion (left column) and Wet-Weak Inversion (right column) simulations and $|U| = 1$ m s^{-1}.

Figure 4.10 shows rainfall rates at the surface. As expected by the limited area of the effect, the general rainfall patterns remain largely unaffected for all simulations. All Dry-Strong Inversion simulations show a similar image, scattered patches of low intensity

rainfall and a stronger response in the lee of the mountain. Wet-Weak Inversion simulations show a different image – larger patches of rainfall with intensity often as much as 10 mm hr^{-1} over the entire mountain. In the lee of the dome in the Wet-Weak Inversion cases there is a patch (approximately 1×1 km^2 in area) associated with the thermal forcing and fixed in space (at approximately $x = -4$–0 km), that has progressively higher rainfall intensity values – up to 2 mm hr^{-1} for $T_a = 20$ K and up to more than 10 mm hr^{-1} for $T_a = 40$ and 60 K. This volcanically-triggered rainfall is not qualitatively different from the typical convective rainfall in the simulations. In the Dry-Strong Inversion case a low rainfall patch is also evident.

As it is difficult to isolate volcanically-triggered rainfall from random convection at scatter plot is constructed to compare rainfall intensity values close to the surface temperature anomaly in the control case (x-axis) and each of the temperature anomaly cases (y-axis; Figure 4.11). Each scatter plot is created using rainfall intensity data for every grid point within a 3 km radius from the surface temperature anomaly, for every time step between 3 and 6 hr. In all cases, random convection is generally confined between 0 and 2.5 mm hr^{-1}. For $T_a = 20$ K there is a small amount of extra rainfall in the heated case, with some rainfall values over 2 mm hr^1, however the effect is very weak (Figure 4.11a). The response is considerably more robust for $T_a = 40$ and 60 K Figure 4.11b,c). For these cases there is an increase in the maximum rainfall intensity values in the heated cases from 3 mm hr^1 to 10 and 6mm hr^1 respectively. This increase in concentrated in areas where there is little or no rainfall in the control case.

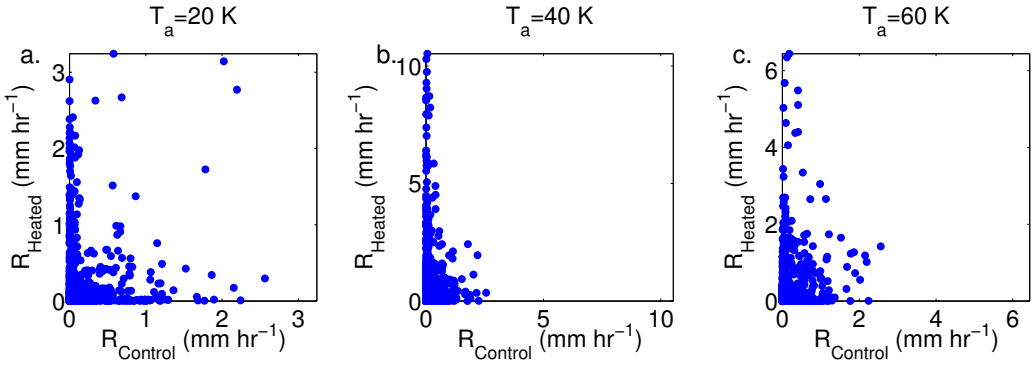

Figure 4.11: Scatter plots comparing rainfall intensity for the control case (x-axis) and the surface temperature experiments (y-axis) for $T_a =$ (a) 20 K, (b) 40 K, and (c) 60 K. Data are shown for each grid point and at every time step from hours 3–6.

These results present the first main confirmations of the study's hypothesis - as the

mean value of the lava dome temperature increases and exceeds a threshold value (depending on the atmospheric conditions) deep convection is generated consistently over or in the lee of the lava dome. However, this volcanically-triggered rainfall is not easily distinguished from the general rainfall in these plots. The focus will now be to differentiate this lava dome-triggered rainfall from other random convection in the model by showing that it is a robust and nearly-constant response once the model has reached a quasi-steady state. For conciseness in the remainder of the thesis this rainfall response to the surface heating will generally simply be referred to as "the rainfall anomaly".

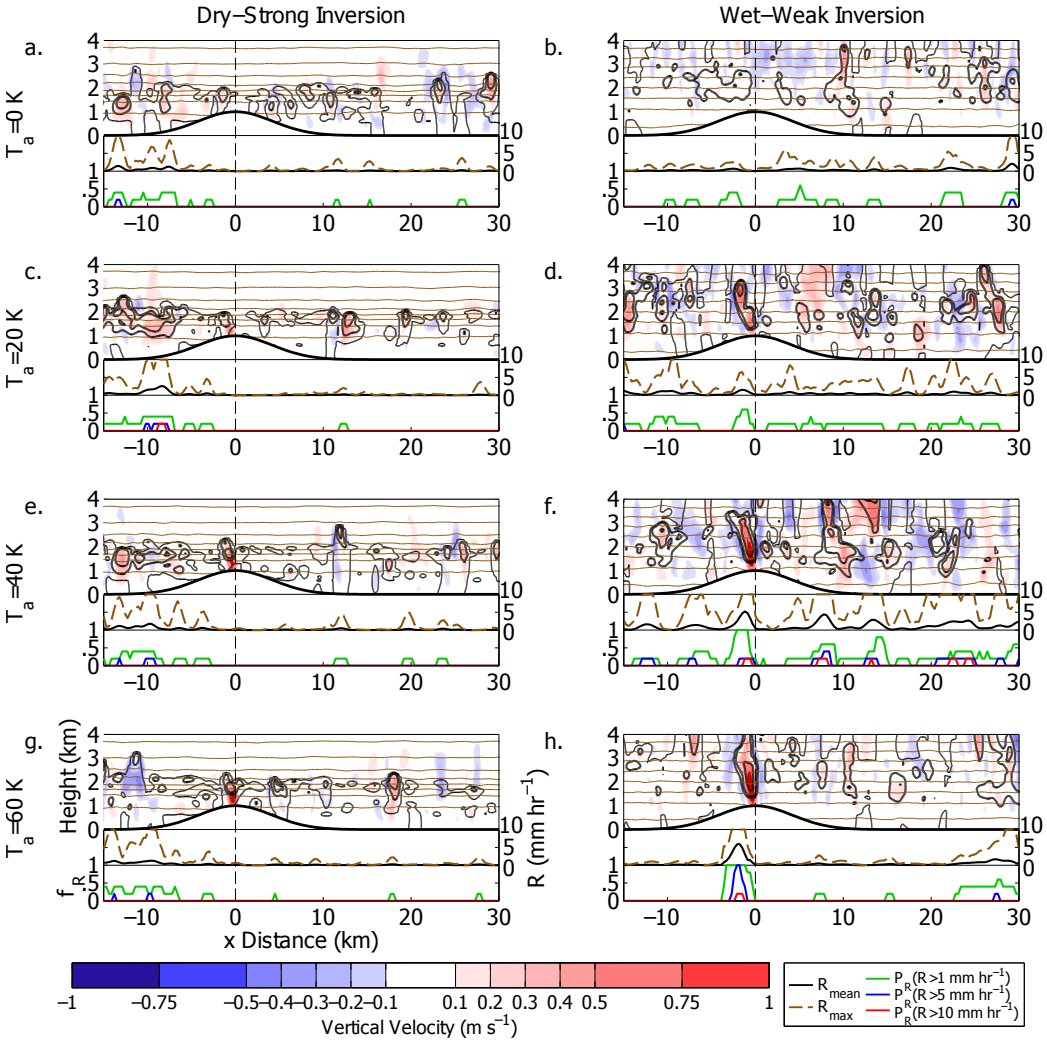

Figure 4.12: Left column: Dry-Strong Inversion, Right column: Wet-Weak Inversion volcanic heating simulations. Vertical velocity (shading) with isentropes (brown lines) and cloud water mixing ratio (black lines) overlaid, along a cross-section in the middle of the domain. Rainfall water mixing ratio of 0.01 g kg^{-1} is denoted by the thin black line and the cloud water mixing ratio is shown at 0.1, 0.2, 0.5, 1 and 2 g kg^{-1}. Isentropes plotted between 299 and 308 K, every 2 K. Beneath each main plot, subplots show mean and maximum rainfall intensity in mm hr^{-1} (black and brown lines; right-hand axis), and the frequency of rainfall intensity over specific limits (green for 1 mm hr^{-1}, blue for 5 mm hr^{-1}, and red for 10 mm hr^{-1}; left-hand axis). Note, axis labels appear only in the lower left-hand side (Panel g). All results are for $|U| = 1$ m s^{-1}.

As previously, vertical cross-sections across the middle of the domain for no surface heating show the shallow cumulus confined below the temperature inversion, strongly in the Dry-Strong Inversion case and more weakly in the Wet-Weak Inversion case (Figures 4.12a,b). However, when the surface temperature forcing is switched on, a plume accompanied by increased cloud cover is introduced. For the Dry-Strong cases this is controlled by the temperature inversion and it never seems to break through the inversion (Figures 4.12c,e,g). The rainfall previously seen in the lee of the dome appears at a consistent distance but is a very weak and erratic response, associated with a frequency of 0.2 for $R > 1$ mm hr^{-1}. In the Wet-Weak Inversion cases there is a stronger vertical development in the plume as it reaches a height of 3–4 km. Rainfall here is triggered beneath the plume and it is a more robust response – for $T_a = 20$ K there is a 0.5 frequency for rainfall over 1 mm hr^{-1} (Figures 4.12d), which becomes a frequency of 1 for $T_a = 40$ K (Figures 4.12f). For $T_a = 60$ K the frequency for $R > 5$ mm hr^{-1} is also 1 (Figures 4.12h). Stronger rainfall rates ($R > 10$ mm hr^{-1}) appears for both $T_a = 40$ and 60 K cases with a low frequency, comparable to deep convective rainfall at other parts of the domain as deep convective bursts are not continuous but cycle on and off over a convective timescale (see Section 4.5).

As in Chapter 3, TKE can be a useful proxy for the convective plume, due to the large amount of sub-scale mixing and turbulence triggered (Figure 4.13). As T_a increases both for the Dry-Strong and Wet-Weak Inversion cases the height of the TKE plume also increases. Note that the Wet-Weak Inversion profile allows for a notable extension of the TKE plume height. The increase is mirrored in both w and U-wind component at the surface, with w increasing from 1 (Figure 4.13c,d) to 1.5 m s^{-1} (Figure 4.13e–h) and forcing a circulation mirrored in the U-wind component. Comparing results from the Dry-Strong and Wet-Weak Inversion cases for the same T_a, the plume is always higher for the latter, following the cloud heights in Figure 4.12. This is also shown as the wind component behaviour is similar both close to the surface and at a height of 1 km from the surface.

Figure 4.14 shows a comparison of the vertical profiles of cloud (black lines) and hydrometeors (gray lines), over the sea (dashed line), over the windward side of the mountain (solid line) and over the lee side (thick line). As expected for the first two cases, results

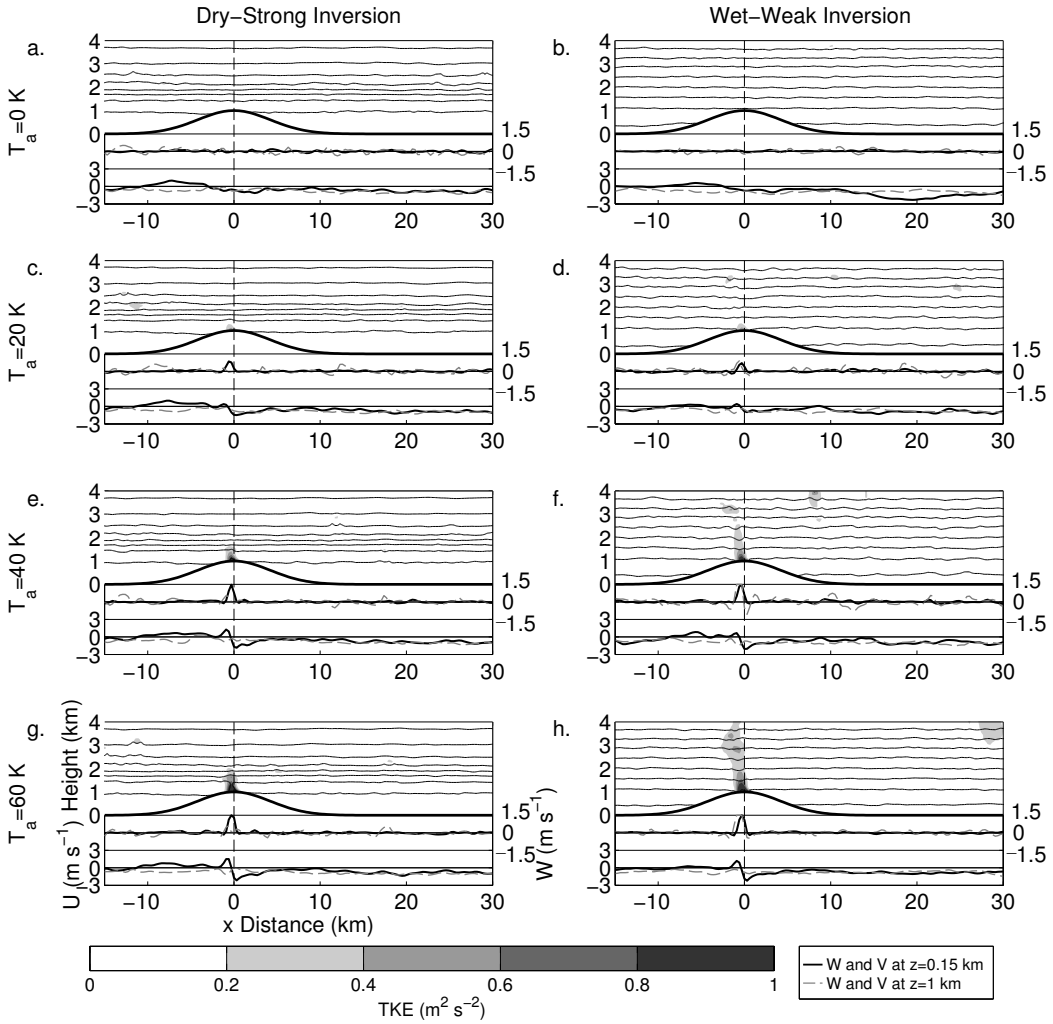

Figure 4.13: Turbulent kinetic energy (TKE; shaded) with isentropes. Beneath the main plot, subplots show vertical velocity and the U-wind component at a height of 150 m (black lines; right-hand axis) and 1 km (dashed gray lines; left-hand axis). Dry-Strong (left column) and Wet-Weak Inversion (right column) simulations and $|U| = 1$ m s^{-1}.

are fairly similar, allowing for small qualitative differences due to the stochastic nature of the convection. This changes for Figures 4.14e–h with the onset of deep convection. As T_a increases over 40 K, there is a robust increase of both the cloud water mixing ratio and the other hydrometeors in the lee, approximately 1.2–1.5 times for the Dry-Strong Inversion and 2–3 times for the Wet-Weak Inversion. The convection structure is illustrated by a secondary peak in cloud water at a height of 4 km for Figure 4.14d,f and an almost equal spread all the way up to the tropopause in Figure 4.14h. The low level cloud below the inversion remains largely unaffected pointing towards the fact that the deeper cloud is generated by moisture brought in by the plume circulation.

The hydrometeor profile for the Wet-Weak Inversion cases shows a large decrease above a height of 4 km in the troposphere (freezing point), where rain water mixing ratio

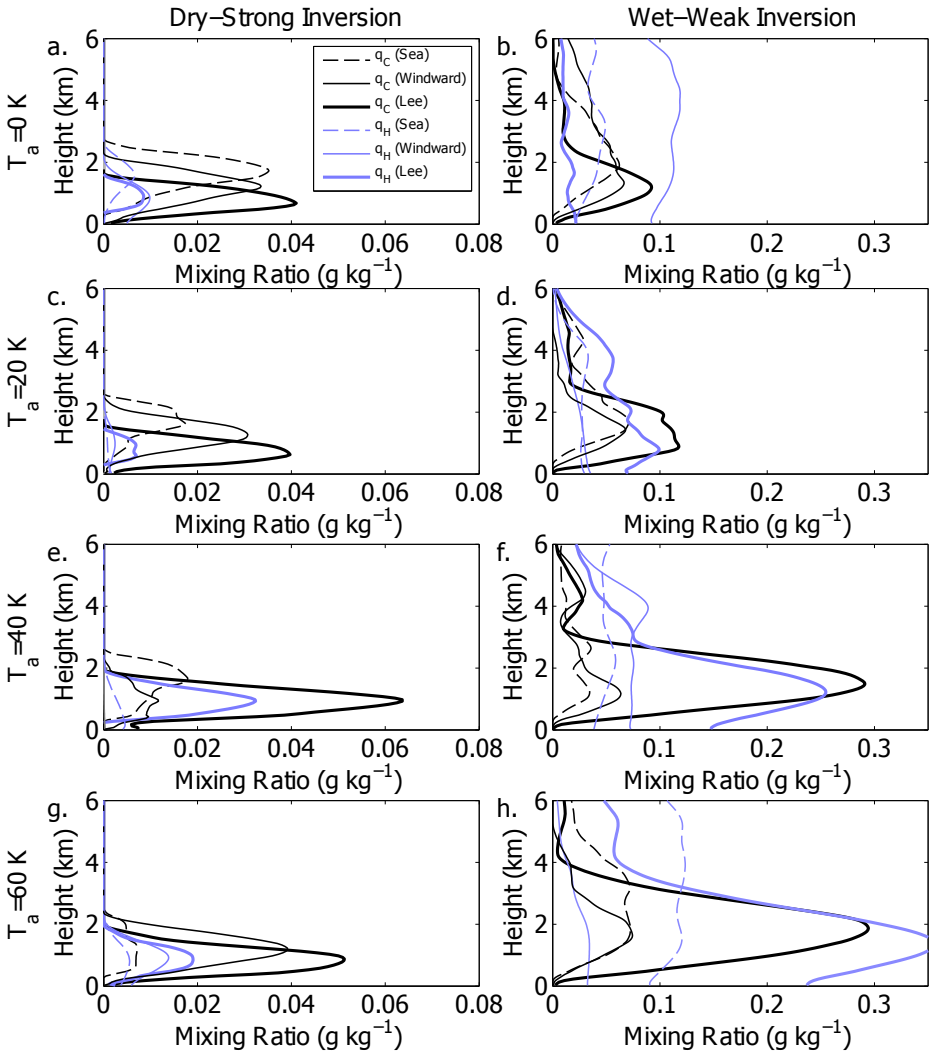

Figure 4.14: Vertical profiles of cloud water mixing ratio (q_C; black lines) and other hydrometeors (rain, snow, ice and graupel; q_H; blue lines) for locations "Sea", "Windward", and "Lee" as illustrated in the insert in Figure 4.8b. Note the change in scale in the x axis.

drops to zero and ice hydrometeors start increasing. This profile matches the theoretically expected profile for an oceanic area in the Tropics. For example, Zipser and Lutz (1994) showed that there is a steep decrease in the radar reflectivity above the freezing point, owing to the relative weakness of the convective cells and the inability to consistently lift raindrops above the freezing level. Furthermore, by examining lower reflectivity values they showed that the decrease in reflectivity over the freezing point does not indicate the cloud top, but rather a layer of low reflectivity cloud - consistent with the cloud water mixing ratio profile seen here.

4.4.1.2 Rainfall anomaly characteristics response

As seen in Section 4.4.1.1 for the Wet-Weak Inversion sounding, deep convection was triggered spontaneously across the domain. However, there was a persistent increase of rainfall in the lee of the lava dome. Characteristics of this volcanically-triggered rainfall will now be examined. The aim here is to identify areas of *intense* and *persistent* rainfall that did not occur during the control simulations. To do this, results from the control case were subtracted from the $T_a > 0$ K cases and, in order to differentiate between random, short-lived rainfall and rainfall as a response to the surface temperature anomaly, the following algorithm was devised. For each experiment and for every point in the domain, rainfall anomalies with $|R_a| > 0.1$ mm hr^{-1} were noted, and a population of rainfall anomaly durations (D) was created. The average ($\overline{D}$) and standard deviation (σ_D) was then calculated for each case; for example in the case of the Wet-Weak Inversion profile with $T_a = 60$ K, $\overline{D} = 57$ min and $\sigma_D = 17$ min. The average duration for the Dry Atmosphere profile cases was roughly 40–45 min, while for the Wet Atmosphere cases it was 55-60 min. For the rainfall anomaly to qualify as being *persistent* (so linked to the surface forcing) it had to satisfy the following conditions: **(i)** $D_a > \overline{D} + 2\,\sigma_D$ (where D_a is the duration of the potential lava dome generated rainfall anomaly), and **(ii)** be located over or in the lee of the dome ($-10 < x < 1$ km).

For the Dry-Strong Inversion experiments no points were found to fulfil these criteria, pointing towards the fact that the rainfall in the lee was either random convection, or not intense or persistent enough. In the Wet-Weak Inversion cases, a significant area in the lee of the domain was found to have persistent rainfall (for example, in the case of the Wet-Weak Inversion profile with $T_a = 60$ K, $D_a = 113 \pm 22$ min). Three characteristics of this rainfall anomaly will now be examined: *Rainfall anomaly area* (grid points in the lee of the dome that received over 0.1, 1 and 5 mm hr^{-1} for at least $\overline{D} + 2\,\sigma_D$ min), *rainfall anomaly intensity* (average and maximum characteristics over these grid points sustained over different time periods), *total rainfall anomaly* (the product of the previous two for $R_a > 0.1$ mm hr^{-1} and average rainfall anomaly intensity for 3 hr), as well as the maximum w over the rainfall anomaly area.

Rainfall anomaly area is studied for three thresholds: 0.1, 1 and 5 mm hr^{-1} (Fig.

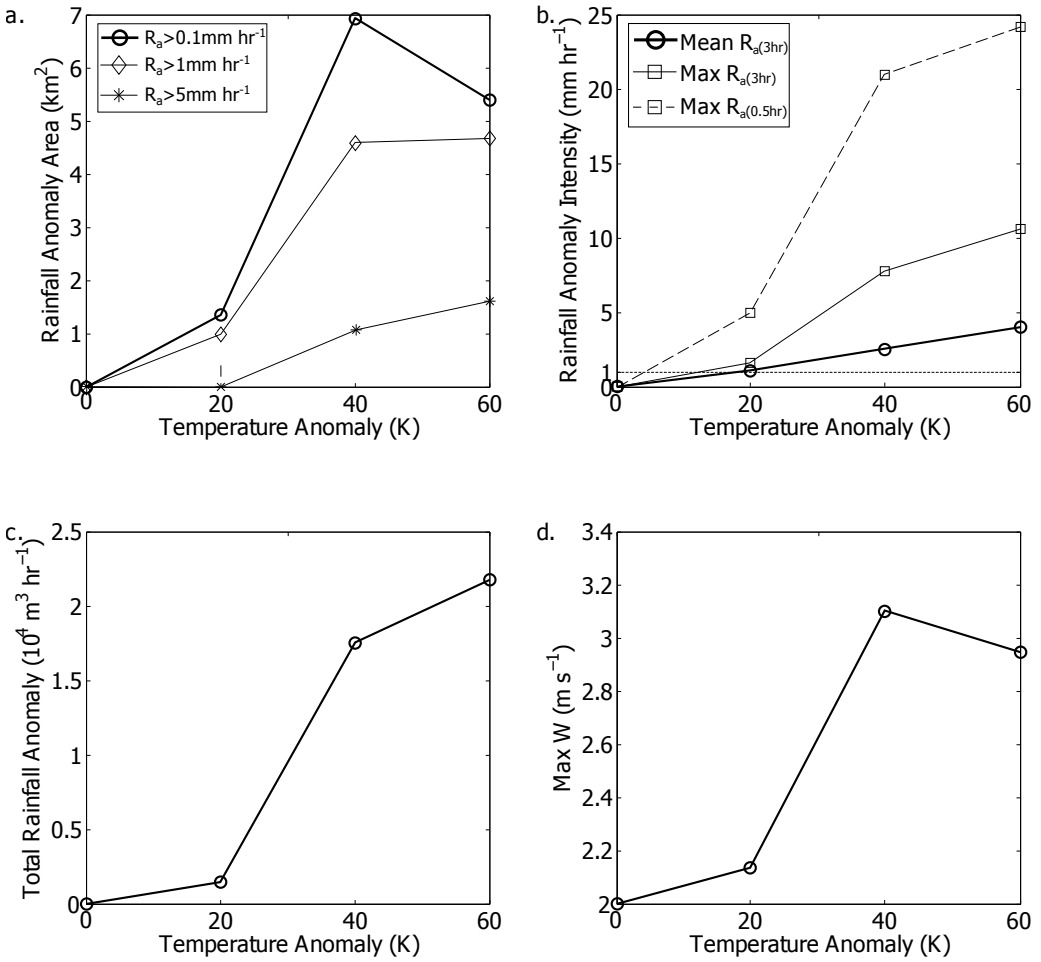

Figure 4.15: (a) Rainfall anomaly area, (b) Rainfall anomaly intensity, (c) Total rainfall anomaly (rainfall volume over 3 hours (in $\mathrm{m}^3\ \mathrm{hr}^{-1}$), (d) Maximum w over the rainfall anomaly area. All plotted against temperature anomaly for Wet-Weak Inversion simulations. Panels b and c are calculated over the storm area. All rainfall intensities are calculated as the results from the $T_a > 0$ K cases minus the control experiments. Note that only rainfall anomaly rates over 0.1 mm hr^{-1} sustained over approximately 100 min were considered.

4.15a). The first threshold shows the full extent of the lava dome influence when considering practically all rainfall intensities. The second threshold, consistent rainfall over 1 mm hr^{-1}, has been linked with the remobilising of sediment on the slopes of a volcano, while the third threshold, over 5 mm hr^{-1}, has been implicated in the triggering of volcanic eruptions and pyroclastic flows (Matthews *et al.*, 2002; Barclay *et al.*, 2006; Matthews *et al.*, 2009). For all rainfall intensity thresholds, rainfall anomaly area generally increases with T_a. Note, this increase is not linear – there is a significant leap in the values between $T_a = 20$ and 40 K. Results are fairly similar for $R_a > 0.1$ and > 1 mm hr^{-1}, with rainfall anomaly area values at 1 km^2 for $T_a = 20$ K and 4–6 km^2 for $T_a \geq 40$ K, but rainfall anomaly area values are significantly smaller for $R_a > 5$ mm hr^{-1},

with 0 km^2 for $T_a = 20$ K, increasing to 1–1.5 km^2 for $T_a \geq 40$ K. Mean rainfall anomaly intensity values over the study period increase linearly with T_a, from 0 up to 5 mm hr^{-1} (Fig. 4.15b). This linear behaviour changes when looking at the maximum rainfall intensity sustained over 3 hr, with a steep gradient between $T_a = 20$ and 40 K, and becomes even more pronounced for maximum rainfall intensity sustained over 30 mins. This points toward a change between $T_a = 20$ and 40 K, with deep convection triggered consistently in the later case. Total rainfall anomaly increases by a factor of 8 between $T_a = 20$ and 40 K but then only by a factor of 1.2 between 40 and 60 K (Fig. 4.15c). Maximum w shows a similar behaviour, with an increase from 2.1 to 3.1 m s^{-1} between the first two experiments and then a small decrease between the last two (Fig. 4.15d). Note, for $T_a = 0$ K the value is the maximum w up to a height of 2 km over the volcano. In short, for $T_a \geq 40$ K, consistent intense (deep convective) rainfall is triggered by the surface heating.

As seen here, once consistent deep convection is triggered (for $T_a \geq 40$ K in the experiments), the rainfall anomaly has relatively similar characteristics, with the largest changes occurring between $T_a = 20$ and 40 K. This behaviour points towards the fact that the temperature anomaly acts to trigger convection, but once triggered the characteristics of both the convection and the rainfall are largely controlled by realistic processes in the atmosphere. The rainfall triggered by the lava dome has also been seen to consistently be over the threshold to affect volcanic hazards around the lava dome.

Sensitivity tests carried out for a number of microphysics modules (WSM5, WSM6, Thompson, Milbrant, and Morrison schemes; Skamarock *et al.*, 2008) and at different grid spacings (Δx =150, and 75 m) revealed that, aside from the well-established sensitivities in both the microphysics schemes (**?**) and the grid spacing (Bryan *et al.*, 2003; Kirshbaum and Smith, 2009), results were qualitatively similar, with the most changeable characteristic being the rainfall anomaly area that ranged between 5–9 km^2 for the different microphysics schemes and increased to 13–14 km^2 for the higher resolution simulations.

4.4.2 Sensitivity to atmospheric conditions

In this section, the effect of the background atmospheric state (wind speed, humidity and inversion strength) on the characteristics of the rainfall over the volcano will be examined using data from across all different atmospheric profiles and incoming flow speeds for $T_a = 60$ K (Figure 4.16). This is similar to Figure 4.5, for the control simulations, but includes results from the Dry-Weak Inversion and Wet-Strong Inversion as well.

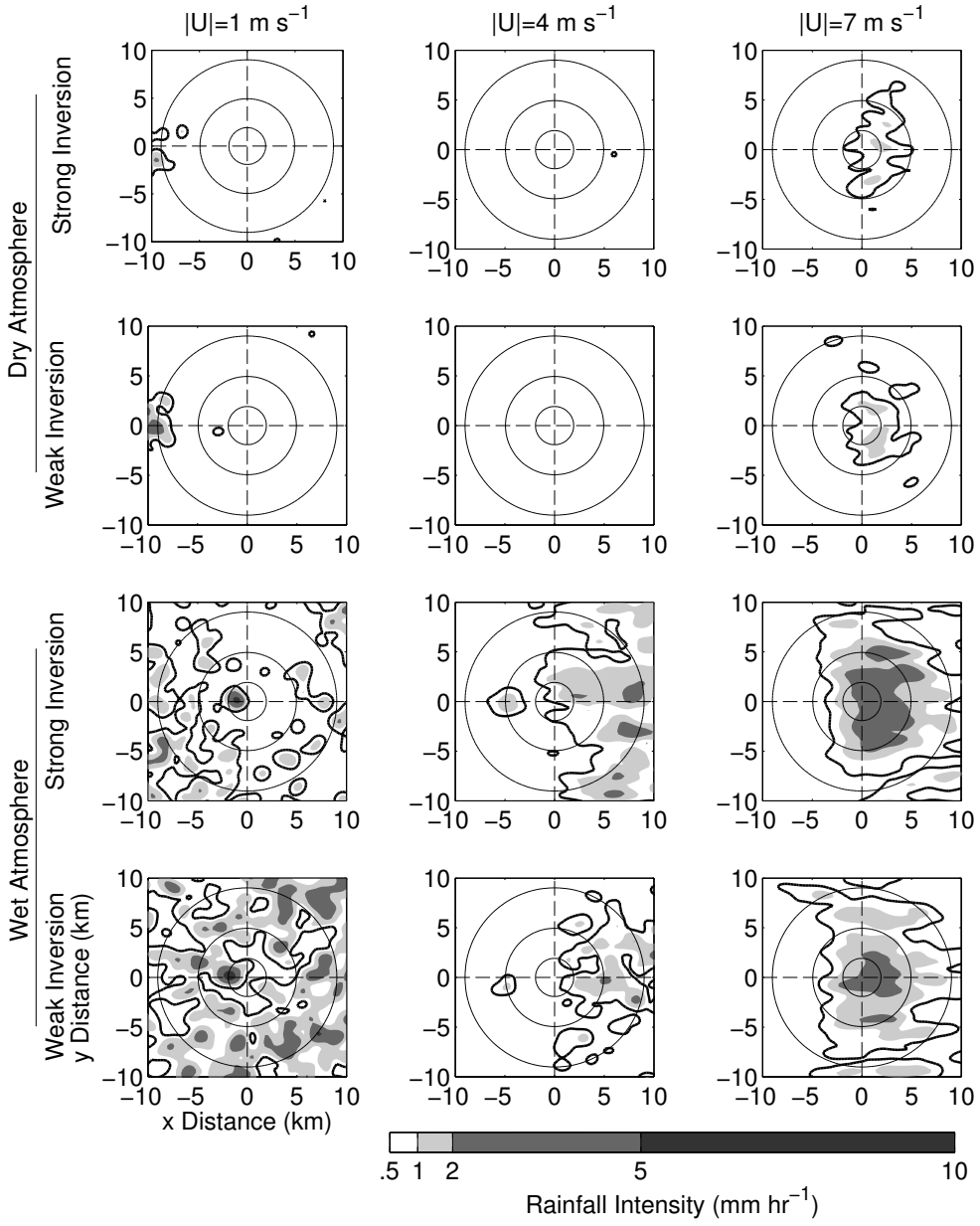

Figure 4.16: Rainfall intensity over the volcano in the $T_a = 60$ K experiments for the $|U| = 1$, 4 and 7 m s^{-1} (columns); a dry ($\overline{RH} = 50\%$) and wet ($\overline{RH} = 60\%$) atmosphere, and a strong ($\theta_I = 308.2$ K) and weak ($\theta_I = 307.2$ K) inversion (rows as marked). The thick black contour line signifies $R > 0.5$ mm hr^{-1}, while shaded areas show R over 1, 2, and 5 mm hr^{-1}. Height contours at 500, 700 and 900 m.

4.4.2.1 Incoming flow speed: Alters flow and rainfall regime

As seen in Section 4.3, as $|U|$ increases (left to right in Figure 4.16) there is a significant change in the rainfall regime: for $|U| = 1$ m s^{-1}, rainfall is mainly convective and appears randomly in the domain, $|U| = 4$ m s^{-1} is an inbetween case where strong convective motion is inhibited and weak to moderate orographic rainfall can be found in the windward side depending on the atmospheric conditions, and $|U| = 7$ m s^{-1} has a strong orographic response, with intense rainfall triggered persistently on the windward side and over the summit, especially for the more convective atmospheric profiles. Volcanically-triggered rainfall can be seen for $|U| =$ 1–4 m s^{-1} for the Wet Atmosphere soundings, while any response for $|U| = 7$ m s^{-1} is mixed with the increased orographic rainfall over the summit, or advected downstream. For $|U|$ between 1–4 m s^{-1} an increase in the incoming flow speed has two effects: (i) a decrease in the average rainfall intensity and (ii) an increase in the downstream distance of the triggered rainfall from the temperature anomaly on the volcano summit.

4.4.2.2 Humidity: Increases chance of triggering rainfall

An increase in the prescribed tropospheric relative humidity has a dramatic effect on the rainfall rates in general and on the generation of volcanically-triggered rainfall. It leads to significantly larger areas of all types of rainfall across the volcano – relatively high humidity is essential for the triggering of rainfall by the lava dome, and also drastically changes the general atmospheric response to the mountain.

4.4.2.3 Inversion strength: Minor changes in rainfall patterns

For the Dry Atmosphere simulations, the effect of the inversion strength is negligible. For the Wet Atmosphere simulations, a decrease in the inversion strength has a mixed effect: for $|U| = 1$ m s^{-1} a weaker inversion leads to more widely spread rainfall, but for stronger incoming wind is seems to limit the rainfall. This could possibly be the result of mixing with drier air above the inversion, however in total the changes are minimal and can also be attributed to the stochastic nature of rainfall generation in the model. This implies that realistic changes in the inversion strength [$\mathcal{O}$(1 K)] are too small to qualitatively affect the rainfall distribution.

4.4.3 Integrated rainfall anomaly characteristics

We now examine the dependence of the integrated rainfall anomaly characteristics on background wind speed, humidity and inversion strength. The conditions for rainfall to be considered as volcanically-triggered were described in Section 4.4.1.2. As previously discussed (see Figure 4.16), the relative humidity profile plays a discerning role. Overall, rainfall is triggered by the surface temperature anomaly consistently in the Wet Atmosphere simulations, but the incoming flow speed proves to be a limiting factor as $U > 4$ m s^{-1} are enough to severely limit the potential of the lava dome to trigger large amounts of rainfall. Note that, additional sensitivity tests at 2.5 m s^{-1} were carried out at this part. For all characteristics there is a noticeable difference between a very low wind regime ($|U| = 1$–2.5 m s^{-1}), a moderate wind regime ($|U| = 4$ m s^{-1}) and a strong wind regime ($|U| = 7$ m s^{-1}). Increased "weak" wind ($|U| = 2.5$ m s^{-1}) has a positive impact on the rainfall generation (possibly due to the increase in sensible heat flux), but too strong advection can act to inhibit it.

Mean rainfall anomaly intensity decreases drastically for higher wind speeds (Figure 4.17a). As seen in the control simulation results, a wind speed of $|U| = 4$ m s^{-1} was enough to severely limit the generation of convection and for $|U| = 7$ m s^{-1} most of the rainfall was orographically-generated. A similar trend can be seen for the maximum rainfall intensity values sustained for 3 and 0.5 hr (Figure 4.17b,c). As noted previously in Section 4.4 the marked decrease in rainfall intensity between $|U|$=1 and 4 m s^{-1} points towards the inability of the thermal forcing to consistently trigger deep convection. However, maximum rainfall sustained for 3 hr is close to 1 mm hr^{-1}, which shows the capability of volcanically-generated rainfall to trigger lahars in the long-term and maximum rainfall sustained for 0.5 hr is in many cases over 10 mm hr^{-1} – the limit for rapid lahar initiation. Note that higher maximum rainfall sustained for 0.5 hr can be seen for $|U| = 7$ m s^{-1}, possibly due to the preconditioning of the flow over the windward side.

Downward drift (Figure 4.17d) was calculated as the average distance of the rainfall anomaly points from the centre of the temperature anomaly. Downwind drift starts with relatively small values (rainfall generated close to the lava dome), increases with incoming flow speed (convection advected by the wind), but then decreases for high wind speeds (the rainfall is once again generated close to the rainfall anomaly). This, along with the

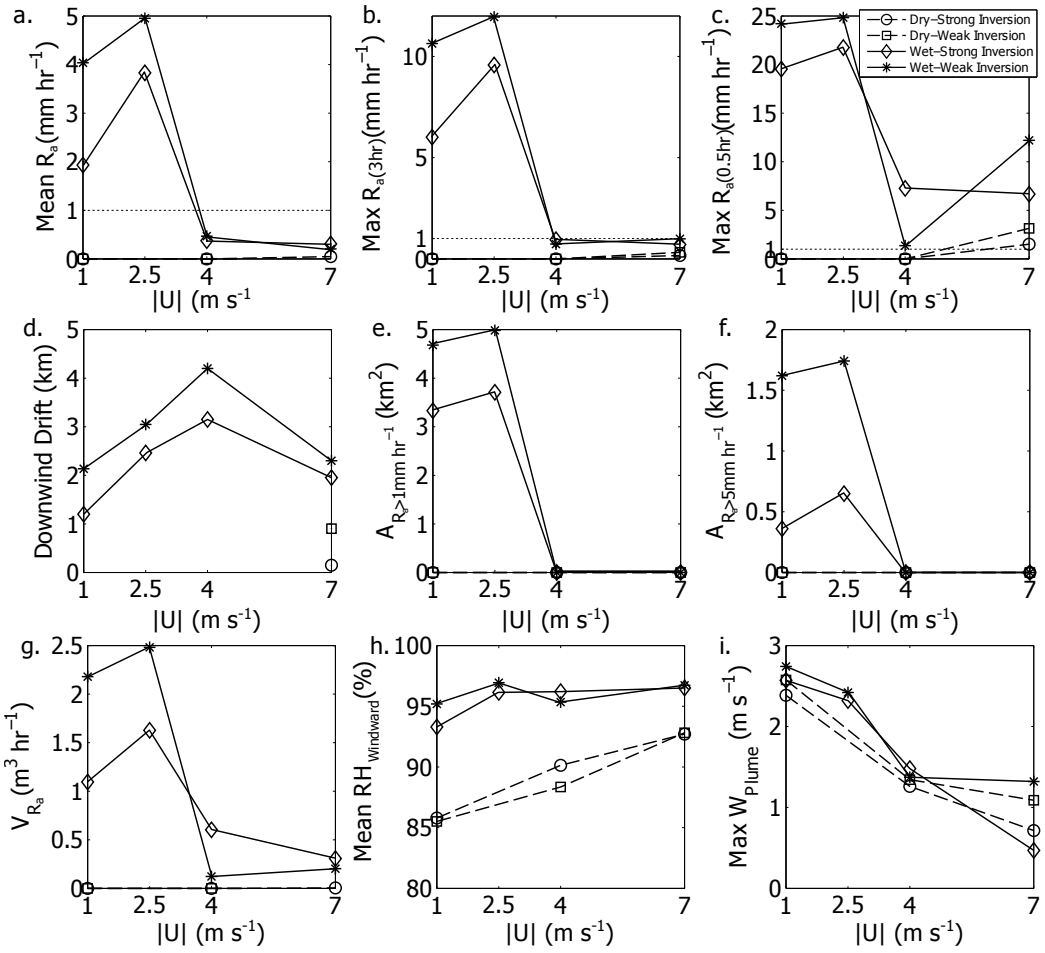

Figure 4.17: (a) Average rainfall anomaly, (b)–(c) Maximum rainfall anomaly intensity sustained for 2 and 0.5 hr respectively, (d) Average rainfall anomaly intensity, (d) Downwind drift, (e)–(f) Rainfall anomaly area for a $R_a > 1$ and 5 mm hr^{-1} respectively, (g) Total rainfall anomaly rainfall, (h) Average relative humidity in the windward side, and (i) Maximum w over the rainfall anomaly area. All characteristics plotted against background wind speed for all simulations with $T_a = 60$ K.

results for the average and maximum rainfall anomaly intensity, points towards a different initiation mechanism: for low Froude number cases (convective rainfall regime) the surface heating acts as the main initiator for the rainfall, while for high Froude number values it acts as a localised perturbation, leading to localised but very small amounts of rainfall. This is in agreement with anomaly area calculations (Figure 4.17e,f). Although small amounts of rainfall where generated for all incoming flow speed values, the only experiments that consistently produced rainfall over 1 and 5 mm hr^{-1} rainfall anomaly intensities where the ones where $|U| = 1$ m s^{-1}. The results here have implications for volcanic hazards – for $|U| = 4$ m s^{-1} rainfall was seen to be triggered further away from the lava dome in areas where no rainfall is expected, while for $|U| = 7$ m s^{-1}, this is extra rainfall close to the temperature anomaly, added on top of a large amount of

orographically-triggered rainfall. In short, $|U|$ of 4 m s^{-1} can act to trigger lahars in areas where rainfall is not expected, while $|U|$ of 7 m s^{-1} the surface heating acts in an already potent environment and the small extra amounts of rainfall generated could trigger lahars in borderline cases.

Total anomaly rainfall (calculated as the product of the average rainfall intensity and the rainfall area; Figure 4.17g) offers a more concise look on the previously discussed results – there is a marked decrease in the total rainfall anomaly as $|U|$ increases, 60% for the Wet-Strong Inversion and approximately 90% for the Wet-Weak Inversion profiles. However, as the calculation here is made using all rainfall rates, the rainfall generated for higher wind speeds is still considerable, as low amounts of rainfall are generated over large areas. Average relative humidity values over the windward side 4.17h) show that a minimum value of approximately 90% is needed for the temperature anomaly to have an effect in the incoming flow. Finally, maximum w values in the plume (up to a height of 2 km) show an inverse relationship with $|U|$, expected as the plume is heavily advected and convection inhibited for larger $|U|$.

4.4.4 Temperature anomaly experiments overview

The main impact of a surface temperature anomaly on the volcano summit has been the introduction of a strong convective plume on, or just downwind of, the thermal anomaly depending on the incoming flow speed and the magnitude of the anomaly. For small values of T_a the plume is capped by the trade wind inversion, but above a critical value of T_a (between 20–40 K in the simulations here) the plume breaks through the inversion and triggers a localised storm; i.e. deep convection accompanied by high rainfall rates. The resulting deep convection has been shown to be sensitive to both the atmospheric conditions and the intensity of the thermal forcing although the associated rainfall intensities are not. A drier atmosphere with a stronger inversion limits this effect as moist convection is inhibited. This leads to a plume and consistent cloud cover but not to rainfall. A moister atmosphere with a weaker inversion allows for a large area of rainfall accompanying the cloud cover.

This rainfall has been shown to be very sensitive to the incoming flow speed. Both the area and the intensity of the rainfall can be impacted as stronger winds can severely

inhibit the generation of deep convection. This high sensitivity to wind strength has been noted by Kirshbaum (2011) who found that for a heated mountain incoming flow speeds of over 3 m s^{-1} were enough to completely inhibit deep convection. In the experiments here an incoming flow speed of 4 m s^{-1} was found to severely limit convection but not completely inhibit it. This difference can be attributed to the intensity of the surface heating – up to 60 K leading up to an $\mathcal{O}(10^3$ W $\mathrm{m}^{-2})$ sensible heat flux. However, in the experiments here, this is confined to a relatively small area (approximately 1×1 km), leading to a strong but very localised perturbation. Further away from the thermal anomaly the strength of the controlling parameters and the large scale flow (stability through the inversion and to a lesser extent a weak katabatic flow) as well as the mixing with drier air above the inversion quickly dilutes the plume, i.e. the storm dissipates if conditions become prohibitive. The dependence on the atmospheric conditions is clear when comparing the Dry-Strong Inversion and Wet-Weak Inversion simulations: a 10% increase in relative humidity and a 1 K decrease in inversion strength controls the initiation of any rainfall.

The resulting rainfall intensity ranges between a few mm hr^{-1} sustained for several hours up to bursts of 10 mm hr^{-1} sustained over shorter periods of time. Generally, rainfall over a threshold of 5 mm hr^{-1} is required to initiate volcanic hazards such as lahars or explosive activity (Barclay *et al.*, 2006). Thus, depending on the state of the dome this initialisation mechanism should be considered when dealing with hazard assessment, especially as it suggests lahars could be expected even on days when synoptic-scale rainfall is not forecast. It should be noted that although for the parameter space studied here the rainfall was generally advected away from the lava dome, the rainfall intensity is enough to increase the possibility of a rainfall-triggered dome collapse or pyroclastic flows and, due to the danger posed by the hazard, this possibility should generally be considered for days with low winds.

Both the convective plume and the resulting rainfall are in qualitative agreement with other studies where there is thermal forcing at the surface, e.g., associated with wildfires (Cunningham and Reeder, 2009) or solar heating (Kirshbaum, 2011). Conceptually the mechanism is the same for all cases, a strong thermal source causes convection that may be able to overpower the convective inhibition of the atmosphere. For wild fires a more

widespread (typically km in scale) thermal forcing leads to more widespread storms covering several square kilometers. For solar heating, the heating regime is usually weaker and the forcing is a function of the mountain height, thus the area of the perturbation is the area of the mountain – typically several kilometers wide (Tian and Parker, 2003; Crook and Tucker, 2005; Kirshbaum, 2011). In contrast, here the volcanic dome sets the scale of the storm.

4.5 Temporal evolution of the plume

So far, results have been presented for steady-state conditions. While the simulations certainly reach a quasi-steady state condition with the periodical repetition of a specific behaviour, some variability with time does exist. Note that as the temperature anomaly is introduced explicitly at the start of the simulations, the normal initialisation of the model and the initial response to the heating cannot be disentangled. Thus the focus of this section will be on studying the periodic cycle of generation of a perturbation and release via deep convection and cloud/rainfall generation, starting at $t = 3$ h using 10 min output data from the Wet-Weak Inversion simulation for $|U| = 1$ m s^{-1} and $T_a = 60$ K.

Figure 4.18 shows the temporal evolution of vertical velocity, total hydrometeor mixing ratio (cloud water, ice and rainwater), relative humidity, and turbulent kinetic energy versus height at a specific point ($x = -0.6$ km) along with a vertical cross-section across the middle of the domain for three different times. As seen in Figures 4.18a–4.18d, there is a periodicity in the behaviour of the plume – both the strength and the height of maximum w alternates between low and high values with a periodicity of approximately 20–30 mins. This is mirrored in the hydrometeor bevaviour and can also be partially seen in relative humidity (here the periodic behaviour is mainly seen in the height of the very high relative humidity layer). Turbulent kinetic energy is generally restricted to low values but is greatly increased as deeper convection is initiated. Overall this behaviour can be explained as follows: As fresh, moist air arrives (note that due to the lack of orographic rainfall the air has lost little of its humidity during the ascent), it is forced to ascend in the plume (Figure 4.18e). This causes condensation and the generation of a thick low cloud just above the inversion. With the influx of fresh air this initial cloud starts rapidly expanding (Figure 4.18f). During this expansion, rainfall is generated and vertical velocity

reaches a maximum, accelerating as it reaches higher altitudes in the troposphere. This generated cloud is then advected with the wind and the formation of a new cloud starts (Figure 4.18g). If deep convection is initiated, the cloud can travel up to 2–3 km but is very strongly mixed with the drier surrounding air before eventually dissipating. The period of this cycle is approximately 20 mins and this cycle continues with small variations throughout the post-spin-up simulation, until the end of the experiment. Note it also continues in the same way after 6 hours of simulations but as time progresses everything diverges as the inversion layer starts breaking up at later stages in the simulations. As an order of magnitude this period is consistent with cumulus cloud development timescales (Cuijipers and Duynkerke, 1993; Kirshbaum and Durran, 2004).

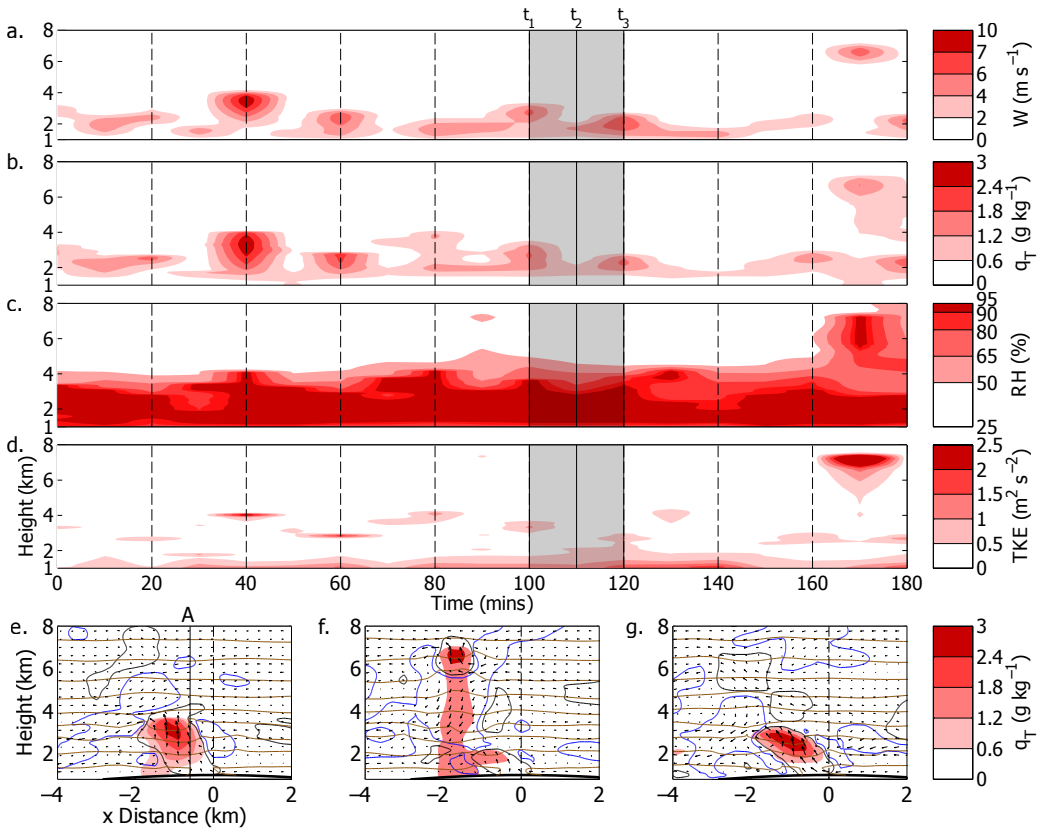

Figure 4.18: Panels a.–d. show the temporal evolution of: (a) vertical velocity, (b) total hydrometeor mixing ratio, (c) relative humidity, and (d) turbulent kinetic energy, versus height at point A, denoted in Panel e. Panels e.-g. show vertical cross-section of cloud water mixing ratio (shading) with vertical velocity (black lines for positive values, blue lines for negative values), potential temperature (brown line) and wind vectors overlaid for times t_1, t_2, and t_3 (shown in Panel f.). All results are from the Wet-Weak Inversion simulation. Time shown in minutes after 3h.

This convective cycle can be seen as similar to the one described by Kirshbaum

(2013). Studying deep convection initialised by thermal forcing in the Black Forest mountains in central Europe, Kirshbaum (2013) investigated several hypotheses for initialisation mechanisms and argued that instead of deep ascent of a single updraft, it is more likely that the convection is caused by a rapid succession of thermals vented through the convergence zone into a deepening cloud mass. Similarly in the simulations studied it was seen that each cycle started with a small core low in the atmosphere that eventually grows into a deep cloud before eventually the process runs out of "fuel", stops and the formation of the core starts anew.

Note that to further investigate the microstructure of the generated cloud and the evolution, very high resolution LES simulations (approximately $\mathcal{O}$(10m)) would be required, and these are beyond the scope of this study. Sensitivity runs conducted at a higher resolution ($\Delta x = \Delta y = 100$ m) revealed that despite some quantitative changes in the maximum values and the period of the cycle, the qualitative behaviour of the phenomenon was unchanged.

4.6 Discussion

Deep convection triggered by the lava dome was seen to have a cyclical temporal evolution. When studying the average response it was seen that the resulting storm was sensitive to various parameters, but to different degrees. These control parameters are now ranked depending on their potential to affect the storm (Table 4.2).

Control Parameter	Change	Effect	Justification
T_a	$\mathcal{O}$(20 K)	Primary	Controls the initialisation and rainfall response.
$\overline{RH}$	$\mathcal{O}(10\%)$	Primary	Controls the initialisation of rainfall.
$\lvert U \rvert$	$\mathcal{O}$(3 m s^{-1})	Primary	Controls rainfall regimes and initiation.
θ_I	$\mathcal{O}$(1 K)	Secondary	Does not force significant changes in rainfall.

Table 4.2: Ranking of control parameters by simulated impact for the changes of the size listed.

Significant changes were brought about by the temperature anomaly, by the increase in humidity, and by the incoming flow speed. Hence, these are noted as "primary" effects. The temperature inversion strength was generally not able to force significant changes in the resulting storm, so was labelled as "secondary". Note that this rationale holds for the order of magnitude of change shown in Table 4.2 – it is possible that smaller or larger changes in the parameters could yield different results.

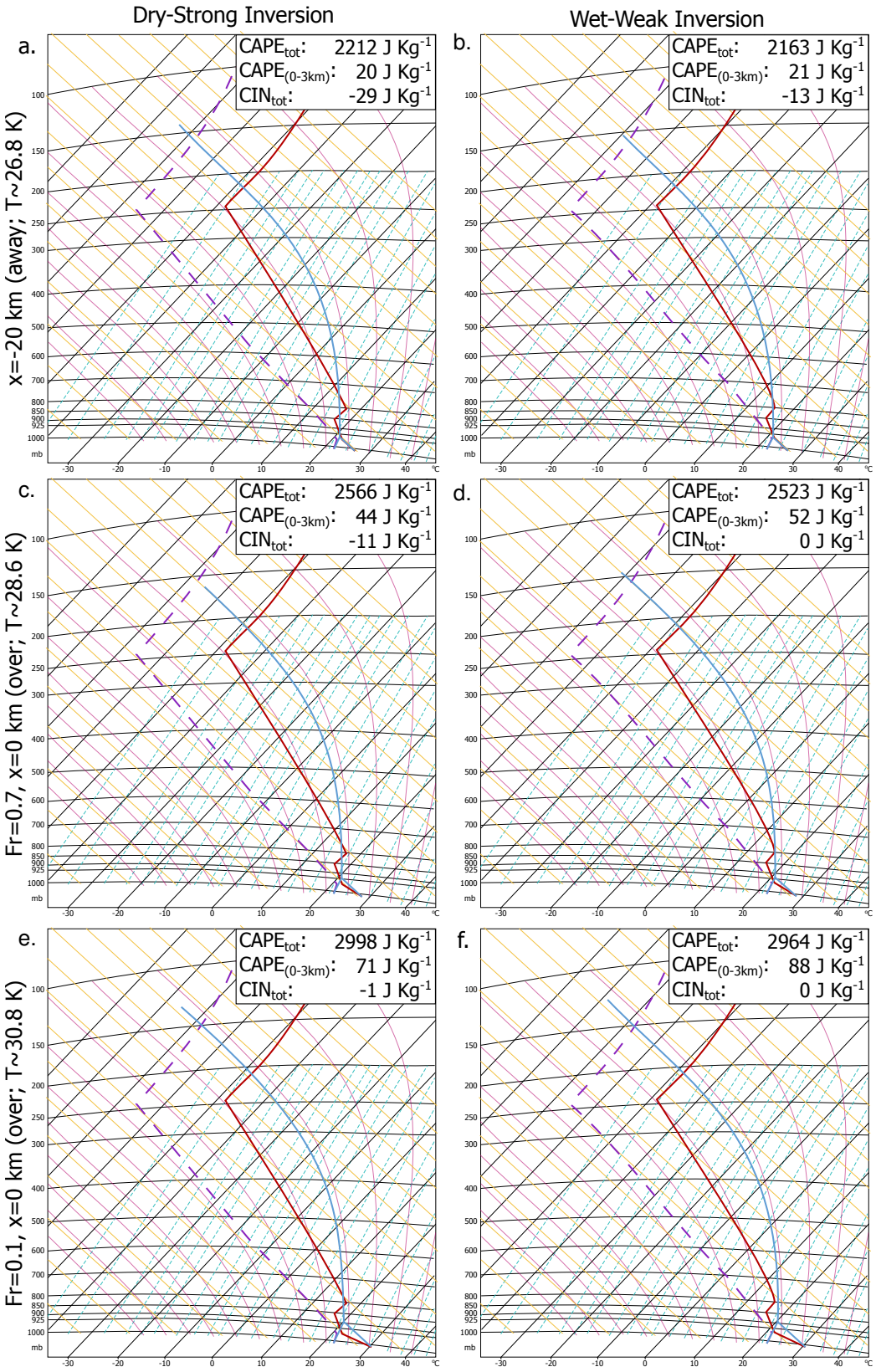

Figure 4.19: Representation of the (a,c,e) Dry-Strong Inversion and (b,d,f) Wet-Weak Inversion initialisation soundings in tephigrams "away" from the temperature anomaly (a,d) and "over" the temperature anomaly for two different incoming flow speeds: $|U| = 7$ m s^{-1} (c,d) and $|U| = 1$ m s^{-1} (e,f). Aside from tephigram lines, dewpoint temperature (dashed), temperature (solid, red) and the air parcel trajectory (solid, blue) lines are shown. Total CAPE, low-height CAPE and total CIN are calculated from RAOB.

Using a theoretical "air parcel" model applied locally at the lava dome can also help interpret the relative importance of some control parameters. To illustrate the points mentioned in the discussion, the RAOB software[1] is used to analyse air parcels at two points along the middle of the domain ($y = 0$ km): one at $x = -20$ km, over the sea ("away" from the dome; Figure 4.19a,d), and "over" the lava dome ($x = 0$ km) for two incoming flow speeds (Figure 4.19b,e for $|U| = 7$ m s^{-1} and Figure 4.19c,f for $|U| = 1$ m s^{-1}). The different incoming flow speeds were used as they led to different low-level heating of the atmosphere.

Profiles are prescribed from the initial soundings and a lower level temperature is set from model output. This is calculated as the average temperature from the lowest 2 model levels over hour 3 of the simulation. Initially, this temperature fluctuates due to turbulent mixing, but as the model reaches a quasi-steady-state, the temperature settles to an almost-constant value. This specific time was chosen as it coincided with the initiation of convection over the lava dome. The analysis was carried out for the Dry-Strong Inversion and Wet-Weak Inversion simulations (Figure 4.19).

All tephigrams show large or very large amounts of CAPE, for example, from 2212 to 2566 to 2998 J kg^{-1} for a location closer to the dome and lower wind speed (for the Dry-Strong Inversion case). As seen in the simulations, the *temperature anomaly* had the largest impact, as heating makes the air parcel buoyant and locally increases the CAPE (Figures 4.19a–c and 4.19d–f). As the surface thermal forcing increases, a larger area is heated over the threshold and starts convecting, increasing the area of the storm. Although not shown directly in the tephigram analysis (all tephigrams are shown for $T_a = 40$ K), this change is reflected in the storm area in Figure **??**a. Relatively small changes in the *inversion strength* do not affect the projected trajectory of a heated, very buoyant air parcel over the dome as the temperature difference of the parcel compared to the environment at the peak of the inversion is 2.5–3.5 K (Figure 4.19c,f). They result in very small changes in CAPE (334 J kg^{-1} over the dome).

Due to increased advection and turbulent mixing, an increase in *incoming flow speed* has a direct effect on the temperature over the lava dome – it rises from 28.6 C for $|U| = 7$ m s^{-1} to 30.8 C for $|U| = 1$ m s^{-1}. In this context increasing incoming flow speeds acts

[1] The RAwinsonde OBservation (RAOB) software is a multi-functional sounding analysis programme that can read radiosonde data, create sounding diagrams, and calculate forecast diagnostics. More information can be found at http://www.raob.com/

similarly to an decreasing thermal forcing. However, the full effect of wind speed (i.e. the switch from convective to orographic rainfall) extends beyond the simplified view of the atmosphere offered by air parcel theory.

An increase in *humidity* also has a large effect as it directly influences the lifting condensation level and indirectly influences the level of free convection and as a results the CAPE and CIN calculations. In the tephigrams the increase in humidity between the left and right columns leads to a decrease in CIN and increase in low-level CAPE. This can be used to explain changes in rainfall between the Dry-Strong Inversion (very little amount of rainfall for $|U| = 1$ m s^{-1}) and the Wet-Weak Inversion simulations (widespread convection for $|U| = 1$ m s^{-1}). However it should be noted that the calculations here are made using a surface value and thus the calculation only provide indicative results.

4.7 Summary

As moist atmospheric flow meets an obstacle, be that a mountain or a ridge, part of it is forced to ascend, which can lead to orographic precipitation. A moist flow can also interact with differentially heated terrain, as baroclinicity is created, forcing localised convection that can, under certain conditions, trigger deep convection and intense rainfall. What has been investigated here is whether a lava dome, a hot but small area on the summit of a volcano, can act to trigger deep convection on an isolated island impacted by moist easterly trade winds. A parameter space covering typical atmospheric conditions has been examined for a range of realistic volcanic surface temperature anomalies.

Depending on the prescribed conditions the volcanically heated dome can create a convective plume which penetrates through the tradewind inversion, resulting in a localised storm, with convergence into the plume from counter-rotating vortices and associated high rainfall rates. For the atmospheric conditions examined, a temperature anomaly of at least 20 to 40 K is required to trigger a volcanic storm. Changes in the surface temperature anomaly, the relative humidity profile and incoming flow speed strongly impact the rainfall location, distribution, and amount. In particular, volcanically-triggered rainfall is most distinct for low wind speeds ($|U| < 4$ m s^{-1}). Modest changes in the inversion strength have a secondary impact.

The simulations presented here are highly idealised. The effects of volcanic emissions, a source of both water vapour and cloud nuclei, as well as short and long wave radiation are not considered and simplifications of topography, heating and the atmospheric conditions have been made. Nevertheless care has been taken to keep the simulations realistic and general. As such, this kind of triggering of deep convection is possible for any active volcano, not undergoing an explosive eruption, provided that the forcing and atmospheric conditions are fulfilled. Consequently, the rainfall generation mechanism proposed here will affect the weather and climate locally and could have an impact on volcanic hazards such as pyroclastic flows, lahars or debris flows. Indeed this mechanism could offer an explanation for occurrences of volcanic hazards in days with little or no synoptic-scale rainfall in various volcanoes in the tropics.

Chapter 5

Deep convective rainfall over Montserrat and implications for volcanic hazards

5.1 Introduction

In the previous chapters an idealised approach has been taken for the problem of atmospheric flow over an active volcano. In Chapter 3, dry, highly-idealised simulations were presented to study the fundamental response with a minimum number of complicating factors; while in Chapter 4, moist processes were added to the simulations allowing a focus on precipitation. The main conclusion from the previous chapters was that a convective plume is created in response to the heated lava dome (an area of heating forced by a local anomaly in surface temperature). This plume can conditionally act to overcome convective inhibition and trigger a localised storm, leading to high rainfall rates. In both the previous chapters the topography was an idealised Gaussian-shaped mountain.

In this chapter, simulations are carried out over realistic topography, based on a high-resolution digital elevation model (DEM) of Montserrat. The aim of the chapter is to analyse the effect of this topography on the atmospheric circulation and associated rainfall (both convective and orographic), and discuss the implications for volcanic hazards in the Soufrière Hills Volcano (SHV), Montserrat – an active and much studied volcano. Although Montserrat is the focus here, many of the results can be generalised to other

tropical island settings, so are relevant for numerous active volcanoes.

As with any fluid, the interaction between the atmosphere and obstacles leads to numerous complex phenomena. In the case of mountains and ridges, it leads to gravity wave generation, flow blocking and reversal, and downslope winds amongst others, depending on numerous parameters controlling the problem (Smith, 1980; Smolarkiewicz *et al.*, 1988; Ólafsson and Bougeault, 1996). In the case of a moist atmosphere the forced ascent can often lead to orographic rainfall (Durran, 1990), while in some cases these localised perturbations can grow and lead to widespread instability and storms (Roe, 2005; Houze, 2012). Such effects play a major role in a humid, usually convective, tropical atmosphere, such as that over Montserrat, increasing precipitation in the winward side up to ten times compared to the sea (Kirshbaum and Smith, 2009; Smith *et al.*, 2009). The Tropics and sub-Tropics are characterised by Trade Winds – near-constant easterly winds stemming from the combined effect of the Hadley cell and the Coriolis force. Tradewind regimes often feature a temperature inversion in the vertical which acts as a barrier to widespread deep convection and the transition into mesoscale systems. This inversion often manifests itself via a field of scattered shallow cumulus clouds (Kirshbaum and Smith, 2009).

Dictated by the alignment of tectonic plates, at present, out of approximately 1500 volcanoes (Simkin and Siebert, 1994) almost half of active volcanoes are in the Tropics or sub-Tropics (Pareschi, 1996). A large number of these are on island arcs (e.g. the Caribbean Sea, Indonesia, etc). So for this first study of orographic flow response to a heated volcano SHV, Montserrat was chosen as the subject of study. The island of Montserrat is a British Overseas Territory, part of the Lesser Antilles in the West Indies, located in the Caribbean Sea. compared to other islands in the West Indies it is relatively small (16 km long and 11 km wide), has four main peak, the Soufrière Hills Volcano (SHV) being the tallest at 1050 m asl a the time of writing (Wadge *et al.*, 2014).

SHV is a relatively small Peléan lava dome complex (Rea, 1974). It has been active since 1995, with a series of devastating eruptions and active dome-building cycles over the last 20 years (Table 5.1) and has been one of the most intensively studied volcanoes of recent years. Since the start of the eruption it has caused 19 deaths and the destruction of settlements on the south part of the island, including Plymouth, the previous capital, and the original airport (Voight *et al.*, 1999; Robertson *et al.*, 2000). It is monitored by the

Montserrat Volcano Observatory (MVO)[1], stationed on the island. For a detailed overview of related research see Sparks and Young (2002) and Wadge *et al.* (2014).

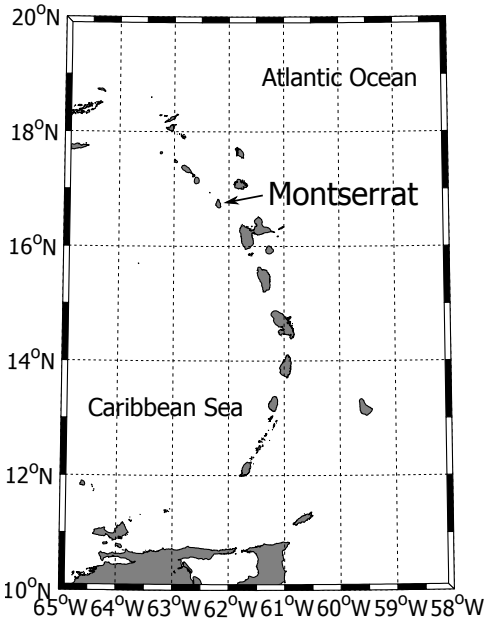

Figure 5.1: Location of Montserrat, West Indies (16.75° N, 62.20° W, approximately 16 by 11 km).

Phase	Dates	Duration (days)	Character
1	15/11/1995 10/3/1998	846	4 month precursory episode. Dome growth with collapses common
1-2		627	Dome collapses and mild explosive activity
2	27/11/1999 28/7/2003	1339	Largest dome built to date after two major collapses. Late increase in pyroclastic flows, ends in wholesale collapse
2-3		735	Very low residual activity until April 2005
3	1/8/2005 20/4/2007	627	Precursory phreatomagmatic. One wholesale collapse, ends with a large dome in place
3-4		465	Very low residual activity until May 2008
4	28/7/2008 3/1/2009	158	Two short episodes. Explosions and extrusion on western flank of dome
4-5		273	Very low residual activity until October 2009
5	9/10/2009 11/2/2010	125	Extrusion to the west, south and north. Explosions later. Ends in large north-directed collapse

Table 5.1: Eruptive history for for the SHV since the initial 1995 eruption. Modified from Wadge *et al.* (2014)

Dome-building volcanoes are a category of volcanoes that extrude high-viscosity magma through a central conduit. The magma cools and solidifies, blocking further flow up the conduit and forming a pressurised lava dome. This lava dome can become unstable, due to its own gravitational weight and internal pressure from within the volcanic

[1] http://www.mvo.ms/

system. Subsequent failure of the lava dome can lead to explosive dome collapse and pyroclastic flows. Heavy rainfall has been implicated in triggering such dome collapses and pyroclastic flows at a number of volcanoes, including SHV, Montserrat (Matthews *et al.*, 2002). Several mechanisms have been hypothesised for this rainfall triggering, including mechanical erosion of the surrounding talus fan and gravitational destabilisation of the dome, and the formation of a rainfall-saturated cap that blocks the upward flow of magmatic gas leading to a pressurised failure (Matthews and Barclay, 2004; Hicks *et al.*, 2010, 2014). Hence, any enhancement of rainfall by the heated surface of the volcanic dome may lead to a positive feedback, increasing the probability of these dangerous volcanic hazards.

Lava domes are mainly connected with two volcanic hazards: pyroclastic flows and lahars. A pyroclastic flow is a density current composed of hot gas and tephra that hugs the ground and travels downhill from the lava dome after an explosion (Figure 5.2a). The speed of a pyroclastic flow can reach 200 m s^{-1} and the temperature can reach 1000 K. Pyroclastic flows are thought to be the deadliest volcanic hazard, causing both damage to infrastructure and more than 36000 deaths in the 20th century (Tilling, 1989). Lahars are another category of lethal secondary volcanic hazards, with more than 28400 recorded deaths after 1900 (Figure 5.2b). A lahar is a mixture of water, rock fragments and pyroclastic material flowing down the slopes of a volcano (Smith and Fritz, 1989). It has the consistency of wet concrete and can carry material ranging from clay to 10 m boulders. The size and composition of a lahar can change drastically throughout its lifetime, starting out as a narrow flow but growing larger and deeper as rock debris is eroded and additional water is incorporated. Hence, a lahar can range between meters wide and centimeters deep, flowing with a speed of a few meters per second; up to hundreds of meters wide and tens of meters deep, flowing with a speed of several tens of meters per second.

The chapter is organised as follows. Initially a short description of the experimental setup is presented (Section 5.2). The results are presented in five sections. Control simulations are presented in Section 5.3 to allow for comparison with results from previous chapters. After this, the focus is on different characteristics of rainfall over Montserrat – convective ($|U| = 1$ m s^{-1}; Section 5.4); mixed ($|U| = 4$ m s^{-1}; Section 5.5); orographic ($|U| = 7$ m s^{-1}; Section 5.6) – and then changes to the overall impact of rainfall (both

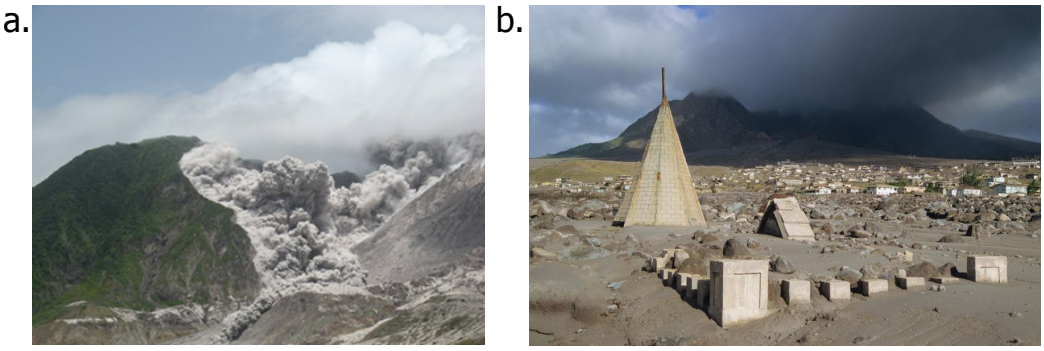

Figure 5.2: Common volcanic hazards in Montserrat. (a) Small pyroclastic flow above Perches Estate, Montserrat, July 2008. The dome is to the right. (Copyright by Greg Scott, Caribbean Helicopters) (b) Remains of Catholic Church, Plymouth, buried under pyroclastic material deposited from consecutive lahars, February 2006 (Copyright by Richard Roscoe, photovolcanica.com)

convective and orographic) on associated hazards on Montserrat (Section 5.7). Finally, there are conclusions in Section 5.8.

5.2 Experimental setup

The simulations presented in this chapter were carried out using the Weather and Research Forecast (WRF) model, version 3.3.1, running in idealised mode. WRF features a fully compressible, three-dimensional nonhydrostatic model, with the governing equations solved in flux-form. The model adopts an Arakawa-C grid, a time-splitting explicit advection scheme and a terrain-following height coordinate (Skamarock *et al.*, 2008). More information about the model can be found at the model's website at http://www.wrf-model.org.

5.2.1 Domain

The model domain consists of an isolated island (Montserrat) featuring the SHV, surrounded by ocean (Figure 5.3). The DEM used in the simulations was derived from data from the Advanced Spaceborn Thermal Emission and Reflection Radiometer (ASTER) mission[2] (Yamaguchi *et al.*, 1998). The 30 m resolution original data were regridded to 300 m resolution, smoothed and then imported into the initialisation code for the simulations. Note that the terrain appears altered due to the smoothing, both horizontally (area, horizontal detail) and vertically (height). Unfortunately, this is an inherent problem in high-resolution modelling over steep terrain (Lundquist *et al.*, 2010; Zhong and

[2]ASTER GDEM is a product of METI and NASA.

Katapodes-Chow, 2013). Although Montserrat does not have very high peaks, it is very steep (an increase of up to 900 m over 3 km in the windward side). This makes it unresolvable at high resolution using parameterisations currently available in WRF, unless a certain amount of smoothing is applied. Thus, care will be taken when presenting results, especially concerning the relative position of the catchments and the rainfall.

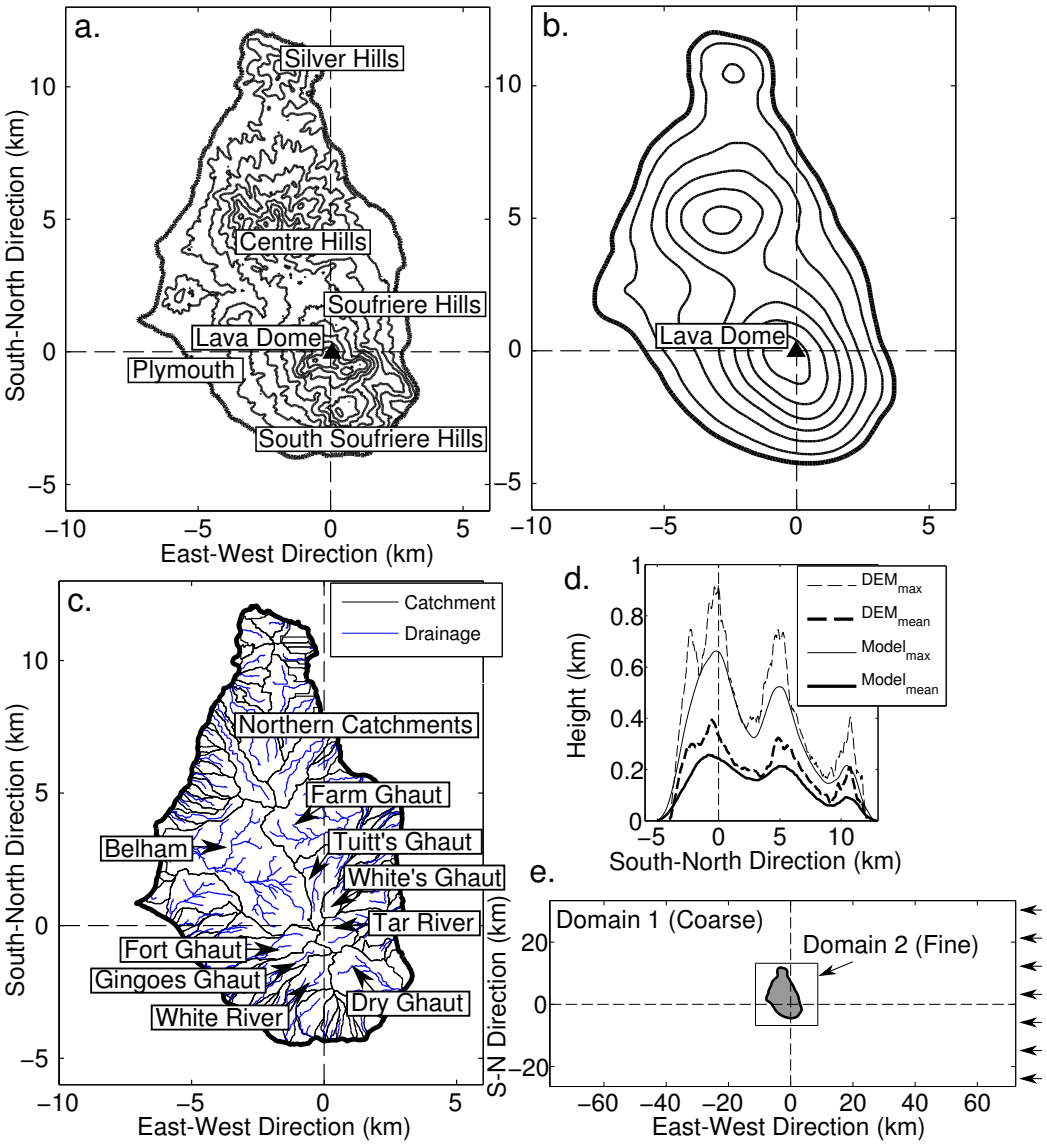

Figure 5.3: (a) ASTER-derived DEM for Montserrat. Contours every 100 m starting at 5 m. (b) Smooth topography used in the simulations. Contours as before. (c) Location of catchments and drainages, projected on the 5 and 100 m contour lines of the DEM used in the simulations (blue lines). (d) Comparison of average and maximum height (over the West-East direction) before (dashed lines) and after (solid lines) smoothing the topography. (e) The domains used in the simulations for easterly winds (indicated by the arrows). Grid points outside of the grey area are set as water.

In order to simulate the flow over this complex orography (Figure 5.3a) but keep computational time reasonable, a nested domain was used with a grid spacing of $\Delta x =$

$\Delta y = 300$ m [500×200 grid points representing 150 km in the x (West-East) and 60 km in the y (South-North) direction] for the coarse domain and a grid spacing of $\Delta x = \Delta y = 100$ m (200×200 grid points representing 20 km in both x and y directions) centred over the island. There are 147 levels in the vertical and the model top is at 16 km. A suite of physical parametrisations are implemented in WRF. These are identical to those used in Chapter 4. In keeping with the previous chapters the radiation and boundary layer schemes were switched off during the simulations (see Chapter 2 for details on the parameterisation choices).

The location of the various river catchments are presented in Figure 5.3b. These were calculated by Froude (2015), using a digital elevation model comprised of the 2010 topography of the Soufrière Hills at 1 m resolution based on LiDAR data (Cole *et al.*, 2010) plus 1983 topography of other volcanic centres on the Island of Montserrat (digitised from the Montserrat Tourist Map) and a 1999 theodolite survey of the Soufrière Hills lava dome at 10 m resolution (Wadge, 2004). The ArcMap 10.1 hydrology tool set was used to compile these data into a catchment database.

5.2.2 Experimental Design

The main objective of this chapter is to study both volcanically- and orographically-generated rainfall for the island of Montserrat. To achieve this, a number of different experiments with varying atmospheric structure, wind and surface temperature anomaly characteristics have been designed (Table 5.2).

Experiment Name	$\overline{\mathrm{RH}}$ (%)	θ_{I} (K)	$\lvert\mathrm{U}\rvert$ (m s^{-1})	Wind Dir. (°)	$\mathrm{T_a}$ (K)
Control	50, 60	307.2, 308.2	1, 7	90	0, 60
Convective	60	307.2	1	45, 70, 90, 110, 135	0, 60
Mixed	60	307.2	4	45, 70, 90, 110, 135	0, 60
Orographic	60	307.2	7	45, 70, 90, 110, 135	0, 60

Table 5.2: All simulations carried out for this chapter. $\overline{\mathrm{RH}}$ is the average relative humidity, θ_{I} is the potential temperature at a height of 2 km (the height of the inversion), $\lvert\mathrm{U}\rvert$ is the incoming flow speed and $\mathrm{T_a}$ is the surface temperature anomaly

In order to facilitate comparisons to previous results, initially, the simulations are carried out using the two idealised profiles from Chapter 4 – the Dry-Strong Inversion and the Wet-Weak Inversion soundings. After these initial experiments only the Wet-Weak Inversion profile was used, to allow for a more detailed investigation of the effect of other parameters: wind speed and wind direction. Note that, due to the large number

of simulations carried out for this chapter, results will be presented from a selected group of simulations per section.

5.2.3 Imposed temperature anomaly on the volcano summit

As in previous chapters, the surface temperature anomaly is specified at initialisation, by a Gaussian increase in the surface temperature towards the summit (Figure 5.4a). The equation for the temperature anomaly is:

$$T'(x,y) = T_a \ \exp\left[-\left(\frac{x-x_0}{W_x}\right)^2 - \left(\frac{y-y_0}{W_y}\right)^2\right] \tag{5.1}$$

where T' is the surface temperature perturbation, x_0 and y_0 are the coordinates of the lava dome's centre (the highest point of the smoothed DEM was chosen here), T_a is the maximum temperature anomaly (60 K) and W_x and W_y are parameters relating to the half-width (both were set at 900 m). The temperature anomaly is set in the coarse domain and the interpolated automatically in WRF for the fine domain. As the response of the flow to an incremental increase in T_a was studied extensively in previous chapters, here the simulations were carried out only for 0 and 60 K in order to focus on other control parameters.

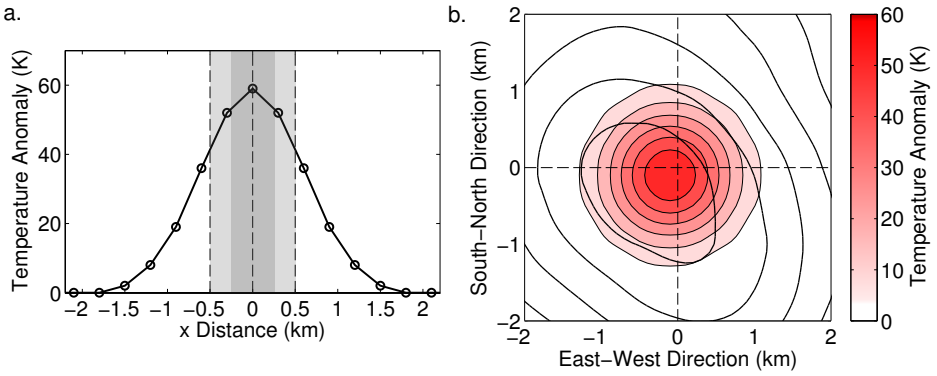

Figure 5.4: (a) Cross-section through the centre of the volcano showing surface temperature anomaly (surface temperature minus ambient surface temperature). The shaded areas show typical lava dome dimensions. (b) Horizontal contour plot of the surface temperature anomaly over the lava dome. Temperature anomaly contours every 10 K. Height contours starting at 200 m and every 100 m.

5.3 Montserrat control experiments

The aim of this section is to present and analyse results from selected control ($T_a = 0$ K) simulations and provide a comparison to idealised topography results of Chapter 4. Potential changes brought on by the use of the DEM and changes in the parametrisation and resolution are investigated. Results are shown for several incoming flow speeds ($|U| = 1$, 4, and 7 m s^{-1}, equivalent to $F_w = 0.1$, 0.5 and 1 calculated for a maximum height of 700 m) for a wind direction of 90° (easterly) and the Wet-Weak Inversion profile ($\theta_I = 307.2$ K, $\overline{RH} = 60$ %). The sensitivity of the results to other wind directions will be investigated in the following sections. All results here are shown from Domain 1 (coarse) in order to include parts of the flow away from the island and are 3h averages from hours 4–6.

Simulations of atmospheric flow over Montserrat show a varied response depending on the incoming flow speed: as easterly winds impinge on the island, for low $|U|$ there is very strong diversion of the flow ("flow around" regime), while for higher $|U|$ there is a shift towards a "flow over" regime (Figure 5.5). However, unlike flow over a simplified Gaussian mountain, Montserrat is made up by a series of peaks, with the most prominent ones being Soufrière Hills in the south, Centre Hills in the middle and Silver Hills in the north. This gives rise to a combination of terrain-related effects such as flow stagnation, channelling and gap flows.

For $|U| = 1$ m s^{-1}, the flow is very strongly diverted and flow reversal can be seen as a series of vortices are created in the lee (Figure 5.5a). Although there is a large degree of randomness in the number and orientation they generally act to bring the flow towards the centre of the island, illustrated by the streamlines. Despite the element of randomness, the overall effect is similar to the twin counter-rotating vortices for flow over a simple Gaussian mountain (Smolarkiewicz and Rotunno, 1989). Aside from flow diversion several areas of gap flow can be seen between the three peaks. This flow regime is also reflected in the vertical cross-section, when looking at the isentropes. As potential temperature is a preserved quantity, flat lines here point towards a flow forced to go around the island and not over (which would be shown by perturbed isentropes). Random convection can be seen all over the domain with the higher rainfall rates concentrated on the windward side and the lee of the island (Figure 5.5d). This flow regime will be referred to as "convective" for the rest of the chapter.

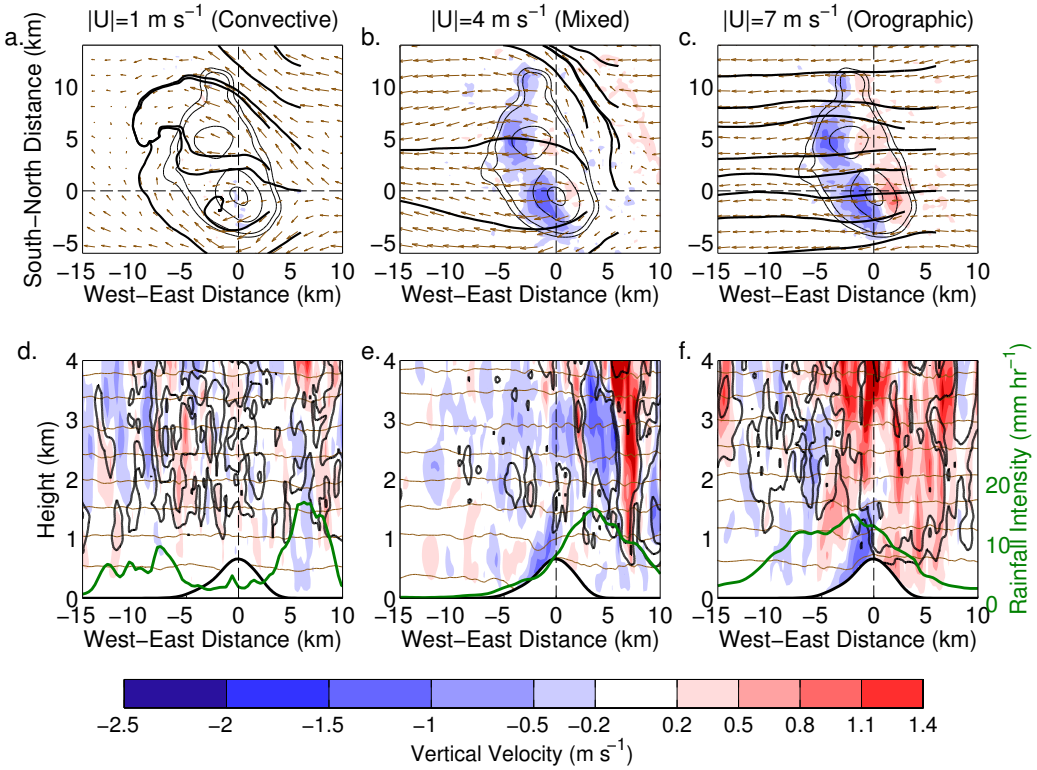

Figure 5.5: Results from the control runs ($T_a = 0$ K) for the Wet-Weak Inversion profile, and $|U| = 1$–7 m s^{-1}. (a)–(c) Vertical velocity (shading) with horizontal wind vectors; (d)–(f) vertical velocity (shading), isentropes (brown lines) and cloud water mixing ratio (black lines) on cross-sections through the middle of the lava dome. In (a)–(c) every 5th vector is plotted and height contours shown for 5, 100, 100, 350 and 600 m. Steamlines (thick black lines) starting at $x = 3$ and 6 km in the windward side are shown to emphasise the flow response. In (d)–(f) isentropes are every 2 K between 299 and 308 K, cloud water mixing ratio contours are at 2, 5, and 10 g kg^{-1} and rainfall intesity (mm h^{-1}) are plotted (in green) against the right-hand axis.

For $|U| = 4$ m s^{-1}, the flow response is similar as there is still very strong divergence on the windward side (Figure 5.5b), however there is a strong element of "flow over", especially in the southern part of the island. This is accompanied by an area of weak ascent on the windward side and strong descent on the lee. No lee vortices are visible here, possibly due to a combination of a relatively high moist Froude number ($F_W \sim 0.5$) and negative interference from the two peaks, however there is weak convergence towards the centre of the island in the lee and a weak wake area mainly concentrated between the two southern peaks. Long island wakes like this are a ubiquitous feature in islands in the Caribbean (Smith *et al.*, 1997). In the vertical cross-section, a number of shallow clouds can be seen mixed with deep convective clouds found mainly over the coastline and the windward side (Figure 5.5e). This is possibly a mixed results of the weak flow over the mountain, along with frictional convergence (Roeloffzen *et al.*, 1986; Kirshbaum and

Smith, 2009). This cloud cover is reflected in the very strong rainfall ($R > 10$ mm hr^{-1}) located over the windward side. The katabatic flow and wave activity (both mountain waves and lee-side waves) can be seen in the lee, however this response is weak due to the instability in the atmosphere. This flow regime will be referred to as "mixed" from now on.

For $|U| = 7$ m s^{-1}, the flow has switched to a "flow over" regime (Figure 5.5c). Some elements of the "mixed" regime can be seen over the island and in the lee (gap flow between the peaks, and a slight convergence along with a wake on the lee), however there is no divergence on the windward side. In the vertical, there is now a very strong response to the mountain as deep convection is triggered consistently over the windward side (Figure 5.5f). This instability spills to the leeside of the island and wave response is now very strongly mixed with the general convection. Also, due to a combination of relatively high Froude number (close to 1) and an aspect ratio close to 2, the flow is still expected to be in the non-linear regime with wave breaking apparent according to the diagram by Smith (1989), presented in Chapter 1 (Figure 1.3a). High rainfall rates can be seen covering the entire island, with the peak located over the windward side due to advection.

Horizontal rainfall intensity contour plots add further evidence to the flow regimes as described previously. For the "convective" regime ($|U| = 1$ m s^{-1}) deep convection can be seen at random across the domain, covering some areas of the island, but mainly concentrated over the sea (Figure 5.6a). This is due to a combination of the flow being diverted from the island, and the lack of moist fluxes over the island. For higher incoming flow speeds the relative timescales negate this effect but for the very low wind speeds here this can potentially affect results. Rainfall in the lee of the island can be attributed to lee-side convergence as in Chapter 4 (Figure 4.5), however, rainfall here appears to generally be more controlled. This could be due to the increase in resolution, for example Kirshbaum and Smith (2009) noted that increased resolution led to decreased rainfall, but it can also be attributed to the differences in the orography. In the "mixed" regime ($|U| = 4$ m s^{-1}), heavy rainfall rates are concentrated on the windward side of the island, and over the northern part, possibly as the flow is able to flow over the relatively short terrain and Silver Hills (Figure 5.6b). Compared to results from Chapter 4 (Figure 4.5) the

more consistent rainfall in the windward side can definitely be attributed to the orography as, unlike the Gaussian mountain studied in Chapter 4, there is strong flow splitting in the windward side. Finally, in the "orographic" regime deep convective rainfall covers the entire island with very high rainfall rates ($R > 10$ mm hr^{-1}) concentrated close to the two main peaks (Figure 5.6c).

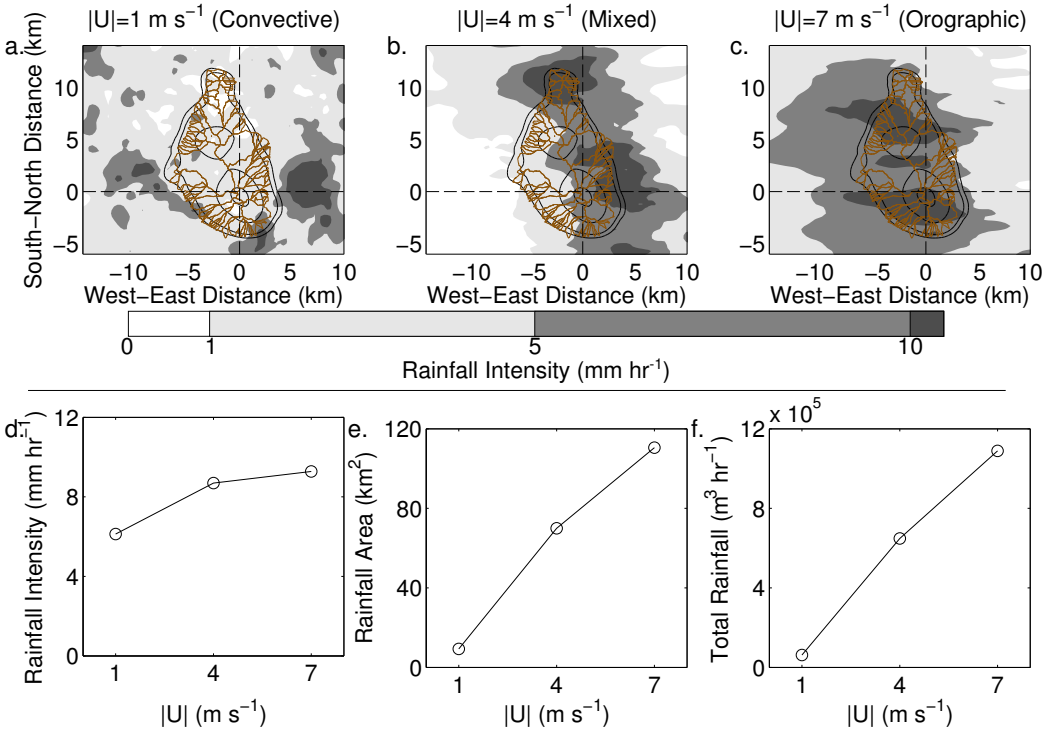

Figure 5.6: Results from the control runs ($T_a = 0$ K) for the Wet-Weak Inversion profile. (a)–(c) Horizontal plots of rainfall intensity for $|U| = 1$, 4, and 7 m s^{-1} (respectively), with terrain height (black lines; contours are 50, 100, 350, and 600 m), and the catchment in Montserrat (brown lines) overlaid. (d) Average deep convective rainfall intensity over the island (only $R > 5$ mm hr^{-1} taken into account), (e) Area that receives rainfall with $R > 5$ mm hr^{-1}, and (f) Total rainfall over the island.

Deep convective rainfall characteristics are presented in Figure 5.6d–f. Only areas with $R > 5$ mm hr^{-1} are taken into account in the calculations here as in most of the cases the entire island is covered with rainfall of $R > 1$ mm hr^{-1}. All characteristics increase as the incoming flow speed increases. Average rainfall intensity over the island (Figure 5.6d) is close to 5 mm hr^{-1} for the convective case as deep convection is limited over the island but reaches a plateau close to 10 mm hr^{-1} for other cases. As noted in Chapter 4 (Section 4.4.1.2) this is due to the fact that deep convective rainfall rates are mainly controlled by the atmospheric structure – once triggered it remains relatively unaffected by the orography. Rainfall area (the area of the island that receives rainfall

with $R > 5$ mm hr^{-1}) increases from 10 km^2 (less than 10% of the island) to 70 km^2 and then to 110 km^2 in the "orographic" regime, covering 100% of the island (Figure 5.6e). The almost linear increase is mirrored in the total rainfall volume (Figure 5.6f).

Results presented here correspond well to previous studies of similar tropical island settings (e.g. Kirshbaum and Smith, 2009; Minder *et al.*, 2013; Cécé *et al.*, 2014), however heavier rainfall is seen here due to the use of the Wet-Weak Inversion profile which allows for more consistent deep convection in the simulations. Results are also similar to those presented in Chapter 4 (for example see Figures 4.4–4.5). Rainfall rates on the windward side differ slightly from the results of the previous chapter, here stronger rainfall is more consistently generated and it is generally stronger over the land. This is caused by the use of the realistic DEM and is in agreement with other studies of islands in the Tropics (for example Kirshbaum and Smith, 2009). Montserrat is not a circular island and its more elliptic shape, coupled with the steep angle of the slopes, creates more of a barrier and forces a larger part of the flow to go over the topography, creating a more intense perturbation to the flow, and resulting in higher precipitation rates (Kirshbaum and Durran, 2004). Another, possibly smaller, source of quantitative differences is the change in the resolution in the experiments here. Grid-size sensitivity is a known issue of numerical weather prediction models and results for the rainfall produced for any given setting are known not to converge for grid resolutions between 300 and 100 m (Bryan *et al.*, 2003). Between the change in the shape and the change in the resolution, quantitative differences in the results can be expected but they do not affect the main qualitative results.

Finally, it must be noted that due to smoothing the shift towards the "flow over" regime might be slightly overemphasised. On average there is an approximately 30% decrease in the height of the mountains (with the top of Soufrière Hills reduced to 700 m from 1000 m), so in reality results might be representative for a 30% higher incoming flow speed. This is an insignificant increase for low $|U|$ but becomes more significant for higher values, i.e. results for $|U| = 7$ m s^{-1} could be seen as more representative of 10 m s^{-1}. This is reflected by the increase in the Froude number – there has been a change from $F_w = 0.7$ in Chapter 4 to $F_w = 1$ here. As mentioned previously, this is a practically unavoidable issue due to an inherent issue that eta-coordinate models have with flow over steep topography (Lundquist *et al.*, 2010; Zhong and Katapodes-Chow,

2013).

Note that simulations were also carried out using the Dry-Strong Inversion profiles and they were qualitatively similar to the ones presented in Chapter 4 – the flow response is the same, with mountain waves appearing more pronounced due to the stronger stability, however rainfall was limited in the high $|U|$ cases and the windward side of the island. As the focus here is on deep convection generation, and especially triggering by the lava dome, the focus on the rest of the chapter will be on the Wet-Weak Inversion profile results.

5.4 Convective Rainfall Regime ($|U| = 1$ m s^{-1})

The sensitivity of the volcanically-generated storm to the impinging wind direction is now evaluated for $|U| = 1$ m s^{-1}. Note a change in wind direction is analogous to a change in the topography encountered by the flow. Results are presented for $T_a = 60$ K simulations, using the Wet-Weak Inversion profile, for three different wind directions, $WD = 45°$, $90°$, and $135°$. Ten simulations were carried out in total for 5 wind directions (45°, 70°, 90°, 110° and 135°), using the Wet-Weak Inversion profile and $T_a = 0$ K and 60 K. The wind direction values were approximately the average, the average plus and minus one standard deviation and the maximum and minimum wind direction encountered using the soundings from Guadeloupe (see Figure 2.12b). Again, results are 3hr averages for hours 4–6, but results are now shown from Domain 2 (fine) and focused over the island to show localised changes in greater detail.

Note that during the experiments presented here, instead of changing the wind direction in the prescribed input sounding, the DEM data were rotated and input at the appropriate angle. This was done to ensure that the background wind was always perpendicular to the upwind boundary for accuracy, and to keep the computational time relatively short. Although all horizontal plots are re-oriented so that the y-axis points S–N, some vertical cross-sections are following the original model coordinates across the wind direction. In these cases the x-axis is marked as "Model x Distance".

A change in wind direction can be seen to have a very strong influence in the general circulation (Figure 5.7). It creates different areas of ascent and descent and shifts the overall circulation. Similar changes of rainfall patterns depending on the mountain shape

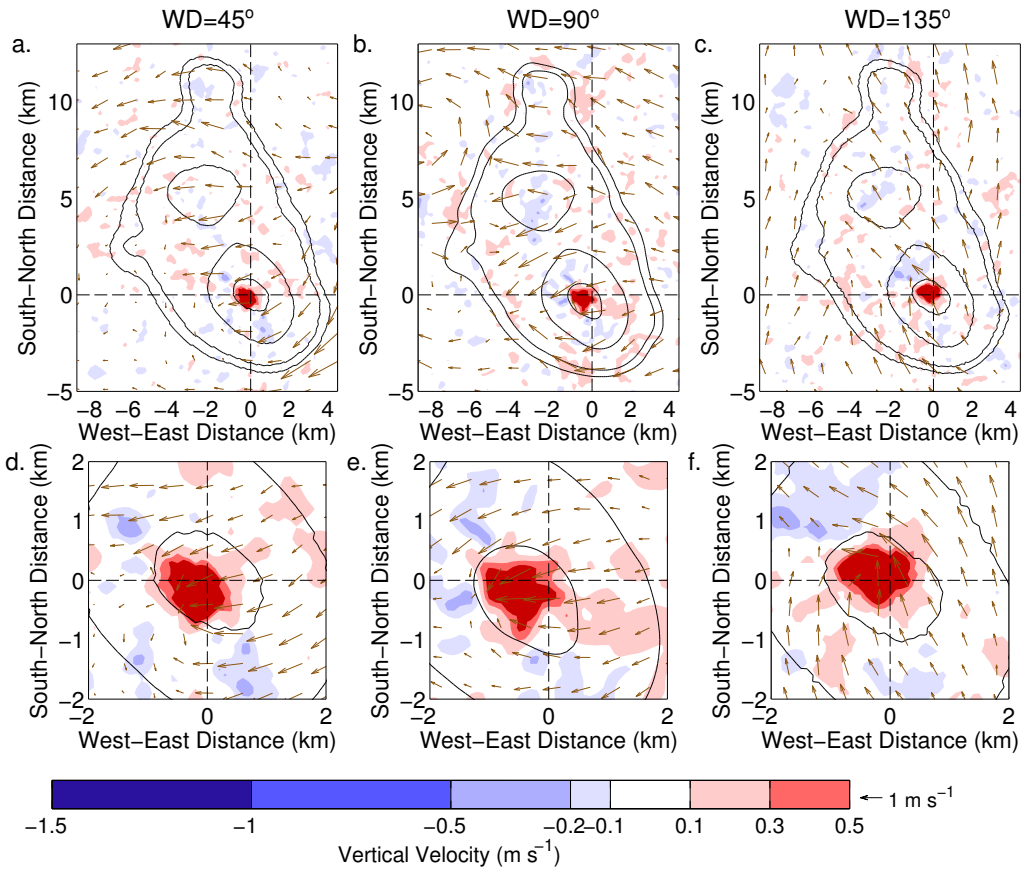

Figure 5.7: Results from the $T_a = 60$ K simulations, using the Wet-Weak Inversion profile, for $|U| = 1$ m s^{-1}. Vertical velocity (shading) with horizontal wind vectors and height contours (black lines) shown for 1, 100, 500 and 900 m for a wind direction of: (a) 45°, (b) 90°, and (c) 135°. (d)–(f) As previous but focused on a 2 × 2 km area over the lava dome.

have been investigated in various studies (for example Watson and Lane, 2014). For $WD = 45°$ the flow impinges on the island at an angle. As expected, this causes flow splitting, however the characteristics of the flow splitting are now very asymmetrical: in the northern part of the island, wind vectors are tilted to an easterly direction, while in the southern part the turn in the wind vectors is less apparent (Figure 5.7a). A gap flow can once again be seen between Centre and Soufrière Hills and channelling can be seen south of the island, as the diverted flow converges with the non-diverted flow. Lee-side vortices can be seen south-west of the island. As in previous chapters, the hot lava dome introduces a localised area of convection that acts to draw in the surrounding flow (Figure 5.7d). The effect of this convective plume is once again limited to a 1 × 1 km area. For $WD = 90°$ the flow strongly resembles the control case (Figure 5.5a) with the exception of the area over the lava dome (Figures 5.7b,e). Differences in some of the characteristics of the flow can be seen, for example the lee vortex in the north of the island

appears stronger here, but these are due to the element of randomness in the flow and the quantitative results is the same. Note that the area of convection over the lava dome is not exactly facing towards 90° and has a small southward tilt. This effect is caused by the general circulation enforced by the orography. The $WD = 135°$ case differs from the previous two as the flow is now oriented across the length of the island (Figure 5.5c,f). As expected from the flow there is divergence in the windward (south-west) side, with the flow in the west side of the island turning to a southerly wind, however there is also strong channelling, mainly across the west side and at points the flow turns towards the island (for example at $x = -5$ km and $y = -1$ km). This can be the effect of random convection that can locally alter the flow, however it can also be cause by weak rotor activity due to the angle at which the flow impinges on the island. The main lee-side vortices can be seen in the north-west side of the island. Note that the area is now reduced compared to the previous cases.

Rainfall generation follows the general flow patterns seen previously (Figure 5.8a–c). Away from the dome rainfall generation appears relatively random in all cases, with large areas of consistent rainfall generated in the lee of the island for $WD = 90°$ and 135° (Figure 5.8b,c). In the vicinity of the lava dome, strong rainfall is generated consistently, covering a 2×2 km area over and in the lee of the temperature anomaly. As noted previously, there is a small influence by the topography but the orientation of the rainfall patch is largely dictated by the wind direction. The volcanically-triggered rainfall can also be easily identified in the rainfall plots along the wind direction (Figure 5.8d–f). As in the control simulation (Figures 5.5d and 5.6a) rainfall is more consistently triggered away or over the coastline, however now there is an additional peak starting over the lava dome and extending for 2–3 km in the lee. Results here are similar to ones presented in Chapter 4 (Figure 4.10), however as in the control simulation, rainfall generation appears more controlled. The average background value of approximately 1 mm hr^{-1} across the domain matches the value found by Derbyshire *et al.* (2004) in a study of deep convection across different models for a relative humidity of 90%. Note that rainfall intensity in the vicinity of the lava dome is consistently over 5 mm h^{-1} (the threshold for the initiation of explosive activity; Matthews *et al.*, 2009) and at parts over 10 mm h^{-1} the threshold for quick lahar generation used in Montserrat (MVO, personal communication).

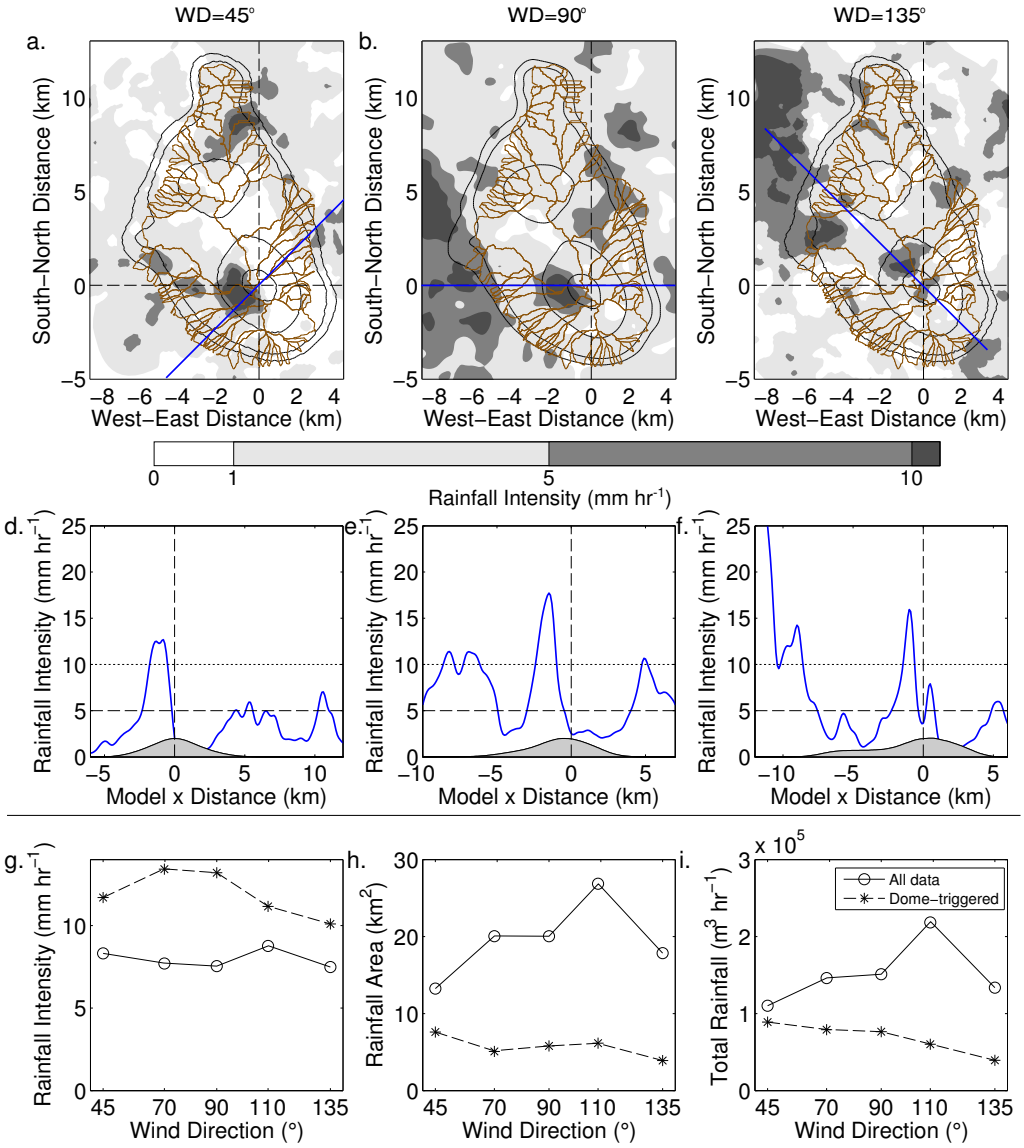

Figure 5.8: Results from the $T_a = 60$ K simulations, using the Wet-Weak Inversion profile, for $|U| = 1$ m s^{-1}. Horizontal plots of rainfall intensity (shaded) for with height contours (black lines) shown for 1, 100, 500 and 900 m and catchments (brown lines) overlaid for a wind direction of: (a) 45°, (b) 90°, and (c) 135°. (d)–(f) Vertical cross-section across the lava dome shown in the direction of the wind (at 45, 90, and 135 degrees respectively). (g) Average deep convective rainfall intensity over the island (solid line) and volcanically-triggered (dashed line), (h) Area that receives rainfall with $R > 5$ mm hr^{-1}, and (i) Total rainfall volume. Note, only $R > 5$ mm hr^{-1} taken into account for the calculations.

Characteristics of the rainfall over the island as well as volcanically-triggered rainfall are now studied for all 5 wind directions (45, 70, 90, 110, and 135 degrees). For rainfall to count as "volcanically-triggered" the same criteria apply as they did in Chapter 4 – after subtracting the results of $T_a = 0$ K simulations the rainfall anomaly needs to be *long-lasting* and *located in the vicinity of the lava dome*. As previously, only $R > 5$ mm hr^{-1} is

considered. As discussed many times average rainfall intensity is one of the more consistent characteristics and appears relatively insensitive to changes in the wind direction (Figure 5.8g). Averaged over time, rainfall intensity is higher for the volcanically-triggered part as it is more consistently triggered. Rainfall area is more changeable characteristic, increasing for the overall rainfall and decreasing for the volcanically-triggered rainfall (Figure 5.8h). For $WD = 45°$ volcanically-triggered rainfall accounts for more than 50% of the total rainfall over the island, while for $WD = 135°$ this decreases down to approximately 25%. As with the control simulation, the total rainfall volume is mostly influenced by the rainfall area. Overall, results here are both qualitatively and quantitatively similar to results previously presented in Chapter 4 (for example Figure **??**). Although results are generally similar for all wind directions there is some variability in the area of the volcanically-triggered rainfall: averaged across the five wind directions the area is approximately 4.5 ± 1.7 km^2. This is most likely due to a combination of the effects of the orography and the stochastic nature of rainfall generation in the model.

In general, the simulations produce results that are consistent with previous chapters. The effect of the surface temperature anomaly fade out over a small distance and the circulation over the island is typical for a flow with a small Froude number. While the general qualitative response is the same as Chapter 4, there are differences due to the use of a realistic DEM, with complex interactions between the plume-induced circulation, gravity waves and the topography. However, this does not seem to affect the resulting rainfall anomaly caused by the lava dome in a significant way. Overall, the combination of the use of realistic topography, an increase in resolution create some changes over the generated rainfall but the main results remain both qualitatively and quantitatively similar. Note that, as in Chapter 4, simulations using the Dry-Strong Inversion profile showed a weak response to the surface heating, however the average rainfall intensity over the simulation was less that $R > 1$ mm hr^{-1} – deep convective bursts occurred, but were not consistent enough to have an important effect.

5.5 Mixed Rainfall Regime ($|U| = 4$ m s^{-1})

The "mixed" rainfall regime is now examined. As with Section 5.4 results are presented for 3 different wind direction, at $WD = 45°$, 90°, and 135° for the Wet-Weak Inversion

profile and $|U| = 4$ m s^{-1} ($F_w = 0.5$). Looking at the general atmospheric circulation over the island, results follow theoretically expected patterns: in all cases there is a degree of flow splitting on the windward side and convergence in the lee (Figure 5.9a–c). The strongest flow splitting occurs for $WD = 45°$ in the north of the island where wind vectors turn easterly and for $WD = 135°$ in the west where wind vectors turn southerly. Flow splitting for $WD = 90°$ is less intense than the control case, signifying a small degree of variability in the simulations. Lee vortices can only be seen for $WD = 45°$ in the south-east side of the island. As noted previously, this different behaviour can be expected from basic orographic flow theory (Smith, 1989). For $WD = 45°$, the relative aspect ratio of the island to the flow is almost 2 and wave breaking in the lee can be expected. On the other hand, for $WD = 135°$ the relative aspect ratio is now close to 0.5 and the flow is expected to be in the linear regime (Figure 1.3a in Chapter 1).

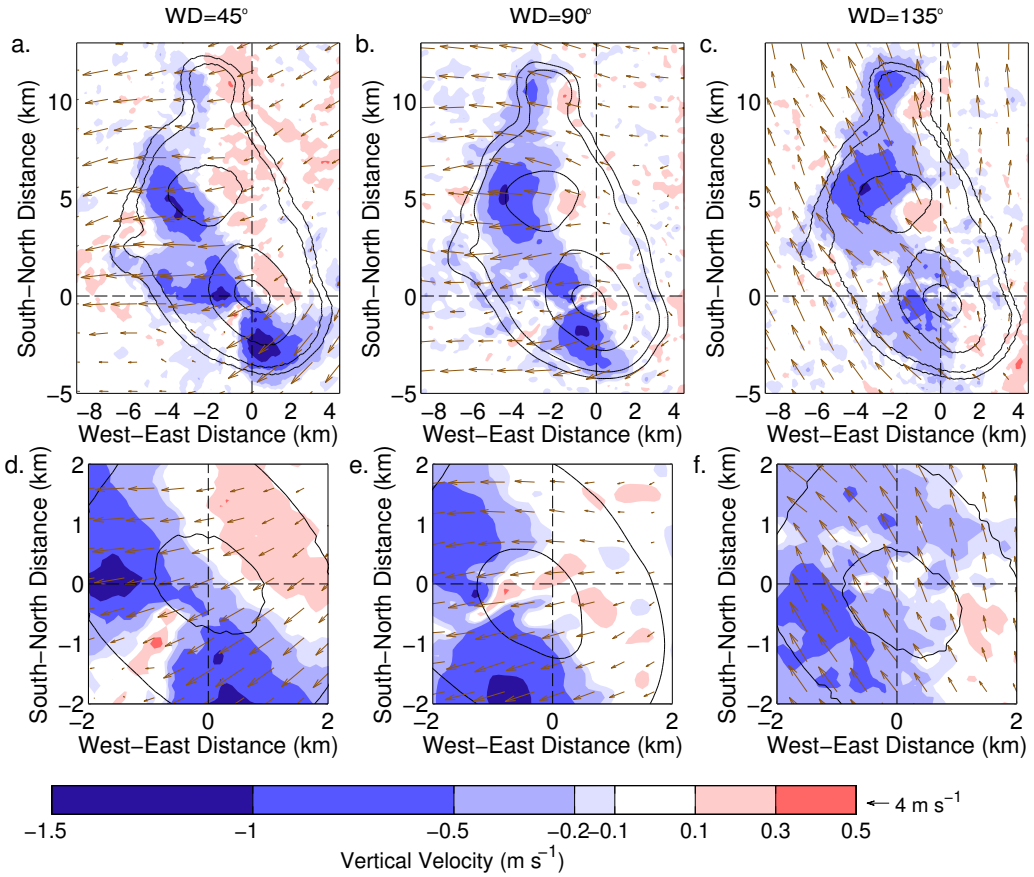

Figure 5.9: As Figure 5.7 for $|U| = 4$ m s^{-1}.

Close to the lava dome, the convective plume is now strongly influenced by the wind. The area of the plume is decreased to approximately 0.5×1 km, advected downwind

and elongated across the general direction of the wind. Unlike the results from the "convective" regime, it is also affected by the orography: in most of the cases the convective plume can be seen to be slightly off-centre from the average wind direction in the area. This is due to the destructive interference between the plume and the downlope winds in the lee. This effect was previously seen in Chapter 3 (for example Figure 3.17), but here it appears off-kilter due to the asymmetry of the terrain and the relative position of the lava dome with respect to the mountain slopes.

Once again, the circulation over the island can be used to explain the occurring rainfall patterns (Figure 5.10a–c). As in the control simulation, deep convective rainfall is largely confined to the windward side. The largest area of deep convective rainfall is generated in the west of the island for $WD = 135°$, possibly due to the fact that due to the northerly component in the wind, much of the flow occurs over the lower slopes and deep convection is more consistently triggered. As seen in Figure 5.9b, flow splitting in the windward side is less intense that the control runs. This is reflected here as less rainfall is generated over the north of the island (Figure 5.10).

As in Chapter 4, volcanic triggering of rainfall is greatly decreased for this wind speed. Looking at rainfall intensity across the wind direction (Figure 5.10d–f), small areas of volcanically-triggered rainfall can be identified for $WD = 90°$ and 135°, approximately 3–5 km downwind of the lava dome, while any response is heavily mixed with orographic rainfall for $WD = 45°$. As previously, average rainfall intensity over the island is relatively independent of the wind direction with an average value of approximately 10 mm hr^{-1} (Figure 5.10g). Volcanically-triggered rainfall on the other hand ranges between 1–4 mm hr^{-1}. This is in agreement with results as seen previously and shows the large impact orography can have once a certain incoming flow speed threshold is passed. Volcanically-generated rainfall is now a very small percentage of the total rainfall ($\sim$ 1–2%), with the total area of the island that receives $R > 5$ mm hr^{-1} now increased to approximately 50 km^2 (Figure 5.10h). However, as noted in Chapter 4, even though rainfall intensity is significantly decreased, it is still an important effect that needs to be considered as the location of this extra rainfall is now on the lee of the island where rainfall is not expected. As previously, the trend is reflected in the total rainfall volume (Figure 5.10i).

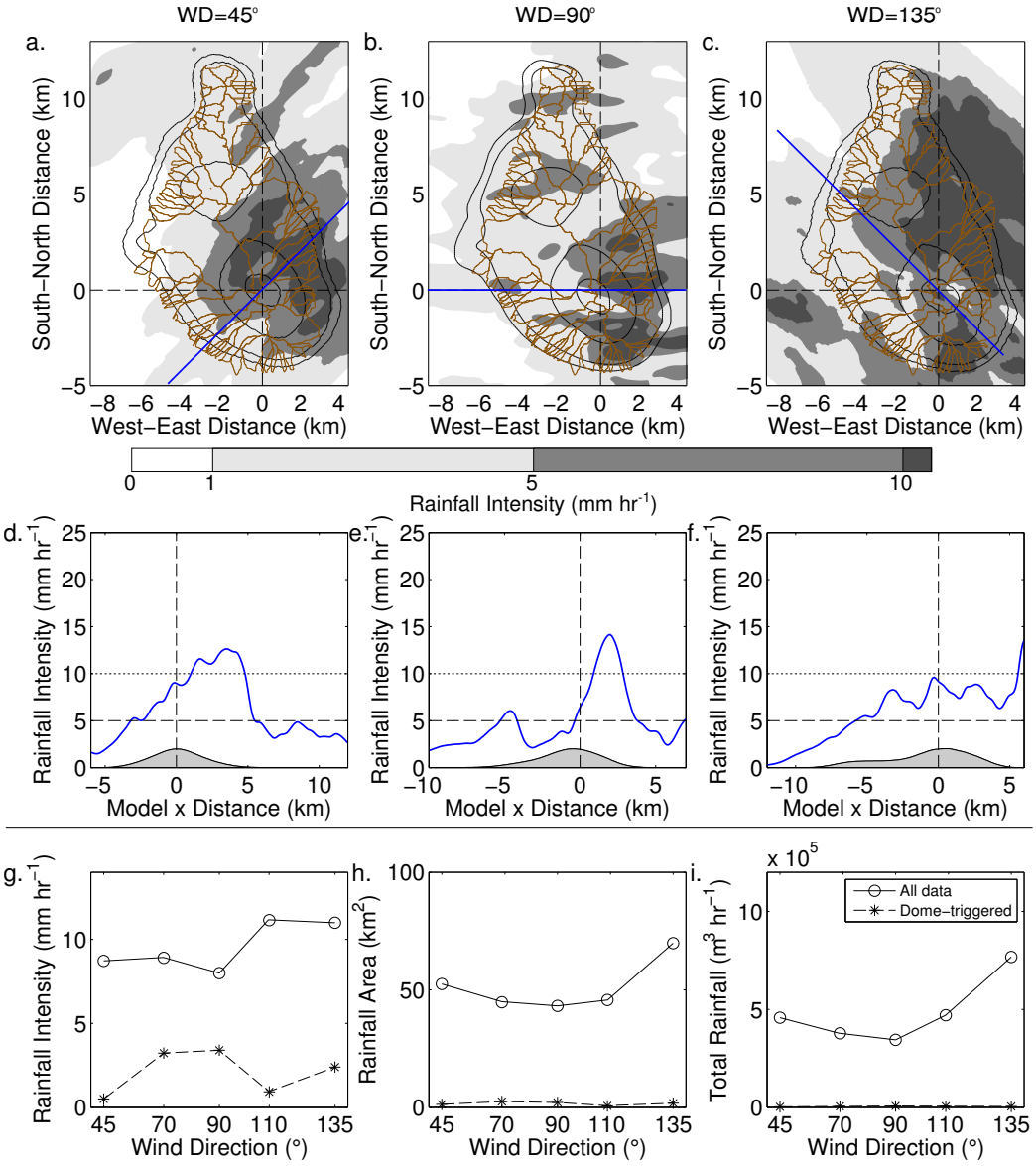

Figure 5.10: As Figure 5.8 for $|U| = 4$ m s^{-1}.

5.6 Orographic Rainfall Regime ($|U| = 7$ m s^{-1})

The "orographic" rainfall regime is now considered. As expected for a Froude number of 1 the island has a smaller impact in the flow for all wind directions (Figure 5.11a–c). As in the control simulation, interaction with the orography is still visible at parts, for example small divergence on the windward side of the hills, a small degree of gap flow and channelling between hills and a wake in the lee of the island, however the wind vector remain fairly consistent and close to the original wind direction. The change towards the "flow over" regime can be seen in all cases, marked by the extended area of ascent in the respective windward side of the island. Over the lava dome the effect of the increase

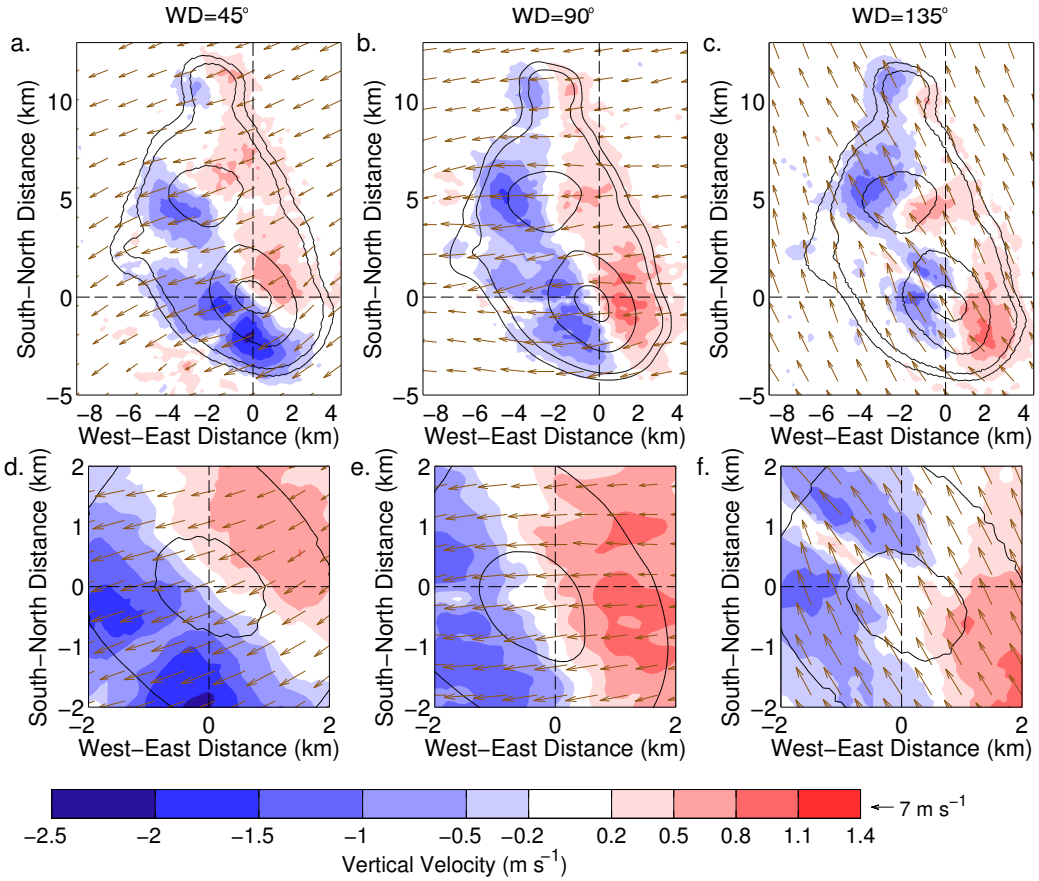

Figure 5.11: As Figure 5.7 for $|U| = 7$ m s^{-1}.

in wind speed is stronger advection and greater reduction in the strength of the plume (Figure 5.11d–f).

Rainfall generation has also switched towards an "orographic" regime (Figure 5.12a–c). As in the control simulation a large part of the island is covered with rainfall over 5 mm hr^{-1} and rainfall rates over 10 mm hr^{-1} can be seen over and in the lee of the mountain peaks. Along the wind direction the rainfall distributions are now relatively uniform along the three cases, with peak rainfall rates located over the crest or on the lee of the island (Figure 5.12d–f). Note that, horizontally, the position of the rainfall peak values sometimes appears off-centre when compared to the peak of the mountains (for example Figure 5.12c). This is due to the combined effect of channelling and convergence (visible in Figure 5.11c). Average rainfall rate over the island is relatively unchanged for all wind direction and is less that the "mixed" regime case. This can be explained as stronger wind (i.e. the vertical wind shear between the boundary layer and the free troposphere) is now acting against single-cell deep convection (Schlesinger, 1973). Volcanically-triggered rainfall is greatly decreased with an average rainfall intensity close

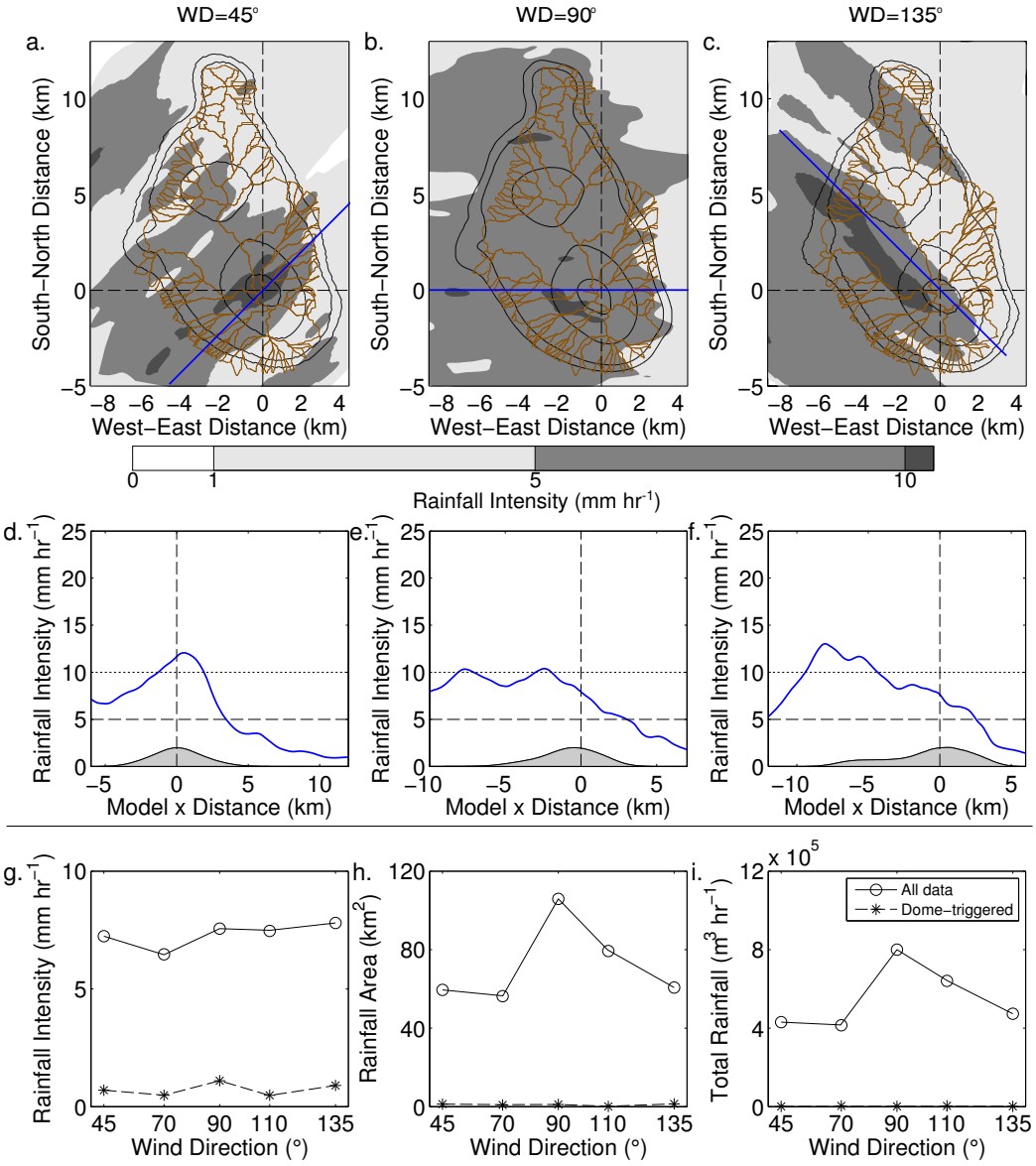

Figure 5.12: As Figure 5.8 for $|U| = 7$ m s^{-1}.

to 1 mm hr^{-1} (Figure 5.12g), similar to results in Chapter 4 (Figure 4.16). The overall significance of this rainfall is greatly decreased as rainfall over 5 mm hr^{-1} is consistently triggered over the island. This is further illustrated in Figures 5.12h and 5.12i. The percentage of the volcanically-triggered rainfall area is now decreased to less than 1%. Interestingly, the total area of the island that receives rainfall over 5 mm hr^{-1} changes considerably between the simulations, ranging between 60 and 110 km^2 – between 55 and 100% of the total area, possibly due to the angle at which the incoming flow meets the island.

Overall, results here are typical for a small island located in the Tropics (Minder *et al.*, 2013; Cécé *et al.*, 2014), however, as noted before, higher than typical rainfall rates are

caused by the use of the Wet-Weak Inversion profile. As far as volcanically-triggered rainfall, it is consistent with existing literature [for example Kirshbaum (2011)] where it was found that advection by the wind plays a major role in inhibiting the generation of deep convection. For a weak incoming flow a strong and robust response can be seen in the generated rainfall. However as the wind increases, this response becomes weaker and more susceptible to influence from the orography. Finally for strong winds ($|U| > 7$ m s^{-1} the rainfall response becomes insignificant. Results were also seen to be consistent between the control and temperature anomaly simulations and also largely consistent with simulations previously presented in Chapters 3 and 4. The use of a realistic DEM adds a significant component of complexity in the resulting rainfall patterns as well as a degree of variability in the results. These findings are summarised in Figure 5.13.

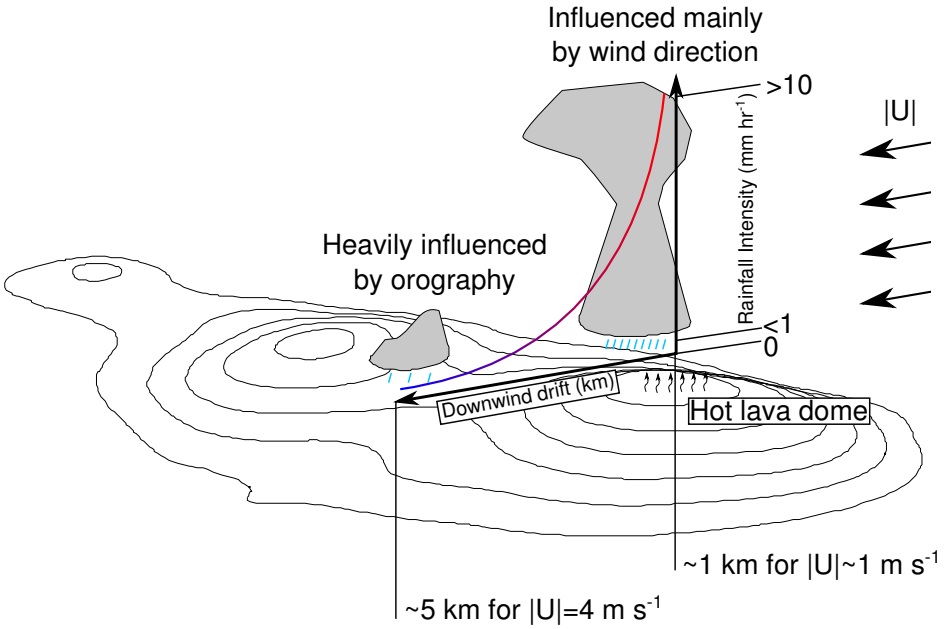

Figure 5.13: Schematic summarising the main findings of the study. As the flow impinges on the island a very strong response can be seen close to the lava dome for low wind speeds. For higher wind values this volcanically-triggered rainfall is advected downwind and the response is weakened.

5.7 Implications for hazard risk assessment in Montserrat

Studying of the volcanically-generated storm has shown (among other findings) that: for low wind speeds, very strong rainfall is triggered close to the lava dome and is relatively unaffected by changes in the terrain, while for stronger wind this response weakens, and

becomes increasingly susceptible to advection and local orographic effects. These findings will be used to investigate the impact volcanically-triggered rainfall could have on volcanic hazards in Montserrat, mainly focusing on lahar generation. For this purpose results from all thirty simulations are used (Wet-Weak Inversion simulations with $T_a = 0$ and 60 K and $|U| = 1$, 4, and 7 m s^{-1} and $WD = 45°$, 70°, 90°, 110°, and 135°). Lahar generation is a complex process, depending on factors such as the time between the eruption and rainfall, antecedent rainfall and the intensity and duration of the triggering rainfall (Major and Newhall, 1989; Froude, 2015), factors that are beyond the scope of investigation here. However a threshold rainfall rate of 10 mm h^{-1} for lahar triggering is given as an approximate value by the MVO and this will be used here.

In order to estimate which catchments would be affected under the common wind conditions, results from different wind direction were averaged for each value of incoming flow speed. These results were plotted over the catchments in Montserrat: each catchment was assigned a colour depending on the amount of rainfall it would receive, red for rainfall over 10 mm hr^{-1}, green for rainfall over 5 mm hr^{-1} and white for anything less than that (Figure 5.14). For a catchment to count as being affected, at least 1 km^2 of the catchment needed to be covered by rainfall.

Overall the results here reflect those presented in Sections 5.4–5.6. In the control runs, for $|U| = 1$ m s^{-1} none of the catchments consistently received more that 10 mm hr^{-1} of rainfall across the different wind directions and the most commonly affected catchments are situated along the coastline, including Farm Ghaut and most of the northern catchments (Figure 5.14a). For $|U| = 4$ m s^{-1} (Figure 5.14b), a large number of catchments in the windward side are now expected to receive more than 10 mm hr^{-1}, including Dry Ghaut, Tar River, White's Ghaut, Tuitt's Ghaut, Farm Ghaut, as well as half of the northern catchments situated towards the west (see Figure 5.3c for locations). The lee side is less affected with some of the catchments expected to receive 5 mm hr^{-1} (White River, Gingoes Ghaut, Fort Ghaut, Belham and the rest of the northern catchments) and the rest expected to receive less than 1 mm hr^{-1}. For $|U| = 7$ m s^{-1} (Figure 5.14c) most of the island is expected to receive 5 mm hr^{-1} for any wind direction. The more heavily affected catchments are not situated towards the centre of island, surrounding Soufrière Hills (Fort

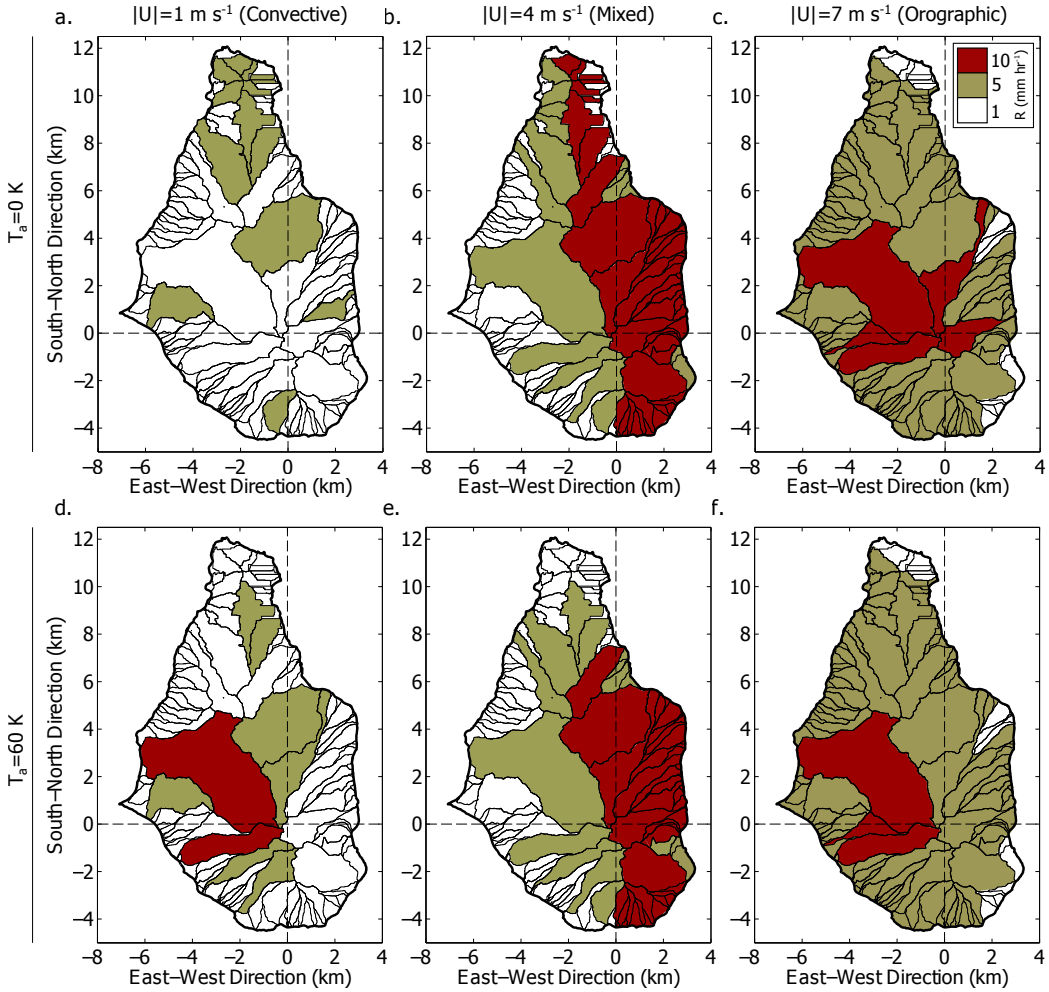

Figure 5.14: Catchments affected by the lava dome-generated rainfall. Catchments in red were seen to receive rainfall over 10 mm hr^{-1}, while catchments in green received rainfall over 5 mm hr^{-1}. All results are averaged over 5 different wind direction. First row: Control simulations ($T_a = 0$ K) with $|U|$ = (a) 1, (b) 4, and (c) 7 m s^{-1}. Second row: Temperature anomaly simulations ($T_a = 60$ K) with $|U|$ = (d) 1, (e) 4, and (f) 7 m s^{-1}.

Ghaut, Belham, Tuitt's Ghaut, and Tar River). As noted previously, aside from lahar generation this regime is also important when considering rainfall-triggered volcanic activity (Matthews *et al.*, 2009).

As seen throughout the chapter, the largest impact lava dome heating has is for low wind speeds (Figure 5.14d). There is a considerable change in the affected catchments as Fort Ghaut in the south-west and Belham in the north-west of the lava dome are now expected to receive 10 mm hr^{-1} for most of the common wind directions. Other catchments surrounding the lava dome are also susceptible to volcanically-triggered rainfall, including Gingoes Ghaut and White River in the south and Tuitt's Ghaut in the north. As expected, for stronger winds (Figure 5.14e–f) the impact of the lava dome is lessened

and is indiscernible for results averaged over the different wind directions. Comparing control and temperature anomaly simulations results show a small variability in the affected catchments, but the main results are similar – heavy rainfall is concentrated in the windward side for $|U| = 4$ m s^{-1} and over the centre of the island for $|U| = 7$ m s^{-1}.

Validating these results is a difficult task and would require extensive fieldwork. Even for the MVO, gathering concrete data about lahars in Montserrat every day is a nearly impossible task due to the number of rivers and the fact that usually lahars occur simultaneously, making accurate recording by seismography impossible. However, visual verification of lahars that fit the description (resulting from persistent localised rainfall in the vicinity of the lava dome) was provided by the MVO, especially for the Fort and Gingoes Ghauts (MVO, personal communication). Futhermore, Froude (2015) studying lahar activity in Montserrat has also argued that consistent rainfall over the Belham catchment might have been the reason for the change in the area of the catchment in recent years – an extension towards the lava dome.

In order to provide a guide to aid the MVO, a handout is compiled to assess the possibility of volcanically-generated rainfall for a given day (Figure 5.15). As this is aimed at a non-atmospheric science audience, care was taken to introduce all aspects discussed and simplify it as far as possible. An effort was made to choose diagnostics directly available from atmospheric soundings made available at the University of Wyoming website[3]. As the main forcing for the rainfall is the surface temperature anomaly, this was chosen as the first check. If the thermal forcing is large enough, the second check is whether the atmosphere is sufficiently humid and that there is instability at a relatively low height. The *mean mixed layer mixing ratio* parameter is calculated as the mean value for the mixing ratio up to a height of 500 m. This gives an indication about the humidity content of the lower atmosphere. In the Tropics (surface pressure of 1013 hPa and a temperature 300 K) an average mixing ratio of 18 g kg^{-1} is equivalent to 85% relative humidity in the boundary layer. In the sounding analysis in Chapter 2 this was the average minus one standard deviation for the relative humidity (so $\sim 33\%$ of the soundings will have MMLR$>$18). The threshold for the *level of free convection* was chosen to represent the atmospheric characteristics in the study here. Finally, the convective inhibition in the atmosphere (CIN, or CINS here) is checked to ensure that the the convective plume will

[3]http://weather.uwyo.edu/upperair/sounding.html

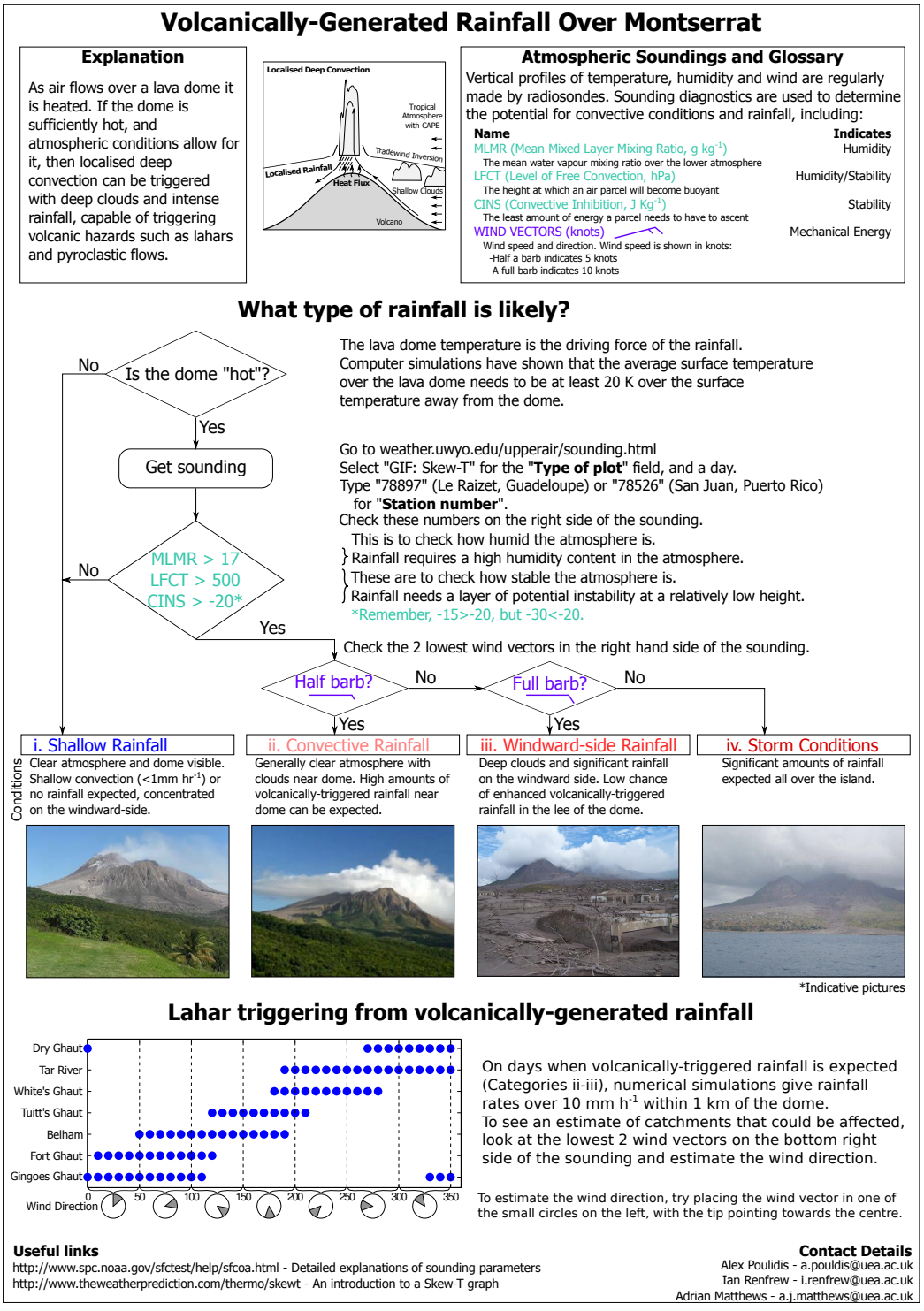

Figure 5.15: A handout detailing the necessary conditions for volcanically-triggered rainfall to be made available to the MVO. To be printed as an A4 or A3 size poster.

be strong enough to trigger deep convection (-20 J kg^{-1} was the amount of CIN in the Dry-Strong Inversion profile). If any of the parameters is below the threshold no rainfall is expected (*Category i* – Shallow Rainfall). Results from the Dry-Strong Inversion presented in Chapter 4 would representative in this case. Based on the sounding study

(Chapter 2, Section 2.6), 63% of the soundings fall into this category.

If all parameters are above the threshold, deep convective rainfall is possible and the *wind speed* close to the surface is checked. For half a barb (5 knots or 2.5 m s^{-1}) this leads to "*Category ii* – Convective rainfall". This limit was chosen as it would lead to the category when volcanically-triggered rainfall has the strongest impact according to the study here and represents the results presented in Section 5.4. Out of the soundings studied, 5% belonged to this category. If the wind is over this threshold, a final check is made. If the wind vectors have a full barb (10 knots or 5 m s^{-1}) this leads to (*Category iii* – Windward-side Rainfall; 10% of soundings, representing the results in Section 5.5) and if its over that to Category iv (Storm Conditions; 22% of soundings, Section 5.6). The percentages calculated here correspond well to the climatological study findings of Dunion (2011). Estimated from the data presented there, percentages for each category would be: Category i: 57%, Category ii: 4%, Category iii: 14%, and Category iv: 25%.

As seen in Section 5.4, a change in the wind direction introduces small changes in the rainfall area, as well as rainfall intensity for low $|U|$. Hence, in order to estimate the catchments that would be affected for any wind speed a 2D rainfall distribution was created based on data from simulations for the 5 available wind direction. This was placed in the lee of the lava dome and rotated from 0–350°, while making note of catchments that would receive more that 10 mm hr^{-1}. The results from this are presented in the lower part of the handout.

Note that this is an empirical guide based on initial estimations from the model experiments conducted during the study and other relevant studies. Based on the soundings studied in Chapter 2, the categories are distributed evenly amongst the 4 categories, with 11% of days displaying potential for volcanically-triggered rainfall. Note that this analysis is based only on the atmospheric soundings, the lava dome temperature – a very discriminating factor – is neglected as long-term data are not available. Due to the large number of experimental parameters in the study, sensitivity to some parameters (such as low-level relative humidity) has not been thoroughly examined. In short, the guide is indicative of likely volcanically triggered storm occurrence, it should not be viewed as definitive.

Even though the study here has been limited to Montserrat and SHV there are numerous volcanoes in the Tropics where this mechanism can occur. In order to use the results

directly, a number of conditions need to be met: it needs to be an *active*, *dome-building* volcano close to the *Tropics*, with a *height* comparable to SHV (below the tradewind inversion). Using the Smithsonian Institution Global Volcanism database[5], several volcanoes with these criteria are found in several locations such as the Caribbean, Nicaragua, Costa Rica, Mexico, Indonesia and the Philippines (Table 5.3). If the location requirement is eased, another match is the Shinmoedake peak in the Kirishima volcano, located in the island of Kyushu in Southern Japan (31.54 N, 130.53 E). It is an active dome-building volcano with recent activity and a height of 1421 m. Although it is north of the Tropics it is still located in a very humid area, with heavy rainfall and lahars.

Name	Country	Location (°)	Height (m)	Latest Eruption (CE)
Arenal	Costa Rica	10.4 N, 84.7 W	1670	2010
Batur	Indonesia	8.2 N, 115.4 E,	1717	2000
Camiguin	Philippines	9.2 N, 124.6 E	1552	1953
Concecion	Nicaragua	11.54 N, 85.6 E	1700	2011
La Soufrière	St. Vincent	13.20 N, 61.11 W	1234	1979
Momotombo	Nicaragua	12.4 N, 86.5 W	1297	1905
Pelee	Martinique	14.8 N, 61.2 W	1394	1932
San Cristobal	Nicaragua	12.7 N, 87.0 E	1745	2014
Soufriere	Guadeloupe	16.0 N, 61.7 W	1467	1977
Soputan	Indonesia	1.1 N, 124.7 E	1784	2012

Table 5.3: List of monitored dome-building volcanoes matching the requirements for volcanically-generated rainfall. Criteria were: i. Existence of lava dome, ii. Latitude $< 23°$, iii. Height < 2000 m, iv. Latest eruption after 1900 CE.

If the dome-building criterion is disregarded there is a number of volcanoes that could be affected mainly in the Philippines, Malaysia, and Indonesia. Examples of volcanoes of comparable height (up to approximately 2 km) that have had activity in recent years and are situated near populated areas include Bulusan, Philippines, and Kelut and Tangkuban-parahu, Indonesia. The analysis has shown that volcanically-triggered rainfall can occur for very low surface temperature anomalies (as low as 20 K). Diffusion of heat in non-lava dome-building volcanoes is very different and a "surface temperature anomaly" cannot be used in the direct way it was used for dome-building volcanoes, but it can be expected that a volcanically-generated rainfall can be triggered in days with a large-scale convective system when a small temperature perturbation by the volcano could act to focus rainfall over the volcano. For volcanoes without a lava dome this could still act to trigger lahars in the lee of the volcano (an area usually protected by the rainfall shadow) as well as non-lava dome related eruptions such as the ones observed in Merapi, Indonesia (Voight *et al.*,

[5]http://www.volcano.si.edu/

2000) and Piton de la Fournaise, Reunion Island (Violette *et al.*, 2001). As the focus of the study here was dome-building volcanoes, further study would be needed to make a correct assessment of this possibility. Taller volcanoes, with the summit above the usual tradewind inversion (> 2 km) can also be studied in this context.

5.8 Summary

The impact of volcanically-generated rainfall for the island of Montserrat has been presented. A series of high-resolution simulations were carried out in order to simulate the flow and rainfall over the island. The change from an idealised mountain to a realistic topography, as well as an increase in grid resolution to 100 m allowed for the testing of the sensitivity of volcanically-triggered rainfall to one new, important parameter – the wind direction. There were changes to the convective core of the plume, but these changes were found to have little effect on the rainfall generated for low wind speeds ($|U| \sim 1$ m s^{-1}). For moderate winds ($|U| \sim 4$ m s^{-1}), the additional rainfall was found to be sensitive to the larger scale orographic flow while higher winds ($|U| \sim 7$ m s^{-1}) where seen to greatly inhibit this effect.

Results for the most common wind directions have shown that two major catchments on Montserrat can be affected by volcanically-triggered rainfall of $R \sim 10$ mm hr^{-1} (Fort Ghaut and Belham) while three can consistently receive volcanically-triggered rainfall of $R \sim 5$ mm hr^{-1} (Gingoes Ghaut, White River and Tuitt's Ghaut). It must be noted, though, that the simulations are still idealised and thus can only be used to provide a first-order estimate of the impact. Despite the fact that data covering lahar generation is difficult to gather in Montserrat, the results broadly agree with what has been seen by the volcanic observatory: lahars triggered in the lee of the dome by heavy localised rainfall.

Using the theoretical analysis of the air parcel model allows for an easy way of estimating days with a high risk of a volcanically-triggered storm and thus a checklist for assessing the possibility of volcanically-generated rainfall for any given day has been compiled for potential use by the MVO and other observatories. Although only Montserrat was considered for this study, the results can be generalised for all volcanoes in the Tropics and sub-Tropics, approximately 45% of all active volcanoes. This effect would thus need to be considered for appropriately sized volcanoes, especially on days without

predicted synoptic-scale rainfall, when heavy localised rainfall could trigger an unexpected hazard.

Chapter 6

Conclusions and future work

6.1 Summary

The interaction of the atmosphere and a hot volcanic lava dome has been studied via a series of high-resolution numerical simulations using the WRF model. A tropical, oceanic setting was used in the simulations with varying degrees of idealisation. In this chapter, the main findings are summarised and future work is suggested.

6.1.1 Dry atmospheric flow over a volcano

In Chapter 3, highly-idealised numerical simulations were used to study the fundamental response of the atmosphere to surface heating from a lava dome – the hot summit of a volcano. The simulations were carried out for several different incoming flow speeds and surface temperature anomaly values.

The heated surface of the volcano triggers a strong convective plume over or on the lee of the lava dome. This response is very localised (typically order of 1 km from the dome) due to the spatial extent of the lava dome but is a very resilient feature, remaining unaffected by the incoming flow speed for most of the simulations. The plume is accompanied by a pair of counter-rotating vortices on the lee side, acting to draw air towards the base of the plume, while the top of the plume acts as "virtual terrain", forcing the flow to go over or around it and triggering a secondary set of gravity waves. The height of the plume depends on the strength of the surface temperature anomaly and reaches a height approximately determined by its equilibrium potential temperature. The thermal

circulation, its structure and associated gravity waves depend on the incoming flow speed (or Froude number) and the strength of the temperature anomaly.

After categorising the results, a regime diagram for dry atmospheric flow over a volcano has been produced. Three regimes were identified – "no plume" (advection stronger than convection), "vertical plume" (convection stronger that advection), and "enhanced rotors" (in-between regime). The most common flow was the no plume regime followed by the strong plume regime depending on the balance between convection and advection, i.e. the surface heating against the Froude number. For low incoming flow speeds and a strong surface temperature anomaly the plume was seen to produce its own convective circulation, but its effects diminish as the incoming flow speed increases. Under increasingly stronger incoming flow speeds the plume was also seen be tilted towards the lee side or dissipate, becoming effectively ventilated by the wind.

6.1.2 Moist atmospheric flow over a volcano

In Chapter 4, numerical simulations were used to study the response of a more realistic, moist atmosphere, based on the atmospheric structure of the Tropics. Although still highly idealised, Montserrat, a volcanic island in the Caribbean, was chosen as a template. The main aim of the simulations was to test whether the convective plume previously seen in the dry simulations was strong enough to counteract low-level convective inhibition (in the simulations manifested by a tradewind inversion) and force the flow into a regime of deep convection with associated convective precipitation. For this purpose a complex, multi-dimensional parameter space was investigated, covering typical atmospheric conditions, temperature inversion strengths and realistic volcanic surface temperature anomalies.

The response was once again the generation of a convective plume. After a threshold surface temperature anomaly value, this plume was seen to break through the tradewind temperature inversion, resulting in localised deep convection over and in the lee of the lava dome, accompanied by high amounts of rainfall. For low winds this rainfall was triggered close to the lava dome. The rainfall rates produced were large but typical for the simulation of deep convection (Kirshbaum and Durran, 2004). Advection by the wind was seen to push the area of rainfall away from the lava dome, but it was never seen to form into a large-scale system.

Three characteristics of this volcanically-triggered rainfall were analysed: rainfall anomaly area, total rainfall anomaly, and rainfall anomaly intensity. The first two were seen to be proportional to the strength of the surface forcing and all characteristics were influenced heavily by the humidity content and the incoming flow speed. For conditions that were not conducive to convection ($RH \sim 80\%$ in the boundary layer), only the surface heating caused increased cloud cover in the lee but any rainfall triggered was weak and intermittent. Conditions that were more conducive to convection ($RH \sim 85\%$ in the boundary layer) allowed the storm to extend spatially (up to 3–4 km^2) and the rainfall distribution to be less concentrated to the centre. Rainfall intensity was the least changeable characteristic, largely unaffected by changed in the control parameters. Air parcel theory was used to explain and provide a theoretical background to the phenomenon. By choosing a realistic low-level air temperature to represent the temperature of a heated parcel over the lava dome, an initial estimation of the local CAPE and CIN was used to gain insight on the storm characteristics as, depending on the conditions and wind speed, low level CAPE was increased from 20–21 J kg^{-1} to 50, and 80 J kg^{-1}, and CIN was decreased from a value between -13–-30 by 10–20 J kg^{-1}.

Studying the initialisation and evolution of the volcanically-triggered rainfall, a periodic behaviour was discovered. As moist air arrives it is forced to ascend, causing condensation and thick, low-level clouds over the lava dome. As new air is forced into this environment the cloud starts expanding, accompanied by the generation of rainfall. Towards the end of the cycle the cloud is advected away and the formation of a cloud begins anew. The cloud that is advected was seen to dissipate quickly after due to mixing with the dry air. The period of this cloud generation was seen to be consistent with cumulus cloud development timescales. Rather than having the deep ascent of a single updraft, this mechanism can be seen as the result of ascent of multiple thermals, ascending through the preconditioned environment, consistent with Kirshbaum (2013).

6.1.3 Moist atmospheric flow over Montserrat

In Chapter 5, high-resolution simulations using realistic topography based on a digital elevation model (DEM) of Montserrat were used to study volcanically-generated rainfall in a realistic context and the impact to volcanic hazards. The result of the flow over the

lava dome was the triggering of a localised storm with similar characteristics to those of the Chapter 4 simulations.

In order to explore the limits of the volcanically-triggered storm, a range of experiments were conducted for 3 different wind speeds (weak, moderate, and strong winds) and different wind directions. For a weak wind field, volcanically-generated rainfall remained a ubiquitous feature for all wind directions, acting to focus rainfall over the lava dome and changes in the topography (expressed by the change in wind direction) were seen to have a secondary effect. Increasingly stronger winds had a large impact in the results, causing a shift between a "convective" rainfall regime, where volcanically-triggered rainfall dominated the results, to an "orographic" regime with mechanically-forced convection, which resulted in the radical decrease in the area of the volcanically-triggered rainfall anomaly up to the point of complete inhibition.

There are two kinds of volcanic hazards tied with rainfall in Montserrat, explosive activity (accompanied by pyroclastic flows) and lahars. Rainfall intensity near the lava dome was over the threshold for triggering both, but the main focus in the chapter was on lahars, as advection by the wind forced the rainfall away from the dome in the parameter space studied here. Results from the most common wind speeds were analysed together in order to provide an estimate for the affected catchments in Montserrat, depending on different wind speeds. For low winds ($|U| \sim 1$ m s^{-1}) it was found that the majority of catchments in the lee of the lava dome were impacted by volcanically-triggered rainfall. For moderate winds ($|U| \sim 4$ m s^{-1}) the effect of volcanically-triggered rainfall was decreased and heavy rainfall occurred mainly on the windward side. Finally, for strong winds ($|U| \sim 7$ m s^{-1}) heavy rainfall occurred over the entire island, more consistent over the the catchments near the peaks. By compiling the main results, a checklist was created to help the observatory in Montserrat assess the hazard on a daily basis.

6.2 Conclusions

The aim of this study was to explore possible interactions between a volcano and a tropical atmosphere, specifically a lava dome-building volcano not undergoing an explosive eruption. The main effect was quickly found to be the introduction of a convective plume, borne from the heated air on top of the volcano. Under realistic conditions this was found

to be able to trigger rainfall by making use of the potential energy of the tropical atmosphere, to generate localised volcanically-triggered rainfall. For weak winds, this was found to occur over and in the lee of the lava dome and featured large, persistent rainfall rates (over 10 mm h^{-1}), sufficient to trigger volcanic hazards. In this way, even though the area of the immediate effect is constrained, the repercussions are not, especially when considering the impact on volcanic hazards. The positioning and persistence of the storm can increase the chance of lahar triggering during days with no large-scale rainfall and, although for the parameter space studied here the rainfall was generally advected away from the lava dome, the rainfall intensity is enough to increase the possibility of a rainfall-triggered dome collapse or pyroclastic flows. For stronger winds ($|U| > 7$ m s^{-1}) the effect of the heating is diminished as orographic rainfall dominates.

Despite the fact that the study was based on idealised simulations and a number of approximations were used, the results were kept realistic and general. In this sense, the studied mechanism can be applied to other lava-dome building volcanoes in the Tropics – the location of almost 45% of the active volcanoes. Considering that pyroclastic flows and lahars are the two most dangerous volcanic hazards, causing loss of both life and property, this illustrates the wider implications of this mechanism and a need for further, individual studies for other candidate volcanoes.

6.3 Future work

There are a number of ways that this work can be expanded, dealing with the degree of idealisation both in the atmosphere and in the way the volcano is represented. Radiation was neglected here as a simplification and to allow us to isolate the direct effect of the volcanic heating patch. However, a more realistic study of the temporal, daily evolution of the dome could be conducted. Another effect that was ignored was the cooling of the dome due to the rainfall – a mechanism that can act to eliminate the storm as the dome cools below the threshold required for convection. This mechanism is one of the triggers for rainfall-generated dome collapses (Matthews and Barclay, 2004) and further study is deemed necessary.

A more realistic representation of the volcano can also be studied, simulating the volcano as more than a heat source and including volcanic emissions such as chemicals

and ash. This would require use of more advanced models (for example WRF-Chem) in order to simulate the volcanic plume chemistry and advection as well as the atmosphere. Finally, the fine details of the plume, both spatially and temporally, can be studied by use of dedicated large eddy simulation (LES) models, such as Cloud Model 1 (CM1) – a high-resolution model specifically created to study deep convection and storm-generation. In order to carry out in-depth simulations of the plume a resolution of order 10 m would be required. The limited spatial extend of the volcanically-triggered storm lends itself to such ultra-high-resolution modelling. Another possible route to explore would be a more accurate representation of the dome topography. Due to their geological composition, volcanoes can be very steep, and this inherent steepness can enhance orographic rainfall. However, WRF, as an eta-coordinate model, is not equipped to deal with this, and as such, a different model would need to be utilised.

An additional way to extend the work would be to focus on other volcanoes in the Tropics. In the simulations presented in the thesis, the volcano characteristics were constrained to those of Montserrat, a relatively small volcano. There is a number of similar dome-building volcanoes where the results of the study could be used, including Arenal, Costa Rica, Concecion, Nicaragua, and Soputan, Indonesia. However, changes in the height of the lava dome, topography of the area, or a non-oceanic setting could all prove to be sources of variation in the results, as well as a change of focus to non-dome building volcanoes, such as Bulusan in the Philippines and Kelut in Indonesia.

Appendix A

A Short Atmospheric Thermodynamics Glossary

This appendix provides a short glossary to accompany the "Volcanically-generated Rainfall" handout (Figures 5.15 and A.1). It is aimed at "users" of the research who may be, for example, volcano observatory scientists. Four example soundings are also included, plotted on Skew-T diagrams, as generated from the University of Wyoming atmospheric soundings web page[1].

Atmospheric Inversion: A layer in which temperature increases with altitude. The principal characteristic of an inversion layer is its marked static stability, so that very little vertical transport can occur within it.

Atmospheric Sounding: A profile of atmospheric measurements (such as temperature or water vapour) at various heights or pressure levels.

Convective Available Potential Energy, *CAPE* (J kg^{-1}): CAPE is a measure of instability through the depth of the atmosphere, related to updraft strength in storms. Forecasters often refer to "weak" (CAPE less than 1000 J kg^{-1}), "moderate" (CAPE from 1000–2500 J kg^{-1}), "strong" (CAPE from 2500–4000 J kg^{-1}), and "extreme" (CAPE greater than 4000 J kg^{-1}) instability.

Convective Inhibition, *CIN* or *CINS* (J kg^{-1}): Convective inhibition represents resistance to convection in the atmosphere. An air parcel must have enough energy to overcome this for storm initiation.

[1] weather.uwyo.edu/upperair/sounding.html

Level of Free Convection, *LFC* or *LFCT* (km or hPa): The LFC is the level at which a lifted air parcel begins to move freely upwards.

Lifted Index, *LI* or *LIFT*: The lifted index is the temperature difference between the 500 hPa temperature and the temperature of a parcel lifted to 500 hPa. Negative values denote unstable conditions. LI is more of a measure of actual "instability" than CAPE because it represents the potential buoyancy of a parcel at a level, whereas CAPE is integrated through the depth of the troposphere.

Mixing Ratio (kg kg^{-1}): The ratio of the mass of a variable atmospheric constituent to the mass of dry air. Here, this refers to water.

Precipitable Water (mm): The total atmospheric water vapour contained in a vertical column of unit cross-sectional area extending between any two specified levels, commonly expressed in terms of the height to which that water substance would stand if completely condensed and collected in a vessel of the same unit cross section.

Shallow/Deep Convection: Convection in the atmosphere occurs when thermally driven turbulent mixing is present. Shallow convection occurs when vertical motions take parcels from the lower atmosphere to a height below 500 hPa (approximately 6 km), while deep convection occurs when the parcels are taken above 500 hPa.

Skew-T Graph: A thermodynamic diagram used for forecasting (see Figures A.2–A.5). It shows curves that depict the paths followed by lifted parcels. The basic curves are temperature (purple lines that slope up to the right), potential temperature (green lines that slope up to the left), and equivalent potential temperature (blue lines).

Definitions are modified from the NOAA "Explanation of SPC Severe Weather Parameters"[2] and the American Meteorological Society "Glossary of Metorology"[3] sites.

[2] http://www.spc.noaa.gov/sfctest/help/sfcoa.html
[3] http://glossary.ametsoc.org/wiki/Main_Page

Volcanically-Generated Rainfall Over Montserrat

Explanation

As air flows over a lava dome it is heated. If the dome is sufficiently hot, and atmospheric conditions allow for it, then localised deep convection can be triggered with deep clouds and intense rainfall, capable of triggering volcanic hazards such as lahars and pyroclastic flows.

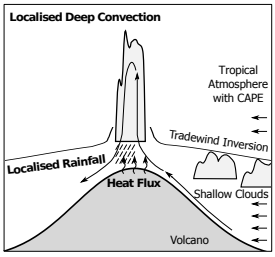

Atmospheric Soundings and Glossary

Vertical profiles of temperature, humidity and wind are regularly made by radiosondes. Sounding diagnostics are used to determine the potential for convective conditions and rainfall, including:

Name	Indicates
MLMR (Mean Mixed Layer Mixing Ratio, g kg^{-1})	Humidity
The mean water vapour mixing ratio over the lower atmosphere	
LFCT (Level of Free Convection, hPa)	Humidity/Stability
The height at which an air parcel will become buoyant	
CINS (Convective Inhibition, J Kg^{-1})	Stability
The least amount of energy a parcel needs to have to ascent	
WIND VECTORS (knots)	Mechanical Energy
Wind speed and direction. Wind speed is shown in knots: -Half a barb indicates 5 knots -A full barb indicates 10 knots	

What type of rainfall is likely?

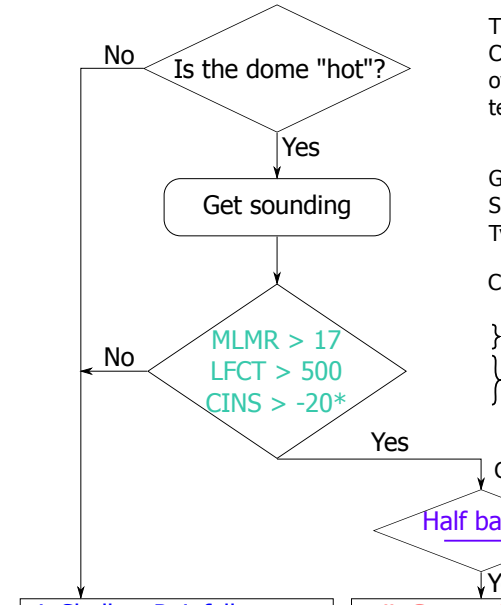

The lava dome temperature is the driving force of the rainfall. Computer simulations have shown that the average surface temperature over the lava dome needs to be at least 20 K over the surface temperature away from the dome.

Go to weather.uwyo.edu/upperair/sounding.html
Select "GIF: Skew-T" for the "**Type of plot**" field, and a day.
Type "78897" (Le Raizet, Guadeloupe) or "78526" (San Juan, Puerto Rico) for "**Station number**".
Check these numbers on the right side of the sounding.
This is to check how humid the atmosphere is.
} Rainfall requires a high humidity content in the atmosphere.
} These are to check how stable the atmosphere is.
} Rainfall needs a layer of potential instability at a relatively low height.
*Remember, -15>-20, but -30<-20.

Check the 2 lowest wind vectors in the right hand side of the sounding.

Conditions	i. Shallow Rainfall	ii. Convective Rainfall	iii. Windward-side Rainfall	iv. Storm Conditions
	Clear atmosphere and dome visible. Shallow convection (<1mm hr^{-1}) or no rainfall expected, concentrated on the windward-side.	Generally clear atmosphere with clouds near dome. High amounts of volcanically-triggered rainfall near dome can be expected.	Deep clouds and significant rainfall on the windward side. Low chance of enhanced volcanically-triggered rainfall in the lee of the dome.	Significant amounts of rainfall expected all over the island.

*Indicative pictures

Lahar triggering from volcanically-generated rainfall

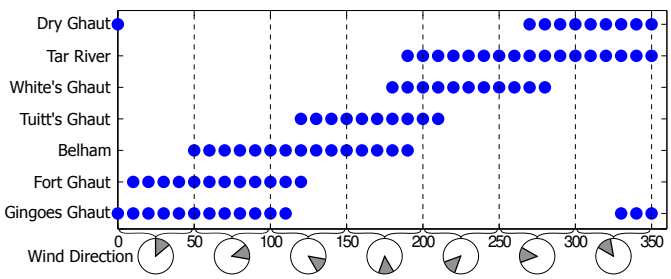

On days when volcanically-triggered rainfall is expected (Categories ii-iii), numerical simulations give rainfall rates over 10 mm h^{-1} within 1 km of the dome.
To see an estimate of catchments that could be affected, look at the lowest 2 wind vectors on the bottom right side of the sounding and estimate the wind direction.

To estimate the wind direction, try placing the wind vector in one of the small circles on the left, with the tip pointing towards the centre.

Useful links
http://www.spc.noaa.gov/sfctest/help/sfcoa.html - Detailed explanations of sounding parameters
http://www.theweatherprediction.com/thermo/skewt - An introduction to a Skew-T graph

Contact Details
Alex Poulidis - a.pouldis@uea.ac.uk
Ian Renfrew - i.renfrew@uea.ac.uk
Adrian Matthews - a.j.matthews@uea.ac.uk

Figure A.1: Larger version of the handout to be made available to volcano observatories.

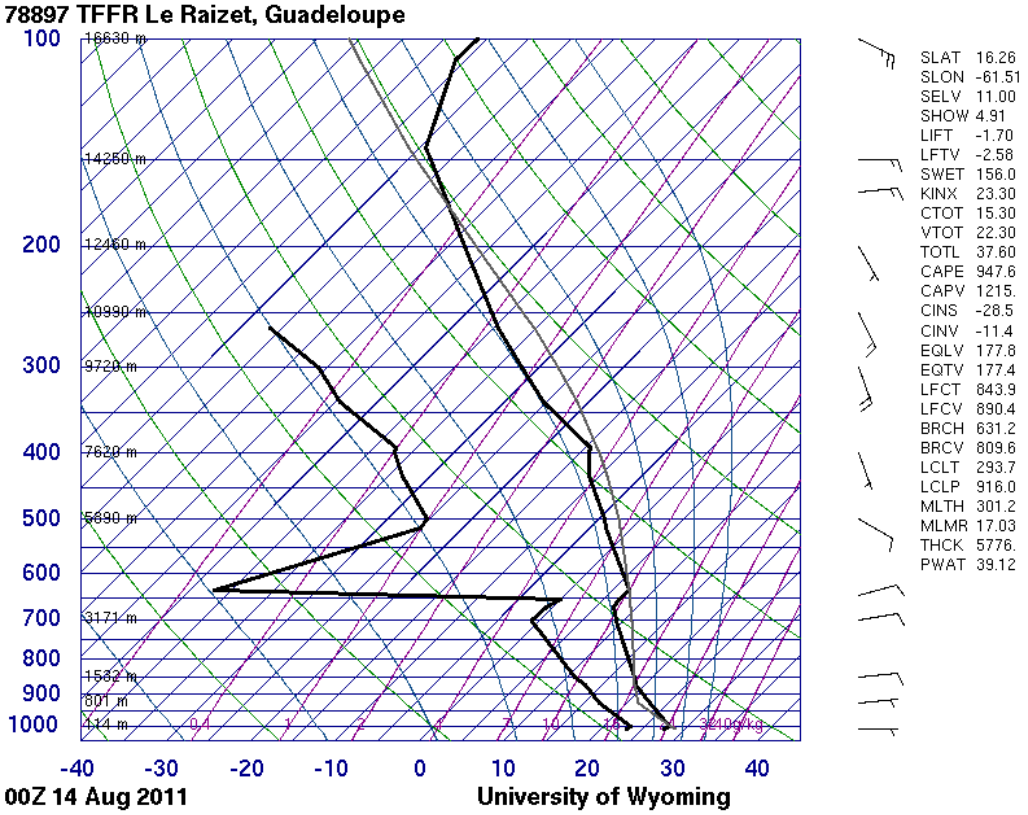

Figure A.2: A sample sounding for Category i (Shallow Rainfall). All soundings are obtained from the University of Wyoming atmospheric soundings web page.

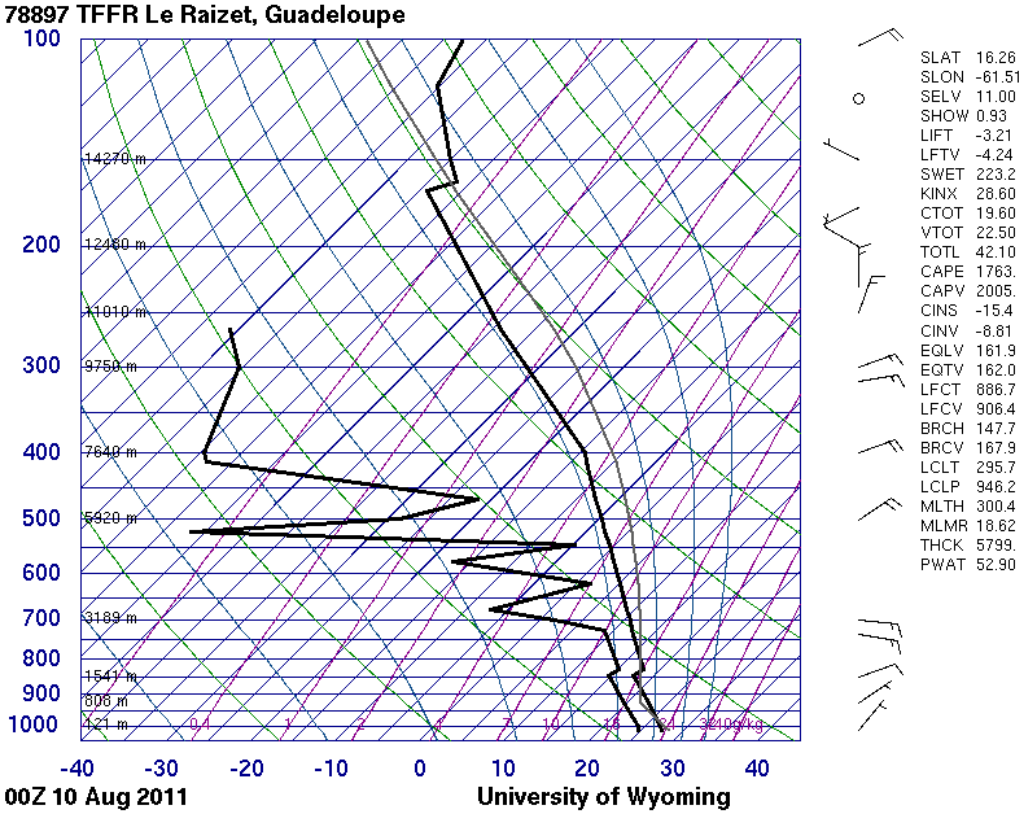

Figure A.3: A sample sounding for Category ii (Convective Rainfall).

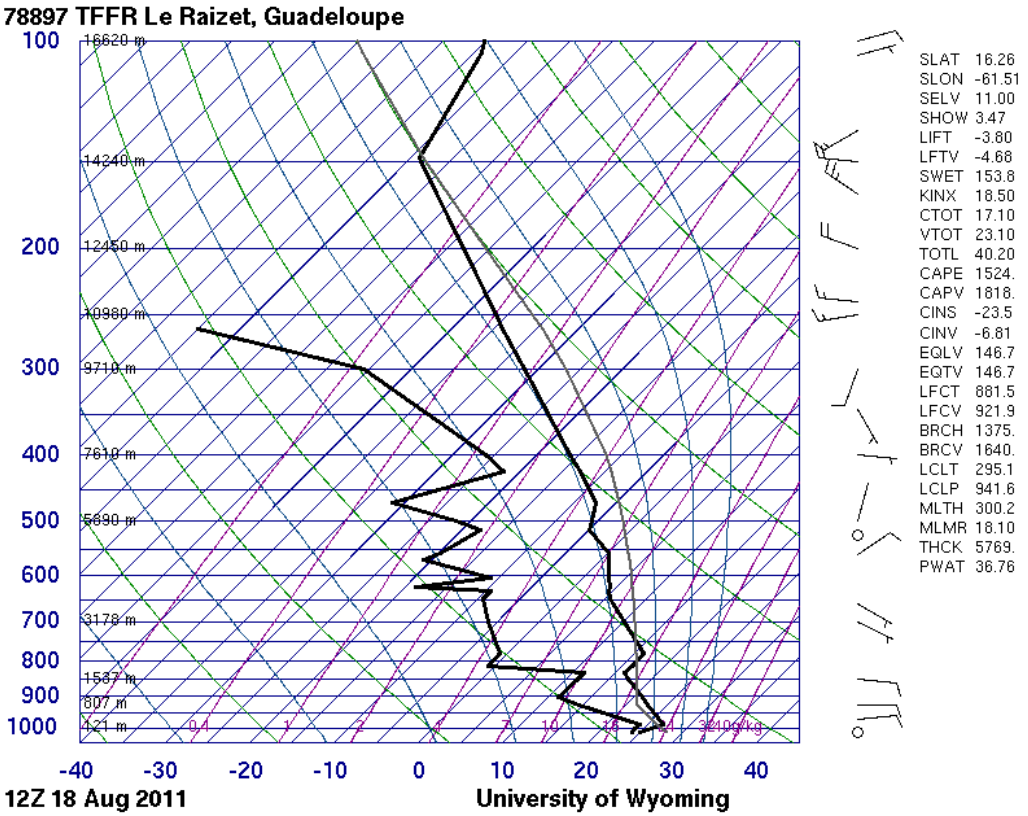

Figure A.4: A sample sounding for Category iii (Windward-side Rainfall).

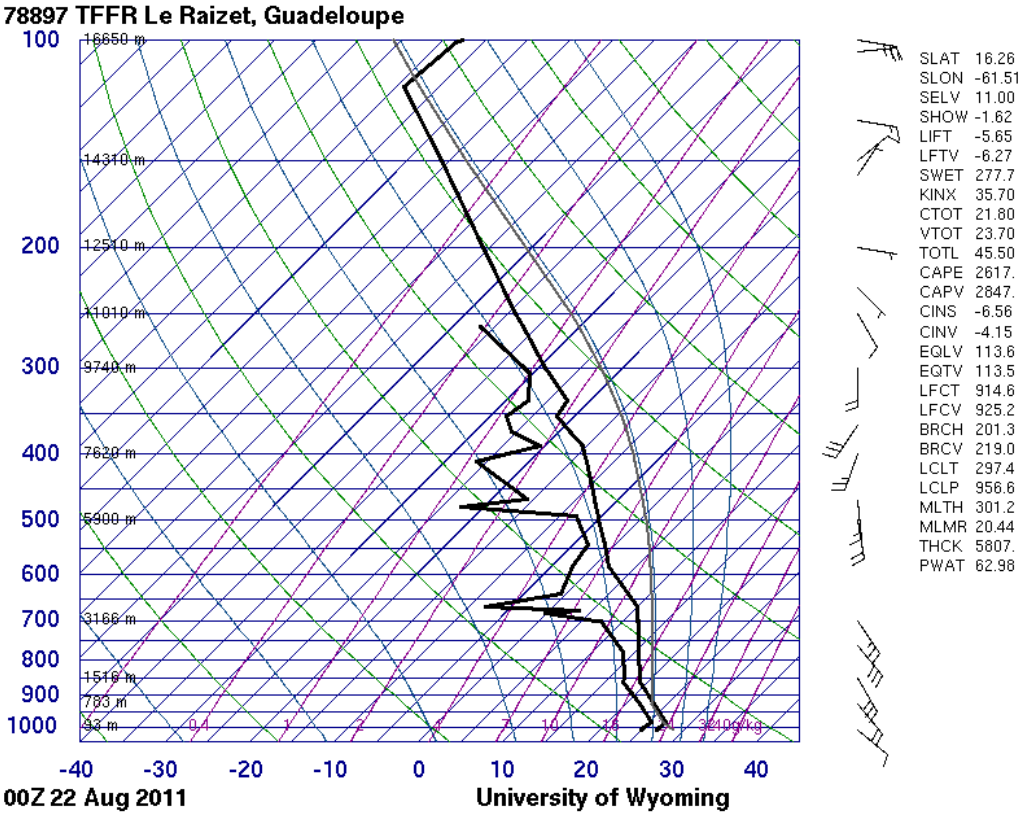

Figure A.5: A sample sounding for Category iv (Storm Conditions).

References

Barclay, J., J. E. Johnstone, and A. J. Matthews (2006), Meteorological monitoring of an active volcano: Implications for eruption prediction, *J. Volcanol. Geoth. Res.*, *150*(4), 339–358.

Barros, A. P., and D. P. Lettenmaier (1994), Dynamic modeling of orographically induced precipitation, *Rev. Geophys.*, *32*(94), 265–284.

Belcher, S. E., and J. C. R. Hunt (1998), Turbulent flow over hills and waves, *Annu. Rev. Fluid Mech.*, *30*(1), 507–538.

Bryan, G. H., J. C. Wyngaard, and J. M. Fritsch (2003), Resolution requirements for the simulations of deep moist convection, *Mon. Weather Rev.*, *131*(10), 2394–2416.

Carn, S. A., R. B. Watts, G. Thompson, and G. E. Norton (2004), Anatomy of a lava dome collapse: the 20 March 2000 event at Soufrière Hills Volcano, Montserrat, *J. Volcanol. Geoth. Res.*, *131*(3), 241–264.

Cécé, R., D. Bernard, C. d'Alexis, and J.-F. Dorville (2014), Numerical simulations of island-induced circulations and windward katabatic flow over the Guadeloupe Archipelago, *Mon. Weather Rev.*, *142*(2), 850–867.

Chen, S.-H., and Y.-L. Lin (2005), Orographic effects on a conditionally unstable flow over an idealized three-dimensional mesoscale mountain, *Meterol. Atmos. Phys.*, *88*(1–2), 1–21.

Cole, P. D., V. Bass, T. Christopher, C. Eligon, C. Murrell, H. M. Odbert, P. Smith, R. C. Steward, A. Stinton, R. Syers, R. Robertson, and P. Williams (2010), *Report to the scientific advisory committee on volcanic activity at Soufrire Hills Volcano, Montserrat: report on activity between 28 February 2010 and 31 October 2010*, Tech. rep., Monsterrat Volcano Observatory.

Crook, N. A., and D. F. Tucker (2005), Flow over heated terrain . Part I : Linear theory and idealized numerical simulations, *Mon. Weather Rev.*, *133*(9), 2552–2564.

Cuijipers, J. W. M., and P. G. Duynkerke (1993), Large eddy simulation of Trade Wind cumulus clouds, *Journal of Atmospheric Sciences*, *50*(23), 3894–3908.

Cunningham, P., S. L. Goodrick, M. Y. Hussaini, and R. R. Linn (2005), Coherent vertical structures in numerical simulations of buoyant plumes from wildland fires, *Int. J. Wildland Fire*, *14*(1), 61–75.

Cunningham, P., and M. J. Reeder (2009), Severe convective storms initiated by intense wildfires: Numerical simulations of pyro-convection and pyro-tornadogenesis, *Geophys. Res. Lett.*, *36*(12), L12,812.

Derbyshire, S. H., I. Beau, P. Bechtold, J.-Y. Grandpeix, J.-M. Piriou, J.-L. Redelsperger, and P. M. M. Soares (2004), Sensitivity of moist convection to environmental humidity, *Q. J. R. Meteorol. Soc.*, *130*(604), 3055–3079.

Dixon, P. G., and T. L. Mote (2003), Patterns and causes of Atlanta's urban heat island initiated precipitation, *J. Appl. Meteorol.*, *42*(9), 1273–1284.

Drazin, P. G. (1961), On the steady flow of a fluid of variable density past an obstacle, *Tellus*, *13*(2), 239–251.

Dunion, J. P. (2011), Rewriting the climatology of the tropical North Atlantic and Caribbean Sea atmosphere, *J. Climate*, *24*(3), 893–908.

Durant, A. J., R. A. Shaw, W. I. Rose, Y. Mi, and G. G. J. Ernst (2008), Ice nucleation and overseeding of ice in volcanic clouds, *J. Geophys. Res.-Atmos.*, *113*(D9), 1984–2012.

Durran, D. R. (1990), Mountain waves and downslope winds, *Atmospheric Processes over Complex Terrain, Meteorological Monographs*, *23*(45), 59–81.

Eckermann, S. D., J. Lindeman, D. Broutman, J. Ma, and Z. Boydeyi (2010), Momentum fluxes of gravity waves generated by variable Froude number flow over three-dimensional obstacles, *J. Atmos. Sci.*, *67*(7), 2260–2278.

Eliassen, A., and E. Palm (1961), On the transfer of energy in stationary mountain waves, *Geofysiske Publikasjoner*, *22*, 1–23.

Francis, P. (2008), *Volcanoes, a planetary perspective*, Oxford University Press.

Froude, M. (2015), *Lahar dynamics in the Belham River Valley, Montserrat: Application of remote camera-based monitoring for improved sedimentological interpretation of post-event deposits*, Ph.D. thesis, University of East Anglia.

Gatebe, C. K., T. Varnai, R. Poudyal, C. Ichoku, and M. D. King (2012), Taking the pulse of pyrocumulus clouds, *Atmos. Environ.*, *52*, 121–130.

Hale, A. J., and G. Wadge (2008), The transition from endogenous to exogenous growth of lava domes with the development of shear bands, *J. Volcanol. Geoth. Res.*, *171*(3), 237–257.

Hicks, P. D., M. J. Cooker, and A. J. Matthews (2014), Saturation front evolution for liquid infiltration into a gas filled porous medium with counter-current flow, *European J. Mech. B/Fluids*, *43*, 202–215.

Hicks, P. D., A. J. Matthews, and M. J. Cooker (2009), Thermal structure of a gas-permeable lava dome and timescale separation in its response to perturbation, *J. Geophys. Res.*, *114*(B7), 1978–2012.

Hicks, P. D., A. J. Matthews, and M. J. Cooker (2010), Triggering of a volcanic dome collapse by rainwater infiltration, *J. Geophys. Res.*, *115*(B9), 1–8.

Hong, S.-Y., and J.-O. J. Lin (2006), The WRF single-moment 6-class microphysics scheme (WSM6), *J. Korean Meteorol. Soc.*, *42*(2), 129–151.

Hort, M., R. Seyfried, and M. Vöge (2003), Radar doppler velocimetry of volcanic eruptions: Theoretical considerations and quantitative documentation of changes in eruptive behaviour at Stromboli Volcano, Italy, *Geophys. J. Int.*, *154*(2), 515–532.

Houze, R. A. J. (2012), Orographic effect on precipitating clouds, *Rev. Geophys.*, *50*(RG1001), 1–47.

Hunt, J. C. R., H. Olafsson, and P. Bougeault (2001), Coriolis effects on orographic and mesoscale flows, *Q. J. Meteor. Soc.*, *127*(572), 601–633.

Jiang, Q., R. B. Smith, and J. D. Doyle (2008), Impact of the atmospheric boundary layer on mountain waves, *J. Atmos. Sci.*, *65*(2), 592–608.

Jordan, C. L. (1958), Mean soundings for the West Indies area, *J. Meteor.*, *15*, 91–97.

Kirshbaum, D. J. (2011), Cloud-resolving simulations of deep convection over a heated mountain, *J. Atmos. Sci.*, *68*(2), 361–378.

Kirshbaum, D. J. (2013), On thermally forced circulations over heated terrain, *J. Atmos. Sci.*, *70*(6), 1690–1709.

Kirshbaum, D. J., and D. R. Durran (2004), Factors governing cellular convection in orographic precipitation, *J. Atmos. Sci.*, *61*(6), 682–698.

Kirshbaum, D. J., and J. Fairman (2014), Cloud trails past the Lesser Antilles, *Mon. Wea. Rev., doi: 10.1175/MWR-D-14-00254.1*.

Kirshbaum, D. J., and R. B. Smith (2009), Orographic precipitation in the Tropics: Large-eddy simulations and theory, *J. Atmos. Sci.*, *66*(9), 2559–2578.

Kirshbaum, D. J., and C.-C. Wang (2014), Boundary layer updrafts driven by airflow over heated terrain, *J. Atmos. Sci.*, *71*(4), 1425–1442.

Klemp, J. B., J. Dudhia, and A. D. Hassiotis (2008), An upper gravity-wave absorbing layer for NWP applications, *Mon. Weather Rev.*, *136*(10), 3987–4004.

Knievel, J. C., G. H. Bryan, and J. P. Hacker (2007), Explicit numerical diffusion in the WRF model, *Mon. Weather Rev.*, *135*(11), 3808–3824.

Lane, S. J., and J. S. Gilbert (1992), Electric potential gradient changes during explosive activity at Sakurajima volcano, Japan, *Bull. Volcanol.*, *54*(7), 590–594.

Lewis, H. W., S. D. Mobbs, S. B. Vosper, and A. R. Brown (2008), The effect of surface heating on hill-induced flow separation, *Bound.-Lay. Meteorol.*, *129*(2), 269–287.

Lin, C. Y., W.-C. Chen, P.-L. Chang, and Y.-F. Sheng (2011), Impact of the urban heat island effect on precipitation over a complex geographic environment in northern Taiwan, *J. Appl. Meteorol. Climatol.*, *50*(2), 339–353.

Lin, Y.-L., R. D. Rarley, and H. D. Orville (1983), Bulk parameterization of the snow field in a cloud model, *J. Appl. Meteorol.*, *22*, 1065–1092.

Long, R. R. (1954), Some aspects of the flow of stratified fluids. II. Experiments with a two fluid system, *Tellus*, *6*(2), 97–115.

Lundquist, K. A., F. Katapodes-Chow, and J. K. Lundquist (2010), An immersed boundary method for the Weather Research and Forecasting model, *Mon. Weather Rev.*, *138*(3), 796–817.

Macfarlane, D. G., H. M. Odbert, D. A. Robertson, M. R. James, H. Pinkerton, and G. Wadge (2012), Topographic and thermal mapping of volcanic terrain using the AVTIS ground-based 94-GHz dual-mode radar/radiometric imager, *IEEE T. Geosci. Remote*, pp. 1–18.

Major, J. J., and C. G. Newhall (1989), Snow and ice perturbation during historical volcanic eruptions and the formation of lahars and floods, *Bull. Volcanol.*, *52*(1), 1–27.

Mastin, L. G. (1994), Explosive tephra emissions at Mount St. Helens. 1989–1991: The violent escape of magmatic gas following storms?, *Geol. Soc. Am. Bull.*, *106*(2), 175–185.

Matthews, A. J., and J. Barclay (2004), A thermodynamical model for rainfall-triggered volcanic dome collapse, *Geophys. Res. Lett.*, *31*(5), 1–4.

Matthews, A. J., J. Barclay, S. Carn, G. Thompson, J. Alexander, R. Herd, and C. Williams (2002), Rainfall-induced volcanic activity in Montserrat, *Geophys. Res. Lett.*, *29*(13), 1–4.

Matthews, A. J., J. Barclay, and J. E. Johnstone (2009), The fast response of volcano-seismic activity to intense precipitation: Triggering of primary volcanic activity by rainfall at Soufrière Hills Volcano, Montserrat, *J. Volcanol. Geoth. Res.*, *184*(3), 405–415.

Melnik, O., and R. S. J. Sparks (1999), Nonlinear dynamics of lava dome extrusion, *Nature*, *402*(6757), 37–41.

Miglietta, M. M., and A. Buzzi (2001), A numerical study of moist stratified flows over isolated topography, *Tellus A*, *53*(4), 481–499.

Minder, J. R., R. B. Smith, and A. D. Nugent (2013), The dynamics of ascent-forced orographic convection in the Tropics: Results from Dominica, *J. Atmos. Sci.*, *70*(12), 4067–4088.

Ólafsson, H., and P. Bougeault (1996), Nonlinear flow past an elliptic mountain ridge, *J. Atmos. Sci.*, *53*(17), 2465–2489.

Pareschi, M. T. (1996), Physical modelling of eruptive phenomena: Lahars, in: *Monitoring and Mitigation of Volcanic Hazards* (Scarpa, R., and R. I. Tilling, eds.).

Parfitt, E. A., and L. Wilson (2008), *Fundamentals of physical volcanology*, Blackwell Publishing.

Petersen, G. N., H. Ólafsson, and J. E. Kristjánsson (2003), Flow in the lee of idealized mountains and Greenland, *J. Atmos. Sci.*, *60*(17), 2183–2195.

Queney, P. (1948), The problem of airflow over mountains: A summary of theoretical studies, *B. Am. Meteorol. Soc.*, *29*, 16–26.

Rea, W. J. (1974), The volcanic geology and petrology of Montserrat, West Indies, *J. Geol. Soc. London*, *130*(4), 341 – 366.

Rennó, N. O., and A. P. Ingersoll (1996), Natural convection as a heat engine: A theory for CAPE, *J. Atmos. Sci.*, *53*(4), 572–585.

Robertson, R. E. A., W. P. Aspinall, R. A. Herd, G. E. Norton, R. S. J. Sparks, and S. R. Young (2000), The 1995-1998 eruption of the Soufrière Hills volcano, Montserrat, WI, *Philos. T. Roy. Soc. A.*, *358*, 1619–1637.

Roe, G. H. (2005), Orographic precipitation, *Annu. Rev. Earth Pl. Sc.*, *33*(1), 645–671.

Roeloffzen, J. C., W. D. Van Den Berg, and J. Oerlemans (1986), Frictional convergence at coastlines, *Tellus A*, *38*(5), 397–411.

Rosenfeld, D., U. Lohmann, G. B. Raga, C. D. O'Dowd, M. Kulmala, S. Fuzzi, R. A., and M. O. Andreae (2008), Flood or drought: How do aerosols affect precipitation, *Science*, *321*, 1309–1313.

Rutledge, S. A., and P. Hobbs (1983), The mesoscale and microscale structure and organization of clouds and precipitation in midlatitude cyclones. Part VIII: A model for the 'seeder-feeder' process in warm-frontal rainbands, *J. Atmos. Sci.*, *40*(5), 1185–1206.

Schlesinger, R. E. (1973), A numerical model of deep moist convection: Part I. Comparative experiments for variable ambient moisture and wind shear, *J. Atmos. Sci.*, *30*(5), 835–856.

Siebasma, A. P., C. S. Bretherton, A. Brown, A. Chlond, J. Cuxart, P. G. Duynkerke, H. Jiang, M. Khairoutdinov, D. Lewellen, C.-H. Moeng, E. Sanchez, B. Stevens, and D. E. Stevens (2003), A large eddy simulation intercomparison study of shallow cumulus convection, *Journal of Atmospheric Sciences*, *60*(10), 1201–1219.

Simkin, S., and L. Siebert (1994), Catalogue of active volcanoes of the world, in: *Internation Association of Volcanology and Earth's Interior*, Rome.

Skamarock, W. C., J. B. Klemp, J. Dudhia, D. O. Gill, D. M. Barker, M. G. Duda, X.-Y. Huang, W. Wang, and J. G. Powers (2008), *A description of the advanced research WRF version 3*, Tech. rep.

Smith, G. A., and W. J. Fritz (1989), Volcanic influences on terrestrial sedimentation, *Geology*, *17*(4), 375–376.

Smith, R. B. (1980), Linear theory of stratified hydrostatic flow past an isolated mountain, *Tellus*, *32*(4), 348–364.

Smith, R. B. (1989), Hydrostatic airflow over Mountains, *Adv. Geophys.*, *31*, 1–41.

Smith, R. B. (2007), Interacting mountain waves and boundary layers, *J. Atmos. Sci.*, *64*(2), 594–607.

Smith, R. B., and I. Barstad (2004), A linear theory of orographic precipitation, *J. Atmos. Sci.*, *61*(12), 1377–1391.

Smith, R. B., A. C. Gleason, P. A. Gluhosky, and G. V. (1997), The wake of St. Vinect, *J. Atmos. Sci.*, *54*(4), 606–623.

Smith, R. B., J. R. Minder, A. D. Nugent, T. Storelvmo, D. J. Kirshbaum, R. Warren, N. Lareau, P. Palany, A. James, and J. French (2012), Orographic precipitation in the Tropics: The Dominica experiment, *B. Am. Meteorol. Soc.*, *93*(10), 1567–1579.

Smith, R. B., P. Schaffer, D. J. Kirshbaum, and E. Regina (2009), Orographic precipitation in the Tropics: Experiments in Dominica, *J. Atmos. Sci.*, *66*(6), 1698–1716.

Smolarkiewicz, P. K., R. M. Rasmussen, and T. L. Clark (1988), On the dynamics of Hawaiian cloud bands: Island forcing, *Journal of Atmospheric Sciences*, *45*(13), 1872–1905.

Smolarkiewicz, P. K., and R. Rotunno (1989), Low Froude number flow past three-dimensional obstacles. Part 1: Baroclinically generated lee vortices, *J. Atmos. Sci.*, *46*(8), 1154–1164.

Smolarkiewicz, P. K., and R. Rotunno (1990), Low Froude number flow past three-dimensional obstacles. Part 2: Upwind flow reversal zone, *J. Atmos. Sci.*, *47*(12), 1498–1511.

Souza, E. P., N. O. Rennó, and M. A. F. Silva Dias (2000), Convective circulations induced by surface heterogeneities, *J. Atmos. Sci.*, *57*(17), 2915–2922.

Sparks, R. S. J., and S. R. Young (2002), The eruption of Soufrière Hills Volcano, Montserrat (1995-1999): Overview of scientific results, *Geol. Soc. London Mem.*, *21*(1), 45–69.

Stevens, B., and G. Feingold (2009), Untangling aerosol effects on clouds and precipitation in a buffered system, *Nature*, *461*(1), 607–613.

Tian, W., and D. J. Parker (2003), A modeling study and scaling analysis of orographic effects on boundary layer shallow convection, *J. Atmos. Sci.*, *60*(16), 1981–1991.

Tilling, R. I. (1989), Volcanic hazards and their mitigation: Progress and problems, *Rev. Geophys.*, *27*(2), 237–269.

Tucker, D. F., and N. A. Crook (2005), Flow over heated terrain. Part II: Generation of convective precipitation, *Mon. Weather Rev.*, *133*(9), 2565–2582.

Violette, S., G. de Marsily, J. P. Carbonnel, P. Goblet, E. Ledoux, S. M. Tijani, and G. Vouille (2001), Can rainfall trigger volcanic eruptions? A mechanical stress model of an active volcano: 'Piton de la Fournaise', Reunion Island, *Terra Nova*, *13*(1), 18–24.

Voight, B., E. K. Constantine, S. Siswowidjoyo, and R. Torley (2000), Historical eruptions of Merapi Volcano, Central Java, Indonesia, 1768–1998, *J. Volcanol. Geoth. Res.*, *100*(1), 69–138.

Voight, B., R. S. J. Sparks, A. D. Miller, R. C. Stewart, R. P. Hoblitt, A. Clarke, J. Ewart, W. P. Aspinall, B. Baptie, E. S. Calder, P. Cole, T. H. Druitt, C. Hartford, R. A. Herd, P. Jackson, A. M. Lejeune, A. B. Lockhart, S. C. Loughlin, R. Luckett, L. Lynch, G. E. Norton, R. Robertson, I. M. Watson, R. Watts, and S. R. Young (1999), Magma flow instability and cyclic activity at Soufrière Hills Volcano, Montserrat, British West Indies, *Science*, *283*(5405), 1138–1142.

Wadge, G. (2004), Measuring the rate of lava effusion by InSAR, in: *Proceedings of FRINGE 2003 Workshop, 1–5 Dec. 2003 (SP-550, June 2004)*.

Wadge, G., B. Voight, R. S. J. Sparks, P. D. Cole, S. C. Loughlin, and R. E. A. Robertson (2014), An overview of the eruption of Soufrière Hills Volcano, Montserrat from 2000 to 2010, *Geol. Soc. London Mem.*, *39*(1), 1–40.

Watson, C. D., and T. P. Lane (2014), Further sensitivities of orographic precipitation to terrain geometry in idealized simulations, *J. Atmos. Sci.*, *71*, 3068–3089.

Weng, W., L. Chan, P. A. Taylor, and D. Xu (1997), Modelling stably stratified boundary-layer flow over low hills, *Q. J. Meteor. Soc.*, *123*(543), 1841–1866.

Yamaguchi, Y., A. B. Kahle, H. Tsu, T. Kawakami, and M. Pniel (1998), Overview of Advanced Spaceborne Thermal Emission and Reflection Radiometer (ASTER), *IEEE T. Geosci. Remote*, *36*(4), 1062–1071.

Yamasato, H., S. Kitagawa, and M. Komiya (1998), Effect of rainfall on dacitic lava dome collapse at Unzen Volcano, Japan, *Pap. Meteorol. Geophys.*, *48*(3), 73–78.

Zhong, S., and F. Katapodes-Chow (2013), Meso- and Fine-Scale Modeling over Complex Terrain: Parameterizations and Applications, in: *Mountain Weather Research and Forecasting* (Katapodes-Chow, F., S. F. J. DeWekker, and B. J. Snyder, eds.), pp. 591–653.

Zipser, E. J., and K. R. Lutz (1994), Vertical profile of radar reflectivity of convective cells: A strong indicator of storm intensity and lightning probability?, *Mon. Weather Rev.*, *122*(8), 1751–1759.